PhD-FSTM-2023-098
The Faculty of Science, Technology and Medicine

DISSERTATION

Defense held on 08/09/2023 in Luxembourg

to obtain the degree of

DOCTEUR DE L'UNIVERSITÉ DU LUXEMBOURG

EN INFORMATIQUE

by

Liz MARTINEZ MARRERO

Born on 1 February 1989 in La Habana, Cuba

DISTRIBUTED COHESIVE RADIO SYSTEMS FOR SPACEBORNE APPLICATIONS

Dissertation defense committee

Dr Juan Carlos Merlano Duncan, dissertation supervisor
Research Scientist, Université du Luxembourg

Dr Adriano Camps
Professor, Universitat Politècnica de Catalunya, Spain
ASPIRE Visiting International Professor, UAE University, UAE

Dr Bhavani Shankar Mysore Rama Rao, Chairman
Assistant Professor, Université du Luxembourg

Dr Alberto Ginesi
Head of the Telecommunication-TT&C Systems, ESA Research and Technology Centre (ESTEC), The Netherlands

Dr Symeon Chatzinotas, Vice-Chairman
Associate Professor, Université du Luxembourg

To my family.

The amazing family to whom I had the chance to be born;

the beautiful family that I'm creating with Luisma and Sammy;

and the wonderful family I have had the fortune of finding during this journey; these friends have become family.

Thank you!

Distributed Cohesive Radio Systems for Spaceborne Applications

Liz Martínez Marrero

Abstract

During the last decade, the use of small satellites has revolutionized the field of space exploration and communications. This has opened up new possibilities, such as the feasibility of grouping them into Cohesive Distributed Satellite Systems (CDSSs). A CDSS is a multi-satellite configuration that appears as a single solid entity from an external perspective, which includes data reception, processing, and transmission operations. This entails improving several DSS applications such as Earth observation, geolocation, navigation, imaging, and communications. The synchronization of CDSSs involves precisely aligning time, frequency, and phase among multiple satellites, which is a significant challenge due to the inherent characteristics of space-based environments. For instance, the spacecraft mobility, the round-trip delay, and the resource constraints make the synchronization of DSSs more challenging than its equivalent in wireless terrestrial networks. However, it is simultaneously an unavoidable challenge for future space communications. This requirement does not only apply to small satellites DSS but also to avoid interference in crowded orbits and enable the federated satellites' system paradigm.

This thesis aims to identify the technical synchronization requirements and design the synchronization and coordination techniques to perform cohesive transmission in a DSS. First, we studied the state-of-the-art synchronization techniques and analyzed their feasibility for DSS. Additionally, we summarized other methods related to the synchronization of DSS, such as inter-satellite ranging and positioning. Then, we considered a first approximation to the problem, assuming accurate time synchronization and relative positioning among the satellites in a DSS. This problem is equivalent to synchronizing the local oscillators' phase in a precoding-enabled multi-beam satellite system.

One of the most significant synchronization impairments for implementing CDSSs is the phase noise of the LOs in different spacecraft. In this regard, the two-state phase noise model was implemented and integrated into the channel emulator of the MIMO end-to-end satellite emulator, which allowed us to validate the results included in this thesis. Next, we analyzed the impact of the phase errors and uncertainties in operating a precoded forward link satellite communication system. We formally demonstrated that the uplink phase variations affect precoding performance even when all the LOs share a single frequency reference. Additionally, we identified the individual contributions of each system element to the overall synchronization uncertainties in practical precoding implementations. Besides, for linear and non-linear precoding, we formally demonstrated that the UTs can track slow time variations in the channel if they equally affect all the beams.

The compensation loop to mitigate these impairments was designed, implemented, and integrated into the GW of the MIMO end-to-end satellite emulator. The solution is a closed-loop algorithm that uses the periodical channel phase measurements sent to the GW by the UTs as part of traditional precoding implementations. The proportional-integral controller included in the GW calculates the compensation phase required to align all the beams to the phase of the designated reference beam. Besides, we compared different approaches to combine the channel phase estimations obtained from the UTs using the amplitude of the estimated channel and the UT's thermal noise. The compensation loop and the combining estimations hardware implementations were used in an experiment to assess the feasibility of the precoding technique for GEO satellite systems.

Acknowledgements

I would like to express my sincere gratitude to Dr. Juan Carlos Merlano Duncan, Prof. Symeon Chatzinotas, and Prof. Adriano Camps for their thoughtful supervision during my Ph.D. research. I would also like to thank Prof. Björn Ottersten, Dr. Jorge Querol, Dr. Jevgenij Krivochiza, Dr. Jorge Luis Gonzalez Rios, Dr. Alireza Haqiqatnejad, Dr. Sumit Kumar, and Dr. Shree Sharma for their collaboration in the scientific publications that are part of this document. Finally, I would like to thank all the colleagues from the Interdisciplinary Centre for Security, Reliability, and Trust (SnT), especially the members of the SIGCOM group, for their constant support, invaluable insights, and collaborative spirit.

Liz Martínez Marrero
Luxembourg, August 2023

Preface

This Ph.D. thesis has been carried out from January 2019 to September 2023, in part at the SIGCOM research group, SnT - Interdisciplinary Centre for Security, Reliability and Trust, University of Luxembourg, under the supervision of Dr. Juan Carlos Merlano Duncan, Prof. Symeon Chatzinotas, Dr. and Prof. Adriano Camps, Dr. (Universitat Politècnica de Catalunya). The time-to-time evaluation of the Ph.D. thesis was duly performed by the CET members constituting the supervisors and co-supervisors.

Contents

This Ph.D. thesis entitled "Distributed Cohesive Radio Systems for Spaceborne Applications" is divided into seven chapters. In Chapter 1, the introduction, motivation, synchronization of local oscillators (LOs) in multibeam satellites, and contributions of this thesis are described. Chapter 2 summarizes and categorizes the most relevant publications on synchronization techniques for distributed satellite systems (DSSs). Next, the impact of the phase errors and uncertainties in operating a precoded forward link satellite communication system are assessed in Chapter 3. Chapter 4 describes the hardware implementation of the model for the local oscillator's phase noise and obtains the resulting signal-to-noise-plus-interference ratio (SNIR) at the receivers. Then, Chapter 5 presents the compensation loop to synchronize the phase of each node of the distributed system and provides an example of its use in a geostationary orbit (GEO) scenario. Besides, the hardware implementation of the proposed solution is described in this chapter. Finally, Chapter 6 provides concluding remarks and future works.

Collaborations

This work was made possible with the generous support of the European Space Agency (ESA) and SES S.A. However, the views expressed in this work are those of the author and do not reflect the views of the European Space Agency (ESA) or SES S.A.

Support of the Thesis

This work was supported by the Luxembourg National Research Fund (FNR) under the CORE project COHESAT: Cognitive Cohesive Networks of Distributed Units for Active and Passive Space Applications, grant reference [FNR11689919] and by the European Space Agency under the project number 4000122451/18/NL/NR "Live Satellite Precoding Demonstration - CCN: MEO case (LiveSatPreDem). The effort of collaborators and dissemination costs were also supported by the ARMMONY project: Ground-Based Distributed Beamforming Harmonization For The Integration Of Satellite And Terrestrial Networks, grant reference [FNR16352790]. Additionally, the substantial support from SIGCOM is also gratefully acknowledged.

Declaration

Except where acknowledged customarily, the material presented in this thesis is, to the best of the authors' knowledge, original and has not been submitted in whole or part for a degree in any university.

Publication List

Journals

[I] J. Merlano-Duncan, L. Martinez-Marrero, J. Querol, S. Kumar, A. Camps, S. Chatzinotas, and B. Ottersten, "A Remote Carrier Synchronization Technique for Coherent Distributed Remote Sensing Systems," *IEEE Journal of Selected Topics in Applied Earth Observations and Remote Sensing,* vol. 14, pp. 1909-1922, 2021, doi: 10.1109/JSTARS.2020.3046776.

[II] L. Martinez Marrero, J. Merlano-Duncan, J. Querol, S. Kumar, J. Krivochiza, S. Sharma,

S. Chatzinotas, A. Camps and B. Ottersten, "Architectures and Synchronization Techniques for Distributed Satellite Systems: A Survey," *IEEE Access,* vol. 10, pp. 45375–45409, 2022, doi: 10.1109/ACCESS.2022.3169499.

[III] L. Martinez Marrero, A. Haqiqatnejad, J. Merlano Duncan, S. Chatzinotas and B. Ottersten, "Multiuser-MISO Precoding Under Channel Phase Uncertainty in Satellite Communication Systems," *IEEE Open Journal of Vehicular Technology,* vol. 4, pp. 127-148, 2023, doi: 10.1109/OJVT.2022.3221841.

[IV] L. Martinez Marrero, J. Merlano Duncan, J. Luis Gonzalez, J. Krivochiza, S. Chatzinotas, B. Ottersten and A. Camps, "Accurate phase synchronization for Precoding-enabled GEO multibeam satellite systems," *IEEE Open Journal of the Communications Society* - submitted

Conference/Workshop Papers

[V] L. Martinez Marrero, J. Merlano Duncan, J. Querol, S. Chatzinotas, A. Camps and B. Ottersten, "Effects of multiple oscillator phase noise in Precoding performance," *ICSSC 2019; 37th International Communications Satellite Systems Conference,* 2019, pp. 699-713, 2021, doi: 10.1109/OJCOMS.2021.3093106.

[VI] L. Martinez Marrero, J. Merlano Duncan, J. Querol, S. Chatzinotas, A. Camps and B. Ottersten, "A design strategy for phase synchronization in Precoding-enabled DVB-S2X user terminals," *ICC 2021; IEEE International Conference on Communications,* 2021, pp. 1-7, doi: 10.1109/ICC42927.2021.9500634.

[VII] L. Martinez Marrero, J. Merlano Duncan, J. Querol, N. Maturo, J. Krivochiza, S. Chatzinotas and B. Ottersten, "Differential Phase Compensation in Over-the-air Precoding Test-bed for a Multi-beam Satellite," *WCNC 2022; IEEE Wireless Communications and Networking Conference,* 2022, pp. 1325-1330, doi: 10.1109/WCNC51071.2022.9771918.

Contents

List of Figures

List of Tables

Abbreviations

ADC	analog-to-digital converter
AP	access point
ARNS	augmented relative navigation system
ASP	adaptive synchronous parallel
BioRARSA	robust adaptive random search algorithm
BS	base station
BSP	bulk synchronous parallel
CDSS	cohesive distributed satellite system
CF	cell-free
CFO	carrier frequency offset
ChEm	channel emulator
CI	constructive interference
CIR	constructive interference region
CNN	convolutional neural network
CoMP	coordinated multipoint
COTS	commercial off-the-shelf
CPU	central processing unit
CRLB	Cramer-Rao lower bound
CSI	channel state information
DBF	distributed beamforming
DCA	distributed consensus algorithm

DOWR	dual one-way ranging
DOWT	dual one-way time
DRT	dehop-rehop transponder
DSP	digital signal processor
DSS	distributed satellite system
DTB	distributed transmit beamforming
DVB-S2X	extension of the Digital Video Broadcasting - Satellite second generation
D1BF	deterministic one-bit feedback
EKF	extended Kalman filter (KF)
E1BF	enhanced one-bit feedback
FDD	frequency division duplex
FDM	frequency division multiplexing
FFT	fast Fourier transform
FH-FDMA	frequency hopping - frequency division multiple access
FLL	frequency-locked loop
FM	frequency modulated
FPGA	field programmable gate arrays
F-RT	frequency-slotted round-trip
FSS	federated satellite system
FTSP	flooding time synchronization protocol
GEO	geostationary orbit
GNSS	global navigation satellite system
GPS	global positioning system
GRACE	gravity recovery and climate experiment
GRAIL	gravity recovery and interior laboratory
GW	gateway
HIL	hardware-in-the-loop

IF	intermediate frequency
IoSat	internet of satellites
InSAR	interferometric synthetic aperture radar
ISL	inter-satellite link
KBR	K-band microwave ranging
KF	Kalman filter
LAMBDA	least-squares ambiguity decorrelation adjustment
LEO	low-Earth orbit
LISA	laser interferometer space antenna
LO	local oscillator
LOS	line of sight
LSTM	long short-term memory
MAE	mean absolute error
MANET	mobile ad-hoc network
MEO	medium-Earth lrbit
MIMO	multiple-input and multiple-output
ML	machine learning
MMSE	minimum mean square error
MUI	multi-user interference
MU-MISO	multi-user multiple-input single-output
NCO	numerically-controlled oscillator
NNLS	non-negative least squares
NTP	network time protocol
OCB	opportunistic collaborative beamforming
OFDM	orthogonal frequency division multiplexing
OLFAR	orbiting low-frequency antennas for radio astronomy
OPLL	optical PLL

OTA	over-the-air
PA	pairwise algorithm
PBS	pairwise broadcast synchronization
PI	proportional-integral
PLL	phase-locked loop
PM	phase margin
PN	phase noise
PoC	proof of concept
POD	precise orbit determination
PRISMA	prototype research instruments and space mission technology advancement
PRN	pseudo-random noise
PSD	power spectral density
PTP	precision time protocol
QoS	quality of service
RBS	reference broadcast synchronization
RF	radio frequency
R-RT	robust round-trip
RSS	received signal strength
SAR	synthetic aperture radar
SER	symbol error rate
SDDB	successive deterministic distributed beamforming
SDR	software-defined radio
SIN	space information network
SLP	symbol-level precoding
SNIR	signal-to-noise-plus-interference ratio
SNR	signal-to-noise ratio
SSP	stale synchronous parallel

TDD	time division duplex
TOA	time of arrival
TOF	time of flight
TPSN	timing synchronization protocol for sensor networks
T-RT	time-slotted round trip
TWTT	two-way time transfer
TWR	two-way ranging
UE	user equipment
UT	user terminal
USRP	universal software radio peripherals
UAV	unmanned aerial vehicles
UWB	ultrawideband
WSN	wireless sensor network
ZF	zero-forcing
0F	zero feedback
1BF	one-bit feedback
2BF	two-bits feedback
2WS	two-way synchronization
3D	3-dimensional

Notations

$\mathbf{I}$	The identity matrix of appropriate dimensions.
$\mathbf{0}$	The zero-matrix (or zero-vector, depending on the context) of appropriate dimens
$\log(z)$	The natural logarithm of z.
e^z	Exponential function of z.
$\mathbb{E}[\cdot]$	Expected value.
$\boldsymbol{b}^{\mathbf{T}}, \boldsymbol{B}^{\mathbf{T}}$	Transpose of vector $\boldsymbol{b}$, transpose of matrix $\boldsymbol{B}$.
$\boldsymbol{b}^{\mathbf{H}}, \boldsymbol{B}^{\mathbf{H}}$	Conjugate transpose (hermitian) of vector $\boldsymbol{b}$, Conjugate transpose (hermitian) of
$\mathrm{diag}(\boldsymbol{b})$, $\mathrm{blkdiag}(\boldsymbol{b})$	Square (block) matrix having main-diagonal (block) entries $\boldsymbol{b}$.
$\mathcal{R}(\mathbf{A})$	column space of matrix $\mathbf{A}$.
$\mathrm{Trace}\{\boldsymbol{B}\}$	The sum of elements on the main diagonal of the square matrix $\boldsymbol{B}$.
$\lvert z\rvert$, $\lvert\mathcal{Z}\rvert$	The absolute value of z, cardinality of set $\mathcal{Z}$.
$\lVert\boldsymbol{b}\rVert$	The norm of vector $\boldsymbol{b}$.
max	Maximum operation.
min	Minimum operation.
$z \in \mathcal{Z}$	Element z belongs to set $\mathcal{Z}$.
$\lvert\mathrm{Z}\rvert$	Cardinality of the set Z.
$\mathcal{Z} \setminus \mathcal{Q}$	Set $\mathcal{Z}$ excluding elements in $\mathcal{Q}$.
$\mathcal{Z} \cup \mathcal{Q}$	Union of set $\mathcal{Z}$ and set $\mathcal{Q}$.
$\mathbb{R}$	Set of real values.
$\mathbb{C}, \mathbb{C}^{n\times m}$	Set of complex values, set of $n \times m$ matrices with complex-valued entries.
$\circ$	Element-wise Hadamard operations
$(\cdot)^T$	Transpose of $(\cdot)$
$\mathcal{Z} \subseteq \mathcal{Q}$	Set $\mathcal{Z}$ is a subset of $\mathcal{Q}$.

Chapter 1

Introduction

1.1 Problem Overview and Motivation

During the last decade, the use of small satellites has revolutionized the field of space exploration and communications [1]. These pint-sized spacecraft's capabilities and versatility opened access to space for a wide range of entities, from government agencies to private companies and even academic institutions. This has opened up new possibilities, such as the feasibility of grouping small satellites into DSS.

Cohesiveness stands as an additional desirable attribute of DSSs. A cohesive distributed satellite system (CDSS) is a multi-satellite configuration that appears as a single solid entity from an external perspective. This cohesive behavior must be extended to data reception, processing, and transmission operations. This entails improving several DSS applications such as Earth observation, geolocation, navigation, imaging, and communications, among others. An example of a technique for cohesive transmission and reception among satellites is distributed beamforming.

Distributed beamforming is a sub-class of multiple-input and multiple-output (MIMO) system in which the multiple elements are stand-alone autonomous active devices working coherently in a cooperative manner. In this way, the complete system can synthesize a radiation pattern towards an intended direction, in reception or transmission [2]. During transmission, DBF allows the system to focus the transmitted energy towards the desired locations, while in reception can be used to mitigate interference from unwanted directions. This technique enables increased system capacity and extended coverage for various applications, from wireless communications to remote sensing. For instance, in 6G networks, the base stations will have multiple antennas to support MIMO transmission and reception. These antennas will be coordinated across different base stations to perform distributed MIMO beamforming which is one of the key technologies to achieve the desired performance [3]. Another example of DBF applications is TerraSAR-X and TanDEM-X Earth observation missions. These missions involve two satellites, TerraSAR-X and TanDEM-X, flying in a close formation with a precise baseline separation. The DBF technique is employed in these missions to combine the signals received by the antennas on both satellites and create a bistatic SAR system with a large effective aperture. The DBF in TerraSAR-X and TanDEM-X enables the acquisition of high-resolution data for applications such as digital elevation modeling, monitoring of natural disasters, and environmental change analysis [4].

The use of DBF in CDSSs could offer several advantages over traditional single-satellite approaches, including enhanced redundancy, increased coverage and data collection capabilities, improved flexibility in mission execution, and the potential for cost-effective scalability. However, it also presents new challenges, such as the need for robust inter-satellite communication and synchronization, complex system management, and potential congestion in orbital space. Among them, achieving accurate synchronization is pivotal to ensure the seamless operation and optimal performance of CDSSs.

For example, deep space communications could be accomplished by DSSs applying distributed MIMO techniques [5] if the terminals at each end of the link are synchronized at the symbol level. This implies that the stations need to maintain synchronized clocks with sub-nanosecond accuracy to guarantee a bandwidth of a few hundred MHz [6]. Another example can be Earth observation applications based on distributed synthetic aperture radar (SAR) interferometry and synthetic aperture microwave radiometer. In this case, the final resolution depends on the accuracy of the phase synchronization achieved between the satellites [7]. For some applications, the synchronization requirement is the critical limiting factor in making practical implementations possible [8]. In those cases, the level of effort, power consumption, and complexity required for the synchronization algorithm may be higher than those needed for the mission itself.

The synchronization of DSS involves precisely aligning time, frequency, and phase among multiple satellites, which is a significant challenge due to the inherent characteristics of space-based environments. For instance, the spacecraft mobility, the round-trip delay, and the resource constraints make the synchronization of DSSs more challenging than its equivalent in wireless terrestrial networks. However, it is simultaneously an unavoidable challenge for future space communications. This requirement does not only apply to small satellites DSSs; it is also a requirement to avoid interference in crowded orbits and to enable the federated satellites' paradigm.

It is within this context that we set our research problem: Finding the synchronization technique to achieve the accuracy to perform beamforming in a DSS. Additionally, we considered the following sub-problems:

- How many resources would be needed?
- How to make the complete system efficient compared to single platform units?
- What level of accuracy could be achieved?

Aiming to answer these questions, the objective of this thesis is to identify the technical synchronization requirements and design the synchronization and coordination techniques to perform beamforming in DSS. Specifically from a practical implementation point of view, considering the resources available in small spacecraft.

To accurately synchronize the nodes in a DSS to perform beamforming, all nodes must share a common time reference. We'll refer to the procedure to guarantee this requirement as time synchronization. Several authors have addressed this topic for small spacecraft CDSSs [9–12]. Once the received signals offset is below a symbol time, the system should synchronize their phases to achieve constructive superposition. We'll refer to this step as phase synchronization. This is a more challenging task than time synchronization. To the best of our knowledge, only [13] approached the problem of synchronizing the phase in a CDSS. The solution proposed in [13] requires an external beacon from a satellite in a higher orbit. Even when this is a valid approach from the resource constraint perspective, using an external beacon represents a limitation. Considering this, we assumed accurate time synchronization and focused on the phase synchronization of CDSSs.

Simultaneously with the time and phase synchronization algorithms, CDSSs must compensate for the different path delays from each node to the receivers. These delays include random fluctuations related to the satellite dynamics. Several authors have addressed the topic of inter-satellite positioning for small spacecraft CDSSs [9,11,14]. Getting to propose algorithms that perform time synchronization and inter-satellite ranging simultaneously [9,11]. In our work, we assumed that inter-satellite ranging and positioning were estimated and compensated for by the algorithms discussed in the previously mentioned articles, which are analyzed in Chapter 2 of this document.

Taking into account the assumptions regarding time synchronization and inter-satellite ranging, we can establish an equivalence between phase synchronization in CDSS and multibeam satellite systems.

1.2 Synchronization of the Local Oscillators in Multibeam Satellites

While the academy is focused on the promising benefits of small spacecraft and DSSs, the space industry still has open challenges related to the phase synchronization of traditional satellites. That is the case of synchronizing the LOs in multibeam satellites. Using a common LO as a clock reference may appear to be a solution to this problem. However, it is not an alternative in practical satellite systems where the whole system should not rely on the same LO due to several technical limitations. These constraints include independence between payloads, autonomy, robustness, cross-interference between RF channels, and redundancy [15]. As a result, the system requires some phase synchronization technique to transmit using those beams cohesively.

An example of cohesive transmission in distributed MIMO systems, such as the previously described multibeam satellites, is the precoding technique [16]. Precoding is a signal processing technique to mitigate interference and enhance system performance. In MIMO systems, precoding algorithms calculate the optimal transmission weights for the antennas at the transmitter, considering the channel conditions, interference, and system constraints. These weights are then applied to the data symbols before transmitting them over the wireless channel. By using precoding, the transmitted signals can be tailored to exploit the channel characteristics, such as reducing the impact of interference and fading and improving the overall spectral efficiency of the system [16].

Traditional multibeam satellites deal with interbeam interference by adopting a spectrum division technique named 4-color frequency reuse. This approach involves partitioning the available spectrum into four distinct sub-bands named colors. Each beam is assigned a specific color, so neighboring beams utilize different colors, ensuring minimal interference between them. The precoding technique represents an improved alternative to the 4-color frequency reuse method since all the beams can use the whole bandwidth. However, because it involves manipulating the transmitted signal phase, its effectiveness depends on the accurate synchronization of the clock references across all beams. Unless this issue is addressed, none of the widely studied and proposed approaches in non-terrestrial networks [16–18] would be feasible.

However, synchronizing in phase the LOs is less challenging when co-located on a spacecraft. In this case, the synchronization algorithm is unaffected by the phase rotations introduced at the inter-satellite links due to atmospheric conditions or signal propagation delays. Additionally, co-locating LOs within the same spacecraft simplifies time synchronization by using the satellite's internal clock as a reference, avoiding complexities associated with signal propagation delays and clock drift between different satellites. Nevertheless, beamforming presents a certain level of robustness when it comes to handling phase synchronization errors. For example, the authors in [19] consider errors resulting from imperfect clock alignment and platform spatial measurements in an open-loop system. As a result, they obtained beamforming's tolerance to phase synchronization errors considering the number of nodes and the desired coherence gain.

Additionally, a number of studies have been conducted on time synchronization in DSSs [9,10,14]. For a more in depth understanding, Chapter 2 will delve into further details on this topic. However, some of these publications targeting small spacecraft achieved accuracies in the order of 100 ps during in-lab demonstrations [9,10].

Results from Chapter 3 to Chapter 5 of this thesis have been validated using precoded-enabled multibeam satellite systems. However, taking into account the analysis from the previous paragraph, they can be used at small spacecraft CDSSs assuming that an additional method such as [9] is applied to guarantee accurate time synchronization and inter-satellite ranging among the satellites.

1.3 Main Contributions of this Thesis

The contributions of this Ph.D. thesis are distributed among chapters 2, 3, 4 and 5 and are as listed below:

- **Chapter 2:**
  - A brief survey of the DSSs architectures is provided, classifying them into five

  general groups: Constellations, Clusters, Swarms, Fractionated, and Federated spacecraft, for which the main features are identified.

  - The distributed time, phase, and frequency wireless synchronization methods reported in the literature are summarized and compared, analyzing their feasibility for DSSs.
  - Other operations closely related to synchronization in DSSs, such as inter-satellite ranging and relative positioning, are also analyzed.
  - It is offered an extensive compilation of the missions and PoCs implementations reported up to the present.
  - Some of the most relevant current research activities and potential research topics are presented, identifying problems and open challenges.

- **Chapter 3:**
  - Identification of the individual contribution of each system element to the overall synchronization uncertainties in practical precoding implementations. This allows for more efficient designs and implementations.
  - Formal demonstration for linear and non-linear precoding, that the UTs can track slow time variations in the channel as long as they equally affect all the beams, as it was suggested, but not demonstrated in [20] for non-linear precoding.
  - Formal demonstration that the uplink phase variations related to the Doppler effect and the multiple LOs required at the transponder affect precoding performance even when all the LOs share a single frequency reference. This chapter demonstrates that these uplink phase variations will not affect the system performance for an ideal loop with a negligible delay between the CSI estimation and the precoding matrix application. However, since the zero-delay loop is unfeasible in actual systems, we demonstrate in this chapter that practical implementations of precoding require an extra synchronization solution as much for a single frequency reference, as for multiple frequency references. Conventional approaches assume that using a single frequency reference was enough for multi-beam satellite systems [20, 21].
  - Comparison of the robustness to synchronization impairments of minimum mean

  square error (MMSE), zero-forcing (ZF), and symbol-level precoding (SLP) techniques.

- **Chapter 4:**
  - Hardware implementation of the two-state phase noise model.
  - The experimental real-time validation of the phase noise generator using the in-house developed MIMO end-to-end satellite emulator based on software-defined radio (SDR) platforms.
- **Chapter 5:**
  - Modeling the phase drift introduced by the LOs in a multi-beam satellite as a two-state clock model.
  - The design of the closed-loop phase synchronization method from a practical implementation point of view, considering the phase drift introduced by the hardware components.
  - The analysis of different approaches for using the phase estimation reported by the UTs in combinatorial and selective algorithms.
  - The hardware implementation of the closed-loop phase synchronization and the combinatorial phase estimation algorithms.
  - The experimental real-time validation of the proposed solution using the in-house developed MIMO end-to-end satellite emulator based on SDR platforms.

1.4 Organization of the Thesis

The thesis is organized as follows:

- Chapter 2 describes the most relevant results on synchronization for DSS and the strict requirements and new technologies related to distributed satellite missions.
- Chapter 3 aims at assessing the impact of the phase errors and uncertainties in operating a precoded forward link satellite communication system from a practical implementation point of view. It contains the formal demonstration that, unlike the uplink case,

the phase uncertainties created in the forward-downlink do not affect the precoding performances for linear and non-linear precoding operations. This chapter demonstrates the need to implement a phase compensation loop.

- Chapter 4 describes the hardware implementation of the oscillator phase noise model and obtains the resulting SNIR at the receivers. The phase noise is modeled according to the two-state model proposed by Galleani in [22]. The model implementation is validated in a hardware testbed emulating a 2 × 2 precoding-enabled system.
- Chapter 5 presents the phase synchronization method required to enable the precoding implementations in the GEO scenario. The proposed solution requires only small modifications to the already deployed satellite system. The only modification with respect to traditional precoding design is including a controller at the GW.
- Chapter 6 concludes the thesis and discusses possible research directions for future work.

Chapter 2

Architectures and Synchronization Techniques for Distributed Satellite Systems

2.1 Introduction of the Chapter

The synchronization of distributed wireless systems is highly challenging and has received much attention in the literature. For example, [23] summarizes some of the timing and carrier synchronization techniques proposed for wireless communication systems. Another review of the synchronization methods used in wireless systems is given in [24], where the authors summarize the clock synchronization protocols in wireless sensor networks (WSNs). However, both articles are limited to terrestrial systems, and they do not address synchronization for DSSs.

The opportunities and challenges of DSSs have been explored in many publications. For example, [25] summarizes the use of WSNs for planetary exploration. In this article, the authors mentioned synchronization as one of the problems encountered in distributed systems design. Besides, [26] provided a comprehensive assessment of modern concepts and technologies of DSSs and analyzed the technical barriers to DSSs implementation. In addition, [17] stated the revolutionary strength of DSSs such as satellite swarms and the limitations in its implementation due to synchronization requirements.

However, the synchronization of DSSs is still an open and challenging research question that has attracted the attention of the scientific community in the last few years. This has resulted in a large body of work appearing in conferences and journals from different fields. This work intends to fill this gap. With this idea in mind, this chapter summarizes and categorizes the most relevant publications on synchronization techniques for DSSs.

The chapter is organized as follows: After the Introduction, some important concepts on the architectures and system models for DSSs are defined in Section 2.2. The synchronization methods reported in the literature are presented and categorized in Section 2.3. Section 2.4 deals with other operations closely related to the synchronization in DSSs such as: inter-satellite ranging and relative position. Sections 2.5 and 2.6 comment examples of synchronization methods in DSSs, whereas Section 2.5 lists some ideas and new methods that have not been implemented yet. Section 2.6 provides to the reader examples of PoCs and launched missions of DSSs with special emphasis on the synchronization methods implemented. Section 2.7 presents the use of machine learning (ML) for synchronization purposes. The most relevant open questions and future research directions are highlighted in Section 2.8. Finally, the chapter conclusions are summarized in Section 2.9.

2.2 Architectures and System Model for Distributed Satellite Systems

2.2.1 Overview of Existing Architectures

DSSs can be classified into five general groups: Constellations, Clusters, Swarms, Fractionated, and Federated spacecraft. Table 2.1 summarizes the main characteristics of these groups.

- **Constellations** refer to a traditional approach where tens of medium to large satellites (over 500 kg each) are distributed around Earth to guarantee global or regional coverage of a service. Some of the most famous satellite constellations are: the global navigation satellite system (GNSS) constellations, such as global positioning system (GPS) and Galileo and; the satellite communication constellations, such as Globalstar [27], Iridium [28], SpaceX [29] and OneWeb [30]. Inter-satellite communication in these networks is scarce or null, except in the Iridium constellation where each satellite can have four Ka-band ISLs [28].
- A **cluster** is a group of at least two mini or micro satellites (from 10 to 500 kg each)

deliberately positioned closely together to enhance or create new system capabilities. These DSSs cover a smaller portion of the Earth and mainly require inter-satellite communications to keep a close formation flying. Some satellite clusters are gravity recovery and climate experiment (GRACE) [31], laser interferometer space antenna (LISA) [32], prototype research instruments and space mission technology advancement (PRISMA) [33], PROBA-3 [34], and TanDEM-X [35].

- Satellite **swarms** are similar to clusters, except they contain a significantly higher number of satellites, often smaller and less expensive (less than 10 kg each). They are envisioned to contain hundreds and even thousands of nanosatellites operating together in a loose flying formation. They will require inter-satellite communications, as each member determines and controls relative positions to the others. Unlike previous DSSs that have several examples, satellite swarms are a new concept yet to be demonstrated. Examples of satellite swarms projects are QB-50 [36], and orbiting low-frequency antennas for radio astronomy (OLFAR) [37].

- **Fractionated spacecraft** is a revolutionary satellite architecture that distributes the functions of a single large satellite into numerous modules that communicate by ISL in a highly dynamic topology [38]. Among the multiple advantages of this concept can be mentioned the flexibility, robustness, and the significant decrease in the required time to launch and deploy a satellite mission. Fractionated satellite systems is a very recent concept that have not yet been implemented.

- Finally, the **Federated Satellite System (FSS)** paradigm visualizes opportunistic collaboration among fully independent and heterogeneous spacecraft [39]. This is one of the most recent DSS concepts, and it is inspired by the current peer-to-peer networks and cloud computing. The main idea is to benefit from the potential of under-utilized space commodities by trading and sharing previously unused resources available in space assets at any given time. It is worth noting that much of federated satellite system (FSS)'s potential relies on the spacecraft capabilities to establish communications through ISL. The recently launched FSSCat mission [40] is an example of FSS.

In addition to this classification, CDSSs can be categorized according to their synchronization scheme as centralized or distributed. The former refers to distributed systems where all the nodes adjust their carriers to follow one controller node, which has the most stable

Table 2.1: Main characteristics of the DSS groups

Classification	Number of Satellites	Satellites Weight	Inter-satellite Comm	Examples
Constellation	tens	> 500 kg	scarce or null	GNSS, Globalstar, Iridium
Cluster	at least 2 satellites	10 to 500 kg	required to keep a close flying formation	GRACE, LISA, PRISMA, PROBA-3, TanDEM-X
Swarm	hundreds in a loose flying formation	< 10 kg	required to determine and control relative position	QB-50, OLFAR
Fractionated spacecraft	at least 2 satellites	< 500 kg	required to achieve the mission objectives	not implemented yet
FSS	dynamic	any	required to share unused resources	FSSCat

oscillator in the system. This synchronization scheme has a relatively simple implementation, but it may have robustness drawbacks. On the other hand, distributed synchronization satellite systems do not rely on a single node but try to find a common carrier considering all the oscillators in the system. This characteristic overcomes the robustness drawback of the former group but makes the synchronization algorithms more complex. The synchronization methods suitable for CDSSs will be addressed in detail in the following sections.

Moreover, considering the communication links between the nodes of the DSS, the space segment can be classified as:

- **Ring**, in which each node connects to two other nodes, forming a single continuous path through all the elements of the DSS. This topology is not suitable for centralized synchronization algorithms.
- **Star**, in which each node connects to a central node that performs specific tasks ranging from communications with the ground segment to leading the synchronization. This topology generally uses centralized synchronization methods.
- **Mesh**, in which each node is connected to every other node in the distributed system. This topology can be implemented fully or partially depending on the complexity of the DSS, and it accepts the implementation of both distributed and centralized synchronization algorithms.
- **Hybrid** topologies combine two or more of the previous ones.

These topologies are shown in Fig. 2.1, where the arrows represent the ISLs.

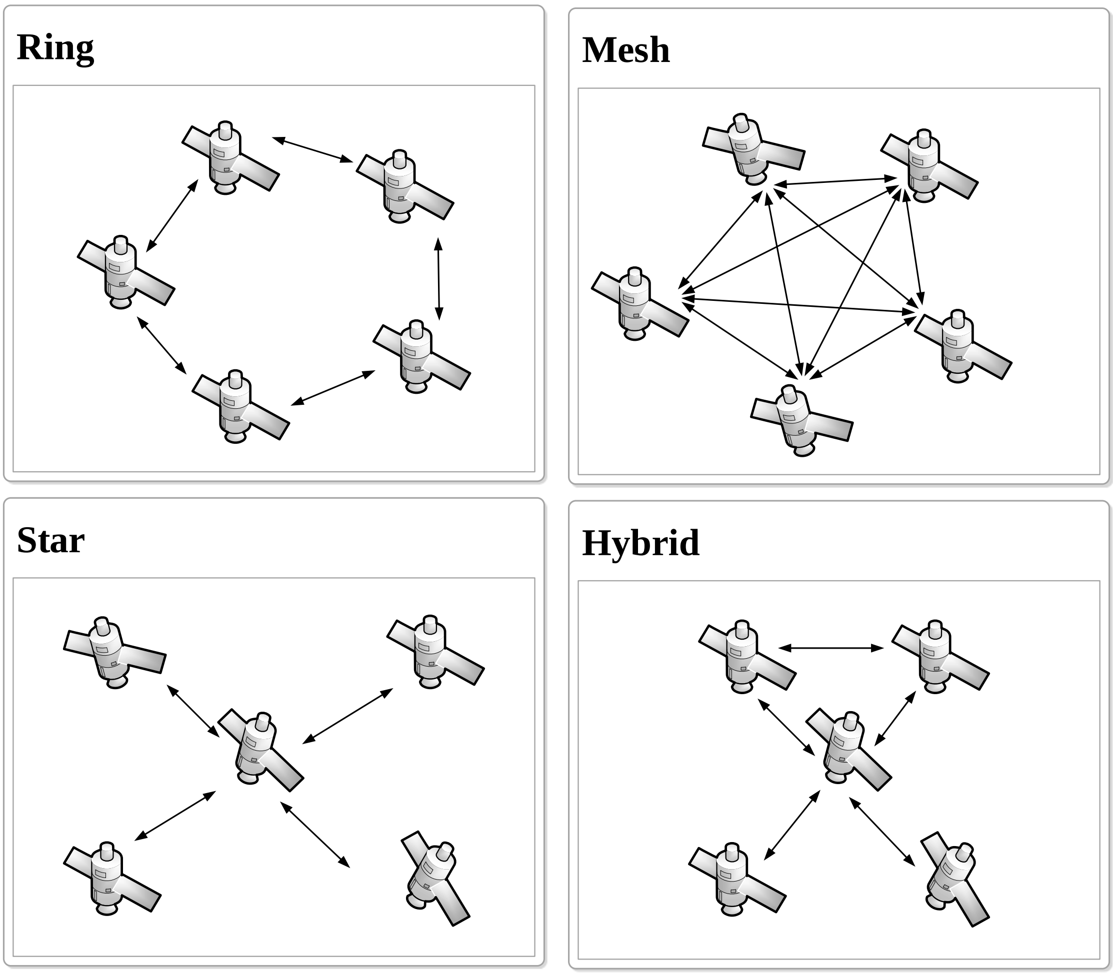

Figure 2.1: Classification of DSS considering the ISLs

2.2.2 Generalized System Model

The general DSS considered in this thesis is a distributed array of autonomous nodes which collaborate to perform distributed beamforming towards an intended target node outside the array. From a general perspective, the nodes of the distributed arrays considered in this survey can be moving while the whole system tries to stay at a fixed position, or the entire array can be following a trajectory or orbit.

For both cases, the nodes require transmission and reception capabilities to synchronize the distributed system. For the general DSS, no specific geometric distribution of the nodes is assumed, none of the previously mentioned classes neither. However, each of them can be described by a state variable $\overrightarrow{x_n} = (\overrightarrow{p_n}, \overrightarrow{v_n})$ where $\overrightarrow{p_n}$ and $\overrightarrow{v_n} \triangleq \frac{\mathrm{d}\overrightarrow{p_n}}{\mathrm{d}t}$ represent the position and the speed of the node n, respectively.

Besides, it is assumed the existence of RF-ISLs between all the elements of the DSS, which implies a Mesh configuration, even if all the links are not activated at the same time. The complex transfer function of these ISLs is formally represented as complex coefficients h_{nm}, where n and m are the node subscripts. The matrix $\mathbf{H}$, containing all the h_{nm}, can be used to describe the DSS. It determines the most suitable synchronization procedure. Fig. 2.2 shows the general DSS considered in the next sections to analyze the synchronization techniques.

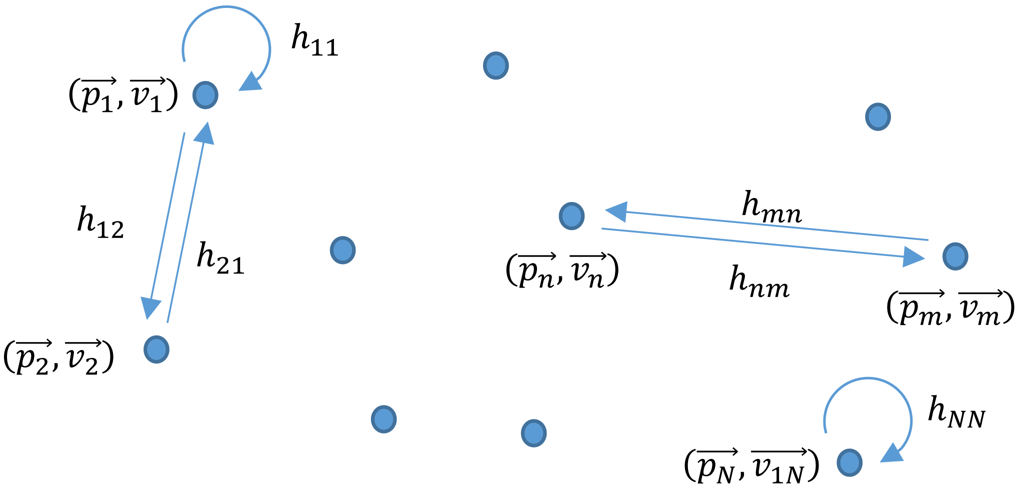

Figure 2.2: General scheme of the DSS performing the required synchronization for a DBF transmission

The quality of the ISL is considered variable as a function of the position and orientation of the nodes, given that omnidirectional antennas are not assumed. Besides, the frequency responses of the RF chains are considered different for each node.

For synchronization purposes, each of the distributed nodes generates its own initial reference signal, the stability of which depends on the available hardware at each satellite. The objective of the synchronization algorithm is to make all of those initial reference signals converge to a common reference with the best possible accuracy.

2.2.3 Summary and Lessons Learnt

- DSS can be classified as Constellations, Clusters, Satellite swarms, Fractionated spacecraft, and, FSS.

- Distributed synchronization algorithms are more robust than centralized synchronization algorithms, but more complex.
- According to the ISL, there are four types of DSS: Ring, Star, Mesh, or Hybrid topology.
- The general DSS model considered in this thesis is a distributed array of autonomous spacecraft that collaborate to perform distributed beamforming towards an intended target node outside the array.
- The general model assumes a Mesh configuration with the reference signals locally generated at each distributed satellite.

2.3 Overview of Synchronization Methods

A critical aspect of the synchronization of distributed radio systems, in general, is the clock or time synchronization in addition to the phase synchronization. This section summarizes the most significant synchronization methods reported in the state of art. These algorithms can be classified as Closed-loop or Open-loop methods based on the use of feedback from a node external to the DSS. The external node can be another satellite, an anchor point, or the intended communication target. The Closed-loop methods require a communication channel to transmit the feedback information between the external node and the DSS. Whereas in Open-loop, the synchronization is achieved without the participation of any node other than the distributed satellites.

Another way to classify the synchronization methods considers the communication between the elements of the DSS. In order to achieve synchronization, some algorithms require the exchange of information among the distributed satellites. This can be done as a two-way message exchange or closed loops, which requires a duplex channel between the nodes of the DSS, or as a broadcast or one-way communication. Another option is to synchronize without any communication among the elements of the DSS. In this case, it is possible to achieve coherence using the feedback from a node out of the DSS. Both classifications can be superimposed, as it is represented in Fig. 2.3. In this figure, some of the missions analyzed in the following sections were included as examples.

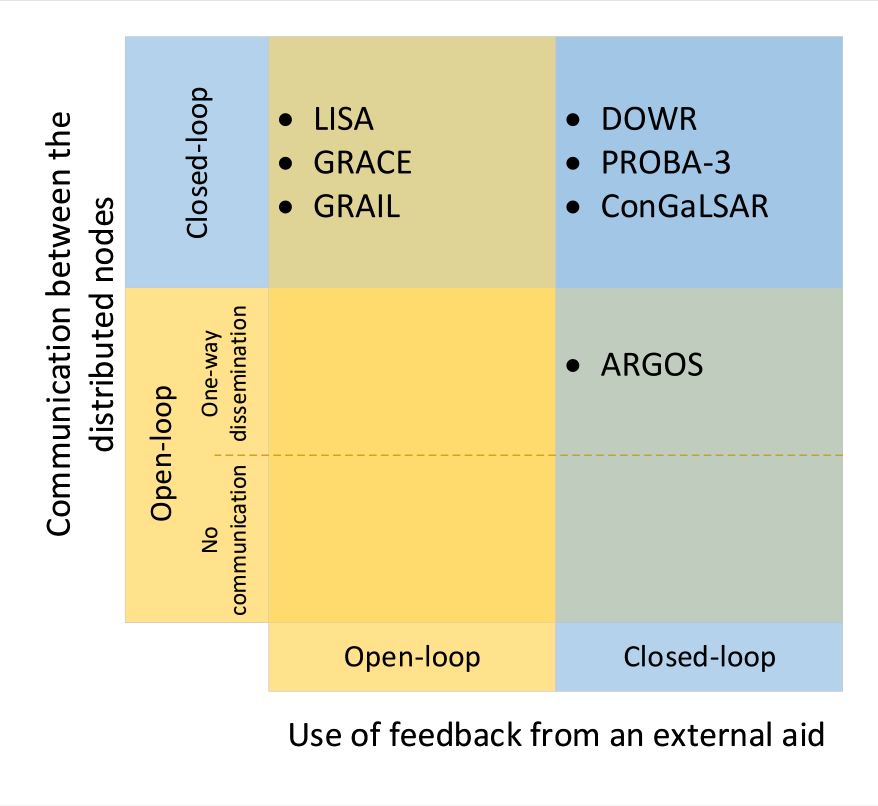

Figure 2.3: Classification of the synchronization methods

2.3.1 Time Synchronization

Time synchronization is critical in the application of many DSS. The coherent transmission in communication applications, for instance, requires aligned signals at the symbol level to achieve the full potential of the beamforming gains. The tight clock and timing synchronization is achieved with different levels of accuracy in other areas, such as wired and optical networks and wireless sensor networks. For example, some distributed applications such as computer networking, distributed signal processing, instrumentation, and Earth observation applications require accurate timing or clock synchronization. The purpose of this section is to explain those timing synchronization methods used in other areas and give advice on how to translate them into DSS, in particular for communications applications.

Previous studies have identified the time or clock synchronization challenge for clock frequencies in the order of tens to thousands of MHz and accuracies ranging between orders of one fractional digit relative to the clock frequency. Recently, it has been studied for multi-static and MIMO radar and distributed beamforming applications where the required precision is orders of magnitude more stringent [41]. Additionally, these systems require what is known as absolute time synchronization, which is different from relative time synchronization on which only the timing of an impingent signal is tracked. The problem of absolute time synchronization was first formally defined by Poincaré and Einstein in 1898 [42], and 1905 [43], respectively. The formal definition of this problem and the TWTT concept was provided in the framework of relativistic-event-simultaneity.

Fig. 2.4 depicts the basic idea of the TWTT concept. Here, an initiating or source node sends a signal (or packet) at time T_1. A slave (or follower node) receives the signal at time T_2 after a delay of $\Delta t_1 = T_2 - T_1$ and responds (or reflects) after a known delay at time T_3. The source node receives the response signal at time T_4. The time offset of the clocks is then $((T_2 - T_1) - (T_4 - T_3))/2 = (\Delta t_1 - \Delta t_2)/2$, and the propagation delay is $((T_2 - T_1) + (T_4 - T_3))/2 = (\Delta t_1 + \Delta t_2)/2$. Therefore, proper knowledge of this propagation time offset will be used to achieve absolute synchronization.

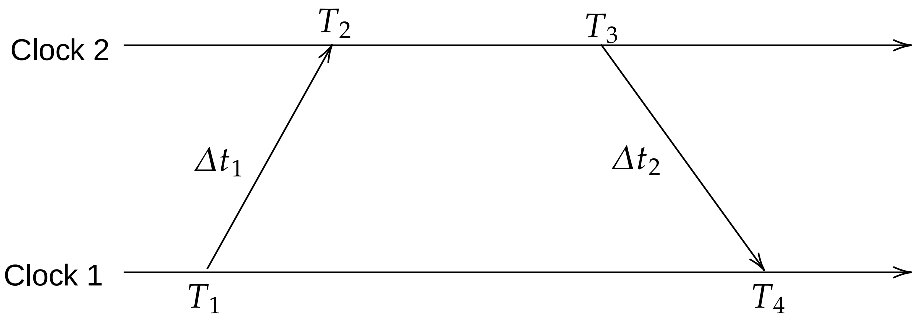

Figure 2.4: Operating principle of the TWTT clock synchronization [41]

The TWTT concept created the foundations for clock synchronization of twenty-century networks and complex systems, such as satellites and the Internet [44]. This general concept can be applied to diverse kinds of systems and networks, including DSS. This section will emphasize the case of DSS. The following subsections describe timing synchronization methods that have been developed in different communications areas and could be extrapolated to DSSs. An example of the use of TWTT in DSS is presented in [45], where the authors compared the performance of three clocks offset prediction algorithms based on this method for a master-slave architecture. In addition, the authors in [14] used TWTT to synchronize four spacecraft in a distributed satellite formation flying, achieving time synchronization simulation errors smaller than ± 10 ns. The work in [46] analyzed the effect of the motion of the satellite on the two-way time synchronization accuracy. Another example based on TWTT calculates the time difference between two satellite clocks by measuring the phase difference of a pseudo-random noise code in a master-slave architecture [10]. The method is proposed to achieve on-orbit synchronization in a micro-satellite cluster [10]. Other authors combined RF carrier ranging methods with TWTT to obtain inter-satellite range and time synchronization simultaneously [47] [11] [9].

Time synchronization in wired networks

The TWTT concept is the basis of most synchronizations protocols in the literature. The network time protocol (NTP) and precision time protocol (PTP) are extensively used in large-scale modern computer networks, and both operate with a TWTT approach. The network nodes exchange timestamps employing (UDP) packets to measure the round-trip propagation latency. NTP generates software timestamps with non-deterministic time offsets and achieves clock accuracies in the order of $\sim 10\ \mu$s [48]. The PTP (IEEE-1588) is an evolution of the NTP, which generates hardware timestamps using the waveforms of the associated clock. This protocol achieves clock alignment by exchanging synchronization packets among the involved nodes. The IEEE-1588 standard limits the maximum rate for the timestamp counters to 125 MHz, providing accuracies of ~ 10 ns [49] [50]. The performance of these systems, such as NTP and PTP, rely directly on the clock rates used, and the achieved accuracy is given by the granularity associated with an integer counter.

Further refinements of the time synchronization mechanism use the clock phase information. A salient example is the White Rabbit project of the European Organization for Nuclear Research (CERN). White Rabbit operates with Ethernet frames to detect the phase difference between the local clock and a clock extracted from the received Ethernet signal. Across large wired networks, White Rabbit operates under specially designed network switches to measure and compensate fractional clock phase differences achieving ~ 10 ps accuracy [51].

Even though these time synchronization mechanisms cannot be used directly on DSS, the main concepts can be extrapolated to DSS scenarios. In the DSSs, the coarse synchronization methods such as NTP and PTP can be used to eliminate the ambiguity in the total channel delay. Then, the time synchronization can be refined with differential time mechanisms at the waveform level, using White Rabbit or similar approaches.

Time synchronization in wireless sensor networks

In wireless communications, absolute time synchronization is also frequently desired, and the wireless channel is typically used to exchange the synchronization messages. The algorithms for absolute time synchronization in wireless networks can be classified as sender-to-receiver and receiver-to-receiver synchronization methods. The former is based on the TWTT between couples of nodes, whereas receiver-to-receiver methods use time readings of a standard signal broadcasted to a set of nodes from a common sender [52].

Some receiver-to-receiver solutions include reference broadcast synchronization (RBS) [53] and pairwise broadcast synchronization (PBS) [54]. The RBS protocol implements a time of arrival (TOA) exchange between the distributed nodes disregarding the signal time of flight (TOF) over the physical medium [53]. PBS is a well-known timing synchronization scheme for WSNs, which is based on sets of node-pairs for network-wide synchronization. PBS operates under the assumption that all the participating nodes will receive and detect the pairwise synchronization frames exchanged between two master/reference nodes. This approach assumes a hierarchically distributed structure [54], and assumes that distances between nodes and their associated delays (TOFs) are known in advance.

The most well-known sender-to-receiver synchronization methods are timing synchronization protocol for sensor networks (TPSN) [55] and flooding time synchronization protocol (FTSP) [56]. TPSN implements TWTT between pairs of nodes preceded by a discovery phase from where each node obtains a level. In FTSP and its variations [57], the distributed nodes synchronize to a signal broadcasted from the root node or a previously synchronized node.

For these protocols to work, synchronization must be performed several times. Additionally, the nature of the WSN, in which the network observes a physical phenomenon (temperature, pressure, etc.), determines synchronization requirements on the order of microseconds. However, this level of accuracy is inadequate to perform distributed coherent (beamforming) radio applications.

For example, the required time synchronization to achieve beamforming maintaining the performance at acceptable levels is around ± 7.5 percent of a symbol duration. For single-carrier communication baud rates of a hundred MHz, this represents a required accuracy of ± 0.75 ns. This accuracy could be achieved with a refinement of the methods mentioned above, such as the work in [58]. This algorithm proposes a step forward in the timing accuracy increase by using frequency-modulated continuous-wave) signals with a relatively high bandwidth of 150-MHz. The method performs the synchronization between two stations using a TWTT approach (similar to the one proposed in [59]). It uses the aforementioned radar-like waveform to provide a joint carrier phase and timing synchronization with an accuracy of 66 ps.

Ultrawideband Pulse Synchronization

Wireless synchronization approaches using ultrawideband (UWB) pulses instead of exchanges of a network packet have recently caught researchers' interest. To estimate the TOA at sub-nanosecond levels, UWB approaches take advantage of high-speed hardware, generally at sampling rates higher than 1 GHz.

Several applications have exploited UWB signaling using high speeds clocks and analog-to-digital converters (ADCs). Some examples are the sets of multiple active receivers locked and synchronous to a single transmitter [60], distributed consensus techniques [61], and distributed sensor positioning [62]. The works in [63] propose a propagation-aware TOF protocol and provide validation for the system using an atomic clock integrated on a chip and a 64 GHz hardware clock timestamp counter [64]. As a result, these experiments achieved a distributed timing accuracy of 5 ns between two sensors. It is essential to mention that the transmission of UWB pulses is not feasible for small satellites such as CubeSats due to power constraints. However, its advantages can be considered for DSS with less strict power consumption requirements.

Nevertheless, it is worth pointing out that increasing clock frequencies is not the only alternative to increase the timing accuracy in synchronization mechanisms. A common misconception in the literature regarding UWB synchronization systems is that the ADC frequency bounds the time resolution. As specified by the Cramer-Rao lower bound (CRLB) [65], accurate TOA measurements within minuscule fractions of a sampling period is attainable, specially in line of sight (LOS) scenarios. The measurement of these time offsets, fractional to the sampling time, can be achieved by time offset mechanisms, also known as timing-error-detectors, such as the Gardner method [66], and the Early-Late-Gate method [67] among others.

2.3.2 Frequency and Phase Synchronization

As previously stated, considering the use of feedback from an external node, frequency, and phase synchronization methods can be classified as:

- Closed-loop methods, where the feedback from the target nodes could be either a single bit or a few bits or could have the form of rich feedback with limited or full CSI [68].
- Open-loop methods that require either intra-node communication or blind beamforming, also known as zero feedback (0F) [68].

In the following sections, some of the most notable examples from each category are discussed.

Closed-Loop Synchronization Methods Considering the Use of Feedback from an External Aid

Fig. 2.5 lists the closed-loop synchronization methods in the literature. They are classified into different groups according to the feedback type for a better understanding, although more detailed information is provided in this section.

The group Iterative Bit Feedback includes the algorithms where the distributed nodes modify their signals according to one or more decision bits received from the target node. Among them, the most well-known algorithm is the classical 1BF, proposed in [69]. This method considers the beamforming nodes synchronized in time and frequency and achieves phase synchronization by applying independent random phase rotations in each beamforming node. At each time slot, transmitter nodes add a random perturbation to their signals. The target node measures the received signal strength (RSS) and sends one bit indicating if the RSS is better than the previous value. Depending on this bit, the transmitters keep or update the phase rotation. The process is repeated during the next time slot until each node's phase has been adjusted to its optimal value. The primary constraint of this algorithm is its convergence time, which was improved in [70] using two-bits feedback (2BF).

Other approaches improve convergence time by reducing the number of collaborative nodes. For example, [71] proposed to separate the distributed nodes in clusters and perform the phase synchronization in two stages. The outcome of this algorithm with respect to 1BF is more evident as the number of nodes increases, when, for $N \approx 100$ nodes, it can decrease to half the required iterations. However, comparing both techniques only by the number of iterations is not fair since the epoch in [71] is more complex and therefore takes

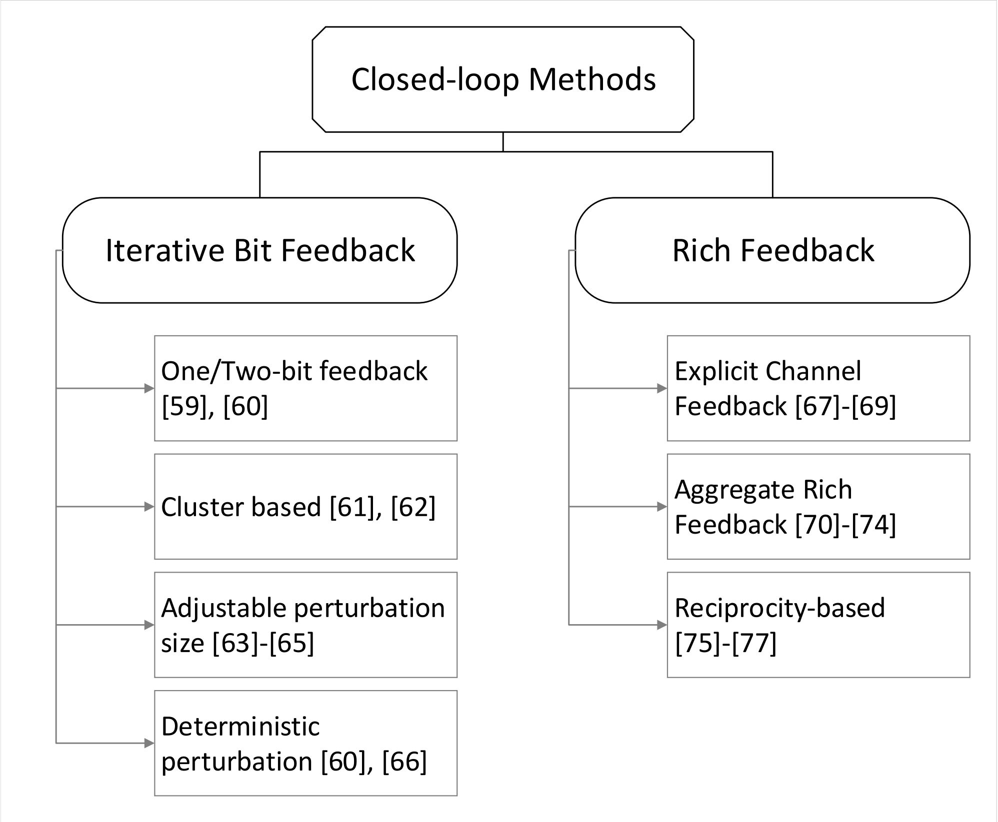

Figure 2.5: Classification of the Closed-loop synchronization methods

a longer convergence time. Another iterative bit feedback method for phase synchronization named opportunistic collaborative beamforming (OCB) was proposed in [72]. In this case, the destination node selects a subset of the distributed nodes whose transmitted signals produce the higher coherence gain at the destination.

Further enhancement of the 1BF is proposed in [73] by emulating the bacterial foraging techniques. In this algorithm which is called the robust adaptive random search algorithm (BioRARSA), the “swim” mechanism, along with the step size adjustment, enables the beamforming nodes to decrease convergence time as well as improve robustness against variation of initial conditions. A comprehensive explanation of this method and its performance can be found in [74]. Another synchronization method that increases the convergence speed by adjusting the perturbation size was presented in [75], where the authors proposed to exploit the cumulative positive feedback information additionally.

The methods discussed above are based on random disturbances of the transmitted signal phase. However, deterministic one-bit feedback (D1BF) [70], and its improved version, successive deterministic distributed beamforming (SDDB) [76] proposed to limit the possible phase perturbations to a set of discrete values from where choose the one that allows achieving the maximum RSS possible. The number of elements in the perturbation set is proportional to the convergence time and determines the performance in terms of maximum achieved RSS. Even though SDDB shows steeper growth rates than D1BF, both deterministic algorithms have limited performance due to the digitization of the perturbation set. Some combinations of deterministic and random methods were considered in [70], where the hybrid methods obtained allow prioritizing the convergence time or the beamforming performance depending on the specific requirements of the network.

Iterative Bit Feedback algorithms are unsuited for DSS due to their slow convergence characteristic. Generally, the long distance between the DSS and the receiver implies a delay in the communication that, combined with the slow convergence of these methods, makes it not suitable to synchronize the system by Iterative Feedback algorithms.

The rich feedback methods use more information instead of just a few feedback bits to achieve synchronization. They can be classified in three categories according to the way the distributed nodes obtain the channel estimation:

- Explicit Channel Feedback method, where each distributed node transmits a known sequence of training symbols to estimate the channel response.
- Aggregate Rich Feedback methods, where the transmitters simultaneously send uncorrelated training sequences used to estimate each channel gain.
- Reciprocity-based methods, where the transmitters observe the uplink feedback signals sent by the target nodes and use reciprocity to estimate their downlink channel gains automatically.

These algorithms have proven to be more robust than the Iterative Bit Feedback methods at the price of considerable feedback overhead. For instance, the enhanced one-bit feedback (E1BF) [77], which is an Explicit Channel Feedback algorithm, compensates for the effect of the average time-varying channel by combining explicit phase information with the 1BF method to provide better convergence and scalability as compared to 1BF. A comprehensive description of this algorithm can be found in [77]. Another Explicit Channel Feedback algorithm that outperforms 1BF for convergence time is the PA for distributed transmit beamforming (DTB) presented in [78], which is also more energetically efficient.

Fig. 2.6 shows the number of iterations required to achieve 90% of the maximum coherent gain for PA and 1BF.

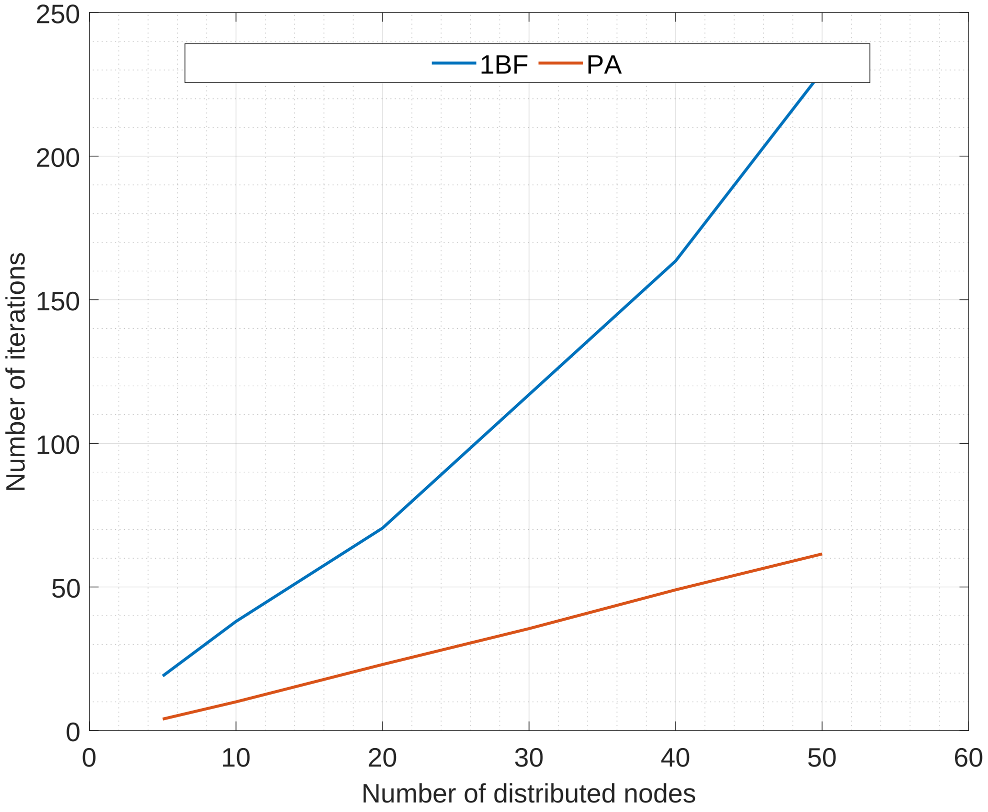

Figure 2.6: Convergence time comparison between 1BF and PA [78]

Generally, nullforming requires far tighter synchronization than beamforming. For that reason, it mainly uses rich feedback approaches. For example, in [79], a distributed gradient-descent algorithm is used to modify the signals' power and phase in consecutive time slots achieving beamforming and nullforming simultaneously. The method works in a time-scheduled way to estimate the CSI and perform the collaborative transmission [79].

In general, Aggregate Rich Feedback methods are more scalable than Explicit ones. For example, the algorithm proposed in [80] is an Aggregate Rich Feedback method based in 1BF that allows each collaborating node to estimate its channel response to the receiver. Similarly, in the scheme proposed in [81], all the distributed nodes simultaneously transmit, and the receiver sends a phase compensation vector to achieve distributed transmit nullforming. However, in this method, the transmitter nodes use Code Division Multiple Access (CDMA) to facilitate signal separation at the receiver. The receiver uses an extended KF (EKF) to generate state estimations for each transmitter, which implies some scalability limitations for this scheme. An improved version of the previous algorithm was proposed in [82].

The Reciprocity-based methods were first introduced as frequency-slotted round-trip (F-RT) synchronization method in [83]. In this work, a distributed network of two nodes, each of them equipped with two PLLs, achieves frequency and phase synchronization by continuously transmitting three unmodulated beacons in a round-trip way. This strategy is effective in highly dynamic networks. Another example of F-RT synchronization is described in [84], where the system performs precise electrical distance measurement and supplies a phase-synchronous signal to a remote location simultaneously. The round-trip phase synchronization method implemented in the article is represented in Fig. 2.7. However, in typical multipath channels, the frequency division duplexing intrinsic of F-RT generates non-reciprocal phase shifts, reducing performance. To overcome the problem, in [85] it is proposed a time-slotted round trip (T-RT) algorithm, which is equivalent to the F-RT, but uses the same frequency for all beacons. Frequency interference is avoided by time division duplexing. Even when this method gives the advantage of simultaneous frequency and phase synchronization, F-RT and T-RT schemes have as a drawback the extreme power consumption due to the extensive signaling.

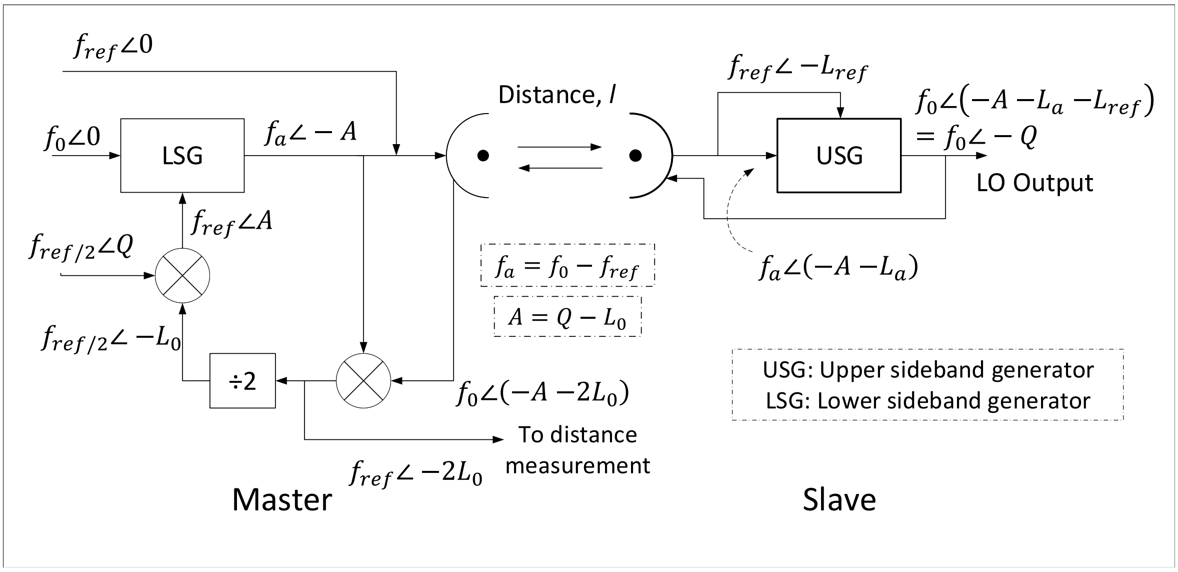

Figure 2.7: Transmission of a phase stabilized LO signal using a round-trip phase synchronization method [84]

All the works listed in this section aim for all carriers to arrive with the same initial phase at the destination based on perfect time alignment. Nevertheless, Mañosa-Caballu and Seco-Granados proposed a robust round-trip (R-RT) synchronization protocol to achieve frequency, phase, and timing synchronization [86]. This algorithm is based on the T-RT method mentioned above. The protocol's robustness allows it to work in dynamic environments because nodes can disappear without severely affecting the system's performance. Other approaches [23] addressed joint time delay and carrier frequency offset (CFO) synchronization in closed-loop systems. For example, [87] covers maximum likelihood synchronization in multi-node decode-and-forward cooperative relaying networks considering time-varying channels. In [88], the same goal was approached through a weighted consensus algorithm to reach synchronization in a dense wireless network.

Open-loop Synchronization Methods Considering the Use of Feedback from an External Aid

Whereas rich feedback may give faster and better convergence than bit feedback, the signaling overhead is substantially more significant. The overhead implies latency problems in real-time applications, representing a considerable challenge for its implementation in cases such as satellite communications systems. In such scenarios where quick and reliable feedback from the target nodes is not possible, Open-loop synchronization methods are the recommended schemes. Fig. 2.8 shows the Open-loop synchronization methods analyzed in this section. It is important to state that almost all the articles included in this section are focused on a single user or target for coherent transmission.

One of the simplest ways to do open-loop synchronization is through Master-slaves architectures, where one primary node broadcasts a beacon, and the secondary nodes lock their oscillators to this reference [8]. This algorithm can be considered as a closed-loop method if the primary node is not part of the DSS [89]. For instance, in [90] all nodes acquire their relative locations from the beacon of a nearby reference point that does not have to be the destination node. This allows open-loop synchronization, but each node requires knowledge of its relative position from a predetermined reference point within the cluster. In [91], frequency and phase synchronization is achieved by locking the secondaries' oscillators to the reference beacon sent by the controller node after pre-compensating the phase mismatch and the propagation delay.

A solution more robust to link and node failures than Master-slave architectures is the

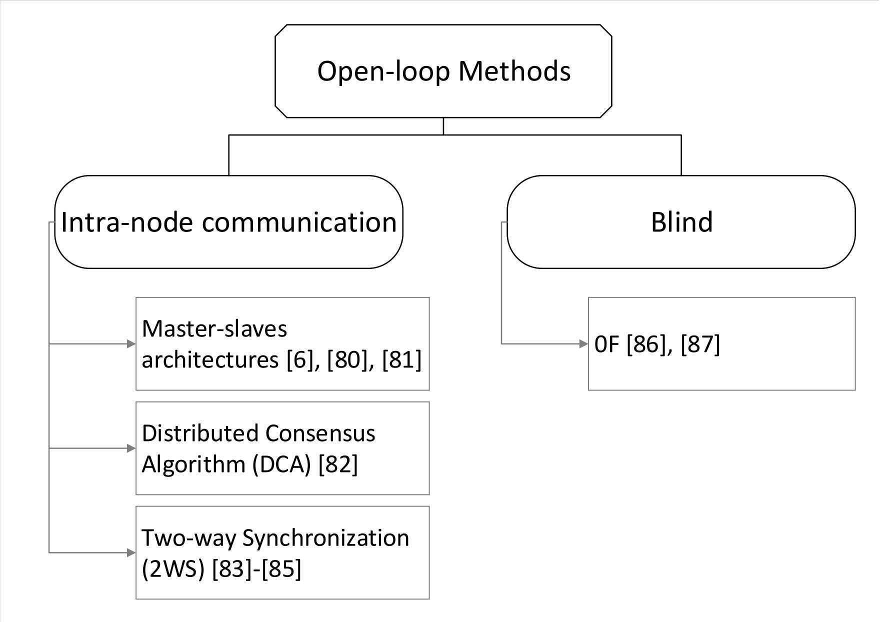

Figure 2.8: Classification of the Open-loop synchronization methods

distributed consensus algorithm (DCA) proposed in [92], where each node broadcasts its carrier signal to all of its neighbors. Thus, the total received signal at any node is the superposition of its neighbors' carrier signals distorted by the channel. The goal of the DCA is to use this received signal to adjust the instantaneous frequency at each distributed node in such a way that all the distributed nodes eventually become frequency locked to a common carrier [92].

Another Open-loop algorithm based on the retrodirective principle is two-way synchronization (2WS), proposed in [93]. The main idea of this method is to implement a retrodirective beamforming between the base stations in a mobile network without the need of CSI or feedback from the mobiles. To this end, a sinusoidal beacon is transmitted in a forward and backward propagation through all the base stations allowing them to compute a common carrier frequency and phase used to perform beamforming. The most significant drawback of retrodirective beamforming methods is that generally, the channel and the RF chains at each transceiver are not reciprocal. A relative calibration method to compensate for this drawback is proposed in [94]. In [95], it is proposed a faster version of 2WS by exploiting the broadcast nature of the wireless links. The difference with [93] is that in the Fast Open-loop protocol, each base station only considers the signal from its adjacent two neighbors and ignores any signal from other base stations. In this way, the algorithm minimizes the latency by reducing the required non-overlapping time slots.

Finally, the blind method or 0F is a synchronization algorithm that intends to synchronize the network without feedback from the target or the rest of the distributed nodes. According to [96], the offsets of the oscillator drift cause intermittent coherent addition of signals at the receiver, which can result in significant beamforming gains. Even though the complexity of the 0F algorithm is simple, the data rate that can be achieved with this method is very low as the coherent beamforming is unstable. In addition, the statistical analysis reported in [97] shows that 0F only works efficiently for a small network.

Table 2.2 provides a summary of the synchronization algorithms analyzed during this section. It includes the target parameter synchronized by the method: Time, Frequency, or Phase; the original application and; the feasibility of using it for the synchronization of DSSs.

2.3.3 Summary and Lessons Learnt

- The synchronization algorithms can be classified as Closed-loop or Open-loop methods based on feedback from a node external to the DSS.

- Another classification considers the communication between the elements of the DSS. It can be Closed-loop when the exchange of information among the distributed satellites is done as a two-way message exchange or; Open-loop when it is done as a broadcast or one-way communication.

- The time synchronization of DSS is mainly based on the TWTT algorithm. Additionally, recent publications refer to the use of pseudo-random noise code and other techniques to achieve time synchronization and inter-satellite ranging simultaneously.

- The time synchronization methods used in WSN do not guarantee the accuracy required by satellite communications applications. However, they could be applied to DSS after some refinement.

- Some methods used for time synchronization in terrestrial distributed wireless networks can be applied to synchronize DSS.

- Among the Closed-loop synchronization algorithms that use the feedback from a node external to the DSS, the rich feedback methods are more suitable to implement in DSS.

Table 2.2: Summary of synchronization methods

Classification	**Method**	**Synch target**	**Application**	**Feasibility of its use in DSS**
Closed-loop: Iterative Bit Feedback	1BF [69] / 2BF [70]	Phase	Terrestrial wireless networks	Not suitable for synchronization of DSS due to their slow convergence.
	OCB [72]	Phase	WSN	
	[71]	Phase	WSN	
	BioRARSA [73]	Phase	Wireless sensor/relay network	
	D1BF [70] / SDDB [76]	Phase	WSN	
Closed-loop: Rich Feedback	TPSN [55] and FTSP [56, 57]	Time	WSN	The basic ideas of these methods can be applied in DSS, specially for large distributed networks. However, some refinement should be considered in order to achieve the accuracy needed for communication applications.
	E1BF [77]	Frequency and phase	Wireless networks	It could be used in some scenarios, depending on the distance between the DSS and the receiver. However, the convergence time, 50% smaller in this method than the original 1BF, can still be an problem. An advantage of this algorithm is that only one element of the DSS processes the feedback from the receiver.
	[79]	Phase	Wireless networks	Even, when the possibility to jointly achieve null and beamforming is a very desirable characteristic in satellite systems, the slow convergence of this method may make it unsuitable for synchronization of DSS
	PA [78]	Frequency and phase	Wireless communication networks	It can be used in a DSS as long as a feedback channel is guarantee. This method presents scalability limitations.
	[80]	Phase	Wireless networks	This method allows simultaneously null and beamforming, which a desirable characteristic in satellite system. However, some limitations could be that (1) most of the calculation are performed by the distributed nodes and, (2) it can produce some latency for large DSS.
	[81] [82]	Frequency and phase	Wireless networks	Allows beam and null-forming considering significant feedback latency, which implies that this method could be used for long baseline communications. However, it can present scalability problems.
	F-RT [83] and T-RT [85]	Frequency and phase	Wireless communication networks	These methods can be used to synchronize DSSs as long as a feedback channel is guarantee. Another constraint related to these methods is that all the satellites in the distributed system have to receive the reference signal broadcasted by the destination node.
	R-RT [86]	Phase, frequency and time	WSN	
	[87]	Phase, frequency and time	Cooperative decode-and-forward communication system	To implement this method in a DSS, all the spacecraft have to simultaneously receive a common training sequence broadcasted by the destination node. In addition, some latency constraints must be taken into account.
Open-loop: Intra-node communication	RBS [53] and PBS [54]	Time	WSN	The basic ideas of these methods can be applied in DSS, specially for large distributed networks. However, some refinement should be considered in order to achieve the accuracy needed for communication applications.
	TWTT [9–11, 14, 44–47]	Time	Satellite communications	It is used in DSS
	Master-Slave [90, 91]	Frequency and phase	WSN	Suitable for DSS with the constraint that it requires accurate inter-satellite ranging.
	DCA [92]	Frequency	Wireless networks	This method can be used to synchronize DSS as long as all the distributed nodes are inside the range of the rest.
	2WS [93–95]	Frequency and phase	Mobile networks	Despite some scalability problems, it can be used to synchronize DSS.
	[88]	Phase, frequency and time	Dense and compact wireless networks	This method is suitable for DSSs, where each node transmission can be received by almost all the satellites in the distributed system. However, algorithms with a central coordinator node acting as a reference for the delay compensation can be a more straightforward solution for less-dense networks.
Open-loop: Blind synchronization	0F [96, 97]	Frequency and phase	Wireless networks	Not recommended for DSSs, since it is limited to small networks, and it allows very low data rate.

Specifically, the PA algorithm for DTB and the reciprocity-based methods are the most recommended.

- Most Open-loop synchronization algorithms without any external aid, but with intra-node communication in the form of two-way message exchange are suitable for the synchronization of DSS.
- Higher synchronization accuracy could be achieved by combining intra-node communication in two-way message exchange and the feedback from a node external to the DSS. However, this configuration is not feasible for all applications.

2.4 Ranging and Relative Positioning in DSSs

There are other operations closely related to the synchronization in DSSs, such as the inter-node ranging and relative position. For these operations, the requirements and accuracy of the coherent operation depend on the performance of the ranging and relative positioning algorithms. Several synchronization methods are based on these measurements [98] [99] [100]. For example, in [98], a dynamic model describes the stochastic kinematics and the clock evolution of each distributed node relative to the frame of the receiver of a DTB system. Other examples are the remote sensing DSSs missions, such as GRACE and PROBA-3, where knowing the relative position among the distributed nodes is fundamental to combining their measurements. For that reason, this section compiles recent advances in inter-node ranging and relative positioning for DSSs.

2.4.1 Inter-Satellite Ranging

For many DSSs, inter-satellite relative range measurement is a requirement for cooperative tasks. Generally, autonomous inter-satellite measurements and communications can reduce the dependence on ground stations, signal transmission delays and improve the resilience and maneuverability of the DSS. To this end, the distributed nodes must have the capability of inter-satellite ranging.

The methods to do inter-satellite ranging can be classified into two main groups represented in Fig. 2.9: those based on RF and those based on optical signals. Measurements made using radio signals are the most mature technology, but optical measurements can achieve better ranging performance. However, the higher directivity of the laser beam, in comparison with the RF antenna's patterns, can represent a limitation for specific applications. Besides, the sunshine can blind optical sensors.

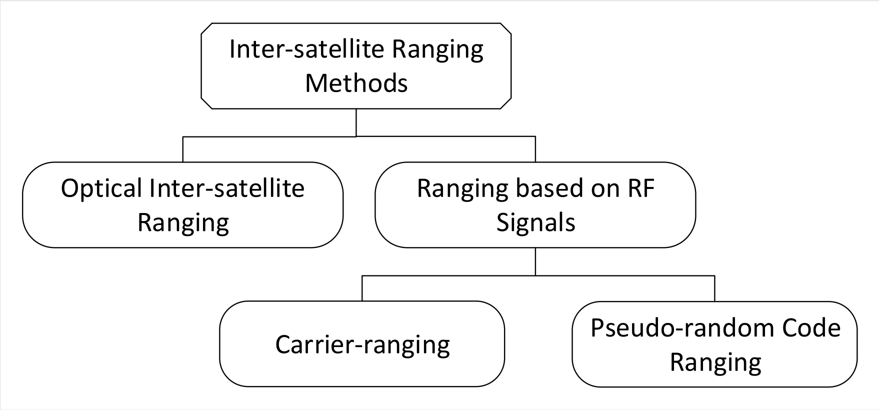

Figure 2.9: Classification of the inter-satellite ranging methods

Optical Inter-Satellite Ranging

The basic principle of optical inter-satellite ranging measurement, also known as transponder laser interferometry, is represented in Fig. 2.10 as explained in [101]. The frequency-stabilized and power-stabilized master laser provides a highly coherent light source to meet interference requirements between the local and receiver laser lights. First, the master's laser light travels through the inter-satellite space and arrives at the slave satellite, where the optical PLL (OPLL) locks the phase of the slave laser to that of the weak light received. Then, the compensated slave laser light points and propagates back to the master satellite. The precision phasemeter measures the phase difference between the master laser and the received light to calculate the inter-satellite distance.

The authors in [101] discussed the state of the art of inter-satellite laser interferometer technologies for spaceborne gravitational-wave detection. However, inter-satellite interferometric ranging has been previously implemented in missions such as GRACE follow-on, where the ranging performance of the former mission was improved by a factor of 10 by including an interferometric laser ranging system [102]. This improvement is due to the laser wavelength being 10,000 times shorter than the microwave wavelength.

As a variant to the methods mentioned before, which required two phase-synchronized lasers on both satellites, a single-laser design was proposed in [103]. This solution included a Mach-Zehnder interferometer on one of the satellites, and a secondary satellite equipped

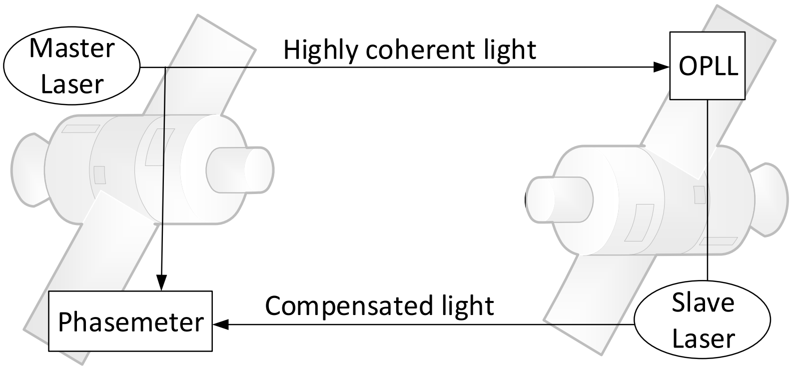

Figure 2.10: Basic principle of optical inter-satellite ranging measurement

with a retro-reflector. The work in [104] overcame the need for highly stable lasers and complex phase-locking solutions of the previous ones. Though, it is required to maintain the coherence properties of the laser light in the reference arm, which is very challenging from the technology point of view for distances larger than 500 km, i.e., twice the expected inter-satellite distance. However, simulation results in [103] showed similar ranging resolution to the two phase-synchronized lasers method.

Recent publications proposed the use of a single optical ISL for ranging and communications simultaneously [105] [106]. For instance, [106] addressed the development of the optical transceivers to transmit ranging and frequency synchronization information through a coherent optical link between the spacecraft of the Kepler constellation. The Kepler system is based on a constellation of 24 Galileo-like medium-Earth lrbit (MEO) and six low-Earth orbit (LEO) satellites carrying stabilized lasers as optical frequency references and equipped with terminals for two-way optical links. This provides a means for broadcasting synchronization, and navigation messages across the DSS without any communication with the ground segment [106]. A ranging precision of 300 µm and 10^{-15} s/s stability (Allan deviation at 1 s) is achieved through an OPLL locked to a pseudo-random noise (PRN) sequence with a chip rate of 25.6 GChip/s. An additional data channel at 50 Mbit/s is multiplexed with the ranging signal to transmit timestamps at a known repetition rate. This allows time alignment of both satellites with the resolution of the field programmable gate arrayss (FPGAs)' clock rate used at both ends. Furthermore, the data link can be used for communication purposes by the constellation. Each MEO satellite has four bidirectional transceivers, two for connecting to neighboring satellites in the same orbit, and two for connecting to LEO satellites.

The terminal aperture size is constrained to 75 mm due to the satellite's weight and size considered. However, to calculate the absolute ranging between terminals with an accuracy of 0.3 mm, the system requires aligning precision of 2.5% the chip length or better [106].

Another example of simultaneous ranging and communications inter-satellite optical link is the coherent optical receiver implemented in [105]. In this article, the authors presented an FPGA-based feedback-homodyne scheme as an alternative to the OPLL to obtain a more flexible coherent optical receiver. Besides, a parallel fast Fourier transform (FFT) wavelength drift estimation algorithm was proposed, aiming at improving the speed and range of wavelength drift tracking simultaneously. Simulation results showed that the wavelength drift tracking performance depends on the number of FFT estimators used in parallel. However, using a real-time FPGA implementation, the authors demonstrated that the design meets the needs of phase offset compensation when three FFT estimators are used in parallel [105].

Inter-Satellite Ranging Based on RF Signals

The use of RF for inter-satellite ranging is not a new concept. Articles such as [107], published in 1985, already proposed a design to measure satellite-to-satellite range-rate with a precision smaller than 1 μm/s in distances between 100 km and 300 km. However, further analyses included the frequency instability of the oscillators [108], the channel noise conditions [109], and the requirements of low-cost small satellites [110] among other specifications. Distances can be determined from either the signal's modulation (PRN codes) or the carrier phase.

One of the most popular carrier-phase based ranging methods is the DOWR [14] [108] [109]. By combining the one-way range measurements from two microwave-ranging devices, the method minimizes the effect of oscillator phase noise. Each satellite uses identical transmission and reception subsystems to send a carrier signal to the other. The recorded measurements are transmitted to a control segment for processing and calculating the inter-satellite range. DOWR method is represented in Fig. 2.11.

Some variations of this method have been proposed. For example, in [14] the authors addressed the use of dual one-way time (DOWT) synchronization and ranging (DOWT&DOWR) in DSSs. Simulation results indicated less than 0.2 m and 0.5 ns precise ranging and time synchronization accuracy and error time synchronization smaller than ±10 ns for inter-satellite distances up to 200 km in satellite formation flying [14]. Another example is the Random Access Inter-satellite Ranging (RAISSR) system proposed in [111]. In this system, each satellite

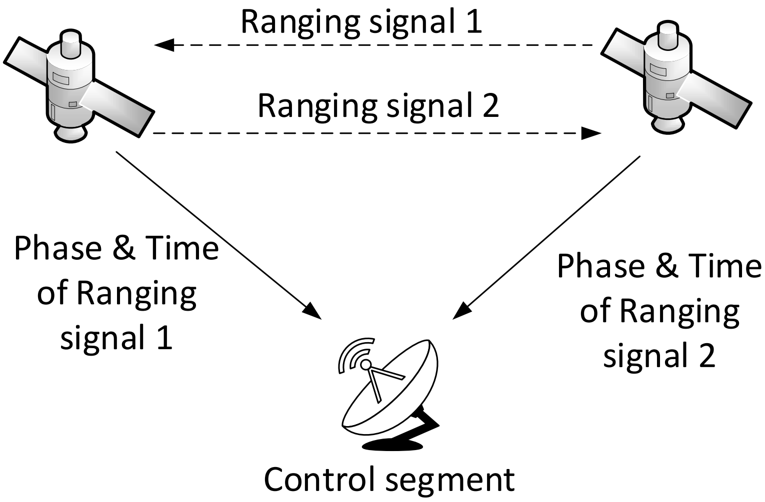

Figure 2.11: Basic principle of RF carrier-ranging by DOWR.

transmits a signal to allow other satellites to perform a one-way distance measurement with respect to it. Even when the authors claimed no strict time synchronization, the method requires all the satellites to share a common time reference.

In [112], an approach to solving the problem of autonomous timing is proposed. This method aims to achieve time synchronization and high precision ranging between onboard oscillators and clocks on Earth, with only scarce information exchange. The main idea is to calculate the satellites CFO using a frequency tracking loop. Then, the inter-satellite range and the satellites' relative radial velocity are estimated on the ground [112]. The reported results showed a precision of 0.1 ns for inter-satellite baseline measurements and the accuracy of velocity measurement around 10^{-3} m/s, for approximately 0.01 Hz carrier frequency tracking error [112].

An essential aspect of DOWR that limits its performance is its synchronization requirements. As this method requires the transmitter and receiver to be synchronized, its accuracy is directly related to the performance of the synchronization algorithm. Clock drifts and offsets between nodes can introduce errors in the order of microseconds which can be too large for specific applications. On the other hand, the two-way ranging (TWR) method does not have this drawback. In TWR, introduced in [110], one satellite sends the ranging signal and activates a counter to calculate the elapsed time until the reception of the other satellite replies. In this way, there is no need to synchronize both satellites' clocks [110]. The evaluation of the algorithm on a SDR platform is reported in [110], showing an accuracy of a few centimeters.

Another hardware demonstration was presented in [99]. In this case, the authors developed a coherent distributed transmission system based on high-accuracy microwave ranging to perform DTB for mobile platforms. The Two-tone ranging method used for the indoor and outdoor experiments was introduced in [100].

The most well-known example of pseudo-random code ranging is the method applied by GNSS constellations. A variation of this method to measure the inter-satellite range in deep-space missions, where the navigation constellation is not available, was suggested in [113]. The design combines the typical GPS receiver with a RF transceiver to use when the satellite does not receive the GPS constellation' signals. The GPS module is a flight-qualified design that performs orbit determination using a EKF and the inter-satellite distance measurement is obtained by differencing both filtered absolute GPS solutions. The core of the whole system is a central processing unit (CPU) core which controls the switch and coordination of the two ranging units [113]. Similarly, an augmented relative navigation system (ARNS) for autonomous satellite formation flying in LEO is proposed in [114]. The idea of this article is that inter-satellite ranging systems can provide additional observation information, which can be used to increase the GPS stand-alone observation dimension. Reported results indicated that the ARNS improved the relative positioning accuracy by one order of magnitude in comparison to the GPS stand-alone solution [114].

In addition, other authors addressed ranging methods based on PRN codes. For instance, in [115] it is presented an algorithm to determine the initial value of smooth pseudo-range for the smoothing method proposed by Hatch [116]. The algorithm uses the least-squares straight line fitting technique to decrease the convergence time and improve the ranging accuracy [115]. On the other hand, the authors of [117] analyzed how it is affected the accuracy of inter-satellite ranging in a direct sequence spread spectrum (DSSS) by the used bandwidth and [118] introduced a new ranging scheme combining continuous phase modulation and a PRN ranging code. The chip pulse used in this method is based on a normally distributed signal, which improves the ranging accuracy and reliability of the system.

Another example of a RF ranging technique using the signal's modulation was proposed in [119]. This paper analyzed a hybrid orthogonal frequency division multiplexing (OFDM) communication-metrology system for a two satellites formation flying. The system uses

OFDM signals for ISL communications and measurements functions. The inter-satellite distance is estimated using a training symbol, which is also used for time and frequency synchronizations and estimation of the channel impulse response. The accuracy of the technique depends mainly on the bandwidth of the transmitted signal [119].

Most recent works focus on carrier ranging methods assisted by pseudo-random code ranging, which allows higher precision range values. For example, [120] proposed a pseudo-code-assisted carrier ranging algorithm, which is the combination of pseudo-range and dual-frequency carrier phase ranging methods. In [121], the impact of the frequency selection on the ranging accuracy was analyzed. Too high frequency leads to problems in the resolution of integer ambiguity, but too low frequency impacts ranging accuracy. Both articles reported range errors on the order of 1 cm for inter-satellite distances around 100 km [120] [121].

Even though the accuracy of carrier-ranging methods is higher than pseudo-random code ranging methods, the integer ambiguity is more difficult to resolve for the former ones. The solution of the phase integer ambiguity problem has been dealt in [114], [122] and [123]. For instance, [122] presents a robust integer-cycle ambiguity resolution method by modifying the well-known least-squares ambiguity decorrelation adjustment (LAMBDA) method [124]. The authors derived the validation threshold in closed-form as a function of the phase noise variance and the antenna baseline geometry. As a result, the success rate of the original LAMBDA is improved. However, the method requires that the spacecraft of which the LOS will be estimated is equipped with a body-fixed array of at least three antennas in different planes [122]. This could be a limitation for small satellites missions. Another procedure based on the LAMBDA method was proposed in [114]. This paper contains two approaches to combine the inter-satellite ranging measurements with GPS. Besides, it proposes a feedback scheme to convert the ambiguity float solutions obtained from the EKF into pseudo-perfect measurements through the LAMBDA method. After the possible integer solutions are verified, they are adopted as pseudo-perfect measurements to update the EKF for the next epoch.

Another approach to the phase integer ambiguity problem was proposed in [123]. In this case, the authors used the simplified time-differenced technique [125] to eliminate the influence of ambiguity in a GPS/inertial navigation system (INS) integrated navigation algorithm [123]. The simplified time-differenced method consists of processing time differences of successive carrier phase measurements at a GPS base station, which increases the velocity and attitude accuracy. It reduces noise in the position information compared to the traditional tightly coupled systems. Unfortunately, the time-differenced carrier phase measurements do not easily fit in the framework of a KF measurement equation, which has adverse effects on the derivation of an appropriate measurement matrix [125].

2.4.2 Relative Positioning

Spacecraft relative positioning in formation flying is a crucial enabler of new space missions and of paramount importance for distributed satellites architectures. Clearly, two subcategories can be distinguished: in-orbit autonomous and assisted from the ground. Relative positioning can be seen as a coordinated operation of the ranging systems described in the section above, which can occur either in-orbit or on-ground.

In-Orbit Autonomous

The primary technology used for precise relative positioning of autonomous formation flying satellites is GNSS.

If the relative position between two GNSS receivers is required, the GNSS data differences from two receivers can be used. This method reduces common data errors, such as the GPS satellite clock offset. The difference is typically calculated using the pseudo-range estimation between the receivers and a GNSS satellite or more. Sub-metric precision is obtained by using this method, once the code ambiguity is resolved [126].

In order to enable cm to mm positioning accuracy levels, it is required the handling of carrier differential GNSS (CDGNSS) estimations [127]. Within the setting of the GRACE formation flying mission, the possibility of 1 mm level relative navigation over a 200 km separation has been illustrated by utilizing carrier GPS estimations from a high-grade dual-frequency BlackJack receiver [128].

A major problem in using CDGNSS is tackling for the unknown integer number of cycles (integer ambiguity) [129]. Especially when the resilience and precision of the integer solution are affected by variations in the number of common-in-view satellites, and ephemeris and ionospheric differential errors. This is enhanced when the inter-satellite distances are highly variable due to the relative orbital trajectory.

A few strategies based on arrays of GNSS sensors have been proposed to unravel the phase ambiguity problem. Since antennas are unbendingly mounted on the stage, the relative antenna position within the local body frame is known in advance. It can be used to improve the accuracy of the estimated integer ambiguity. In [130], the use of the Multivariate Constrained Least-squares AMBiguity Decorrelation Adjustment (MC-LAMBDA) strategy [131] successfully utilizing nonlinear geometrical constraints. By consolidating the known antenna geometry into its ambiguity objective function, this strategy has been appeared to illustrate reliable and immediate single-frequency integer ambiguity determination.

DSSs operating above LEO loses coverage of the GNSSs infrastructure and has to rely on other means for tracking and navigation. For those missions, a trilateration scheme is proposed in [132] that evaluates the 3-dimensional (3D) relative position between a reference spacecraft and a target spacecraft using raw-range measurements from a distance baseline of known locations, which is called "anchors". The anchors can be antennas of a ground-based network or satellites of a space-based network (e.g., GPS). The method assumes the clocks of the anchors to be perfectly synchronized and requires some synchronization between the anchors and the reference spacecraft. However, the synchronization errors between the reference spacecraft and the rest of the satellites in the DSS is compensated by using an additional anchor. This method achieves sub-meter accuracy for a GEO DSS with two spacecraft, using a baseline network of three ground stations as anchors.

Another example of very accurate tracking and control of the relative position is the PROBA-3 mission. PROBA-3 is a European Space Agency (ESA) mission to obtain highly accurate formation flying. A couple of satellites, the Coronagraph Spacecraft (CSC) and the Occulter Spacecraft (OSC) will work together as an externally occulted solar coronagraph. The CSC hosts the optical assembly of the coronagraph as the primary payload, while the OSC carries the coronagraph external occulter disk. The mission requirements are a longitudinal accuracy better than 1 mm for the inter-satellite distance of 144 m [34]. To make this feasible, the formation flight system is distributed between both spacecraft: the CSC hosts the formation flying sensors, while the OSC performs the data processing [133]. The formation flight task requires the use of several metrology subsystems, from coarse accuracy and large scale range determination to very accurate and shorter scale range measurement and absolute positioning. All the data generated by these subsystems are processed in real-time by the Guidance and Navigation Control system, obtaining an unprecedented accuracy [134].

IRASSI is an interferometry-based mission concept composed of five free-flying telescopes orbiting the Sun-Earth/Moon second Lagrangian point, L2. It focuses on observing specific regions of the sky to study star formation, evolution processes, and early planetary origins. The study of these processes requires a telescope with angular resolution lower than 0.1 arcsec [135]. The interferometer relies on dynamically changing baselines obtained through the physical separation during scientific observations to achieve such strict resolution values. For example, the baseline vectors between the telescope reference points must be determined with an accuracy of 5 μm to guarantee the precise correlation of the detected signals. The navigation concept capable to achieve these strict requirements consist of two components: the absolute position estimation concerning Earth and the relative position estimation, which determines the satellite's positions to each other [136]. The description of two autonomous relative positioning algorithms based on a geometric snapshot approach can be found in [137].

For formation flying missions, in addition to the inter-satellites position, it is imperative to estimate and control the satellites' attitudes accurately. In [138], the relationship between the precision estimation against the ranging accuracy, ranging distance, and satellite relative position were analyzed. As a result, it was concluded that obtaining accurate measurements required a balanced number of transmitting and receiving antennas with suitable configurations. It is a necessity to install more antennas to improve the precision estimation of the attitude angles [138].

Another critical requirement of formation flying is accurate relative navigation. Significant research results have been published about this topic. For example, [139] used the nonlinear dynamics describing the relative positioning of multiple spacecraft for formation flying trajectory tracking control. Using Lyapunov-based control design and stability analysis techniques, the authors developed a nonlinear adaptive higher-order sliding mode control commonly known as adaptive super twisting sliding mode control. On the other hand, [140] develops an efficient approach of autonomous relative orbit determination for satellite formation flying. The proposed solution uses the inter-satellite local measurements by the microwave radar and laser devices on board the satellites to perform the relative navigation. The design uses a decentralized Schmidt KF [140] to estimate the state of relative orbit between the satellites and proves that this approach is immune to the single satellite failure. Simulation results showed that the relative position estimation might achieve centimeter-level accuracy, and relative velocity estimation may achieve mm/s-level accuracy for a circular spatial formation consisting of three satellites where the chief satellite is at the center. The radius is about 1 km [140]. Similarly, in [141] a method for autonomous orbit determination combining X-ray pulsar measurements and inter-satellite ranging during Mars orbiting phase was presented. The method calculates an observability index reflecting the measurement information quality and optimizes the observable target selection and the observation scheduling. Then, the Unscented KF is used to estimate the autonomous pulsar assisted orbit determination [141].

Assisted from Ground

Determining the orbital position of satellites from the ground requires obtaining azimuth and elevation view angles of the satellite and the distance from the ground station to the satellite (range).

One of the most accurate precise orbit determination (POD) measurements assisted from the ground can be achieved by Radio Interferometry methods. Interferometry is a technique for passive tracking. A simple interferometer consists of two receivers represented in Fig. 2.12. Using the phase difference between the signals received by the two antennas, the direction of the target can be determined. Connected-Element Interferometry (CEI) is a technique for determining the phase offset from the TOA difference of a downlink radio signal to two antennas on a short baseline. In [142], the authors used a small-scale CEI system of two orthogonal baselines (75 m × 35 m) to track a GEO satellite. Reported results showed accuracies smaller than 1 km in the radial and the cross-track directions, and 3D position accuracy in the order of 2 km. Another example of the positioning of GEO satellites by Radio Interferometry was proposed in [143]. In this case, the authors focused on determining the view angles of GEO satellites with an estimation accuracy of 0.001° at Ku band.

In addition, ISLs can improve the accuracy of orbit determination for GNSSs constellations. One example of this was presented in [144], where it was demonstrated that the POD of the Kepler system could be performed with just one ground station achieving orbit accuracies of 5 cm in 3D and 0.24 cm in radial direction [144]. On the other hand, in [145], it was proven that the use of ISL ranging measurements could reduce the first positioning time about six times in conventional navigation receivers.

2.4.3 Summary and Lessons Learnt

- In a DSS, the inter-node ranging and relative position are closely related to the synchronization algorithm. Generally, the requirements and accuracy of the coherent operation

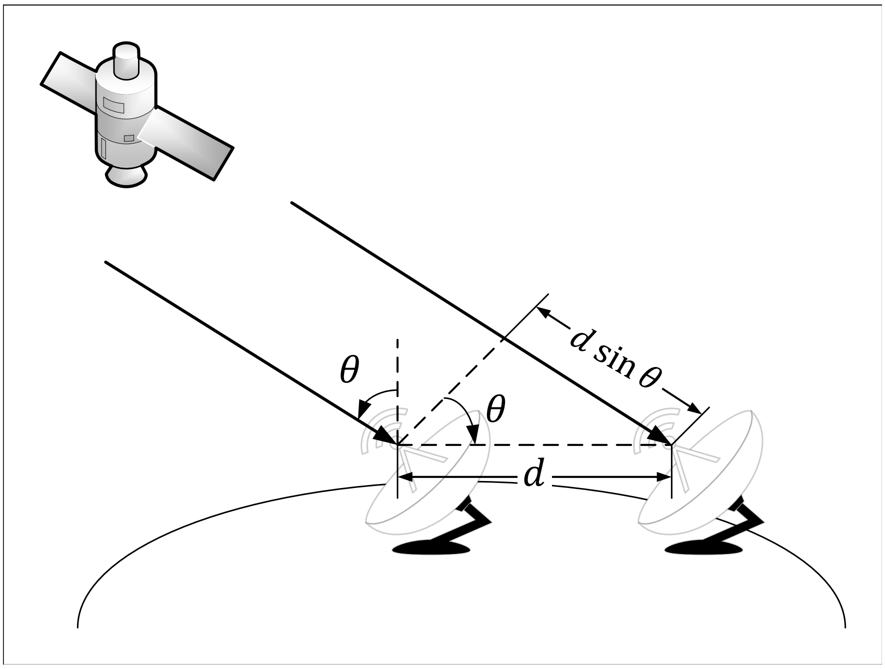

Figure 2.12: Orbit determination by Interferometry

depend on the performance of the ranging and relative positioning algorithms as much as the synchronization itself.

- Optical inter-satellite ranging methods can achieve higher accuracy, but the higher directivity of the laser beam can represent a limitation for specific applications.
- The use of a single optical ISL to simultaneously perform ranging and communication is a trending topic in this field.
- Inter-satellite ranging based on RF can use measurements of the carrier's phase or use the signal modulation. Recent publications considered the combination of both: carrier ranging assisted by pseudo-random code ranging methods.
- Both optical and RF-based ranging algorithms have to deal with the phase integer ambiguity problem.
- Spacecraft relative positioning can be seen as a coordinated operation of the ranging systems described above, which can take place either in-orbit autonomously or assisted from the ground.
- The leading technology used for precise relative positioning of autonomous formation flying satellites is GNSS.

- DSSs operating above LEO loses coverage of the GNSS infrastructure and has to rely on more complex schemes. Examples of these schemes were analyzed in this section.
- One of the most precise POD measurements assisted from the ground can be achieved by Radio Interferometry methods.

2.5 Applications of DSSs Synchronization

As stated above, carrier and time synchronization are critical and very challenging requirements for CDSS. Consequently, the research in the area is very prolific. In this section, the most significant articles about synchronization for DSS found in the literature are summarized. They are arranged in two groups attending to its application: Communications and Remote Sensing.

2.5.1 Communications

Small satellite distributed systems are envisioned to be the future of space communications [17]. Forming a dynamic phased array in space with the nodes of a DSS can improve the communications capabilities between the network and the Earth. However, implementing such an array requires effective open-loop carrier synchronization [1]. In [146], the phase synchronization constraints of a DSS of very simple, resource-limited femto-satellites communicating with Earth were derived and discussed [146]. Fig. 2.13 from [146] shows the normalized amplitude of the received signal as a function of the number of transmitters for different accuracies of phase synchronization. As it can be appreciated in the figure for a high number of nodes, the effects of phase synchronization inaccuracies are more evident.

In [13], a time and phase synchronization solution to perform beamforming in a LEO-DSS is proposed. The mathematical framework and analysis of the synchronization scheme is developed, which relays in an external beacon transmitted from a GEO spacecraft above the intended ground receiver. This open-loop method achieves subcentimeter-level (subnanosecond-level) phase synchronization with localization accuracy on the order of meters [13]. However, these results are restrained to a particular array geometry, which is not always feasible.

In [14], the simulation and performance evaluation of the two-way range and time synchronization method for a DSS were presented. The DSS consisted of four satellites in a formation flying mission, with 50 km of inter-satellite distance and a carrier frequency of 400 MHz sim-

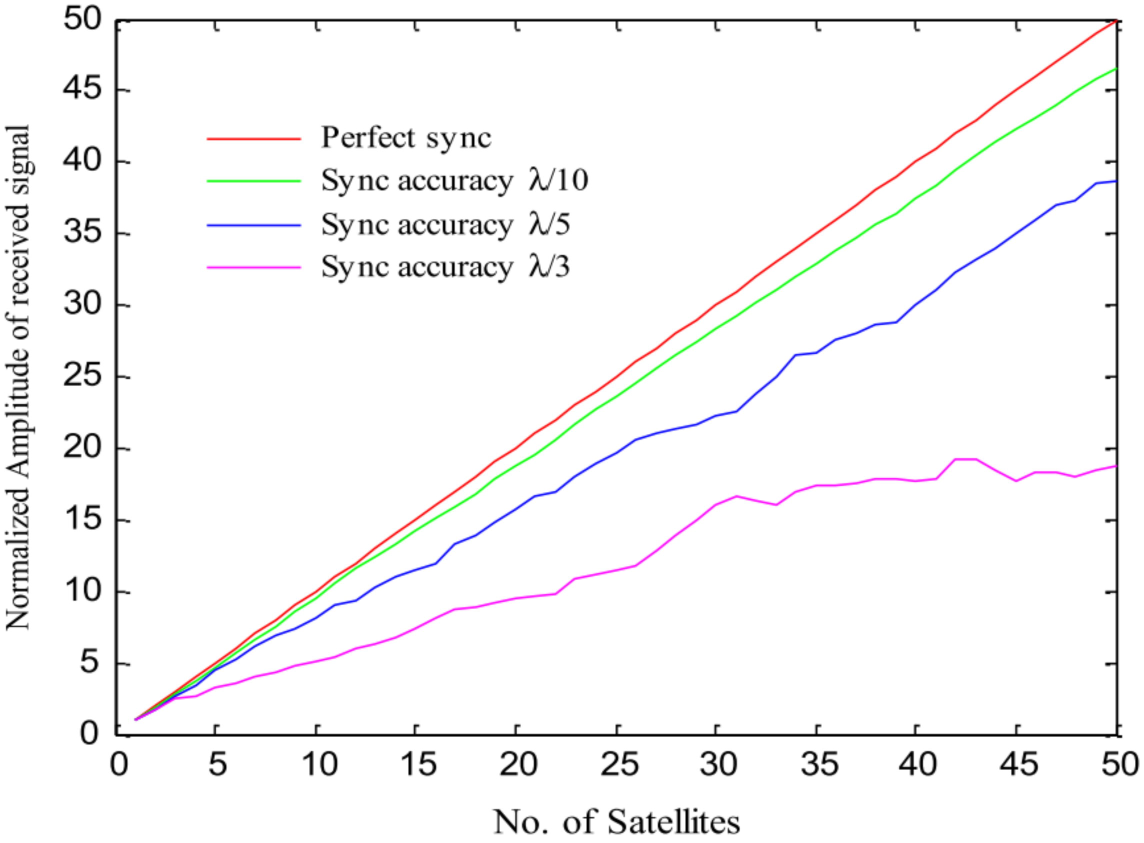

Figure 2.13: Normalized amplitude of the received signal vs. the number of satellites for different values of phase synchronization accuracy [146]

ulated in the Systems Tool Kit (STK) platform from Analytical Graphics, Inc. According to the simulation results, the error of the time synchronization was less than 10 ns [14].

2.5.2 Remote Sensing

Remote sensing and Earth observation from DSSs have become attractive for the community in the last years. New concepts, like distributed synthetic aperture radiometers or fractionated radars, offer the potential to significantly reduce the costs of future multistatic SAR missions [147] [148]. Besides, the low radar power budget and high spatial resolution requirements of future remote sensing satellite missions seem to be only possible to achieve through multistatic configurations [149]. However, the frequency, phase, and time synchronization is still the major challenge that slows down the launch of new missions. For that reason, new synchronization methods for Remote Sensing DSSs are published daily.

For instance, an inter-satellite time synchronization algorithm for a micro-satellite cluster was proposed in [10]. The authors proposed a time control loop that dynamically adjusts each satellite reference frequency according to the time difference with the time benchmark of the cluster. Consequently, time synchronization is achieved by locking the clocks of all the satellites to a chosen one. Similarly, [150] presents a method to relatively synchronize the clocks in a DSSs without the use of GNSS signals. A reference pulse transmitted by a master satellite is received and time-stamped by all the secondary satellites in its broadcast domain. The method estimates the clock offsets relative to the other secondary satellites by calculating the receive-time differences between two secondary satellites. Simulation results reported in [150] showed excellent convergence rates. However, this method requires that all the distributed nodes are in the same broadcast domain of a single master satellite, and the LOS from one satellite to all others must always be available. Besides, the algorithm is affected by the difference in propagation time between two receivers. This is not a problem for relatively small networks but, for DSSs with longer inter-satellite distances, these propagation delays have to be compensated.

Other authors have studied the effects of time and frequency synchronization on DSS SARs [151] [152]. In [151], a model considering the time and frequency synchronization errors in interferometric synthetic aperture radar (InSAR) were presented. The performance of the range and azimuth compression with the synchronization errors was analyzed to obtain the time and frequency synchronization requirements for parasitic InSAR system design. On the other hand, [152] studied the performance degradation in bi-static and multi-static SARs due to the oscillators' phase noise. Using a dedicated synchronization link to quantify and compensate the oscillators phase noise was proposed considering three different synchronization schemes: continuous duplex, pulsed duplex and, pulsed alternated. The analysis included additional factors such as receiver noise and the Doppler effect and contributions known from sampling theory like aliasing and interpolation errors. According to the reported results, successful oscillator phase noise compensation is possible if the compensation algorithm and the signal timing are adapted to the link hardware and SAR parameters [152].

More advanced works have reached the implementation and test steps, which are fundamental to using a synchronization method in a mission. For example, [153] proposed a hardware-in-the-loop simulation and evaluation approach for DSSs SAR. The proposal was used to model a typical bi-satellite formation spaceborne distributed SAR system in the X band. The SARs' central electronic equipment was implemented in hardware, whereas the echo generation and the processing and evaluation of the results were performed in software. In [154], a phase synchronization scheme based on F-RT for the operation of the airborne based bistatic SAR receiver, SABRINA-UAV was prototyped and tested in the laboratory. Another example is the testbed for coherent distributed remote sensing systems proposed in [149]. This platform is composed of two satellites, the channel emulator, and two targets, all implemented in universal software radio peripherals (USRP). The authors proposed and validated a dual carrier point-to-point synchronization loop through the testbed. The synchronization algorithm is based on a Master-Slave architecture to autonomously synchronize both satellite clocks with a common reference using ISLs [149]. Generally, the hardware simulations include features that cannot be easily or accurately considered with computer-based simulations. First, there are coupling relationships among the channel mismatch, the time and phase synchronization errors, and other error sources. The single error analysis method used in the computer-based simulation cannot meet this requirement. Besides, the hardware implementation of the synchronization algorithm gives a more accurate description of its performance. Computer-based simulations cannot precisely measure features like processing time and resources. On the other hand, the error source characteristic has to be known for data analysis and evaluation, which is more complicated for hardware simulations.

Several remote sensing distributed satellite missions have been proposed and deployed in recent years. Section 2.6 will refer to already deployed missions, but the proposed synchronization algorithms for future missions are of interest to this section.

1. ARGOS: The Advanced Radar Geosynchronous Observation System (ARGOS) will be a MIMO SAR system hosted on a swarm of mini-satellites in quasi-geostationary orbits [155]. It consists of: a swarm of active and passive spacecraft in a zero inclination quasi-GEO orbit; a data-link to a telecommunication satellite that is used for both data download and synchronization; a ground segment and; a network of active calibrators for precise estimation of sensors clocks and orbits. According to [156], the link with the telecommunication satellite can be used to synchronize the DSS to a common clock and support the estimation of the precise orbits, in a similar way to a cloud PLL. Besides, the oscillators' phase noise can be compensated by exploiting a network of Compact Active Transponders or through an on-ground synchronization scheme capable of estimating the phase on very bright point targets.

2. LuTan-1: LuTan-1 (LT-1), also known as TwinSAR-L mission, is an innovative spaceborne bistatic SAR mission based on the use of two radar satellites operating at L-band with flexible formation flying, to generate the global digital terrain models in a bistatic interferometry mode [157]. Several articles about the LT-1 phase synchronization scheme have been published [157] [158] [159] [160]. The algorithm, proposed in [158], considers the time multiplexing of the synchronization pulses with the radar pulse-repetition intervals avoiding any interference in the SAR data acquisition. Besides, [157] proposed a KF phase-error estimation and compensation method, which improves the synchronization accuracy for low signal-to-noise ratio (SNR). On the other hand, [159] evaluated the performance of the LT-1's synchronization scheme for multipath effects, and [160] presents its experimental verification.

3. ConGaLSAR: A Constellation of Geostationary and LEO SAR (ConGaLSAR) radars has been proposed in [148]. The phase and time synchronization of this constellation would be supported by a novel transponding mode known as MirrorSAR, where the LEO satellites work as relay nodes for the ground echoes to the illuminating GEO satellite. The key idea of MirrorSAR is to redirect the radar echoes to the spacecraft, where they can be coherently demodulated with the same clock references previously used to generate the radar pulses [147]. The authors introduce two alternatives for synchronization. In the most simple one, the LEO subsystem functionality is limited to amplify and forward the received RF signal. The second possible configuration, named Double Mirror Synchronization, requires the transmission of a very stable reference signal from the illuminator to the LEO-satellites by using a dedicated low-gain antenna. Even though this method increases the synchronization processing considerably and requires more complex LEO-satellites, it still assumes that the distance between the transmitter and receiver satellites is almost constant, and it can be accurately estimated [147].

2.5.3 Summary and Lessons Learnt

- Not many publications consider CDSS for communications applications. However, there are some simulations for LEO DSS, synchronized with the aid of a GEO spacecraft. In addition, the two-way time and range synchronization method has been considered for the synchronization of a DSS of four satellites in a formation flying mission.

- Remote sensing and Earth observation from DSSs has become attractive for the community in the last years. However, the frequency, phase, and time synchronization is still the major challenge that slows down the launch of new missions. For that reason, new synchronization methods for Remote Sensing DSSs are published constantly.
- Time and phase synchronization by master-slave architecture using intra-node communications are the preferred methods for remote sensing DSSs. However, the system's complexity increases with the number of distributed nodes to be synchronized due to the increment of ISLs required.
- Information about the synchronization algorithms for future remote sensing distributed satellites missions was discussed in this section, specifically ARGOS, LuTan-1, and ConGaLSAR missions.

2.6 Examples of Synchronization for DSSs

The development of new synchronization techniques in DSSs as in any other wireless network requires three main steps: design, prototyping, and deployment. The new synchronization methods are theoretically analyzed, tested, and improved using software simulators during the design step. However, regardless of the extent to which the design phase is conducted, new algorithms should comply with the prototyping before deployment. Theoretical design - software simulation - prototyping is a closed-loop that must be executed repeatedly to improve a synchronization technique before its deployment in DSSs. Theoretical design and simulation of synchronization algorithms suitable for DSS were already covered in previous sections. This section summarizes the most relevant hardware implementations and prototyping of such algorithms.

The most relevant and advanced examples of synchronization techniques for cohesive distributed systems are analyzed in the following. Unlike the previous section, where concepts and theoretical methods were discussed, this section presents synchronization algorithms that have been implemented and tested at least as a hardware PoC. Similar to the previous section, the examples are classified according to their application as Synchronization Examples in Distributed Communications Systems and Synchronization Examples in Remote Sensing DSSs.

2.6.1 Synchronization Examples in Distributed Communications Systems

Hardware development for communication satellite systems has been pointing toward reconfigurable SDR System-on-a-Chip ground receivers, and to the ultimate extreme of Satellite-on-a-chip during the last years, [17]. In general, recent trends in prototyping and deployment of spacecraft are based on commercial off-the-shelf (COTS) [161], FPGA [162] and SDR [163] designs. This trend can be explained due to its reconfigurable characteristics and because they allow less expensive and faster development processes. Several examples of using SDR for inter-satellite communication in small satellite systems can be found in [1]. Fig. 2.14 and 2.15 show a graphic representation of the synchronization methods and the hardware platforms analyzed in this section.

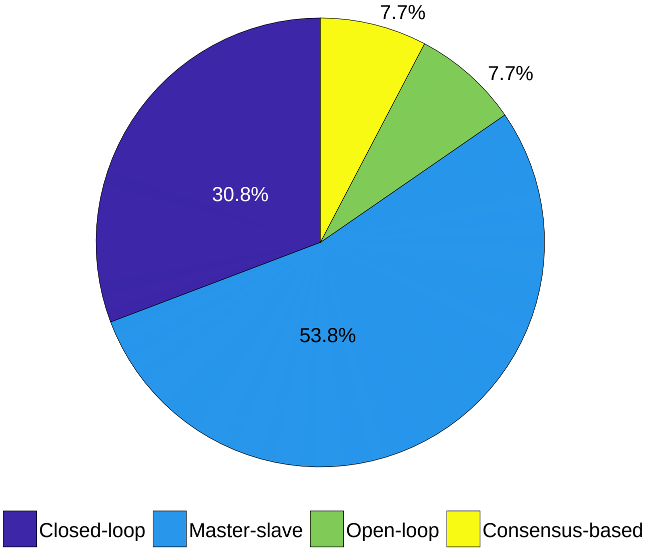

Figure 2.14: Distribution of prototypes per synchronization method

However, there are not many publications about the hardware prototypes of synchronization algorithms, specifically in Communications CDSS. Mainly because the use of CDSSs for communications is a very recent topic that does not have any launched missions yet. Nevertheless, it is helpful to analyze the PoC of the synchronization algorithms used in distributed terrestrial communications that DSSs could adopt. This can support the selection of the synchronization technique and the hardware platform during the design of a prototype for Communications CDSS. The examples are presented in order of increasing complexity, and

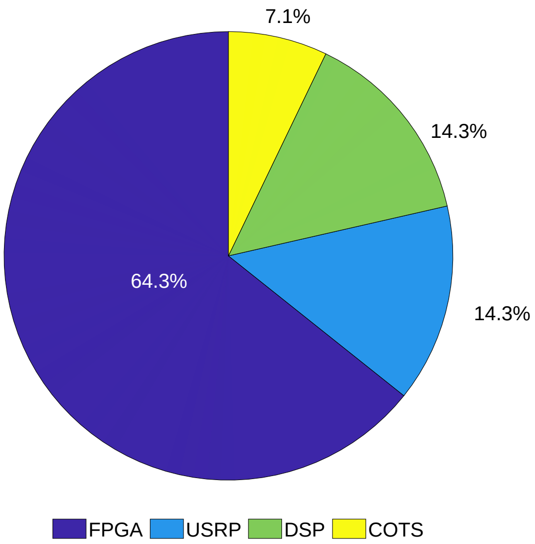

Figure 2.15: Distribution of hardware platforms used to implement the synchronization methods

some technical details are listed in Table 2.3 at the end of the section.

Mobile Communications Networks

One example of distributed coherent radio system that shows some similarities with the DSSs is the recently proposed cell-free (CF) massive MIMO concept. In CF operation, the network infrastructure performs beamforming towards the user equipments (UEs) using multiple distributed radio nodes. The beamforming coordination relies on the time division duplex (TDD) operation and uses a densely distributed network topology [164,165]. Although there is a CPU in CF Massive MIMO system, the exchange of information happens only in the form of payload data while the power control coefficients change slowly. Neither is there a provision of sharing the instantaneous CSI among the access point (AP) or the CPU. Channel estimation is performed only at the AP using uplink pilot signals and further used for decoding uplink symbols and precoding the downlink symbols. [166].

A crucial requirement of the CF Massive MIMO is the global synchronization of RF carriers and information symbols across the geographically distributed service nodes network. In [167], CFO estimation for Distributed Massive MIMO and CF Massive MIMO is studied. Specifically, the article evaluates the performance of distributed large-scale MIMO systems with two collaborative (successive and joint), and one non-collaborative (independent) CFO estimation techniques [167]. According to [168], the global synchronization of RF carriers and information symbols across a distributed MIMO network can be done with a common 1 pps (pulse per second) GPS timing signal used to provide GPS disciplined oscillators [168]. This solution was demonstrated for two 50 MHz carriers tracked by frequency lock loops implemented on FPGA development platforms. Results showed a locking time of 500 s and a coherence time of 10 s, which is enough for the MIMO processing [168].

The TDD operation implemented in CF Massive MIMO is not very appealing for a DSSs used for communication applications due to the long latency of the satellite orbits. However, an extrapolation of the method to frequency division duplex (FDD) scenarios can be applied. In such a case, more robust synchronization in time and phase is required between the distributed satellite nodes. One example of FDD standardized technology in mobile networks is the coordinated multipoint (CoMP) transmission and/or reception used in Long Term Evolution Advanced (LTE-A) standard.

In CoMP operation, multiple transmission points coordinate to combine the user's information signal from neighboring evolved Node B (eNB) to improve the received signal quality. To this end, CoMP transmission requires sharing coordination information, usually consisting of user's feedback CSI, through the backhaul links [169]. It can be implemented in four different types depending on the degree of coordination among cells: (1) Coordinated Scheduling and Beamforming and, (2) Joint Processing, both in the downlink; (3) Coordinated Scheduling and, (4) Joint Reception and Processing, both in the uplink. Even though multiple types of CoMP can be used together [169]. For example, in [170] proposed to switch the CoMP transmission mode between Coordinated Beamforming and Joint Processing adaptively to maximize the average achievable rate, considering that the last one is more sensitive to phase synchronization errors than Coordinated Beamforming [170].

CoMP requires the transmission points to be tight time and frequency synchronized. This constraint mostly affects coordination between base stations (BSs) because some additional solution is needed to provide accurate phase synchronization. Large distances between the BSs result in unavoidable differences in TOA between the users' signals which in turn lead to inter-symbol interference in OFDM systems if the cyclic prefix length is exceeded. Moreover, CFOs which are caused by imperfect oscillators, lead to inter-carrier interference and are a problem, particularly in the downlink due to the feedback delay of the measured CSI. The most extended approach to synchronization in CoMP at outdoor BSs is to obtain a precise clock reference from GNSS [171]. This could be extended to DSS in LEO MEO. However, indoor BSs require to be synchronized over the backhaul network using standard protocols such as PTP or proprietary solutions like synchronous Ethernet [172] [173] [174].

In any typical cellular system, the users perform synchronization with a single BS where the BS transmits predefined signals to the UEs to adjust their transmit timings so that signals received from many UEs to the BS are time-aligned. However, a concern in CoMP is that the UEs needs to be synchronized to multiple BS simultaneously. Hence, the previously discussed technique is not going to work in the CoMP case. Due to this, the use of CoMP becomes limited to deployments where the inter-site distances between BSs are small [175].

Different approaches to the time synchronization problem stated before have been proposed. The most straightforward is to use a larger cyclic prefix, but it reduces the system's throughput. Another widely used approach is adjusting the time advance based on the nearest BS. However, such a solution is not capable to fully solve the problem, since some of the users may not be able to use the CoMP. In [175], the authors propose a linear combination of samples corresponding to the two consecutively received OFDM symbols to identify multiple transmitted signals. Such a scheme enables the mitigation of Multi-user Interference by applying Successive Interference Cancellation, as also proposed in [176] and [177]. Another approach considers the positions of the serving and interfering BSs and the estimated location of the UE to timely relate the synchronization signals received from adjacent BSs [178]. Several other approaches which consider asynchronous interference mitigation are discussed in [179] and [180]. All these methods could be extrapolated to time synchronization in DSS.

Joint processing of the carrier phase (along with frequency) is one of the significant challenges in CoMP as in DSS. The time difference of arrivals imposes a phase offset on the transmit covariance matrix leading to improper precoding matrix index selection and therefore limiting the promised performance of CoMP [181]. It is a two-fold problem: (a) The RF-LO of the participating BS in CoMP are required to be synchronized among them, (b) the LO of the UEs are also required to be synchronized with the corresponding BS. Since the phase noise of the oscillator evolves quickly and only with the help of backhaul information, it becomes challenging to establish synchronization between the participating BSs. For achieving an acceptable level of synchronization, the phase noise needs to be very low in the LOs, which makes such deployment cost-inefficient. In another approach, the UE can also keep tracking the phase noise. The effect of BSs coordination and synchronization on the phase noise estimation at the user receiver was studied in [182], where the authors derived the data-aided and non-data-aided CRLB for the phase noise estimation in a CoMP system. Another approach presented in [183] addresses the data-aided joint synchronization and channel estimation for the uplink of CoMP systems based on the MMSE criterion. This proposal considers an alternating minimization method to simplify the MMSE cost function such that the multiuser CFO, sampling timing offset, and channel frequency response can be estimated in an iterative approach more feasible for practical systems. Another method that addresses the estimation and compensation of time and frequency offsets in CoMP was proposed in [184]. In this case, the authors compare two solutions to the time-frequency offset estimation problem, one in which the UE is not aware of the transmitting point, and one in which the UE is provided with assistance information.

Implementation Examples of Closed-Loop Synchronization Methods

- **One Bit Feedback**: In [69], a Spartan-3 FPGA based hardware prototype was developed to demonstrate 1BF. Phase synchronization is achieved over-the-air (OTA) whereas the frequency synchronization is attained via RF cables, and a frequency distribution source Octoclock [185]. The implementation used three single transmitters (beam-formers) and a single antenna receiver. At a feedback rate of 300 ms, convergence within 90% of the theoretical limit is achieved after 60 iterations. The experiments were performed inside the laboratory, i.e., static environment. Hence, the performance under the realistic time-varying channels was not investigated. Besides, frequency synchronization was also required to be achieved OTA.

  A hardware prototype of the 1BF method, using USRP SDR [186] was presented in [187]. This prototype functionality is ”all-wireless”, i.e., no wired connections are used to attain frequency and timing synchronization. This experimental setup used three single-antenna transmitters and one single antenna receiver. With a feedback interval of 50 ms, nine times beamforming amplitude gain was achieved. However, like the implementation in [69], the experiments were performed indoors. Then, the performance of the system against the time-varying channel was not investigated. Besides, only phase synchronization is achieved OTA whereas frequency synchronization is achieved through coaxial cables and frequency distribution source.

Another prototype described in [188] performs both frequency and phase synchronization using 1BF, which has been derived from [69]. Individual components of the hardware prototype have been developed by the authors themselves and the beamforming algorithms have been programmed on digital signal processor (DSP) cores. At a test frequency of 60 GHz, using three elements distributed phased array, 9.2 dB of distributed beamforming gain is achieved. In contrast to the methods discussed previously, i.e., [69] and [187], both frequency and phase synchronization are achieved OTA. However, the feedback interval of 0.5 ms is excessively high as compared to the other 1BF methods discussed ([69] and [187]). Besides, the prototype was tested considering static channel environments; hence the system's performance against the time-varying channel was not investigated.

- **Full-feedback**: Very few PoC demonstrators are available for Full-Feedback implementations. For example, in [189] a notable range extension by performing outdoor OTA tests was shown using COTS handheld radio (based on FPGA and DSP) equipment. Also, the KF is used to predict the offset in frequency and phase, which further assists in tackling the time variation of the channels. Thus making the system perform satisfactorily even when the nodes are mobile. It is shown that as compared to a COTS radio transmitter (approximate range 2 km), by performing distributed beamforming, the range can be extended up to 6 km using ten such radio nodes. Further extension of range up to 10 km can be achieved by using 30 such radio nodes. In [190], using the same experimental setup and beamforming method, 0.1 dB distributed beamforming gain was demonstrated using ten COTS radio nodes. OTA operation and application of KF for prediction makes this implementation suitable for DSS scenarios.

Implementation Examples of Open-Loop Synchronization Methods

Among the open-loop algorithms, in [191] an SDR implementation (USRP X310 [192]) using transmitter nodes was demonstrated. OTA tests confirmed reliable frequency lock even at very low power. In another open-loop SDR implementation (USRP N210 [193]), a solution for OFDM based frames is developed by designing specific preambles to estimate the frequency and timing offset. The system is capable to operate reliably under frequency selective and slow fading channels. OTA showed performance gains from 2.5 dB to 2.8 dB.

Implementation Examples of Master-Slave Synchronization Methods

In [194], an SDR implementation of Master-Slave closed-loop synchronization procedure named as NetBeam was demonstrated. NetBeam involves a network of radios that broadcast information locally and jointly transmit it to a remote receiver. This is equivalent to a Master-Slave closed-loop synchronization. The performance is further enhanced by the creation of a cluster of beamformers based on CSI. As for the hardware implementation: a dual antenna configuration of USRP X310 is used as a receiver, and a single antenna configuration of USRP B210 is used as a transmitter. A significant aspect of this implementation is that the 3D distribution of radio nodes is considered, which is crucial for DSSs (full-dimensional beamforming). Besides, faster convergence is attained through machine learning techniques.

A SDR (USRP) implementation for parallel frequency and phase synchronization was demonstrated in [195]. In this case, the Master-Slave method was used for frequency synchronization whereas 1BF was used for phase synchronization. This is an all-wireless implementation, where no wired medium is used for CSI feedback or clock/frequency distribution. The convergence time for the beamforming is of the order of several milliseconds. Another example of frequency and phase synchronization by the Master-Slave method is described in [196] using a SDR (USRP X310). In this case, coherent pulses are received with more than 90% of the ideal coherent energy. Similarly, [197] provided a comparison between wired and wireless clock distribution to achieve frequency and phase synchronization by Master-Slave. OTA tests showed a near-ideal 6 dB gain from a two-transmitter system at a distance of 85 m, and coherent gain up to 90% of the ideal signal summation is achieved.

On the other hand, in [198] a SDR (USRP N210) implementation of a Master-Slave architecture for phase synchronization is presented. The external frequency source is used for stable clock distribution, whereas phase synchronization is achieved through the Master-Slave method. Channel reciprocity is exploited to obtain CSI without needing feedback. Besides, the nodes cooperate in disseminating the CSI. This testbed achieves beamforming gains as close as 90% to the ideal beamforming gain.

Besides, in [15] the authors analyze the wireless carrier frequency and sample timing synchronization by performing an exchange of RF signals between the master and slave nodes. Further, the proposed solution was implemented in GNU Radio, and wireless tests were performed using Ettus USRP N210 SDRs. Besides, the estimation of the fractional clock phase was performed using matched filter bank consisting of sixteen fractionally delayed

Zadoff-Chu sequences [199] which were capable of estimating residual timing offsets as small as 1/16 of the sample duration. However, the system did not address propagation delays, and also the system bandwidth was limited to only 1 MHz. The method yields a residual timing precision of approximately 500 ns which exceeds the expectation of CRLB.

In addition, authors in [200] used a SDR implementation (using USRP-E312) to perform synchronization, which did not require time-stamps. The observed accuracy of the method was less than 1 μs (0.8 μs) for 150 kHz sampling rate with precision limited to 1/10 of the sample rate. The authors reported the limited real-time processing capability of the USRP-E312 as the reason behind using such a low sampling rate. Three E310s were used in the over-the-wire setting: one as the master node, a second as the slave node, and a third as the measurement device for determining the resulting clock offset.

Implementation Examples of Consensus-Based Synchronization Methods

The PoC presented in [201] demonstrates consensus-based synchronization through SDR (USRP N210) implementation. GNU Radio was used for software-based signal processing. Both time delay and CFO estimation, as well as tracking, are addressed in the implementation. Convergence time is of the order of seconds when different nodes have different CFO. OTA tests showed carrier frequency offsets to be within 100 parts per billion (ppb) while timing offset were correctly estimated. Besides, the implementation also showed tracking capabilities.

Another notable consensus-based implementation can be found in [15]. For OFDM type frames, a specific frame structure was designed to facilitate frequency synchronization. A residual timing offset within 1/16 of symbol duration and a residual frequency offset of 5 Hz is achieved. With such residual frequency and timing offset, a near-optimal received signal power gain is shown when distributed beamforming is performed.

2.6.2 Synchronization Examples in Remote Sensing DSSs

This section analyzes the synchronization methods used by DSSs missions to perform Earth observation and remote sensing tasks. At the end of the section, Table 2.4 summarizes the technical details of these missions.

Table 2.3: Summary of PoC hardware implementations of distributed synchronization techniques

Ref.	**Synch. Method**	**Frequency Synch**	**Phase Synch.**	**Feedback rate (ms)**	**Beamforming Gain / Convergence**	**Static / Time-Varying**	**Platform**
[69]	Closed-Loop	Wired	Wireless	300	90% of theoretical limit	Static	FPGA
[187]	Closed-Loop	Wired	Wireless	50	9x	Static	FPGA
[188]	Closed-Loop	Wireless	Wireless	0.5	9.2 dB	Static	DSP
[189]	Closed-Loop	Wireless	Wireless	NA	0.1 dB	Time varying	FPGA and DSP
[191]	Open-Loop	Wireless	Wireless	NA	2.5 - 2.8 dB	Time Varying	FPGA
[194]	Master-Slave	Wireless	Wireless	NA	10x	Time Varying	FPGA
[195]	Master-Slave	Wireless	Wireless	NA	NA	Static	FPGA
[197]	Master-Slave	Wireless	NA	NA	90% of theoretical limit	Time Varying	COTS
[198]	Master-Slave	Wireless	Wireless	NA	90% of theoretical limit	Static	FPGA
[196]	Master-Slave	NA	Wireless	NA	90% of theoretical limit	Time Varying	FPGA
[15]	Master-Slave	Wireless	Wireless	NA	NA	Static	USRP
[200]	Master-Slave	Wired	Wired	NA	NA	Static	USRP
[201]	Consensus-Based	Wired	Wireless	NA	NA	Time Varying	FPGA

GRACE

The gravity recovery and climate experiment (GRACE) was a mission devoted to monitoring changes of the Earth's gravity field irregularities from its dispatch in March 2002 to the conclusion of its science mission in October 2017 [31]. GRACE comprised two equal satellites in near-circular orbits at $\sim$ 500 km elevation and 89.5° inclination, detached from each other by around 220 km along-track, and connected by an exceedingly precise inter-satellite, K-band microwave ranging (KBR) system. The satellites were nominally held in a 3-axis stabilized, nearly Earth-pointed orientation, such that the KBR antennas were pointed accurately at each other. The KBR gives a micron-level precision (10 μm) using carrier phase estimations within the K (26 GHz) and Ka (32 GHz) frequencies [202]. A single horn serves as the K/Ka antenna for both transmitting and receiving the inter-satellite dual-band wave signals [203]. Each satellite transmits two sinusoidal signals (at K and Ka bands) with a frequency offset (nominally set to 0.5 MHz). The two 0.5 MHz down-converted RF signals are sampled at approximately 19 MHz and passed to the digital signal processing part of the receiver. Dedicated digital signal processing channels are used to digitally counter-rotate the phase of each down-converted signal, track the phase with a digital phase-locked loop, and extract the phase.

LISA

LISA stands for Laser Interferometer Space Antenna [204]. It is a distributed satellite mission formed of three spacecraft operating in formation flying at a 5,000,000 km distance, being the three peaks of an equilateral triangle. This arrangement composes a huge interferometer to monitor the gravitational waves coming from galactic and out of the galaxy sources. Each spacecraft contains two verification masses and laser bars that measure the separation between its masses and those from the other nodes with a required precision of 20 pm. This is the most extreme example of accurate ranging between flying payloads ever seen before. The spacecraft use inertial sensors and micro-newton thrusters to determine and control their orbits, whereas laser interferometry is used to measure the distance with the required accuracy.

OLFAR

The orbiting low-frequency antennas for radio astronomy (OLFAR) is a space-based low-frequency radio telescope that investigates the universe's so-called dark ages, maps the interstellar medium, and finds planetary and sun-powered bursts in other solar systems. The telescope, which is composed of a swarm of fifty satellites, would be sent to an area distant from Earth to maintain a strategic distance from the high Radio Frequency Interference found at frequencies underneath 30 MHz, coming from Earth [205]. The satellites can be maintained in a 3D configuration with a maximum diameter of 100 km [206] by using round-trip pulse-based synchronization.

TanDEM-X

TanDEM-X was a scientific mission that comprised of two X-band SAR satellites following an orbit in near arrangement, with variable separation between them between 500 and 1100 m [59]. The mission produces high accuracy SAR snapshots at X-band in both monostatic and bistatic setups. For the bistatic design, one of the two satellites works as a transmitter and the other one as a receiver, and the mission performs a closed-loop synchronization scheme to get the required coherence.

GRAIL

The gravity recovery and interior laboratory (GRAIL) was a NASA mission to outline the gravity field of the Moon to a remarkable level of detail [207]. Twin shuttles were propelled on 10 September 2012 and were embedded into lunar orbit on 31 December 2011 and 01 January 2012 [208] correspondingly. The instrument for this mission was based on GRACE. Nevertheless, there were a few contrasts between both missions. The principal difference between the GRAIL and GRACE instruments emerged because GRAIL was not suffering the

Earth's atmosphere drag, nor GPS navigation system was accessible. GRACE compensated for air disturbance basically by having an accelerometer to measure non-gravitational speed variations and by using two independent microwave ranging frequencies instead of only a single one.

GRAIL was streamlined by excluding the K-Band frequency (26 GHz) as well as the accelerometer (non-gravitational strengths are small enough to be modeled rather than measured). Furthermore, for GRACE, GPS was utilized to estimate the relative delay between the two spacecraft, calibrate on-board ultra-stable oscillators, and track the two satellite orbits. Without GPS accessible at the Moon, GRAIL included an extra S-Band (2 GHz) Time Transfer System to supplant the GPS timing measurements, and an extra X-Band (8 GHz) Radio Science Signal used for Doppler following of the shuttle and ultra-stable oscillator frequency calibrations through the Deep Space Network [207].

Table 2.4: Summary of synchronization requirements for Remote Sensing DSSs missions

Mission	**Application**	**Distance between nodes**	**Band of operation**	**Required accuracy**	**Number of nodes**	**Synch. signal**	**Phase (P) Timing (T) Ranging (R)**
GRACE [31] [202, 203]	Gravity	220 km	K (26 GHz) Ka (32 GHz)	10 μm	2	CW	R
LISA [204]	Gravitational waves	$5 \cdot 10^6$ km	Optical	20 pm	3	CW	R
OLFAR [205, 206]	Radio telescope	100 km	TBD	< 1 m	10 - 50	Pulsed	PT
TanDEM-X [59]	SAR	0.5 - 1.1 km	X	$\pm 0.1°$	2	Pulsed chirp	PT
GRAIL [207]	Lunar gravity	50 - 225 km	S (2 GHz) X (8 GHz) Ka (32 GHz)	1 μm	2	CW	PTR

2.6.3 Summary and Lessons Learnt

- Hardware development for communication satellite systems has been pointing toward re-configurable SDR System-on-a-Chip ground receivers and to the ultimate extreme of Satellite-on-a-chip during the last years. In general, recent trends for prototyping and deployment of spacecraft are based on COTS, FPGA and SDR designs.

- Synchronization algorithms from Mobile Networks performing cohesive distributed communications, such as CF Massive MIMO and CoMP, can be extrapolated to synchronize CDSSs.

- Most prototypes of synchronization methods for distributed wireless communication networks implemented Master-Slave architecture and FPGA platforms.
- DSSs missions performing Earth observation and remote sensing tasks were discussed in this section. Most of them do not include more than three distributed nodes, and the synchronization is achieved using RF signals. Missions included in the section are: GRACE, LISA, OLFAR, TanDEM-X and, GRAIL.

2.7 Synchronization Using Machine Learning

ML techniques can be significantly useful in addressing various synchronization problems associated with end-to-end communication systems. Some applications of ML in facilitating the synchronization process include frame synchronization, compensation of the errors caused by sampling frequency/time offsets, carrier synchronization, and phase noise characterization. While modeling an end-to-end communication system, there may arise synchronization problems between transmitter and receiver due to various reasons including sampling frequency offset, sampling timing error, and mismatch about the beginning of each frame, i.e., frame header, at the receiver. To address these problems, a convolutional neural network (CNN) could be promising to build an additional synchronization model to achieve better frame synchronization and also to compensate for the impairments caused due to sampling timing error and sampling time offset. To this end, a CNN-based synchronization model with softmax activation function proposed in [209] has demonstrated 2 dB better detection than the direct correlation detection in terms of correctly detecting the actual position of a frame header. Furthermore, the traditional frame synchronization techniques based on maximum likelihood and correlation may fail due to hardware implementation constraints or frequency deviation problems. To address this, ML techniques such as multi-instance learning can solve the frame synchronization problem under different frequency ranges without additional modifications [210].

Moreover, ML techniques can be used to accurately characterize amplitude and phase noises, which are essential parameters in the synchronization process of distributed satellite systems. In this regard, in [211] a Bayesian filtering-based framework was used in combination with the expectation-maximization to characterize the amplitude and phase noise characterization of the lasers. The carrier synchronization has been experimentally demonstrated using the proposed framework, and the Bayesian filtering has been shown as an efficient method to estimate laser phase noise even in the presence of low SNR.

Due to limited computing power, the complexity of the ML model, and the increased data volume, a single learning node/machine is generally not able to execute an ML model, and this will require the distributed implementation of ML models across several distributed nodes in a network. In distributed learning, a local node computes a data subset's local updates/models. It updates the local updates/model parameters to the centralized server, which then calculates the global parameters [212]. The computed global parameters are then distributed to the local nodes to all distributed nodes. This distributed approach significantly reduces the communication burden required to communicate all the local raw data to the centralized server and utilize the local computational power to generate local models.

However, the application of ML techniques in distributed systems may result in relatively low accuracies and poor convergence rate due to differences in the transmission delays and computational capabilities of distributed nodes/clusters. Therefore, it is crucial to have a proper synchronization among different nodes/clusters of distributed systems to enhance the accuracy of the ML training model and to accelerate the training time. The synchronization cost may result in a significant performance loss of a distributed ML model [213]. In general, to parallelize the data across distributed clusters, ML techniques utilize bulk synchronous parallel (BSP) strategy [214], in which all computational nodes need to commit and receive new global parameters before starting the next iteration, resulting in a load imbalance problem. This load imbalance problem can be addressed with an asynchronous strategy as it enables the distributed learning nodes to utilize local model parameters for the next iteration [215]. The main problem with this asynchronous method is that the model may not provide the accuracy guarantee since the model can be trapped in a local optimum without converging to a globally optimum solution. Another approach is stale synchronous parallel (SSP) strategy [216], in which the modes can utilize the stale global parameters to train the local model; however, this may not guarantee convergence due to the limitations of stale global parameters. A promising approach to address the drawbacks of the methods above is to dynamically adapt the communications method between the centralized/parameter server and the distributed nodes based on the performance of each node. In this regard, the adaptive synchronous parallel (ASP) strategy proposed in [213] has been shown to achieve higher convergence speed and provide better accuracy than the SSP methods. However, the applicability of the ASP method in a large-size distributed ML framework remains an open problem.

The emerging cyber-physical systems requiring time synchronization are vulnerable to the threat of time synchronization attacks, which mainly focus on modifying the measurements' sampling time/time stamps without modifying the system measurements. Such time synchronization attacks may lead to serious consequences in cyber-physical systems, such as incorrect voltage stabilization in smart grid networks. The existing attack detection techniques such as residual-based bad data detection and the conventional supervised ML-based detectors may not be able to effectively detect such attacks, leading to the need for innovative ML-based solutions [217]. In this regard, "first difference aware" ML classifier proposed in [217] could be promising to detect two types of time synchronization attacks, namely, direct time synchronization, which only modifies some time stamps, and stealth time synchronization attack, which modifies all the timestamps at a certain time. The First Difference ML (FDML) techniques utilize the backward first difference of the time-series data in order to process the input data stream before employing an ML method.

For a satellite system with a dehop-rehop transponder (DRT) working in the frequency hopping - frequency division multiple access (FH-FDMA) mode, it is common to use different hopping sequences for the uplink and downlink communications to avoid possible jamming or interference in both the links [218]. However, the synchronization between DRT and ground equipment with different hopping sequences becomes very complicated, and it is a crucial challenge to investigate an efficient synchronization method. In this regard, authors in [219] proposed an ML-based novel method to carry out synchronization with the Frequency Hopping signal for tactical SatCom system by utilizing serial search for coarse acquisition and long short-term memory (LSTM) network for fine acquisition. The main objective of the proposed work is to reduce the synchronization time. It has been shown that the proposed LSTM-based method enables the fast and quick fine acquisition in comparison to the existing methods in the literature and provides benefits in saving the overall synchronization time by allowing the fine acquisitions for both downlink and uplink and learning the temporal trend of the signal.

In the context of 5G integrated SatCom utilizing OFDM, authors in [220] proposed a Cyclic Prefix based multi-symbol merging blind timing algorithm to enhance the timing accuracy. Also, an improved synchronization method has been submitted to realize more accurate time-frequency error correction in the considered 5G integrated SatCom system.

With the help of simulations results, it has been depicted that the proposed multi-symbol merging method provides better performance than the single-symbol method in low SNR conditions, and the proposed synchronization method can provide a good Bit Error Ratio (BER) performance.

Due to the availability of massive volumes of high-resolution videos and images taken by LEO satellites and unmanned aerial vehicless (UAVs), many data sources have become available for space information networks (SINs). However, the application of ML becomes challenging due to limited computing and communication resources and also the low frequency and orbit resources in SINs. Also, the unstable connections of SINs further create the challenges of employing ML among a swarm of satellites and UAVs. To address this, authors in [221] considered the application of distributed ML in SINs, called SpaceDML, to effectively reduce the communication overhead among the SIN devices. The proposed SpaceDML utilizes adaptive loss-aware quantization and partial weight averaging algorithms to compress models without sacrificing their quality and selectively average the active agents' partial model updates, respectively. The evaluation with public dataset and realistic model presented in [221] has demonstrated that the proposed SpaceDML can enhance the model accuracy by about 2-3 % and reduce the communication burden among SIN devices can be up to 60 % as compared to the baseline algorithm.

2.7.1 Summary and Lessons Learnt

- ML can be considered as a promising technique to address several synchronization problems related to frame synchronization, compensation of the errors caused due to sampling frequency/time offsets, carrier synchronization, and characterization of phase noise in communication systems, including a SatCom network.

- For distributed satellite systems, ML techniques can be used to accurately characterize amplitude and phase noises, which are essential parameters in the synchronization process of a distributed satellite system.

- Distributed learning techniques find significant importance in distributed satellite systems as they enable the distributed implementation of ML models across several distributed nodes in a network.

- Synchronization cost may result in a significant performance loss in a distributed ML implementation, and it is imperative to have a proper synchronization among different nodes/clusters of a distributed system to enhance the accuracy of the ML training model and to accelerate the training time.

- Time synchronization attack is one important problem to be considered in the emerging cyber-physical systems involving a distributed satellite system as it may lead to severe consequences in the overall system operation. The conventional supervised ML-based detectors may not be able to effectively detect such attacks, leading to the need for innovative ML-based solutions such as ”first difference aware” ML classifier proposed in [217].
- Synchronization between DRT and ground equipment with different hopping sequences in an FH-FDMA-based satellite system becomes very complicated, and ML-based synchronization techniques such as LSTM seem to be promising as illustrated in [219].
- ML techniques could also be promising to enhance timing accuracy in 5G integrated satellite system [220] and to reduce the communication burden among different distributed SIN nodes in emerging SINs with the help of distributed ML [221].

2.8 Research Challenges and Opportunities

This section summarizes some of the critical research challenges and opportunities identified while conducting this survey.

2.8.1 Synchronization through ISLs in Next Generation GNSSs

Multiple research results have indicated significant performance improvements on navigation constellations, thanks to the introduction of inter-satellite ranging and communication links [118] [222]. At the same time, a consolidation of the technologies enabling this improvement is essential to reduce further the complexity of the inter-satellite ranging and communication payload and simplify the ground-based orbit determination and clock synchronization algorithms. ISLs currently perform navigation and communication functions through independent low-rate telemetry and high-rate data channels, respectively. The integration of both functionalities into one common channel would simplify the onboard equipment and improve the electromagnetic compatibility, which implies the reduction of power consumption and the required frequency resources.

Current GNSSs employ a network of ground stations to track the satellite clocks and estimate their deviations for a single time scale. The estimated time offsets are included in the navigation messages sent to the final user, which use the information to correct the satellite clock delays in the received signals. This procedure would be simplified if the satellites of the GNSSs could synchronize their carriers without the intervention of the ground segment. The use of optical ISLs could be a feasible solution to achieve this goal enabling a novel GNSS architecture in which, rather than independently maintaining a time scale, each navigation satellite would synchronize the emitted broadcast navigation signals to a common system time [223] [224].

2.8.2 Federated Satellite System (FSS)

To fully achieve the potential that FSS represents for space systems, several challenges need to be addressed to achieve its successful implementation and operation [225]. Some of the technical challenges that need to be considered in the development of FSSs are [226]:

- Coordination/cooperation between heterogenous satellites belonging to the same network. This requires the definition of **compatible communication standards**, including allocation of the appropriate frequency bands, bandwidths, and the definition of the modulations. Inter-satellite links can be either radio or optical. Both impose different requirements on the spacecraft in terms of pointing accuracy and jitter and have different ranges and transmission speeds.

- The different layers of the **protocol stack** also need to be defined. Routing protocols have to be able to properly manage the fast switches/handoffs and bottlenecks that for polar LEO satellites typically occur in the polar regions, where the satellite density is larger. Quality of service (QoS) must also be maintained to keep latency bounded. Some works have proposed the use of mobile ad-hoc network (MANET) routing protocols to autonomously determine the optimum route in a context where all nodes are constantly moving. In the internet of satellites (IoSat) context MANETs can provide the self-organization, self-configuration, and flexibility required by FSS [225].

- Additionally, all the **backbone technologies** to support FSS operations so as to interconnect seamlessly in-situ sensors and user terminals from ground to/from the space infrastructure (e.g. [227]), to become the IoSat paradigm [228], will also have to be developed.

- Depending on the above requirements and technologies, this can be achieved by **multi-layer constellations** formed by LEO satellites at different heights and/or MEO satellites, and/or possibly GEO satellites.
- Last, but not least, **privacy and security problems** must be addressed to prevent potentially malicious users from operating and taking control of the FSS [57] or preventing third parties from sniffing the information gathered by or transmitted through the satellites forming the FSS. In this line, the use of distributed keys and blockchain offers a new field of research.

2.8.3 DBF as an Enabler for DSSs with Small Satellites

Despite the well-known advantages of small satellites over traditional ones, small satellites present some limitations in mass and volume that lead to restrictions in power consumption and the antennas' location. These constraints could be overcome by their use in DSSs configurations [149] [229]. Key challenges to achieve this potential benefit include distributed timing, carrier frequency, and phase synchronization [1]. Besides, the limited kinematic capabilities and the small cross-section of these satellites affect the accurate measurement of inter-satellite range and precise orbit determination and control, making the synchronization tasks even more difficult. However, several research results have proved the advantages of DBF for distributed wireless networks in terrestrial communications. Results such as the increment of the transmission range [230] and the SNR [231], as well as the experimental demonstration of DBF by a swarm of UAVs [232] could be extrapolated to DSSs. Future research in the field should focus on the synchronization algorithms to perform DBF with small satellites systems.

2.8.4 Synchronization Algorithms Suitable for Communications CDSSs

Generally, closed-loop synchronization methods are not the ideal solution for space-ground or long distances communication links due to the intrinsic delay between the DSS and the target nodes. In addition, other constraints such as the slow convergence of the iterative bit feedback algorithms [73]; the high power consumption and scalability problems of T-RT [85] and; the self-interference problem of F-RT algorithm [8] makes them not suitable for synchronization in CDSSs. Maybe the most promising solution among the closed-loop methods for CDSSs could be the consensus synchronization algorithm proposed in [88]. However, it is still required to analyze the effect on this algorithm of the transmission delay between the CDSS and the target node, especially when the design proposed in [88] considered the channel time invariant.

Unlike the previous group, open-loop methods do not require feedback from the target node. That makes them the preferable algorithms for CDSSs dedicated to communications and the only available solution for remote sensing applications. However, these algorithms require accurate inter-satellite ranging measurement [90] [91]. In most remote sensing missions, it is necessary to know precisely the exact position of each spacecraft in the CDSS for the primary mission goal. For that reason, using this measurement for synchronization purposes does not represent an additional cost. However, implementing these synchronization methods in Communications CDSSs would require including both subsystems: the accurate inter-satellite ranging and the synchronization algorithm, which may incur in excessive resource consumption.

Therefore, a synchronization method suitable for Communications CDSSs using small satellites is still missing. The most promising solution seems to be related to the development of open-loop synchronization methods independent of the DSS geometry. Another possibility is the development of very efficient (in volume and resources consumption) ranging and synchronization methods.

2.8.5 Hardware Implementation of Synchronization Algorithms

As stated before, one of the most relevant open problems in Synchronization for DSSs is the development of algorithms capable of working in small satellites. To this end, the hardware implementation of these methods has to consider the low power, volume, and computational resources available in these spacecraft. Some general solutions could include distributed computation and wireless power transfer. However, developing new hardware components for micro and nanosatellites is a critical research field that highly impacts the implementation of the synchronization algorithms for DSSs.

Another approach that has not been taken into account sufficiently is to consider the hardware limitations during the design of the synchronization algorithms. For example, the distortions produced by the power amplification and the phase noise introduced by the local oscillators are some of the hardware impairments that are obviated in most of the synchronization methods proposed. These physical phenomena are treated as random errors during the hardware implementation. However, including their description as part of the design can improve the performance of the synchronization methods.

Finally, there is another practical limitation related to the hardware implementation of F-RT synchronization algorithms. In this case, the method's accuracy relies on the assumption that all the synchronization signals exchanged by the distributed nodes are in the same frequency band [83]. However, this assumption implies that the nodes should simultaneously transmit and receive signals in the same frequency band, which is impossible in practice due to self-interference. Assigning different frequencies affects the method's accuracy; performing time division multiple access introduces delays and scalability problems. The feasible solution to this problem can be using In-band Full Duplex techniques, as suggested in [149].

2.8.6 Efficient Inter-Satellite Ranging Methods

The methods for Inter-Satellite Ranging are still an open research topic. Advanced DSS will require an accurate inter-satellite ranging and baseline determination for sensing and communication applications. These accuracy requirements become ever more stringent when no external or ground-based aids are used for synchronization.

The required accuracy also depends on the final mission goals. For instance, Remote Sensing DSSs missions without any feedback from external aids, as is the case of a spaceborne distributed radiometer or radio-telescopes, will require a stringent level of accuracy because the image quality will depend directly on the accuracy of the inter-satellite ranging [233]. The most promising advances in precise ranging methods for Remote Sensing missions point to using inter-satellite optical links as the most accurate alternatives [101]. However, solving the integer ambiguity problem remains an open research question for ranging methods based on optical or RF technologies either for communications or remote sensing applications [123].

On the other hand, Communications DSSs require more efficient algorithms in terms of resource consumption. In this case, one possible solution could be the implementation of methods to simultaneously perform range measurements and communications over ISLs in a similar way to the solutions proposed in [118], and [106].

2.8.7 ML-Enabled Synchronization

As described in section 2.7, ML techniques could be promising in distributed satellite systems for various synchronization aspects such as frame synchronization carrier synchronization, characterization of phase noise, and the compensation of errors caused due to time/frequency offsets. The estimation of carrier frequency offset with low-resolution ADCs is necessary for the synchronization process as low-resolution ADCs can enable the operation of advanced MIMO operations with the help of full digital architectures. However, this becomes challenging at the higher carrier frequencies due to the higher channel bandwidth. To address this problem, ML techniques based on various deep Neural Network (NN) architectures could be used in finding the best estimate of the involved nonlinear function towards performing carrier frequency offset estimation [234]. Some of the critical design aspects to be considered in employing ML-based carrier frequency offset estimation include the sensitivity to noise, length of the training sequence, and computational complexity of the ML model. Also, the convergence rate and accuracy of the ML models should be carefully considered while employing ML techniques in distributed satellite systems due to differences in the propagation delays and heterogeneous capabilities of the distributed nodes.

Due to the distributed nature of the considered satellite applications, analyzing the feasibility of distributed ML techniques such as federated learning in distributed satellite systems could be a promising future research direction. One of the main problems to be considered while employing ML in distributed satellite systems is the synchronization cost. Although some synchronization techniques such as BSP [214], SSP [216], and ASP [213] have been proposed in the literature to deal with the performance loss caused due to distributed ML, application of distributed ML in large-scale distributed satellite systems remains an open problem. Moreover, another future research direction is to investigate suitable ML techniques to address time synchronization attacks [217] in distributed satellite systems caused by the modification of time/time stamps of the underlying measurements.

2.9 Conclusions of the Chapter

The use of small satellites grouped as CDSSs is a new paradigm of the space industry. Many researchers worldwide are currently working to overcome the technical challenges that restrict their development. Among them, the synchronization of the distributed spacecraft is one of the most challenging open problems. For that reason, the volume of information about the synchronization of DSSs is already considerable and continues increasing daily. In this context, this chapter has captured the latest advances in architectures and synchronization methods for DSSs. A brief survey of the DSSs architectures was provided, classifying them into five general groups: Constellations, Clusters, Swarms, Fractionated, and Federated spacecraft. Other criterium for classifying the DSSs were the ISLs: Ring, Star, Mesh, or Hybrid topology and their synchronization scheme. Generally, Distributed synchronization algorithms are more robust than centralized synchronization algorithms but more complex.

The distributed time, phase, and frequency wireless synchronization methods reported in the literature were summarized and compared, analyzing their feasibility for DSSs. The synchronization algorithms were classified as Closed-loop or Open-loop methods based on feedback from a node external to the DSS. In addition, another classification considered the communication between the elements of the DSS as Closed-loop, when the exchange of information among the distributed satellites was done as a two-way message exchange or; Open-loop when it was done as a broadcast or one-way communication or when there is no communication among the nodes.

The time synchronization of DSS is mainly based on the TWTT algorithm. Additionally, recent publications referred to using pseudo-random noise code and other techniques to achieve time synchronization and inter-satellite ranging simultaneously. Among the Closed-loop synchronization algorithms that use the feedback from a node external to the DSS, the rich feedback methods are more suitable to implement in DSS. Specifically, the PA algorithm for DTB and the reciprocity-based methods are the most recommended. On the other hand, most of the Open-loop synchronization algorithms are suitable for synchronizing DSSs. In conclusion, higher synchronization accuracy could be achieved by combining intra-node communication in the form of two-way message exchange and the feedback from a node external to the DSS.

This chapter analyzes other operations closely related to synchronization in DSSs, such as inter-satellite ranging and relative positioning. Generally, the requirements and accuracy of the coherent operation depend on the performance of the ranging and relative positioning algorithms as much as the synchronization itself. These operations can be performed by optical or RF inter-satellite ranging methods. The former one can achieve higher accuracy, but the higher directivity of the laser beam can represent a limitation for specific applications. The use of a single ISL to simultaneously perform ranging and communication and the solution to the phase integer ambiguity problem are trending topics in this field.

An extensive compilation of missions and proof of concept implementations have been included. Besides, this chapter considered ML as a promising technique to address several synchronization problems, such as frame synchronization, compensation of the errors related to sampling frequency/time offsets, carrier synchronization, and characterization of phase noise in communication systems, including a SatCom network. Besides, it analyzed distributed learning techniques as enablers of the distributed implementation of ML models across several distributed nodes in DSS. Finally, a collection of current research activities and potential research topics was proposed, identifying problems and open challenges that can be useful for researchers in the field.

Chapter 3

Multiuser-MISO Precoding under Channel Phase Uncertainty in Satellite Communication Systems

3.1 Introduction of the Chapter

Multi-user multiple-input single-output (MU-MISO) precoding is an interbeam interference technique based on the channel estimation feedback from the UTs to the GW. It has been studied in several telecommunication areas to compensate for multi-user interference (MUI), allowing more aggressive frequency reuse approaches. Several examples of this trend are present in the latest WiFi [235], MIMO power line communications [236], and 5G New Radio standards [237].

In this context, linear precoding approaches have been increasingly popular in recent years as an appealing method to mitigate MUI while ensuring specific service requirements. In particular, precoding techniques proved to be effective against MUI for multibeam satellite communications [238, 239].

Broadband data services have become a driver for satellite systems, and precoding technologies have received much attention as they can significantly increase the spectral efficiency of multibeam systems. It became a natural consequence of the evolution of satellite systems to provide broadband services despite the scarcity of spectral resources [16, 240].

The research community has been extensively studying the linear precoding design problem. The main research directions include the extension of precoding to multicast scenarios [241], making it more robust to payload imperfections, including non-linearities and distortions [242, 243], and making it robust to imperfections in the CSI estimation [244].

Moreover, precoding is now supported through dedicated framing and signaling in the latest DVB-S2X standard; see in particular [245]. The industry has also shown interest, corroborated by a live demonstration of precoding over the satellite [239]. Some more sophisticated techniques propose advanced non-linear precoding methods. In such methods, the output of the precoding operation is a non-linear operation combining the vector of input data symbols and the CSI, laying the foundation for what is known as SLP [246]. SLP technique is a promising approach that can achieve additional gains as compared to the linear channel inversion methods at the cost of additional computational complexity [219, 247]. In many cases, the additional complexity of the proposed algorithms is prohibitive for practical systems. However, many computationally efficient techniques have been proposed in the literature to make SLP feasible under realistic scenarios; see, for example, [248–252].

Despite the increasing interest in standardizing precoding use in multibeam satellite systems, of which the latest DVB-S2X standard [245] is an example; there are not many precoding over satellite examples, mainly due to the strict synchronization requirements for both linear [238, 239] and symbol level [248, 249] precoding implementations. Some authors mention this problem as part of precoding designs, proposing a general solution without a detailed analysis of the synchronization impairments [238, 239].

Specifically for geostationary multibeam satellite systems, the synchronization problem is addressed considering that all the beams are generated using a single frequency reference at the satellite transponder [20, 21, 245]. However, practical transponders avoid transmitting all their beams with a single frequency reference for scalability, reliability, and security reasons, among others. The synchronization impairments are even worse for distributed satellite systems [238], where it is impossible to use a common frequency reference for different spacecraft, and for non-geostationary orbit (NGSO) satellites, where the Doppler effect produces phase variations. As we will demonstrate in the next sessions, even for the best synchronization scenario, with all the beams generated using a single frequency reference, the performance of precoding implementations is affected by synchronization impairments inherent to the satellite communication systems.

Some authors have analyzed in detail the impact of the implementation's phase uncertainties and the channel estimation errors on precoding performance for Massive MIMO systems.

For instance, [253] studied the performance of linear precoding techniques in Massive MIMO systems considering memoryless non-linear distortions at the transmitter side (high power amplifier (HPA), as an example) and imperfect CSI estimation. In this work, the authors approximated the precoded signal by a complex Gaussian distribution. This assumption only applies to Massive MIMO systems, where the precoding matrix has large dimensions. Similarly, [254] studies the impact of the phase noise of free-running oscillators on the performance of linear Massive MIMO precoding systems. Meanwhile, [255] compared two linear precoding techniques for a Massive MIMO systems considering channel non-reciprocity and errors in the CSI estimation. In addition, other authors assessed the performance of Massive MIMO linear [256] and non-linear [257] precoding techniques but without considering any of the synchronization impairments previously mentioned. None of these works deal with satellite communication systems but terrestrial mobile communications. The communication channel is different for precoding-enabled terrestrial and satellite communications. While the UTs and the BS, where the precoding is calculated, share a direct link in mobile communications, in satellite systems, the precoding is calculated at the GW, which transmits the precoded data streams to the satellite using FDM and the satellite transponder generates the precoded beams towards the UTs.

Other authors have studied the performance of linear [21,258], and non-linear [20] precoding in satellite communication systems. However, most of them limit the analysis to including synchronization impairments in their simulations without any formal demonstrations [20,21]. In [20], the authors point out that the channel slow time variations can be followed by the receiver as long as they are equal to all the beams. This requirement intrinsically leads to the recommendation of using a common reference for all the onboard oscillators [20]. Meanwhile, the simulations results presented in [21] suggested that linear precoding techniques such as ZF and MMSE can compensate for the receivers' SNIR degradation related to the use of multiple onboard oscillators.

Therefore, it is evident the need for a formal analysis considering the effects of the synchronization impairments over the performance of precoding-enabled satellite systems. Based on the previous works [20,21], and considering the characteristics of satellite communication systems, where the precoding is calculated at the GW and generated at the satellite transponder, it is advisable to analyse independently the impact on the uplink (from GW to satellite) and the downlink (from satellite to UTs) channels. Consequently, we propose a model in which we decompose the entire channel matrix into three different matrices that are the factorization of the entire one. Two of those three matrices are the forward uplink and downlink phase-uncertainty matrices, respectively. This methodology lays the foundations for designing the different components of an end-to-end satellite system using the precoding technique, such as the CSI estimation, the precoding matrix computation, and the precoding application.

This chapter aims at assessing the impact of the phase errors and uncertainties in operating a precoded forward link satellite communication system. It formally demonstrates that the phase uncertainties created in the forward-downlink do not affect the precoding performances for linear precoding operations. Then, we also confirm this fact in the case of non-linear precoding systems. Additionally, this chapter shows that the UTs estimate the phase variations added in the forward-uplink channel as part of the CSI. We confirm our analytical findings by employing computer simulations for different system configurations. We consider three different phase noise level profiles for the transponder frequency reference in a typical end-to-end GEO satellite system in these simulations. It is essential to clarify that during this work, we name frequency reference to the crystal oscillator used as a reference for one or more LOs. For the sake of simplicity, we will assume that all the LOs at the transponder have a common frequency reference for our simulations. Finally, this chapter suggests alternatives to be explored in future non-linear precoding techniques under the aforementioned phase variations and phase uncertainties seen in the forward link of a multibeam satellite channel.

This chapter is organized as follows. Section 3.2 presents the system model, and Section 3.3 provides a detailed analysis of the phase errors and uncertainties sources in a precoding satellite system. Section 3.4 discusses the effects of the absolute phase uncertainty in linear and non-linear precoding methods. The effects of the phase variations in the forward-uplink channel for linear precoding methods are also analyzed in 3.4. Section 3.5 focuses on robust designs considering the phase impairment seen in practical implementations, and section 3.6 presents some simulation results to validate the analytical discussion. Finally, the conclusions of the chapter are provided in Section 3.7.

3.2 System Model

We consider a wireless multi-antenna downlink system where the transmitter, equipped with N antennas, serves K ($K \leq N$) single-antenna UTs by sending K spatially-multiplexed (i.e., precoded) independent data streams. We collect in $\mathbf{h}_k \in \mathbb{C}^{N\times 1}$ the complex (i.e., magnitude plus phase) coefficients of the frequency-flat slow fading channels between the transmitter's antennas and the kth UT. At a given symbol period, independent data symbols $\{s_k\}_{k=1}^{K}$ are to be transmitted to the UTs, where s_k denotes the symbol intended for the kth user. Under the above assumptions, the received vector containing the symbol-sampled complex baseband received signals of all K UTs can be modeled as

$$\mathbf{r} = \mathbf{H}\mathbf{W}\mathbf{s} + \mathbf{z}, \tag{3.1}$$

where $\mathbf{H} = [\mathbf{h}_1, ..., \mathbf{h}_K]^{\mathrm{T}}$ denotes the $K \times N$ complex-valued channel matrix, $\mathbf{W}$ stands for the $N \times K$ precoding matrix, $\mathbf{s} = [s_1, s_2, ..., s_K]^{\mathrm{T}}$ is a $K \times 1$ complex-valued vector containing the UTs' intended modulated symbols, and $\mathbf{z}$ collects independent additive noise components at the UTs' receivers, which are modeled as circularly symmetric complex Gaussian (CSCG) random variables with zero mean and variance σ^2.

The physical channel matrix collecting the complex channel coefficients for all K UTs can be written as

$$\mathbf{H} = \begin{bmatrix} |h_{11}|e^{\mathrm{j}\psi_{11}} & |h_{12}|e^{\mathrm{j}\psi_{12}} & \cdots & |h_{1N}|e^{\mathrm{j}\psi_{1N}} \\ |h_{21}|e^{\mathrm{j}\psi_{21}} & |h_{22}|e^{\mathrm{j}\psi_{22}} & \cdots & |h_{2N}|e^{\mathrm{j}\psi_{2N}} \\ \vdots & \vdots & & \vdots \\ |h_{K1}|e^{\mathrm{j}\psi_{K1}} & |h_{K2}|e^{\mathrm{j}\psi_{K2}} & \cdots & |h_{KN}|e^{\mathrm{j}\psi_{KN}} \end{bmatrix}, \tag{3.2}$$

where h_{kj} denotes the channel coefficient between the kth UT and the jth transmit antenna element, for any $k \in \{1, 2, ..., K\}$ and $j \in \{1, 2, ..., N\}$, and $|h_{k,j}|$ and $\psi_{k,j}$ denote its magnitude and phase, respectively.

It is further assumed that the UTs' intended symbols are taken from an equiprobable constellation set, denoted by $\mathbb{X}$, which is represented in the complex domain as

$$\mathbb{X} = \left\{ x_i \,|\, x_i \in \mathbb{C}, i = 1, 2, ..., M, \frac{1}{M}\sum_{i=1}^{M} |x_i|^2 = 1 \right\}.$$

Accordingly, at any given symbol period, we have $s_k = x_i$ for some $x_i \in \mathbb{X}$. For the brevity of analysis and without loss of generality, we assume identical modulation schemes for all K UTs. The constellation set $\mathbb{X}$ is assumed to be symmetric with respect to (w.r.t.) the origin and has unitary average power. We respectively denote by $\mathbf{bd}(\mathbb{X})$ and $\mathbf{int}(\mathbb{X})$ the sets of boundary and interior points of $\mathbb{X}$, with $|\mathbf{bd}(\mathbb{X})| = M_\mathrm{b}$ and $|\mathbf{int}(\mathbb{X})| = M - M_\mathrm{b}$. Note that the set of boundary points refers to the symbols that reside on the convex hull of the constellation. We further confine ourselves to constellation sets with uniformly distributed symbols on $\mathbf{bd}(\mathbb{X})$, e.g., PSK, but we do not make any assumption on the geometry of $\mathbf{int}(\mathbb{X})$.

For our later use, we define some real-valued notations: $\mathbf{x}_i \triangleq [\mathrm{Re}(x_i), \mathrm{Im}(x_i)]^\mathrm{T}$, $\bar{\mathbf{s}}_k \triangleq [\mathrm{Re}(s_k), \mathrm{Im}(s_k)]^\mathrm{T}$, $\bar{\mathbf{z}} \triangleq [\mathbf{z}_1, ..., \mathbf{z}_k]^\mathrm{T}$ with $\mathbf{z}_k \triangleq [\mathrm{Re}(z_k), \mathrm{Im}(z_k)]^\mathrm{T}$, and $\bar{\mathbf{H}}_k \triangleq \Omega(\mathbf{h}_k)$ where

$$\Omega(\mathbf{y}) \triangleq \begin{bmatrix} \mathrm{Re}(\mathbf{y}) & -\mathrm{Im}(\mathbf{y}) \\ \mathrm{Im}(\mathbf{y}) & \mathrm{Re}(\mathbf{y}) \end{bmatrix},$$

for any complex input vector $\mathbf{y}$.

3.3 Phase Error Sources in the Forward Channel of a MU-MISO Precoding System

Typical satellite communication systems consist of a gateway, a satellite transponder, and the UTs [259]. During precoding operations, the gateway calculates the precoding matrix $\mathbf{W}$ and applies it to the UT's intended modulated symbols $\mathbf{s}$. The resulting precoded data streams $\mathbf{u}_j(t)$ with $j \in \{1, ..., N\}$ are transmitted to the satellite by FDM using the uplink carrier frequencies f_{u_j}. The transparent satellite transponder simultaneously transmits each data stream to its intended receiver. Traditional multibeam satellite systems divide the bandwidth among the beams, known as four colors reuse. On the other hand, full-frequency reuse approaches, such as precoding, allows the use of the total bandwidth for each beam, which implies that each data stream is converted to the same downlink carrier frequency f_D. Since the precoding matrix $\mathbf{W}$ is calculated as the inverse of the channel $\mathbf{H}$, each UT receives its intended beam without interference ($\mathbf{WH} = \mathbf{I}$, where $\mathbf{I}$ is the Identity matrix). The GW calculates the precoding matrix using the channel estimated at the UTs for each beam. To this end, the GW transmits non-precoded pilots periodically inserted between the precoded payload. The non-precoded pilots contain orthogonal sequences predefined for each beam in such a way that each UT can estimate the channel response for each beam to itself by the correlation of the received signal and the expected signal for that beam. The result of this operation is known as CSI, and it is sent to the GW for the calculation of the following precoding matrix in a continuous closed-loop way. The previous explanation refers to the ideal system; practical implementations present phase errors and uncertainties that impact the final result. This section delves into the phase errors and uncertainties inherent to precoding-enabled satellite systems.

Fig. 3.1 represents each component's contribution to the system's total phase uncertainty. This work considers an ideal frequency reference at the gateway without phase noise. As explained before, the jth beam uses the uplink carrier frequency f_{U_j}. In addition, we assume the optimal design choice in synchronization terms: to process all the beams at the transponder with a common frequency reference. However, this transponder frequency reference is not ideal, but it presents a phase drift represented as $\phi_0(t)$ in Fig. 3.3. The phase noise of the transponder frequency reference produces different phase drifts at the output of each LO. These are represented in Fig. 3.1 as $\phi_{T_1}(t) ... \phi_{T_N}(t)$.

At the downlink channel, all the signals received by the UTs share a common carrier frequency f_D and the phase noise introduced by the LO of the kth UT is represented as $\phi_{D_k}(t)$. For precoding purposes, the CSI estimated by each UT is sent to the gateway through the satellite. In this case, the phase estimations are quantized and digitally transmitted over the return link, and they are protected against channel distortions. For that reason, the feedback channel can be considered ideal. The following subsections will individually analyze the contribution of each system's element to the total phase uncertainty.

3.3.1 Uncertainty of the Phase Estimation at the UTs' Receivers

Using the non-precoded pilots sent by the GW, a UT acquires its CSI by estimating the magnitudes and the phases of the associated complex channel coefficients. To this end, the non-precoded pilots contain orthogonal sequences specific for each beam. The UT can estimate the CSI from the jth beam to itself as the correlation between the jth orthogonal sequence and the received signal. The UTs estimate the received carrier signal's phase through synchronization loops based on PLLs. Then, all the phase measurements performed by the kth UT are relative to the phase of its intended beam. This implies that the remaining channel phases corresponding to the kth UT are estimated w.r.t. $\hat{\psi}_{k,k}$. More precisely, any $\psi_{k,j}$ with $j \neq k$ is estimated as $\hat{\psi}_{k,j} = \psi_{k,j} - \psi_{k,k}$. On the other hand, we assume that each

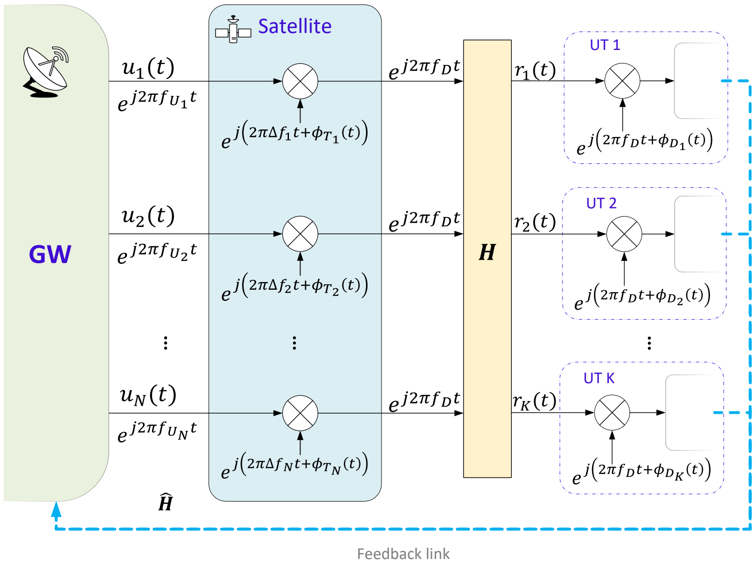

Figure 3.1: Graphical representation of the phase variations and uncertainty sources in a MU-MISO precoding satellite system. In the figure, $u_1(t)...u_N(t)$ are the uplink beams transmitted at carrier frequencies $f_{U_1}...f_{U_N}$ respectively. $\Delta f_1...\Delta f_1$ represent the different frequencies required to downconvert the uplink signals to the precoding carrier f_D. As mentioned before, $r_1(t)...r_K(t)$ identify the received signal at each UT and terms $\phi_{D_1}(t)...\phi_{D_K}(t)$ represent the phase noise of the LOs at the UTs.

UT can perfectly estimate the magnitudes of its complex channel coefficients towards the transmitter's antennas.

The phase at the input of the CSI estimator depends on the phase of the received signal $[\psi_{k1} \quad \psi_{kn} \quad ... \quad \psi_{kN}]$ and the carrier synchronization loop. This is represented in Fig. 3.2. After the carrier synchronization loop is locked, its output is $[\psi_{k1} - \psi_{kk} + \phi_{D_k}(t) \quad \psi_{kn} - \psi_{kk} + \phi_{D_k}(t) \quad ... \quad \psi_{kN} - \psi_{kk} + \phi_{D_k}(t)]$, where ψ_{kn} and ψ_{kk} are the phase rotation introduced by the channel and ϕ_{D_k} is the phase noise of the frequency reference of the kth UT. The system response of the PLL at the UTs is optimized to minimize the phase noise introduced by the loop $\phi_{D_k}(t)$ [18] in order that $\psi_{kn} - \psi_{kk} >> \phi_{D_k}(t)$ and the phase noise introduced by the UTs can be discarded.

Collecting the estimated channel vectors of all UTs into a matrix form, we can write the measured channel matrix $\hat{\mathbf{H}}_{\mathrm{D}}$ as (3.4) at the bottom of this page, which relates to the physical channel $\mathbf{H}$ as

$$\hat{\mathbf{H}}_{\mathrm{D}} = \mathbf{\Psi}_{\mathrm{D}}\mathbf{H}, \tag{3.3}$$

where $\mathbf{\Psi}_{\mathrm{D}} \triangleq \mathrm{diag}(e^{-\mathrm{j}\psi_{11}}, e^{-\mathrm{j}\psi_{22}}, ..., e^{-\mathrm{j}\psi_{KK}})$ is referred to as *phase rotation matrix* and con-

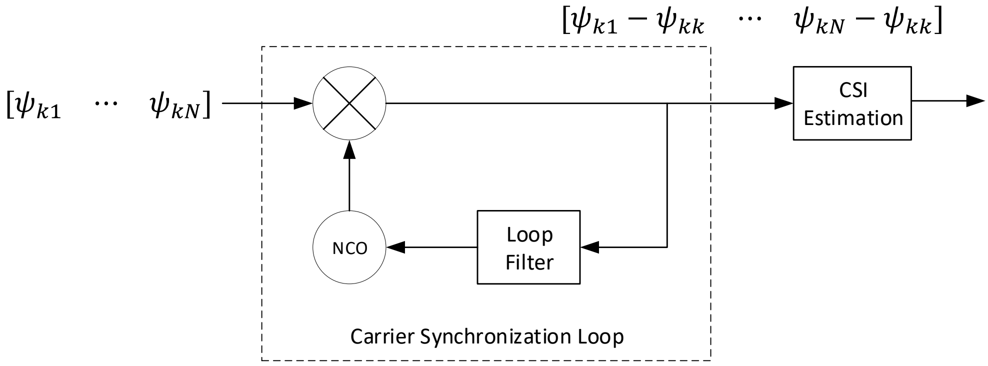

Figure 3.2: Relative phase estimation at the UT due to the carrier synchronization loop.

tains the absolute phase rotation introduced by the physical channel to each intended beam. These coefficients cannot be measured due to the practical limitations of conventional PLL algorithms.

Each UT feeds its own CSI estimation back to the transmitter. Therefore, only the measured channel matrix $\hat{\mathbf{H}}_{\mathrm{D}}$, and not $\mathbf{H}$, is assumed to be available at the transmitter. The transmitter uses the phase-normalized channel $\hat{\mathbf{H}}_{\mathrm{D}}$ to compute the precoding matrix for the subsequent data transmission towards the UTs.

In what follows, we aim to evaluate the effect of CSI imperfections due to differential phase estimation at the UTs, on the precoding performance. In practice, the phase rotation matrix $\mathbf{\Psi}_{\mathrm{D}}$ is unknown at the UTs' receivers. Nonetheless, a pilot-aided phase synchronization loop at the UTs can remove the effect of the phase rotation.We mathematically model this process by assuming that the kth received signal is rotated by the corresponding phase offset ψ_{kk} before detection. We can equally express this operation by multiplying the received signal vector by the rotation matrix $\mathbf{\Psi}_{\mathrm{D}}$.

$$\hat{\mathbf{H}}_{\mathrm{D}} = \begin{bmatrix} |h_{11}| & \cdots & |h_{1K}|e^{\mathrm{j}(\psi_{1K}-\psi_{11})} & \cdots & |h_{1N}|e^{\mathrm{j}(\psi_{1N}-\psi_{11})} \\ |h_{21}|e^{\mathrm{j}(\psi_{21}-\psi_{22})} & \cdots & |h_{2K}|e^{\mathrm{j}(\psi_{2K}-\psi_{22})} & \cdots & |h_{2N}|e^{\mathrm{j}(\psi_{2N}-\psi_{22})} \\ \vdots & \ddots & \vdots & & \vdots \\ |h_{K1}|e^{\mathrm{j}(\psi_{K1}-\psi_{KK})} & \cdots & |h_{KK}| & \cdots & |h_{KN}|e^{\mathrm{j}(\psi_{KN}-\psi_{KK})} \end{bmatrix}. \tag{3.4}$$

3.3.2 Phase Variations Added During the Frequency Down-conversion at the Transponder

Even if a common crystal oscillator is used to process all the beams at the transponder, some phase variations are introduced during the frequency down-conversion. Fig. 3.3 can be used to illustrate this fact. Considering that all the f_{U_j} with $j \in \{1, 2, ..., N\}$ uplink carrier frequencies have to be converted to the same downlink carrier frequency f_D, the transponder has to mix each input with a different single-frequency signal. Using frequency synthesizers can generate different output frequencies from a single reference. However, the phase noise at the output of each LO is determined by the frequency synthesizers in a magnitude proportional to the ratio $\frac{\Delta f_j}{f_0}$ where Δf_j is the synthesized frequency, and f_0 is the nominal frequency of the frequency reference. This implies that the PSD of the phase noise introduced to the jth beam, $\phi_{T_j}(t)$, is

$$S_{\phi_{T_j}(t)} = S_{\phi_0(t)} + 20\log_{10}\left(\frac{\Delta f_j}{f_0}\right) \quad \text{(dBc/Hz)}, \tag{3.5}$$

where $S_{\phi_0(t)}$ is the PSD of the frequency reference phase noise $\phi_0(t)$ at a nominal frequency f_0. The term Δf_j is defined as $\Delta f_j \triangleq f_D - f_{U_j}$ with $j \in \{1, 2, ..., N\}$.

Similar to the previous section, we can represent the phase variations introduced to each beam at the transponder as part of the channel estimated at the UTs. In a matrix form,

$$\hat{\mathbf{H}}_{\mathrm{U}}(t) = \mathbf{H}\mathbf{\Phi}_{\mathrm{U}}(t), \tag{3.6}$$

where $\mathbf{\Phi}_{\mathrm{U}}(t) \triangleq \mathrm{diag}(e^{\mathrm{j}\phi_{T_1}(t)}, e^{\mathrm{j}\phi_{T_2}(t)}, ..., e^{\mathrm{j}\phi_{T_N}(t)})$ is the diagonal matrix containing the phase variations added at the transponder to the jth beam.

Note that (3.6) does not include the phase estimation uncertainties considered in (3.3). We address both impairments independently for simplicity in our analysis and without loss of generality.

3.4 Precoding with Differential Phase Estimation and Phase Noise at the Transponder's Frequency Reference

In this section, we study different multiuser precoding techniques by assuming that the available CSI used for precoding computation at the transmitter is obtained via a differential phase estimation process described in the previous section. The precoding schemes of interest are

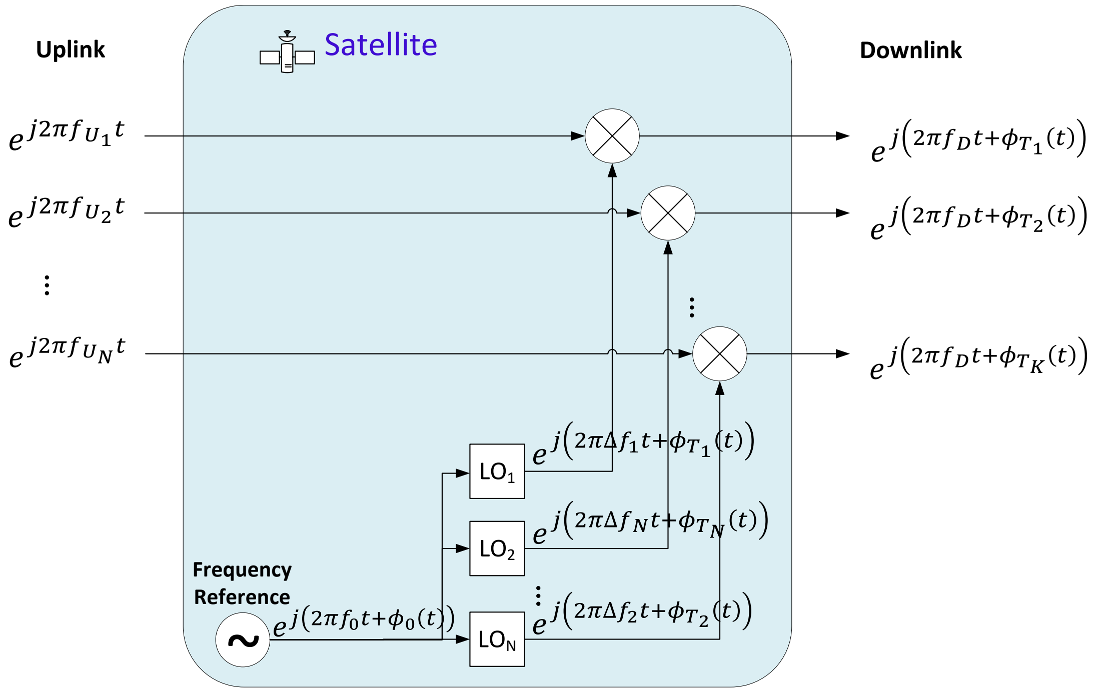

Figure 3.3: Graphical representation of how the FDM at the uplink and the LOs phase noise affect MU-MISO precoding even when a common frequency reference is used at the transponder.

the minimum mean squares error (MMSE), as an example of linear precoding techniques, and the optimal distance preserving constructive interference region (DPCIR) based symbol-level precoding.

3.4.1 MMSE Precoding

Given an average total transmit power of p, the MMSE precoder aims to minimize the variance of the difference between the UTs' intended and received symbols. The corresponding optimization problem can be expressed as [260]

$$\underset{W,\eta}{min} \quad \mathrm{E}\left\{\|\mathbf{s}-\eta^{-1}\mathbf{r}\|^2\right\} \quad \text{s.t.} \quad \mathrm{E}\left\{\|\mathbf{W}\mathbf{s}\|^2\right\}=p, \tag{3.7}$$

with η denoting the normalization factor to be optimized. The MMSE precoding matrix can then be obtained in a closed form as [261]

$$\mathbf{W}_{\mathrm{MMSE}}=\eta_{\mathrm{MMSE}}\,\mathbf{H}^{\mathrm{H}}\left(\mathbf{H}\mathbf{H}^{\mathrm{H}}+\frac{K\sigma^2}{p}\mathbf{I}\right)^{-1}, \tag{3.8}$$

where

$$\eta_{\mathrm{MMSE}}=\sqrt{\frac{p}{\mathrm{Tr}\left(\mathbf{H}\mathbf{H}^{\mathrm{H}}\left(\mathbf{H}\mathbf{H}^{\mathrm{H}}+(K\sigma^2/p)\mathbf{I}\right)^{-2}\right)}}, \tag{3.9}$$

denotes the normalization factor ensuring the average transmit power of p. In the case where the measured channel matrix $\hat{\mathbf{H}}$ is used to calculate the MMSE precoding matrix, we obtain

$$\begin{aligned}
\hat{\mathbf{W}}^{\mathrm{D}}_{\mathrm{MMSE}} &= \hat{\eta}_{\mathrm{MMSE}}\,\hat{\mathbf{H}}^{\mathrm{H}}_{\mathrm{D}}\left(\hat{\mathbf{H}}_{\mathrm{D}}\hat{\mathbf{H}}^{\mathrm{H}}_{\mathrm{D}}+\frac{K\sigma^2}{p}\mathbf{I}\right)^{-1}\\
&= \hat{\eta}_{\mathrm{MMSE}}\,\mathbf{H}^{\mathrm{H}}\mathbf{\Psi}^{\mathrm{H}}_{\mathrm{D}}\left(\mathbf{\Psi}_{\mathrm{D}}\mathbf{H}\mathbf{H}^{\mathrm{H}}\mathbf{\Psi}^{\mathrm{H}}_{\mathrm{D}}+\frac{K\sigma^2}{p}\mathbf{\Psi}_{\mathrm{D}}\mathbf{\Psi}^{\mathrm{H}}_{\mathrm{D}}\right)^{-1}\\
&= \hat{\eta}_{\mathrm{MMSE}}\,\mathbf{H}^{\mathrm{H}}\mathbf{\Psi}^{\mathrm{H}}_{\mathrm{D}}\mathbf{\Psi}_{\mathrm{D}}\left(\mathbf{H}\mathbf{H}^{\mathrm{H}}+\frac{K\sigma^2}{p}\mathbf{I}\right)^{-1}\mathbf{\Psi}^{\mathrm{H}}_{\mathrm{D}}\\
&= \hat{\eta}_{\mathrm{MMSE}}\,\mathbf{H}^{\mathrm{H}}\left(\mathbf{H}\mathbf{H}^{\mathrm{H}}+\frac{K\sigma^2}{p}\mathbf{I}\right)^{-1}\mathbf{\Psi}^{\mathrm{H}}_{\mathrm{D}}.
\end{aligned} \tag{3.10}$$

Furthermore, using the symmetry property of Tr(·) operation, we can write

$$\begin{aligned}
&\mathrm{Tr}\left(\hat{\mathbf{H}}_{\mathrm{D}}\hat{\mathbf{H}}_{\mathrm{D}}^{\mathrm{H}}\left(\hat{\mathbf{H}}_{\mathrm{D}}\hat{\mathbf{H}}_{\mathrm{D}}^{\mathrm{H}}+(K\sigma^2/p)\mathbf{I}\right)^{-2}\right)\\
&=\mathrm{Tr}\left(\mathbf{\Psi}_{\mathrm{D}}\mathbf{H}\mathbf{H}^{\mathrm{H}}\mathbf{\Psi}_{\mathrm{D}}^{\mathrm{H}}\left(\mathbf{\Psi}_{\mathrm{D}}\mathbf{H}\mathbf{H}^{\mathrm{H}}\mathbf{\Psi}_{\mathrm{D}}^{\mathrm{H}}+(K\sigma^2/p)\mathbf{\Psi}_{\mathrm{D}}\mathbf{\Psi}_{\mathrm{D}}^{\mathrm{H}}\right)^{-2}\right)\\
&=\mathrm{Tr}\left(\mathbf{\Psi}_{\mathrm{D}}\mathbf{H}\mathbf{H}^{\mathrm{H}}\mathbf{\Psi}_{\mathrm{D}}^{\mathrm{H}}\mathbf{\Psi}_{\mathrm{D}}\left(\mathbf{H}\mathbf{H}^{\mathrm{H}}+(K\sigma^2/p)\mathbf{I}\right)^{-2}\mathbf{\Psi}_{\mathrm{D}}^{\mathrm{H}}\right)\\
&=\mathrm{Tr}\left(\mathbf{\Psi}_{\mathrm{D}}^{\mathrm{H}}\mathbf{\Psi}_{\mathrm{D}}\mathbf{H}\mathbf{H}^{\mathrm{H}}\left(\mathbf{H}\mathbf{H}^{\mathrm{H}}+(K\sigma^2/p)\mathbf{I}\right)^{-2}\right)\\
&=\mathrm{Tr}\left(\mathbf{H}\mathbf{H}^{\mathrm{H}}\left(\mathbf{H}\mathbf{H}^{\mathrm{H}}+(K\sigma^2/p)\mathbf{I}\right)^{-2}\right).
\end{aligned}\tag{3.11}$$

It immediately follows that $\eta_{\mathrm{MMSE}}=\hat{\eta}_{\mathrm{MMSE}}$. As a result, the MMSE precoding matrix under differential phase estimation can be written as

$$\hat{\mathbf{W}}_{\mathrm{MMSE}}^{\mathrm{D}}=\mathbf{W}_{\mathrm{MMSE}}\mathbf{\Psi}_{\mathrm{D}}^{\mathrm{H}}.$$

The UTs' intended symbols precoded with $\hat{\mathbf{W}}_{\mathrm{MMSE}}^{\mathrm{D}}$ are received as

$$\begin{aligned}
\hat{\mathbf{r}}&=\mathbf{H}\hat{\mathbf{W}}_{\mathrm{MMSE}}^{\mathrm{D}}\mathbf{s}+\mathbf{z}\\
&=\mathbf{\Psi}_{\mathrm{D}}\left(\hat{\eta}_{\mathrm{MMSE}}\,\mathbf{H}\mathbf{H}^{\mathrm{H}}\left(\mathbf{H}\mathbf{H}^{\mathrm{H}}+\frac{K\sigma^2}{p}\mathbf{I}\right)^{-1}\mathbf{\Psi}_{\mathrm{D}}^{\mathrm{H}}\mathbf{s}+\mathbf{z}\right)\\
&=\hat{\eta}_{\mathrm{MMSE}}\,\mathbf{\Psi}_{\mathrm{D}}\mathbf{H}\mathbf{H}^{\mathrm{H}}\left(\mathbf{H}\mathbf{H}^{\mathrm{H}}+\frac{K\sigma^2}{p}\mathbf{I}\right)^{-1}\mathbf{\Psi}_{\mathrm{D}}^{\mathrm{H}}\mathbf{s}+\hat{\mathbf{z}}.
\end{aligned}\tag{3.12}$$

To evaluate the effect of differential phase estimation at the UTs on the MMSE precoding performance, we compare the value of the objective function in (3.7), denoted by $f_{\mathrm{MMSE}}(\cdot)$, in two cases where $\mathbf{H}$ or $\hat{\mathbf{H}}_{\mathrm{D}}$ is used to calculate the precoding matrix. Given the optimal MMSE precoding matrix and the normalization factor $\hat{\eta}_{\mathrm{MMSE}}$ obtained from the physical channel $\mathbf{H}$, we obtain

$$\begin{aligned}
&f_{\mathrm{MMSE}}(\mathbf{W}_{\mathrm{MMSE}},\eta_{\mathrm{MMSE}})\\
&=\mathrm{E}\left\{\left\|\mathbf{s}-\eta_{\mathrm{MMSE}}^{-1}(\mathbf{H}\mathbf{W}_{\mathrm{MMSE}}\mathbf{s}+\mathbf{z})\right\|^2\right\}\\
&=\mathrm{E}\left\{\|\mathbf{s}-\eta_{\mathrm{MMSE}}^{-1}\mathbf{H}\mathbf{W}_{\mathrm{MMSE}}\mathbf{s}-\eta_{\mathrm{MMSE}}^{-1}\mathbf{z}\|^2\right\}\\
&=\mathrm{E}\left\{\mathbf{s}^{\mathbf{H}}\mathbf{s}\right\}+\mathrm{E}\left\{\eta_{\mathrm{MMSE}}^{-2}\mathbf{s}^{\mathrm{H}}\mathbf{W}_{\mathrm{MMSE}}^{\mathrm{H}}\mathbf{H}^{\mathrm{H}}\mathbf{H}\mathbf{W}_{\mathrm{MMSE}}\mathbf{s}\right\}\\
&-2\mathrm{E}\left\{\eta_{\mathrm{MMSE}}^{-1}\mathbf{s}^{\mathrm{H}}\mathbf{H}\mathbf{W}_{\mathrm{MMSE}}\mathbf{s}\right\}+\mathrm{E}\left\{\eta_{\mathrm{MMSE}}^{-2}\mathbf{z}^{\mathrm{H}}\mathbf{z}\right\},
\end{aligned}\tag{3.13}$$

where the last equality holds true under the assumption that $\mathbf{s}$ and $\mathbf{z}$ are uncorrelated. To further simplify (3.13), we use an equivalent expression for the expectation of quadratic forms provided as follows. Given any square matrix $\mathbf{P}$, it holds true that $\mathrm{E}\{\mathbf{s}^{\mathrm{H}}\mathbf{P}\mathbf{s}\} = \mathrm{Tr}(\mathbf{P}\mathbf{B}) + \mathbf{c}^{\mathrm{H}}\mathbf{P}\mathbf{c}$, where $\mathbf{c} \triangleq \mathrm{E}\{\mathbf{s}\}$ and $\mathbf{B} \triangleq \mathrm{E}\{\mathbf{s}\mathbf{s}^{\mathrm{H}}\} - \mathrm{E}\{\mathbf{s}\}\mathrm{E}\{\mathbf{s}^{\mathrm{H}}\}$. Under the assumption made in Section 3.2 that the constellation $\mathbb{X}$ is symmetric w.r.t. the origin, we have $\mathbf{c} = \mathrm{E}\{\mathbf{s}\} = \mathbf{0}$. Moreover, the assumption of $\mathbb{X}$ having unit average power along with the independence of UTs' symbols result in $\mathrm{E}\{\mathbf{s}\mathbf{s}^{\mathrm{H}}\} = \mathbf{I}$, yielding $\mathbf{B} = \mathbf{I}$. As a consequence, $\mathrm{E}\{\mathbf{s}^{\mathrm{H}}\mathbf{P}\mathbf{s}\} = \mathrm{Tr}(\mathbf{P})$ holds true. Thereby, we can write (3.13) as

$$\begin{aligned}
&f_{\mathrm{MMSE}}(\mathbf{W}_{\mathrm{MMSE}}, \eta_{\mathrm{MMSE}})\\
&= \mathrm{E}\left\{\mathbf{s}^{\mathbf{H}}\mathbf{s}\right\} + \eta_{\mathrm{MMSE}}^{-2}\mathrm{Tr}\left(\mathbf{W}_{\mathrm{MMSE}}^{\mathrm{H}}\mathbf{H}^{\mathrm{H}}\mathbf{H}\mathbf{W}_{\mathrm{MMSE}}\right)\\
&- 2\eta_{\mathrm{MMSE}}^{-1}\mathrm{Tr}\left(\mathbf{H}\mathbf{W}_{\mathrm{MMSE}}\right) + \mathrm{E}\left\{\eta_{\mathrm{MMSE}}^{-2}\mathbf{z}^{\mathrm{H}}\mathbf{z}\right\}.
\end{aligned} \tag{3.14}$$

On the other hand, with $\hat{\mathbf{W}}_{\mathrm{MMSE}}$, the objective function of the MMSE design evaluates as

$$\begin{aligned}
&f_{\mathrm{MMSE}}(\hat{\mathbf{W}}_{\mathrm{MMSE}}^{\mathrm{D}}, \hat{\eta}_{\mathrm{MMSE}})\\
&= \mathrm{E}\left\{\left\|\mathbf{s} - \hat{\eta}_{\mathrm{MMSE}}^{-1}\mathbf{\Psi}_{\mathrm{D}}(\mathbf{H}\hat{\mathbf{W}}_{\mathrm{MMSE}}^{\mathrm{D}}\mathbf{s} + \mathbf{z})\right\|^2\right\}\\
&= \mathrm{E}\left\{\|\mathbf{s} - \eta_{\mathrm{MMSE}}^{-1}\mathbf{\Psi}_{\mathrm{D}}\mathbf{H}\mathbf{W}_{\mathrm{MMSE}}\mathbf{\Psi}_{\mathrm{D}}^{\mathrm{H}}\mathbf{s} - \eta_{\mathrm{MMSE}}^{-1}\mathbf{\Psi}_{\mathrm{D}}\mathbf{z}\|^2\right\}\\
&= \mathrm{E}\left\{\mathbf{s}^{\mathbf{H}}\mathbf{s}\right\} + \mathrm{E}\left\{\eta_{\mathrm{MMSE}}^{-2}\mathbf{s}^{\mathrm{H}}\mathbf{\Psi}_{\mathrm{D}}\mathbf{W}_{\mathrm{MMSE}}^{\mathrm{H}}\mathbf{H}^{\mathrm{H}}\mathbf{H}\mathbf{W}_{\mathrm{MMSE}}\mathbf{\Psi}_{\mathrm{D}}^{\mathrm{H}}\mathbf{s}\right\}\\
&- 2\mathrm{E}\left\{\eta_{\mathrm{MMSE}}^{-1}\mathbf{s}^{\mathrm{H}}\mathbf{\Psi}_{\mathrm{D}}\mathbf{H}\mathbf{W}_{\mathrm{MMSE}}\mathbf{\Psi}_{\mathrm{D}}^{\mathrm{H}}\mathbf{s}\right\} + \mathrm{E}\left\{\eta_{\mathrm{MMSE}}^{-2}\mathbf{z}^{\mathrm{H}}\mathbf{z}\right\}.
\end{aligned} \tag{3.15}$$

Similarly, using $\mathrm{E}\{\mathbf{s}^{\mathrm{H}}\mathbf{P}\mathbf{s}\} = \mathrm{Tr}(\mathbf{P})$, we can simplify (3.15) as

$$\begin{aligned}
&f_{\mathrm{MMSE}}(\hat{\mathbf{W}}_{\mathrm{MMSE}}^{\mathrm{D}}, \hat{\eta}_{\mathrm{MMSE}})\\
&= \mathrm{E}\left\{\mathbf{s}^{\mathbf{H}}\mathbf{s}\right\} + \eta_{\mathrm{MMSE}}^{-2}\mathrm{Tr}\left(\mathbf{\Psi}_{\mathrm{D}}\mathbf{W}_{\mathrm{MMSE}}^{\mathrm{H}}\mathbf{H}^{\mathrm{H}}\mathbf{H}\mathbf{W}_{\mathrm{MMSE}}\mathbf{\Psi}_{\mathrm{D}}^{\mathrm{H}}\right)\\
&- 2\eta_{\mathrm{MMSE}}^{-1}\mathrm{Tr}\left(\mathbf{\Psi}_{\mathrm{D}}\mathbf{H}\mathbf{W}_{\mathrm{MMSE}}\mathbf{\Psi}_{\mathrm{D}}^{\mathrm{H}}\right) + \mathrm{E}\left\{\eta_{\mathrm{MMSE}}^{-2}\mathbf{z}^{\mathrm{H}}\mathbf{z}\right\}\\
&= \mathrm{E}\left\{\mathbf{s}^{\mathbf{H}}\mathbf{s}\right\} + \eta_{\mathrm{MMSE}}^{-2}\mathrm{Tr}\left(\mathbf{\Psi}_{\mathrm{D}}^{\mathrm{H}}\mathbf{\Psi}_{\mathrm{D}}\mathbf{W}_{\mathrm{MMSE}}^{\mathrm{H}}\mathbf{H}^{\mathrm{H}}\mathbf{H}\mathbf{W}_{\mathrm{MMSE}}\right)\\
&- 2\eta_{\mathrm{MMSE}}^{-1}\mathrm{Tr}\left(\mathbf{\Psi}_{\mathrm{D}}^{\mathrm{H}}\mathbf{\Psi}_{\mathrm{D}}\mathbf{H}\mathbf{W}_{\mathrm{MMSE}}\right) + \mathrm{E}\left\{\eta_{\mathrm{MMSE}}^{-2}\mathbf{z}^{\mathrm{H}}\mathbf{z}\right\}\\
&= \mathrm{E}\left\{\mathbf{s}^{\mathbf{H}}\mathbf{s}\right\} + \eta_{\mathrm{MMSE}}^{-2}\mathrm{Tr}\left(\mathbf{W}_{\mathrm{MMSE}}^{\mathrm{H}}\mathbf{H}^{\mathrm{H}}\mathbf{H}\mathbf{W}_{\mathrm{MMSE}}\right)\\
&- 2\eta_{\mathrm{MMSE}}^{-1}\mathrm{Tr}\left(\mathbf{H}\mathbf{W}_{\mathrm{MMSE}}\right) + \mathrm{E}\left\{\eta_{\mathrm{MMSE}}^{-2}\mathbf{z}^{\mathrm{H}}\mathbf{z}\right\}.
\end{aligned} \tag{3.16}$$

From (3.14) and (3.16), it is evident that

$$f_{\text{MMSE}}(\mathbf{W}_{\text{MMSE}}, \eta_{\text{MMSE}}) = f_{\text{MMSE}}(\hat{\mathbf{W}}^{\text{D}}_{\text{MMSE}}, \hat{\eta}_{\text{MMSE}}).$$

As a result, both $\mathbf{W}_{\text{MMSE}}$ and $\hat{\mathbf{W}}^{\text{D}}_{\text{MMSE}}$ lead to the same value for the objective function of the MMSE design problem. Recall, further, that $\eta_{\text{MMSE}} = \hat{\eta}_{\text{MMSE}}$, i.e., the average transmitted power is the same with either $\mathbf{W}_{\text{MMSE}}$ or $\hat{\mathbf{W}}^{\text{D}}_{\text{MMSE}}$. Therefore, we conclude that the MMSE precoding's performance is preserved under differential phase estimation at the UTs' receivers.

The equivalent demonstration for ZF can be easily obtained by making zero the term $\frac{K\sigma^2}{p}\mathbf{I}$ in (3.8) and (3.9) since the Precoding matrix for ZF is calculated according to

$$\mathbf{W}_{\text{ZF}} = \eta_{\text{ZF}}\,\mathbf{H}^{\text{H}}\left(\mathbf{H}\mathbf{H}^{\text{H}}\right)^{-1}, \tag{3.17}$$

where

$$\eta_{\text{ZF}} = \sqrt{\frac{p}{\text{Tr}\left(\left(\mathbf{H}\mathbf{H}^{\text{H}}\right)^{-1}\right)}}. \tag{3.18}$$

A similar analysis considering the noise introduced by the frequency down-conversion at the transponder leads to

$$\hat{\mathbf{W}}^{\text{U}}_{\text{MMSE}} = \mathbf{\Phi}^{\text{H}}_{\text{U}}(t)\mathbf{W}_{\text{MMSE}}. \tag{3.19}$$

However, in this case the received signal at the UTs is

$$\begin{aligned}\hat{\mathbf{r}} &= \mathbf{H}_{\text{U}}\hat{\mathbf{W}}^{\text{U}}_{\text{MMSE}}\mathbf{s} + \mathbf{z}\\ &= \mathbf{H}\mathbf{\Phi}_{\text{U}}(t_0+\tau)\mathbf{\Phi}^{\text{H}}_{\text{U}}(t_0)\mathbf{W}_{\text{MMSE}}\mathbf{s} + \mathbf{z}\\ &= \eta_{\text{MMSE}}\mathbf{s} + \mathbf{z}.\end{aligned} \tag{3.20}$$

Equation (3.20) suggests that the precoding loop compensates for the phase errors introduced in the transponder, which is true, but it only holds under certain conditions. The multiplication $\mathbf{\Phi}_{\text{U}}(t_0+\tau)\mathbf{\Phi}^{\text{H}}_{\text{U}}(t_0) = \mathbf{I}$ assumes that the phase noise remains constant between the estimation of the CSI $\mathbf{\Phi}^{\text{H}}_{\text{U}}(t_0)$ at time t_0 and the use of the precoding matrix $\mathbf{\Phi}_{\text{U}}(t_0+\tau)$ after a delay τ. This assumption can be valid for specific conditions where the distance between transmitter and receiver is small, such as some terrestrial networks, and for excellent frequency references, which is not the general case in GEO satellite systems. As a result, we can conclude that the phase noise introduced by the transponder affects the performance of linear precoding systems. This demonstration can be easily extended to other linear precoding methods such as ZF.

3.4.2 Symbol-Level Precoding

A SLP technique directly calculates the precoded transmit signal (hence, no precoding matrix) on a symbol-by-symbol basis by exploiting the UTs' instantaneous data symbols. Accordingly, the transmit signal is designed so that each UT's (noise-free) received signal is located within the so-called CIR corresponding to its intended symbol. The CIRs are typically defined to improve the symbol detection accuracy at the receiver side; hence, they depend on the modulation scheme in use. These regions have been defined in several different ways in the literature; see, e.g., [262–264]. In this work, we focus on a specific family of CIRs, namely, distance-preserving CIRs [264], which are presented in a generic form that applies to any given modulation scheme. This general family of CIRs will be described in detail in the next section. For the moment, let us focus on the resulting SLP design problem. In what follows, we use the equivalent real-valued notations introduced in Section 3.2.

Let $\mathbf{u}$ denote the complex-valued $N \times 1$ precoded transmit vector to be directly obtained as a result of solving the SLP optimization problem. We further denote the equivalent real-valued representation of $\mathbf{u}$ by $\bar{\mathbf{u}} \triangleq [\mathrm{Re}(\mathbf{u}), \mathrm{Im}(\mathbf{u})]^{\mathrm{T}}$. Assume, also, that a set of SNIR requirements $\{\gamma_1, ..., \gamma_K\}$ are provided to be met for the UTs. Then, given the physical channel $\bar{\mathbf{H}}$, the power minimization SLP problem under distance-preserving CIR constraints can be expressed as

$$\min_{\bar{u},d} \quad \|\bar{\mathbf{u}}\|^2 \quad \text{s.t.} \quad \mathbf{A}(\bar{\mathbf{H}}\bar{\mathbf{u}} - \boldsymbol{\Sigma}\boldsymbol{\Gamma}\,\bar{\mathbf{s}}) = \mathbf{d},\ \mathbf{d} \succeq \mathbf{0}, \tag{3.21}$$

where the following definitions are used: $\bar{\mathbf{H}} \triangleq [\bar{\mathbf{H}}_1^{\mathrm{T}}, ..., \bar{\mathbf{H}}_K^{\mathrm{T}}]^{\mathrm{T}}$; $\mathbf{A} \triangleq \mathrm{blkdiag}(\mathbf{A}_1, ..., \mathbf{A}_K)$ with $\mathbf{A}_k = [\mathbf{a}_{k,1}, \mathbf{a}_{k,2}]^{\mathrm{T}}$ and $\mathbf{a}_{k,1}$ and $\mathbf{a}_{k,2}$ denoting the normal vectors of the maximum-likelihood (ML) decision boundaries (Voronoi regions) of $\mathbf{s}_k$; $\boldsymbol{\Sigma} \triangleq \mathrm{diag}(\sigma_1, ..., \sigma_K) \otimes \mathbf{I}_2$; $\boldsymbol{\Gamma} \triangleq \mathrm{diag}(\sqrt{\gamma_1}, ..., \sqrt{\gamma_K}) \otimes \mathbf{I}_2$; $\mathbf{s} \triangleq [\mathbf{s}_1, ..., \mathbf{s}_K]^{\mathrm{T}}$; and $\mathbf{d} \triangleq [\mathbf{d}_1^{\mathrm{T}}, ..., \mathbf{d}_K^{\mathrm{T}}]^{\mathrm{T}}$ is a $2K \times 1$ vector of distances between the received symbols, without noise, and the DPCIR edges. The elements $\mathbf{d}_k$ are 2×1 vectors defined as $\mathbf{d}_k \triangleq [d_{k,1}, d_{k,2}]^{\mathrm{T}}$ for all $k = 1, ..., K$. Equivalently, the optimal symbol-level precoded transmit vector can be obtained by the following lemma [265].

$\succeq$

Lemma 1. *Given the physical channel* $\bar{\mathbf{H}}$, *the minimum-power precoded signal vector satisfying the distance-preserving constructive interference (CI) constraint of* (3.21) *is given by*

$$\bar{\mathbf{u}} = \bar{\mathbf{H}}^{\dagger}\left(\boldsymbol{\Sigma}\boldsymbol{\Gamma}\bar{\mathbf{s}} + \mathbf{A}^{-1}\mathbf{d}\right), \tag{3.22}$$

where $\mathbf{d}$ *is the optimal solution to the following non-negative least squares (NNLS) problem*

$$\underset{d\succeq 0}{min} \quad \|\bar{\mathbf{H}}^{\dagger}\boldsymbol{\Sigma}\boldsymbol{\Gamma}\bar{\mathbf{s}} + \mathbf{H}^{\dagger}\mathbf{A}^{-1}\mathbf{d}\|^{2}. \tag{3.23}$$

Having the optimal precoded vector provided by Lemma 1, we can obtain the received signal vector at the UTs' as

$$\begin{aligned}\mathbf{r} &= \bar{\mathbf{H}}\bar{\mathbf{u}} + \bar{\mathbf{z}}\\ &= \bar{\mathbf{H}}\bar{\mathbf{H}}^{\dagger}\left(\boldsymbol{\Sigma}\boldsymbol{\Gamma}\bar{\mathbf{s}} + \mathbf{A}^{-1}\mathbf{d}\right) + \bar{\mathbf{z}}\\ &= \boldsymbol{\Sigma}\boldsymbol{\Gamma}\bar{\mathbf{s}} + \mathbf{A}^{-1}\mathbf{d} + \bar{\mathbf{z}}.\end{aligned} \tag{3.24}$$

Now, assume that instead of the physical channel matrix $\mathbf{H}$, the measured channel $\hat{\mathbf{H}}_{\mathrm{D}}$ is given to calculate $\bar{\mathbf{u}}$. Let us denote by $\hat{\bar{\mathbf{H}}}_{\mathrm{D}}$ the equivalent real-valued representation of $\hat{\mathbf{H}}_{\mathrm{D}}$. Then, the relation between $\bar{\mathbf{H}}$ and $\hat{\bar{\mathbf{H}}}_{\mathrm{D}}$ in the real domain is given as

$$\hat{\bar{\mathbf{H}}}_{\mathrm{D}} = \bar{\boldsymbol{\Psi}}_{\mathrm{D}}\bar{\mathbf{H}}, \tag{3.25}$$

where $\bar{\boldsymbol{\Psi}}_{\mathrm{D}} \triangleq \mathrm{blkdiag}(\boldsymbol{\Psi}_{\mathrm{D}_1}, ..., \boldsymbol{\Psi}_{\mathrm{D}_K})$ with

$$\boldsymbol{\Psi}_{\mathrm{D}_k} = \begin{bmatrix}\mathrm{Re}(e^{-\mathrm{j}\psi_{kk}}) & -\mathrm{Im}(e^{-\mathrm{j}\psi_{kk}})\\ \mathrm{Im}(e^{-\mathrm{j}\psi_{kk}}) & \mathrm{Re}(e^{-\mathrm{j}\psi_{kk}}),\end{bmatrix}$$

for any $k \in \{1, 2, ..., K\}$. According to this definition, we can simplify $\bar{\boldsymbol{\Psi}}_{\mathrm{D}}$ as

$$\bar{\boldsymbol{\Psi}}_{\mathrm{D}} = \begin{bmatrix}\cos(\psi_{11}) & \sin(\psi_{11}) & \cdots & 0 & 0\\ -\sin(\psi_{11}) & \cos(\psi_{11}) & \cdots & 0 & 0\\ \vdots & \vdots & \ddots & \vdots & \vdots\\ 0 & 0 & \cdots & \cos(\psi_{KK}) & \sin(\psi_{KK})\\ 0 & 0 & \cdots & -\sin(\psi_{KK}) & \cos(\psi_{KK})\end{bmatrix}, \tag{3.26}$$

where each block of $\bar{\mathbf{\Psi}}_{\mathrm{D}}$ is a two-dimensional rotation matrix. In this case, we obtain

$$\begin{aligned}\hat{\mathbf{u}} &= \hat{\bar{\mathbf{H}}}^{\dagger}\left(\mathbf{\Sigma}\mathbf{\Gamma}\bar{\mathbf{s}}+\mathbf{A}^{-1}\hat{\mathbf{d}}\right)\\ &= (\bar{\mathbf{\Psi}}_{\mathrm{D}}\bar{\mathbf{H}})^{\dagger}\left(\mathbf{\Sigma}\mathbf{\Gamma}\bar{\mathbf{s}}+\mathbf{A}^{-1}\hat{\mathbf{d}}\right)\\ &= \bar{\mathbf{H}}^{\dagger}\bar{\mathbf{\Psi}}_{\mathrm{D}}^{-1}\left(\mathbf{\Sigma}\mathbf{\Gamma}\bar{\mathbf{s}}+\mathbf{A}^{-1}\hat{\mathbf{d}}\right).\end{aligned} \tag{3.27}$$

Accordingly, the vector $\hat{\mathbf{d}}$ is obtained as the solution to the following NNLS problem:

$$\underset{\hat{d}\succeq 0}{min} \quad \|\bar{\mathbf{H}}^{\dagger}\mathbf{\Sigma}\mathbf{\Gamma}\bar{\mathbf{\Psi}}_{\mathrm{D}}^{-1}\bar{\mathbf{s}}+\bar{\mathbf{H}}^{\dagger}\bar{\mathbf{\Psi}}_{\mathrm{D}}^{-1}\mathbf{A}^{-1}\hat{\mathbf{d}}\|^{2}, \tag{3.28}$$

where in deriving (3.28), we have used the property that diagonal matrices are commutative, i.e., $\bar{\mathbf{\Psi}}_{\mathrm{D}}^{\dagger}\mathbf{\Sigma}\mathbf{\Gamma}=\mathbf{\Sigma}\mathbf{\Gamma}\bar{\mathbf{\Psi}}_{\mathrm{D}}^{\dagger}$. Having the precoded vector (3.27), the UTs' received signal in the real domain can be expressed as

$$\begin{aligned}\hat{\mathbf{r}} &= \bar{\mathbf{\Psi}}_{\mathrm{D}}\left(\bar{\mathbf{H}}\hat{\mathbf{u}}+\bar{\mathbf{z}}\right)\\ &= \bar{\mathbf{\Psi}}_{\mathrm{D}}\left(\bar{\mathbf{H}}\bar{\mathbf{H}}^{\dagger}\bar{\mathbf{\Psi}}_{\mathrm{D}}^{-1}\left(\mathbf{\Sigma}\mathbf{\Gamma}\bar{\mathbf{s}}+\mathbf{A}^{-1}\hat{\mathbf{d}}\right)+\bar{\mathbf{z}}\right)\\ &= \mathbf{\Sigma}\mathbf{\Gamma}\bar{\mathbf{s}}+\mathbf{A}^{-1}\hat{\mathbf{d}}+\bar{\mathbf{\Psi}}_{\mathrm{D}}\bar{\mathbf{z}}\\ &= \mathbf{\Sigma}\mathbf{\Gamma}\bar{\mathbf{s}}+\mathbf{A}^{-1}\hat{\mathbf{d}}+\hat{\bar{\mathbf{z}}},\end{aligned} \tag{3.29}$$

where $\hat{\bar{\mathbf{z}}} \triangleq \bar{\mathbf{\Psi}}_{\mathrm{D}}\bar{\mathbf{z}}$ is a CSCG vector with zero mean and variance σ^2. Comparing (3.24) with (3.29), we can see that the received signal vector $\hat{\mathbf{r}}$ with phase-normalized channel resembles in the form to $\mathbf{r}$ obtained with the physical channel. However, they differ in the vector-valued variables $\mathbf{d}$ and $\hat{\mathbf{d}}$, which are not equal since they are solutions to two different optimization problems.

In the NNLS problem (3.28), $\mathbf{A}^{-1}$ and $\bar{\mathbf{s}}$ are rotated as

$$\begin{aligned}\bar{\mathbf{\Psi}}_{\mathrm{D}}^{-1}\mathbf{A}^{-1} &= \begin{bmatrix}\mathbf{\Psi}_{\mathrm{D}_1} & \cdots & 0\\ \vdots & \ddots & \vdots\\ 0 & \cdots & \mathbf{\Psi}_{\mathrm{D}_K}\end{bmatrix}^{-1} \times \begin{bmatrix}\mathbf{A}_1 & \cdots & 0\\ \vdots & \ddots & \vdots\\ 0 & \cdots & \mathbf{A}_K\end{bmatrix}^{-1}\\ &= \begin{bmatrix}\mathbf{\Psi}_{\mathrm{D}_1}^{-1}\mathbf{A}_1^{-1} & \cdots & 0\\ \vdots & \ddots & \vdots\\ 0 & \cdots & \mathbf{\Psi}_{\mathrm{D}_K}^{-1}\mathbf{A}_K^{-1}\end{bmatrix},\end{aligned} \tag{3.30}$$

and

$$\bar{\mathbf{\Psi}}_{\mathrm{D}}^{-1}\bar{\mathbf{s}} = \begin{bmatrix} \mathbf{\Psi}_{\mathrm{D}_1} & \cdots & 0 \\ \vdots & \ddots & \vdots \\ 0 & \cdots & \mathbf{\Psi}_{\mathrm{D}_K} \end{bmatrix}^{-1} \times \begin{bmatrix} \mathbf{s}_1 \\ \vdots \\ \mathbf{s}_K \end{bmatrix} = \begin{bmatrix} \mathbf{\Psi}_{\mathrm{D}_1}^{-1}\mathbf{s}_1 \\ \vdots \\ \mathbf{\Psi}_{\mathrm{D}_K}^{-1}\mathbf{s}_K \end{bmatrix}, \tag{3.31}$$

from which it follows that each symbol $\mathbf{s}_k$ and its corresponding sub-matrix $\mathbf{A}_k$ are rotated by ψ_{kk}. Note that the distance-preserving CIR of $\mathbf{s}_k$ can be identified by $\mathbf{s}_k$ and its matrix of normal vectors $\mathbf{A}_k$. Keeping in mind that the same angular value rotates both $\mathbf{s}_k$ and $\mathbf{A}_k$, we can interpret this rotation as follows. With phase rotated channel $\hat{\bar{\mathbf{H}}}_{\mathrm{D}}$, the constellation sets of UTs, at any given symbol period, are rotated versions of their original constellations, where the rotation angles correspond to those in the rotation matrix $\bar{\mathbf{\Psi}}_{\mathrm{D}}$. It is important to note that the symbol constellation of each UT undergoes a rotation by an angular value that corresponds to the reference phase value of its own channel vector. Therefore, the UTs' constellations are not equally rotated in general. In Fig. 3.4, we illustrate how the intended symbols and their corresponding distance-preserving CIRs of two different UTs may be rotated. It can be seen that the relative positioning of the constellation symbols is preserved under this rotation. Further, the shape of distance-preserving CIRs (including the angle between their two edges) remains unchanged. As a result, the relative geometry of the constellation is preserved under differential phase estimation.

Let us denote $\bar{\mathbf{s}}_{\mathrm{r}} \triangleq \bar{\mathbf{\Psi}}_{\mathrm{D}}^{-1}\bar{\mathbf{s}}$ and $\mathbf{A}_{\mathrm{r}}^{-1} \triangleq \bar{\mathbf{\Psi}}_{\mathrm{D}}^{-1}\mathbf{A}^{-1}$. Then, the following lemma encapsulates the solution of the SLP problem in the case with differential phase estimation.

Lemma 2. *Given the phase-normalized channel $\hat{\bar{\mathbf{H}}}_{\mathrm{D}}$, with rotation matrix $\bar{\mathbf{\Psi}}_{\mathrm{D}}$, the minimum-power solution of the SLP design under distance-preserving CI constraints is given by*

$$\hat{\mathbf{u}} = \bar{\mathbf{H}}^{\dagger}\left(\mathbf{\Sigma}\mathbf{\Gamma}\bar{\mathbf{s}}_{\mathrm{r}} + \mathbf{A}_{\mathrm{r}}^{-1}\hat{\mathbf{d}}\right), \tag{3.32}$$

where $\hat{\mathbf{d}}$ is the optimal solution to the following NNLS problem

$$\underset{\hat{d}\succeq 0}{min} \quad \|\bar{\mathbf{H}}^{\dagger}\mathbf{\Sigma}\mathbf{\Gamma}\bar{\mathbf{s}}_{\mathrm{r}} + \mathbf{H}^{\dagger}\mathbf{A}_{\mathrm{r}}^{-1}\hat{\mathbf{d}}\|^2, \tag{3.33}$$

with $\bar{\mathbf{s}}_{\mathrm{r}}$ and $\mathbf{A}_{\mathrm{r}}^{-1}$ representing rotated constellations w.r.t. the original ones.

The difference between the SLP design with the physical channel $\bar{\mathbf{H}}$, and the one with the phase-normalized channel $\hat{\bar{\mathbf{H}}}_{\mathrm{D}}$ originates from the vector-valued design variables $\mathbf{d}$ and $\hat{\mathbf{d}}$ as the solutions to the NNLS problems (3.23) and (3.33), respectively. In fact, given the channel matrix and the UTs' symbols, this is the design variable that controls the performance of the SLP. Now, the question is how the performance differs in these two cases. In other words, how the differential phase estimation process affects the SLP's performance. Based on the above discussion, we should analyze the NNLS problem associated with the SLP design and its dependency on different parameters to answer this question. The following theorem states the result of such an analysis, where its proof is provided in the next section.

Theorem 3. *The average performance of an SNIR-constrained power minimization SLP design with distance-preserving CIR constraints is preserved under differential phase estimation.*

The proof of Theorem 3 is not straightforward, but it requires a closer look into the structure of the SLP's NNLS formulation, as we will see in Section 3.5.

3.5 Analysis of the NNLS-Based SLP Design

This section analyzes the solution to the SLP problem with distance-preserving CI constraints to reveal its dependency on the constellation-dependent design parameters. More specifically, the main result of this section is the proof of Theorem 3. To this end, we derive an explicit function that can assess the SLP's performance as a function of the constellation parameters. The results can be applied in the SLP design process. Expecificly, for the cases where the phase-normalized channel $\hat{\mathbf{H}}_\mathrm{D}$ is modeled as rotated UTs' constellations.

We mentioned earlier in Section 3.4 that differential phase estimation at the UTs and its subsequent effects on the SLP design at the transmitter can be modeled as a rotation applied to the symbol constellation of each UT. This rotation preserves the relative geometry of the constellation; however, the symbols' exact positioning and corresponding CIRs will be affected. Therefore, it becomes interesting to know whether the average performance of SLP depends on the relative or the exact geometry of the constellation or even on both.

Let us start our analysis by reviewing the characteristics and definitions of distance-preserving CIRs. Recall that the UTs' intended symbols are taken from the constellation set $\mathbb{X}$, i.e., $s_k = x_i$ for some $x_i \in \mathbb{X}$. In the sequel, with a slight deviation in notation, we use the subscript i for the matrix $\mathbf{A}$ and the vector $\mathbf{d}$ that corresponds to the ith constellation symbol.

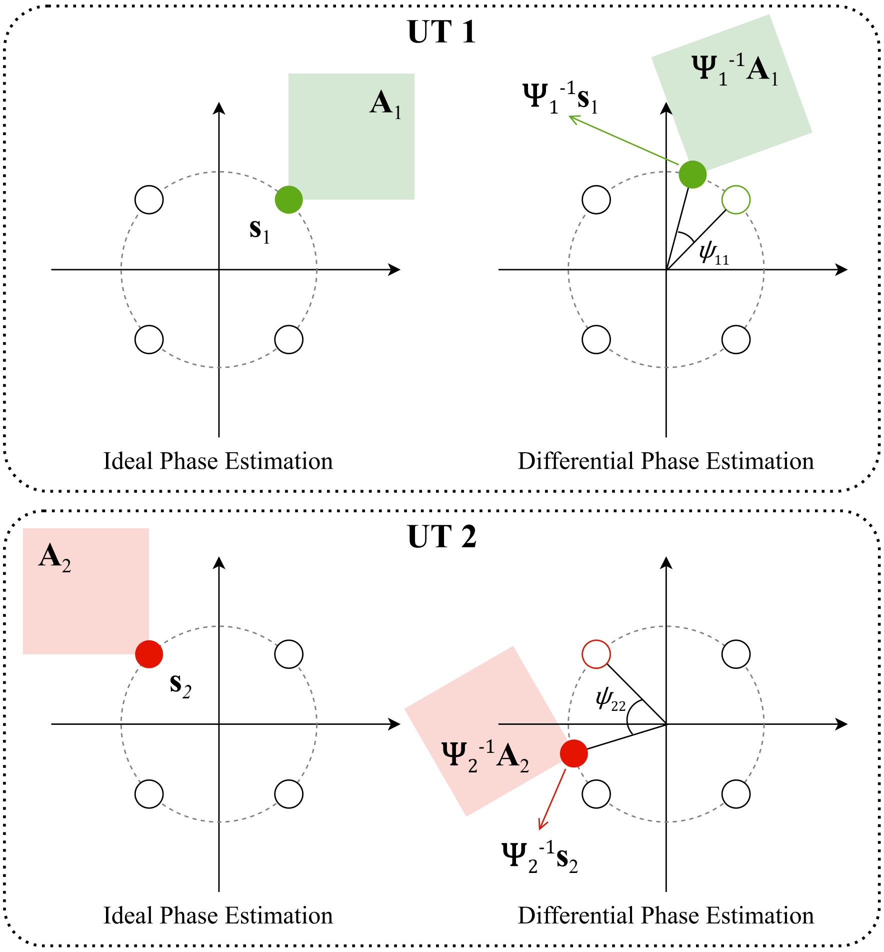

Figure 3.4: An illustrative example of original and rotated QPSK symbols and their corresponding distance-preserving CIRs.

As defined in [265], any two points belonging to two distinct distance-preserving CIRs are distanced by at least the distance between the corresponding constellation symbols. Therefore, given a constellation point $\mathbf{x}_i$, any $\mathbf{x} \in \mathbb{R}^2$ belonging to the distance-preserving CIR of $\mathbf{x}_i$ satisfies

$$\mathbf{A}_i\left(\mathbf{x}-\mathbf{x}_i\right)=\mathbf{d}_i, \text{ where } \begin{cases} \mathbf{d}_i \geq \mathbf{0}, & \mathbf{x}_i \in \mathbf{bd}(\mathbb{X}), \\ \mathbf{d}_i = \mathbf{0}, & \mathbf{x}_i \in \mathbf{int}(\mathbb{X}), \end{cases} \tag{3.34}$$

where $\mathbf{A}_i = [\mathbf{a}_{i,1}, \mathbf{a}_{i,2}]^{\mathrm{T}}$ contains the normal vectors of the maximum-likelihood decision boundaries (Voronoi regions) of $\mathbf{x}_i$. The two normal vectors $\mathbf{a}_{i,1}$ and $\mathbf{a}_{i,2}$ can simply be obtained using the following criteria:

- If $\mathbf{x}_i \in \mathbf{bd}(\mathbb{X})$, we obtain $\mathbf{a}_{i,1}$ and $\mathbf{a}_{i,2}$ by subtracting symbol $\mathbf{x}_i$ from its two neighboring constellation points on $\mathbf{bd}(\mathbb{X})$, namely, $\mathbf{x}_{i,1}$ and $\mathbf{x}_{i,2}$. In this case, we have

$$\mathbf{A}_i = \begin{bmatrix} \mathbf{a}_{i,1}^{\mathrm{T}} \\ \\ \mathbf{a}_{i,2}^{\mathrm{T}} \end{bmatrix} = \begin{bmatrix} (\mathbf{x}_i - \mathbf{x}_{i,1})^{\mathrm{T}} \\ \\ (\mathbf{x}_i - \mathbf{x}_{i,2})^{\mathrm{T}} \end{bmatrix} \in \mathbb{R}^{2\times 2}.$$

- If $\mathbf{x}_i \in \mathbf{int}(\mathbb{X})$, we set $\mathbf{a}_{i,1} = \mathbf{0}$ and $\mathbf{a}_{i,2} = \mathbf{0}$, and therefore, we have $\mathbf{A}_i = \mathbf{0} \in \mathbb{R}^{2\times 2}$.

Without loss of generality, let us further assume that, for any $\mathbf{x}_i \in \mathbf{bd}(\mathbb{X})$, the normal vectors $\mathbf{a}_{i,1}$ and $\mathbf{a}_{i,2}$ are normalized such that $\|\mathbf{a}_{i,1}\| = \|\mathbf{a}_{i,2}\| = 1$. It is worth noting that such an assumption does not affect the inequality (3.34). Accordingly, we have

$$\mathbf{A}_i\mathbf{A}_i^{\mathrm{T}} = \begin{bmatrix} \mathbf{a}_{i,1}^{\mathrm{T}}\mathbf{a}_{i,1} & \mathbf{a}_{i,1}^{\mathrm{T}}\mathbf{a}_{i,2} \\ \\ \mathbf{a}_{i,2}^{\mathrm{T}}\mathbf{a}_{i,1}^{\mathrm{T}} & \mathbf{a}_{i,2}^{\mathrm{T}}\mathbf{a}_{i,2}^{\mathrm{T}} \end{bmatrix} = \begin{bmatrix} 1 & \cos\phi_i \\ \\ \cos\phi_i & 1 \end{bmatrix}, \tag{3.35}$$

where $\phi_i \triangleq \angle(\mathbf{a}_{i,1}, \mathbf{a}_{i,2})$ denotes the angle between the normal vectors $\mathbf{a}_{i,1}$ and $\mathbf{a}_{i,2}$. From (3.35), it further follows that

$$(\mathbf{A}_i\mathbf{A}_i^{\mathrm{T}})^{-1} = \frac{1}{\sin^2\phi_i} \begin{bmatrix} 1 & -\cos\phi_i \\ \\ -\cos\phi_i & 1 \end{bmatrix}. \tag{3.36}$$

Next, let us focus on the NNLS problem in (3.23), which is the key step in the derivation of the optimal SLP solution. Denoting $\mathbf{Q} \triangleq -\bar{\mathbf{H}}^{\dagger}\mathbf{A}^{-1}$ and $\mathbf{y} \triangleq \bar{\mathbf{H}}^{\dagger}\boldsymbol{\Sigma}\boldsymbol{\Gamma}\bar{\mathbf{s}}$, we can rewrite the NNLS optimization (3.23) in the standard form as

$$\underset{d\succeq 0}{min} \quad \|\mathbf{y}-\mathbf{Q}\mathbf{d}\|^2. \tag{3.37}$$

It can be easily verified that the optimum of (3.37) can be equally achieved by the following dimensionality-reduced problem:

$$\underset{d_r\succeq 0}{min} \quad \|\mathbf{y}-\mathbf{Q}_{\mathrm{r}}\mathbf{d}_{\mathrm{r}}\|^2, \tag{3.38}$$

where $[\bar{\mathbf{H}}^{\dagger}]_{\mathrm{r}}$ denotes the matrix obtained by removing those columns of $\bar{\mathbf{H}}^{\dagger}$ that correspond to the UTs with a symbol in $\mathbf{int}(\mathbb{X})$, and similarly, $[\mathbf{A}^{-1}]_{\mathrm{r,r}}$ denotes the matrix obtained by removing those columns and rows of $\mathbf{A}^{-1}$ that correspond to the UTs with a symbol in $\mathbf{int}(\mathbb{X})$. Therefore, $\mathbf{Q}_{\mathrm{r}} \triangleq -[\bar{\mathbf{H}}^{\dagger}]_{\mathrm{r}}[\mathbf{A}^{-1}]_{\mathrm{r,r}}$ is a $2N \times 2L$ matrix, with L denoting the number of UTs with a symbol in $\mathbf{d}(\mathbb{X})$. As a result, the equivalent NNLS design in (3.38) has a dimension of $2L$, where $L \leq K$. Any minimizer $\mathbf{d}^*$ of the original design can simply be obtained by appropriately padding $\mathbf{d}_{\mathrm{r}}^*$ with $2K-2L$ zeros.

3.5.1 Sparsity Analysis of the NNLS Design

To analyze the sparsity of the (unique) solution to the NNLS problem in (3.37), we start from a quantitative measure called *separation quantity* [266], which is defined as

$$\tau^2 \triangleq \underset{p\in S^{2L-1}}{min} \; \frac{1}{2L}\,\mathbf{p}^{\mathrm{T}}\mathbf{Q}_{\mathrm{r}}^{\mathrm{T}}\mathbf{Q}_{\mathrm{r}}\,\mathbf{p}, \tag{3.39}$$

where $\mathcal{S}^n = \{\mathbf{p} \in \mathbb{R}^{n+1} : \mathbf{1}^{\mathrm{T}}\mathbf{p} = 1,\ \mathbf{p} \succeq \mathbf{0}\}$ represents an n-simplex (i.e., an n-dimensional simplex with $n-1$ degrees of freedom), and $1/(2L)$ is a normalization factor with respect to the problem size. From a geometric point of view, τ equals the orthogonal distance of the convex hull of the columns of $\mathbf{Q}_{\mathrm{r}}$ to the origin. This quantity can be used to determine whether the non-negativity constraints are effective. Otherwise, the optimization in (3.38) is nothing more than an ordinary least squares problem. Moreover, none of the non-negativity constraints introduced by the element-wise inequality $\mathbf{d}_{\mathrm{r}} \succeq \mathbf{0}$ are active if $\tau > 0$ does not hold true. This elementary condition is always satisfied for the NNLS design in (3.38). Due to the facts that $\mathbf{Q}_{\mathrm{r}}$ is a full column rank matrix and that $\mathbf{Q}_{\mathrm{r}}^{\mathrm{T}}\mathbf{Q}_{\mathrm{r}}$ is symmetric, we have

$\mathbf{Q}_\mathrm{r}^\mathrm{T}\mathbf{Q}_\mathrm{r} \succ 0$, i.e., $\mathbf{Q}_\mathrm{r}^\mathrm{T}\mathbf{Q}_\mathrm{r}$ is positive definite. Hence $\mathbf{p}^\mathrm{T}\mathbf{Q}_\mathrm{r}^\mathrm{T}\mathbf{Q}_\mathrm{r}\mathbf{p} > 0$ for all $\mathbf{p} \neq \mathbf{0}$. Note that the positive definiteness is sufficient here since the constraint $\mathbf{p} \in \mathcal{S}^{2L-1}$ prevents the case $\mathbf{p} = \mathbf{0}$ in our problem. In light of the separation quantity (3.39), a fundamental result states that an NNLS design may inherently leads to sparse solutions if it satisfies the following so-called *self-regularizing* property [266].

Proposition 4. *The NNLS problem (3.38) has a self-regularizing property if there exists a constant* $\tau_{\min} > 0$ *such that* $\tau \geq \tau_{\min}$.

It should be noted that $\tau_{\min}$ may not be unique in general; however, Proposition 4 emphasizes the existence of such a lower bound. Accordingly, the NNLS problem (3.38) automatically generates a regularizing term if the condition in Proposition 4 is met. As a consequence, one can make an explicit connection between a self-regularizing NNLS design and a non-negative LASSO problem as in [266], i.e.,

$$\begin{aligned} \underset{d_r \succeq 0}{min} \, \|\mathbf{y} - \mathbf{Q}_\mathrm{r}\mathbf{d}_\mathrm{r}\|^2 = \underset{d_r \succeq 0}{min} \, &\|\mathbf{y} - \tilde{\mathbf{Q}}_\mathrm{r}\mathbf{d}_\mathrm{r}\|^2 \\ &+ g(\tau_{\min})\mathbf{1}^\mathrm{T}\mathbf{d}_\mathrm{r} + \mathcal{O}(N^{-1/2}), \end{aligned} \tag{3.40}$$

with $\tilde{\mathbf{Q}}_\mathrm{r} = \mathbf{\Pi}\mathbf{Q}_\mathrm{r}\mathbf{D}$, where $\mathbf{\Pi}$ is the orthogonal projection onto the subspace spanned by $\mathbf{p}$, and $\mathbf{D}$ is a diagonal matrix; see [266] for a precise proof. Further, $g(\tau_{\min}) = \tau_{\min}^2\mathbf{1}^\mathrm{T}\mathbf{d}_\mathrm{r} = \tau_{\min}^2\|\mathbf{d}_\mathrm{r}\|_1$ is a non-negative increasing function of $\tau_{\min}$. Therefore, the term $g(\tau_{\min})\mathbf{1}^\mathrm{T}\mathbf{d}_\mathrm{r}$ in the right-hand side of (3.40) can be viewed as the LASSO penalty, i.e., it behaves as a sparsity-promoting ℓ_1-norm regularization. It is well known that a larger ℓ_1-norm penalty leads to sparser optimal solutions for the (non-negative) LASSO problem. Since the regularizing multiplier $g(\tau_{\min})$ is an increasing function of $\tau_{\min}$, from the analogy provided in (3.40), it follows that the larger the lower bound $\tau_{\min}$, the sparser minimizer for the NNLS design (3.38) is achieved.

3.5.2 Performance Analysis of the NNLS-Based SLP Design

We consider the average transmitted power, i.e., the optimal value of the objective function (3.38) as a measure of the SLP performance. More precisely, we define

$$p \triangleq \mathrm{E}_t\left\{\|\bar{\mathbf{u}}\|^2\right\}, \tag{3.41}$$

implying that the SLP with a smaller p has a more favorable performance. It is important to note that the expectation in (3.41) is taken over symbol time t. This is due to the fact that the transmitted signal $\bar{\mathbf{u}}$ as well as some other design parameters, such as $\mathbf{A}$, $\mathbf{W}$, and $\mathbf{d}$, are all functions of the UTs' symbol vector $\mathbf{s}$, and therefore, they vary over symbol time. However, we drop the symbol time index from our notation for brevity of notation. Furthermore, as explained in the following, p has an implicit dependence on $\mathbf{d}_{\mathrm{r}}$.

Consider the reduced NNLS problem in (3.38) with optimal solution $\mathbf{d}_{\mathrm{r}}^{*}$. In addition, let

$$\begin{aligned} \underset{d_r}{min} \quad & \|\mathbf{y}-\mathbf{Q}_{\mathrm{r}}\mathbf{d}_{\mathrm{r}}\|^2 \\ \text{s.t.} \quad & d_j \geq 0,\ \forall j \in \mathbb{K}, \\ & d_j = 0,\ \forall j \notin \mathbb{K}, \end{aligned} \tag{3.42}$$

be another design with minimizer $\hat{\mathbf{d}}_{\mathrm{r}}^{*}$ and $\mathbb{K}$ denoting an arbitrary subset of $\{1, 2, ..., 2K\}$. Recalling that the objective function values read as the total transmitted power, it is clear that the solution to (3.38) is never worse than that to (3.42), i.e.,

$$\|\mathbf{y}-\mathbf{Q}_{\mathrm{r}}\mathbf{d}_{\mathrm{r}}^{*}\|^2 \leq \|\mathbf{y}-\mathbf{Q}_{\mathrm{r}}\hat{\mathbf{d}}_{\mathrm{r}}^{*}\|^2,$$

which is immediate from the fact that (3.38) is a relaxation of (3.42). Therefore, we conclude that the design in (3.38) yields lower-power solutions than those of (3.42). In other words, one expects a larger transmitted power if the design imposes more zero constraints on the elements of $\mathbf{d}_{\mathrm{r}}$. This implies that p is a decreasing function of $\tau_{\min}$.

Based on the above discussion, as far as the solution to the SLP problem is concerned, sparsity is not favorable as it reflects reduced degrees of freedom in solving (3.38). It is also worth noting that as $\mathbf{d}$ becomes sparser, the optimal SLP converges to the (symbol-level) ZF precoder. In the extreme case, where $\mathbf{d} = \mathbf{0}$, the potential gain of the SLP design over the symbol-level ZF completely vanishes. Using this extreme case, a lower bound on the average transmitted power can be obtained as

$$p \geq \mathrm{Tr}\left(\boldsymbol{\Sigma}\boldsymbol{\Gamma}^2\bar{\mathbf{H}}^{\dagger}\bar{\mathbf{H}}^{\dagger^{\mathrm{T}}}\right). \tag{3.43}$$

The separation quantity τ, as defined in (3.39), depends on the matrix $\mathbf{Q}_{\mathrm{r}}$, so does its positive lower bound $\tau_{\min}$, if exists. From the definition of $\mathbf{Q}_{\mathrm{r}}$, it further follows that $\tau_{\min}$ is in fact a function of the two matrices $[\bar{\mathbf{H}}^{\dagger}]_{\mathrm{r}}$ and $[\mathbf{A}^{-1}]_{\mathrm{r,r}}$, where the latter matrix itself depends on the UTs' intended symbols $\mathbf{s}$. Note that our discussion so far applies to instantaneous realizations of $\tau_{\min}$ at a given symbol period; however, to have a more meaningful analysis of the SLP performance, long-term characteristics of $\tau^2_{\min}$ are of more concern. In particular, for a given channel realization $\mathbf{H}$, we define the *inverse regularizing function* as

$$\mathrm{E}_t\left\{\tau^2_{\min}\right\} \triangleq f(\bar{\mathbf{H}}, \mathbb{X}), \tag{3.44}$$

which relates the sparsity of the SLP solution to the adopted modulation scheme. This enables us to study the power consumption performance of the SLP design for different modulation schemes and even different channel characteristics by analyzing the inverse regularizing function $f(\bar{\mathbf{H}}, \mathbb{X})$. Note that having $\tau^2 \geq \tau^2_{\min}$, we are guaranteed that $\mathrm{E}_t\left\{\tau^2\right\} \geq \mathrm{E}_t\left\{\tau^2_{\min}\right\}$. The following corollary concludes this subsection by providing a qualitative inverse relation between the transmitted power p and $f(\bar{\mathbf{H}}, \mathbb{X})$.

Corollary 5. *Let $\tau_{\min,1}$ and $\tau_{\min,2}$ be associated with two SLP designs with two (possibly) different modulation schemes $\mathbb{X}_1$ and $\mathbb{X}_2$, respectively. Further, let $\mathrm{E}_t\left\{\tau^2_{\min,1}\right\} = f(\bar{\mathbf{H}}, \mathbb{X}_1)$ and $\mathrm{E}_t\left\{\tau^2_{\min,2}\right\} = f(\bar{\mathbf{H}}, \mathbb{X}_2)$ be the regularizing functions associated with $\mathbb{X}_1$ and $\mathbb{X}_2$. Then, under identical channel realizations, $f(\bar{\mathbf{H}}, \mathbb{X}_1) \leq f(\bar{\mathbf{H}}, \mathbb{X}_2)$ implies that $p_1 \leq p_2$.*

Finally, we provide an analytical measure of power efficiency by deriving an explicit expression for (3.44) as a function of modulation parameters. The results of this section will be used in evaluating/comparing the downlink performance with different modulation schemes.

Theorem 6. *A positive lower bound on the separation quantity τ associated to the NNLS design in (3.38) can be found as*

$$\tau^2 \geq \frac{\lambda}{2L}\left(\frac{1}{L + \sum_{l=1}^{L}\cos\phi_l}\right) \triangleq \tau^2_{\min}, \tag{3.45}$$

where $\lambda = \lambda_{\min}\left([(\bar{\mathbf{H}}\bar{\mathbf{H}}^{\mathrm{T}})^{-1}]_{\mathrm{r,r}}\right) > 0$ with $\lambda_{\min}(\cdot)$ denoting the minimum eigenvalue.

Proof. See Appendix A.1. ☐

Based on the lower bound in (3.45), the following theorem states the main result of this section by providing an approximation for the regularizing function.

Theorem 7. *Given* $\bar{\mathbf{H}}$ *and* $\mathbb{X}$*, for the NNLS-based SLP design, we have*

$$f(\bar{\mathbf{H}}, \mathbb{X}) \approx \frac{\lambda}{2} \left(\frac{1}{K\beta(1-\beta) + K^2\beta^2} \right) \times \left(\frac{M_{\mathrm{b}}}{M_{\mathrm{b}} + \sum_{i \in \mathbf{bd}(\mathbb{X})} \cos \phi_i} \right), \tag{3.46}$$

where $\beta = M_{\mathrm{b}}/M$*.*

Proof. See Appendix A.2. ☐

In the special case, where the boundary constellation points are uniformly distributed, $\mathbf{bd}(\mathbb{X})$ is an equilateral and equiangular convex polygon (i.e., a regular polygon). For this special geometry, we have

$$\phi_i = \phi, \ \forall i \in \mathbf{bd}(\mathbb{X}), \tag{3.47}$$

and therefore,

$$f(\bar{\mathbf{H}}, \mathbb{X}) \approx \frac{\lambda}{2} \left(\frac{1}{K\beta(1-\beta) + K^2\beta^2} \right) \left(\frac{1}{1 + \cos \phi} \right). \tag{3.48}$$

It should be noted that this special geometry does not make any assumption on the placement of the interior constellation points belonging to $\mathbf{int}(\mathbb{X})$. The condition specified by (3.47) is met by constellation sets of some well-known modulation schemes, e.g., PSK and APSK. In the particular case of PSK modulations with uniformly-distributed boundary symbols, since the constellation has no interior points, we have $\beta = 1$, which yields

$$f(\bar{\mathbf{H}}, \mathbb{X}) \approx \frac{\lambda}{2K^2} \left(\frac{1}{1 + \cos \phi} \right). \tag{3.49}$$

It can be seen from (3.48) that the regularizing function $f(\bar{\mathbf{H}}, \mathbb{X})$ does not depend on the exact locations of the constellation symbols but only on the relative angular positioning of the symbols (this latter specification is reflected in the shape of distance-preserving CIRs). Based on (3.48), the same statement holds true for the SLP's performance, completing the proof of Theorem 3.

3.6 Simulation Results

In this section, we provide some simulation results to verify our analytical discussions in the earlier sections. In particular, we aim to verify via simulation results that the performance of different precoding techniques of interest, i.e., MMSE, ZF, and SLP, is invariant to the differential phase estimation process at the receiver but the system performance is affected by the phase noise at the transponder LOs. Even if the problem formulation for these precoding techniques are different, ZF and MMSE formulation are power constraint problems, while the SLP method analyzed considers the power minimization with quality of service (QoS) constraints, this work is mainly focused on the constructive interference constraints in the SLP design problem and on how they are affected by phase uncertainty. This appears with the same formulation in both power minimization and QoS-constrained SLP problems. Besides, as shown in [265], the SLP power minimization problem solution for PSK modulations is sub-optimal for the QoS-constrained SLP problem under proper power scaling. For this reason, we considered equal transmit power for all the precoding schemes in our simulations. More specifically, we normalized the SLP power minimization problem solution so that the precoded vector has the same power as the ZF and MMSE precoding schemes.

To analyze the results, we focus on three performance metrics: spectral efficiency, SER, and receive SNIR. We calculate the spectral efficiency as the ratio of the product of the average UTs' bit error rate (BER) and the per-user achievable rate divided by the total consumed power. Due to the lack of closed-form expressions for SLP, we use empirical probability distributions obtained over a sufficiently high number of independent realizations of the channel and the users' symbols to approximate the mutual information for each user, as done in [267]. The SER is calculated as the ratio of the number of symbols received with errors of the total number of transmitted symbols. Finally, the SNIR is defined as the ratio of the received signal's power over the interference plus noise power at the receivers.

The simulation setup considered a downlink MU-MISO system with multiuser precoding, where independent data symbols are intended for the UTs. At the UTs, identical noise distributions $z_k \sim \mathcal{CN}(0, \sigma^2)$ with $\sigma^2 = 1$ are assumed, for all $k = 1, ..., K$. Independent Rayleigh block fading channels are further assumed between each transmitter-UT antenna pair, where IID realizations $\{\mathbf{h}_k\}_{k=1}^{K}$ are randomly generated for each fading block from the standard circularly symmetric complex Gaussian distribution, i.e., $\mathbf{h}_k \sim \mathcal{CN}(\mathbf{0}, \mathbf{I})$. The use of this channel model is fundamented by the intention to prove the performance of the precoding method is invariant to the differential phase estimation process at the receiver for any communication scenario, terrestrial o satellite.

Fig. 3.5a represents the simulation diagram of this experiment. As it can be appreciated

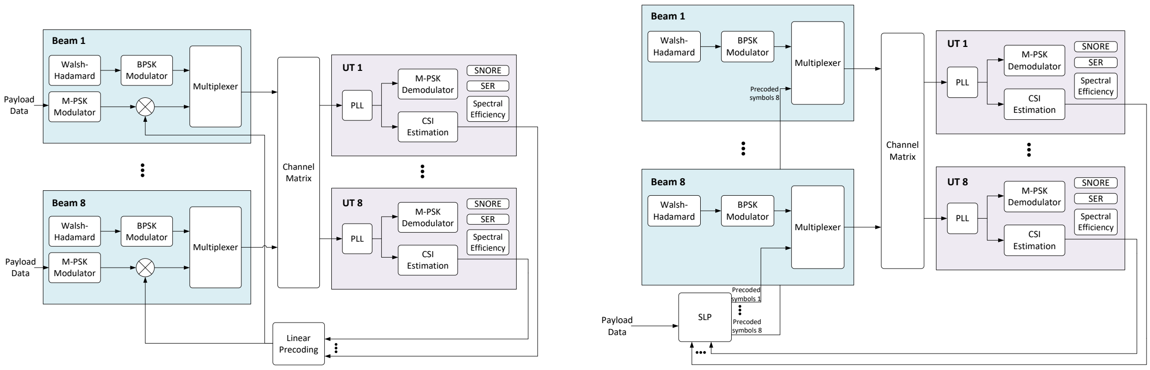

(a) Linear precoding (b) SLP

Figure 3.5: Simulation diagram for the experiment to verify that the performance of different precoding techniques is invariant to the differential phase estimation process at the UTs.

in the figure, the signal for each beam is the concatenation done at the ”Multiplexer” block of the non-precoded pilots and the precoded data. The formers are BPSK-modulated Walsh-Hadamard sequences, precisely predefined and fixed for each beam. For the modulation of the payload data, we evaluate two alternatives, QPSK and 8PSK. In the linear precoding techniques, the payload data is multiplied by the precoding matrix after being modulated. The precoding matrix is calculated by the ”Linear Precoding” block, considering the linear precoding techniques mentioned before. However, as mentioned in previous sections, the SLP method directly calculates the precoded transmit signal on a symbol-by-symbol basis. For that reason, the ”M-PSK Modulator,” the mixers, and the ”Linear Precoding” blocks in 3.5a are replaced by a ”SLP” block that calculates the precoded symbols for each beam. These modifications are represented in Fig. 3.5b. In both simulation diagrams, the ”Channel Matrix” block introduces the interbeam interference and the independent additive noise at the receivers, as described by (3.1).

The block ”PLL” is essential in any practical implementation to acquire and track the phase of the received signal. However, it makes all the phases measured at the UTs relative to the phase of the intended beams. In this simulation, we compare the performance of the system for an ideal ”PLL” block which can obtain the absolute phase measurement against the actual ”PLL” block.

The block ”CSI Estimation” estimates the channel matrix as the correlation between the received signal and the expected non-precoded pilot for each beam. In this way, each UT can estimate the channels from each beam. These estimations are the input of the ”Linear

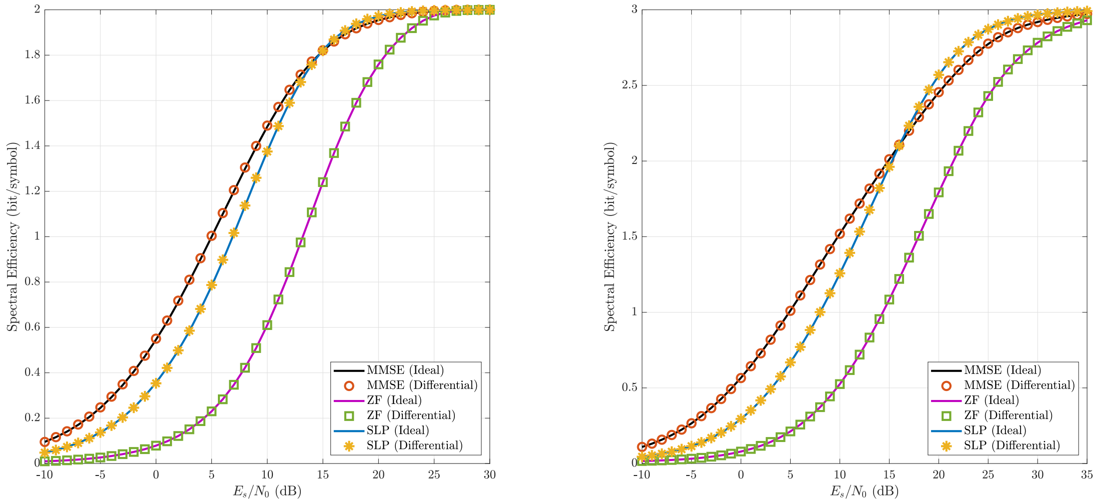

(a) QPSK signaling

(b) 8PSK signaling

Figure 3.6: Spectral efficiency comparison of different precoding techniques with ideal and differential phase estimation for $N = K = 8$.

Precoding" and the "SLP" blocks. Meanwhile, the precoded payload data is demodulated and used to calculate the different performance metrics. The simulation is run under a set of SNR $E_s/N_0 = \{-10, ..., 30\}$ dB and the results are the average of all the UTs' performance for each instance of E_s/N_0. The SNR is defined as the ratio of the average power received over the receiver additive white Gaussian noise (AWGN).

Fig. 3.6 shows a comparison using the spectral efficiency as a metric to evaluate the performance of an ideal system, where the PLL can obtain absolute phase measurements at the UT against the realistic system, with relative phase measurements. As it can be appreciated in the figure, there is no difference between both results for QPSK or 8PSK signaling with any of the precoding techniques evaluated. The equivalent results for SER and SNIR metrics are shown in Fig. 3.7 and Fig. 3.8, respectively. For these metrics, there is also no difference between the ideal and the actual system for any evaluated modulation or precoding techniques.

In addition, we designed another set of experiments to verify that the system performance is affected by the hardware impairments at the transponder. Similar to the previous simulations, we used the spectral efficiency, the SER, and the receive SNIR as performance metrics under the simulation setup previously described. The simulation diagram is represented in Fig. 3.9, which is very similar to the previous setup except for the removed "PLL" block, the

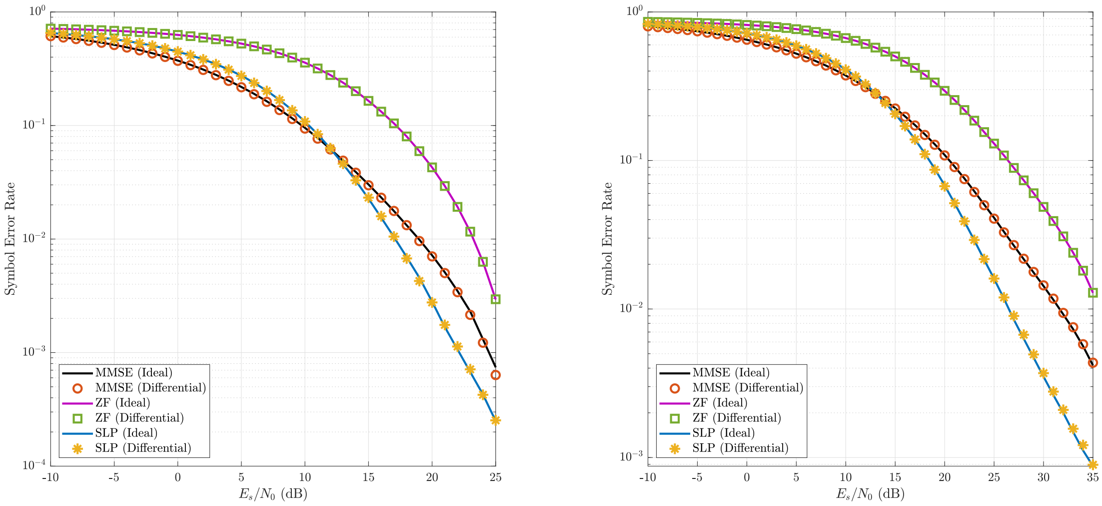

(a) QPSK signaling

(b) 8PSK signaling

Figure 3.7: Average SER performance of different precoding techniques per UT with ideal and differential phase estimation for $N = K = 8$.

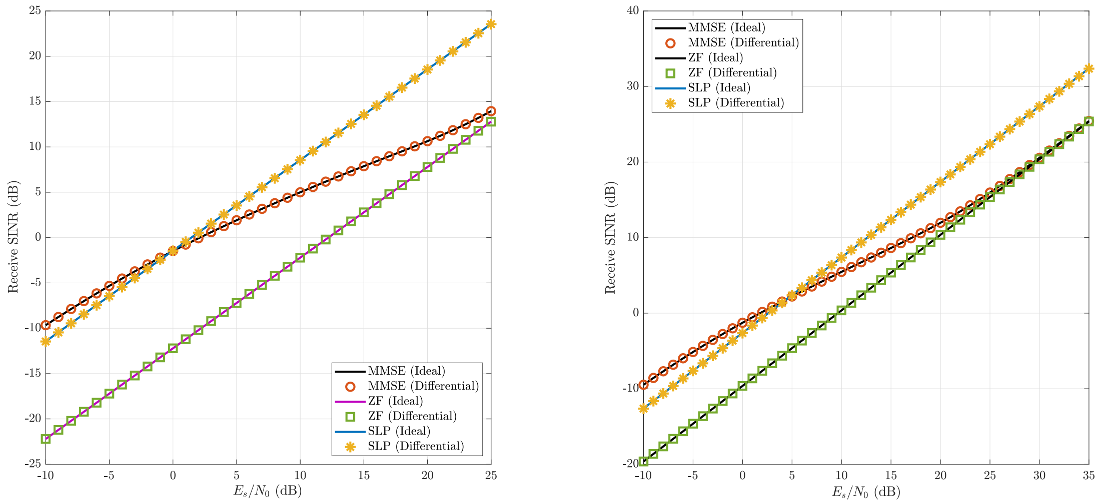

(a) QPSK signaling

(b) 8PSK signaling

Figure 3.8: Average receive SNIR of different precoding techniques per UT with ideal and differential phase estimation for $N = K = 8$.

"Frequency Reference" and eight "LOs" blocks that were added at the transponder. Considering the results of the previous simulations and for the sake of simplicity, we used ideal "PLLs" for this experiment, which are not represented in Fig. 3.9. On the other hand, we included the "Frequency Reference" and the "LOs" blocks to emulate the phase noise of the transponder's LO. In this experiment, we consider the best possible configuration in synchronization terms, using a single frequency reference to transmit all the beams. Another modification of this simulation setup with respect to the previous one is the channel model considered for this experiment, which is the flat fading model typically used in GEO satellite systems.

We considered an ideal LO at the gateway and three different options for the frequency reference at the transponder: a very stable crystal oscillator with Allan variance $\sigma_y^2(0.5) = 0.232$, a medium-class ($\sigma_y^2(0.5) = 2.321$), and an economic crystal oscillator ($\sigma_y^2(0.5) = 23.208$), all with nominal frequency $f_0 = 10$ MHz. The value $\tau = 0.5$ in the Allan variance is related to the loop delay (0.5 s), which considers the feedback link from the UTs to the gateway through the GEO satellite. Fig. 3.9 represents the simulation diagram for linear precoding methods, the equivalent diagram for SLP is not included for the sake of space. However, both experiments (Fig. 3.5 and Fig. 3.9) analyzed the same precoding techniques: ZF, MMSE, and SLP.

The phase noise was generated using the two-state model described in [22]. We considered eight uplink-forward carrier frequencies between $f_{U_1} = 47.5$ GHz and $f_{U_8} = 48.9$ GHz with 200 MHz bandwidth each. The downlink-forward carrier frequency, common to all the beams using precoding, was 20 GHz. The PSD of the phase noise obtained for these parameters is represented in Fig. 3.10. As it can be appreciated in the figure, the difference between the PSD of each beam for the same frequency reference is small. However, even this small difference can affect the precoding performance, as we can see in figures Fig. 3.11 to Fig. 3.13.

Fig. 3.11 to Fig. 3.13 show the results of the simulations to evaluate the effects of the phase noise at the transponder LOs for the different metrics: Fig. 3.11 shows the receiver SNIR, Fig. 3.12 the SER and Fig. 3.13 the spectrum efficiency. In these figures, the ideal curves represent the case with a perfect frequency reference without phase noise (PN) at the transponder, which means that the "Frequency Reference" and the "LOs" blocks do not add any phase rotation to the signal. The (No FDM) curves represent the case of a realistic

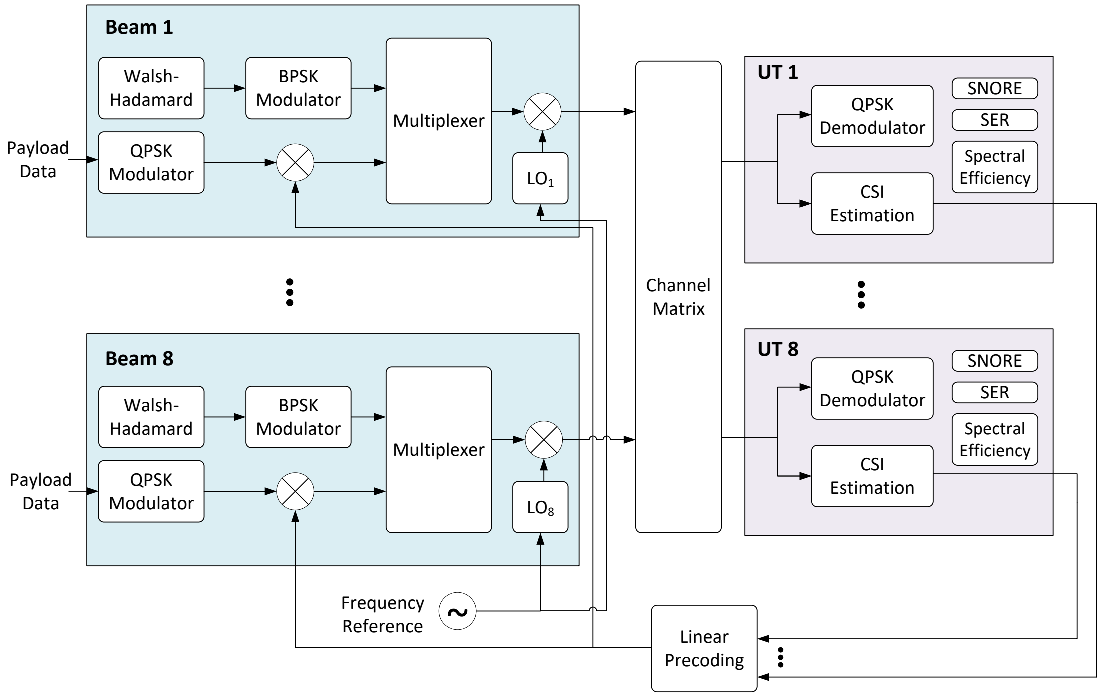

Figure 3.9: Simulation diagram for the experiment to verify that the system performance is affected by the phase noise at the transponder LOs.

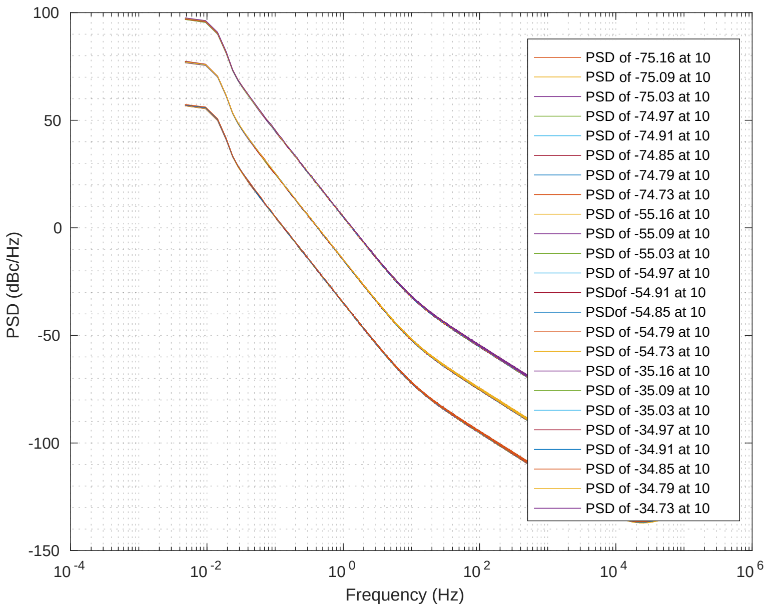

Figure 3.10: PSD of the phase noise at each of the eight beams for the three frequency references considered in the simulations: high quality ($\sigma_y^2(0.5) = 0.232$), medium-class ($\sigma_y^2(0.5) = 2.321$) and economic crystal oscillator ($\sigma_y^2(0.5) = 23.208$).

frequency reference with PN and ideal uplink transmission without FDM. This implies that a phase variation from the "Frequency Reference" is added to the signal, but in this case, it is constant for all the beams, *i.e.*, the "LOs" blocks have the same value for all the beams. The solid curves represent the realistic case, where the frequency reference has PN, and the uplink transmission uses different carrier frequencies for each beam's datastream, in other words, FDM. In this case, the phase noise added to each beam is generated by the "LOs" blocks considering the "Frequency Reference" phase noise PSD represented in Fig. 3.10.

As it can be appreciated in Fig. 3.11, for the same frequency reference, the receiver SNIR is more affected in SLP, Fig. 3.11c than in linear precoding systems, Fig. 3.11a and 3.11b. For instance, for linear precoding techniques with $E_s/N_0 = 0$ dB, the receivers SNIR degradation concerning the expected value without considering the hardware impairments is less than 1 dB for medium-class frequency references: 1.55 dB for MMSE and 0.26 dB for ZF while the equivalent value for SLP is 2.93 dB. However, according to the receivers SNIR metric, the performance of the system is barely affected when high-quality frequency references ($\sigma_y^2(0.5) = 0.232$) are used; see the blue curves in Fig. 3.11. Besides, the performance degradation is stronger for high SNR values. It can be up to 8.66 dB for ZF, 9.42 dB (MMSE), and 8.63 dB (SLP) at $E_s/N_0 = 25$ dB, where the inter-beam interference is stronger.

On the other hand, for the SER comparison, the transponder phase noise's effects are more evident in SLP than in linear precoding methods. Specifically for $E_s/N_0 \geq 5$ dB, the SER of the system using SLP degrades significantly. This can be corroborated in Fig. 3.12c, where the blue curve moves away from the ideal one and stays constant for $E_s/N_0 \geq 15$ dB. However, even with performance degradation related to the hardware implementation's phase uncertainties, the SER of SLP outperform the SER of linear precoding systems for SNR values under 20 dB ($E_s/N_0 \leq 20$ dB). Besides, as it can be appreciated in the figures, the SER deteriorates considerably for the medium and economic frequency references independently of the precoding technique considered.

Similar to the previous comparisons, the spectral efficiency analysis (Fig. 3.13) shows that linear precoding systems are more resilient to the hardware implementation's phase uncertainties than SLP. In this case, the spectral efficiency of the system using a medium-class frequency reference ($\sigma_y^2(0.5) = 2.321$) is strongly degraded for SLP, which can be corroborated by analyzing the separation between the ideal (dashed black) and the realistic (solid yellow) curves in Fig. 3.13c. However, for high-quality frequency references ($\sigma_y^2(0.5) = 0.232$), the

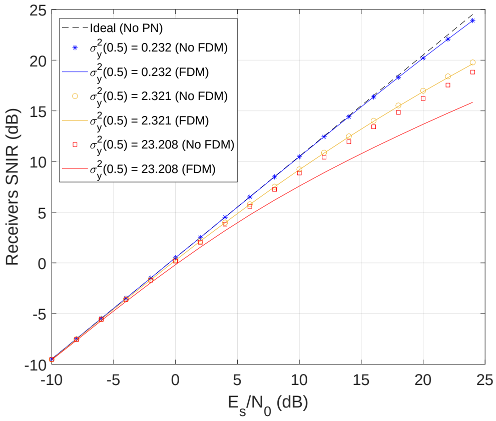

(a) ZF precoding

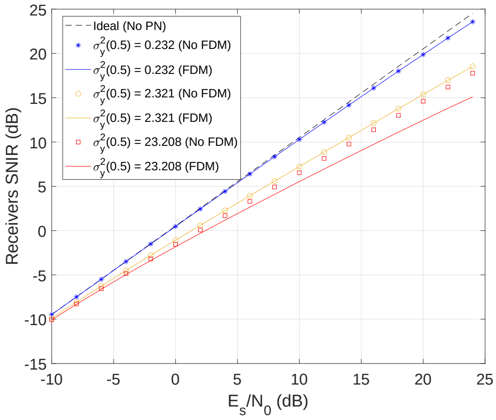

(b) MMSE precoding

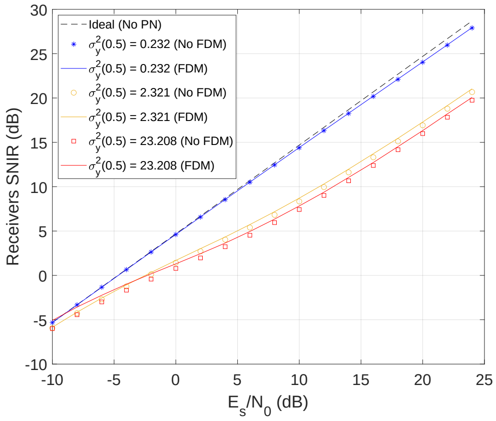

(c) SLP precoding

Figure 3.11: Comparison of the average SNIR at the UTs for $N = K = 8$, and QPSK signaling for three different frequency references: a very stable (Allan variance $\sigma_y^2(0.5) = 0.232$), a medium-class ($\sigma_y^2(0.5) = 2.321$) and an economic crystal oscillator ($\sigma_y^2(0.5) = 23.208$)

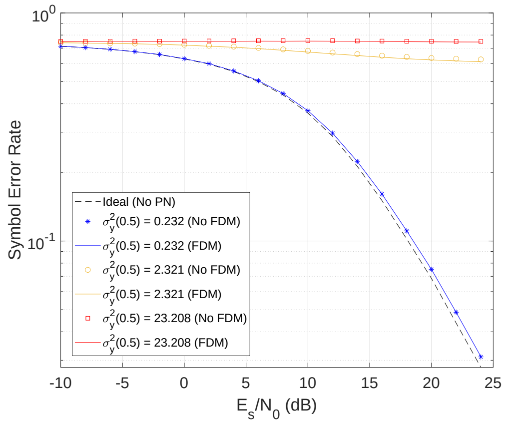

(a) ZF precoding

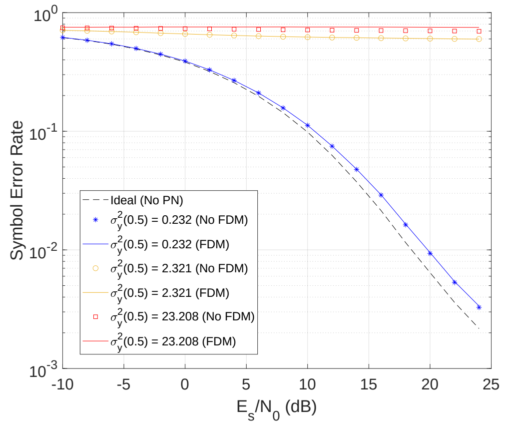

(b) MMSE precoding

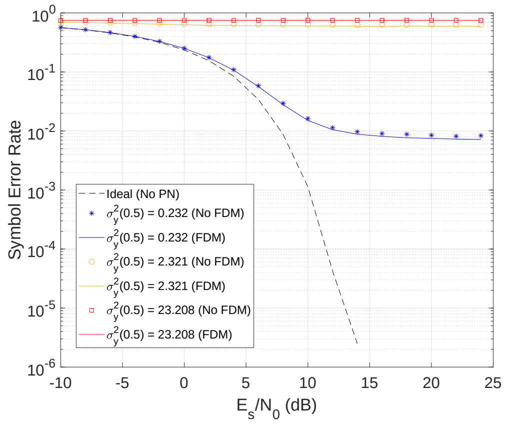

(c) SLP precoding

Figure 3.12: Average SER comparison for $N = K = 8$ and QPSK signaling for three different frequency references: a very stable (Allan variance $\sigma_y^2(0.5) = 0.232$), a medium-class ($\sigma_y^2(0.5) = 2.321$) and an economic crystal oscillator ($\sigma_y^2(0.5) = 23.208$)

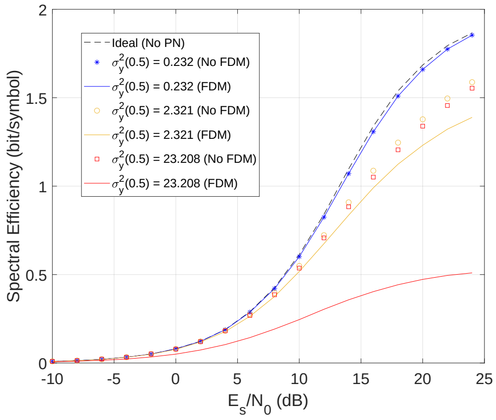

(a) ZF precoding

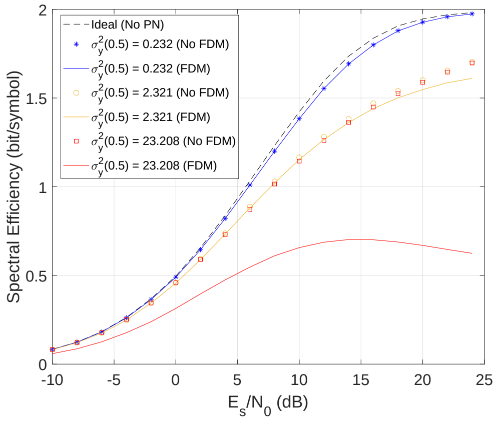

(b) MMSE precoding

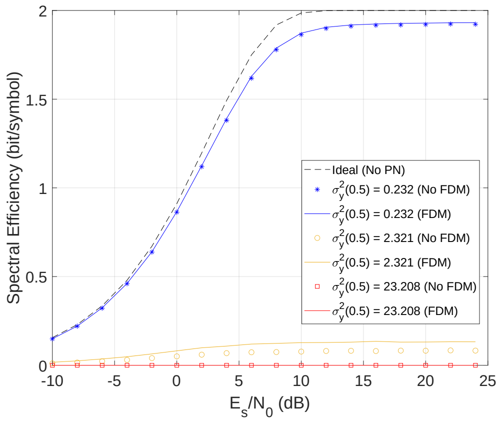

(c) SLP precoding

Figure 3.13: Spectral efficiency comparison for $N = K = 8$ and QPSK signaling for three different frequency references: a very stable (Allan variance $\sigma_y^2(0.5) = 0.232$), a medium-class ($\sigma_y^2(0.5) = 2.321$) and an economic crystal oscillator ($\sigma_y^2(0.5) = 23.208$)

spectral efficiency of SLP systems is much better than linear precoding ones.

Analyzing the simulation results considered during this section, we can arrive at some conclusions:

- In general, SLP outperforms ZF and MMSE for high E_s/N_0 scenarios.
- For low values of E_s/N_0, the performance of SLP and MMSE is very similar and superior to ZF performance.
- The E_s/N_0 threshold value where SLP outperforms MMSE increases with the modulation order.
- The expected system performance for precoding-enabled satellite communication systems considerably degrades when the phase noise of the transponder's LO is included in the analysis. Even for the optimal synchronization configuration and the typical frequency reference ($\sigma_y^2(0.5) = 2.321$).
- Although linear precoding techniques are more resilient to the hardware impairments inherent to satellite communication systems than SLP, the system's performance using high-quality frequency reference is better for SLP than linear precoding techniques.

3.7 Conclusions of the Chapter

Linear and symbol-level precoding in satellite communications have received increasing research attention thanks to its capacity to solve the problem of inter-beam interference by applying a full frequency reuse approach. However, there are still challenges and open questions for the practical implementation of precoding systems. Some examples of this are the inability to measure the absolute phase offset induced by the propagation channel and the phase uncertainties related to using FDM in the forward uplink.

This chapter has addressed the impact of these phase variations and uncertainties in operating a precoded forward link satellite communication system. It has formally demonstrated that the phase uncertainties created in the forward downlink do not affect the precoding performance for linear and non-linear precoding operations. This result was validated using three performance metrics: spectral efficiency, SER, and receivers SNIR, in a downlink MU-MISO system with eight beams and an equal number of UTs. The precoding schemes analyzed were MMSE, ZF, and DPCIR-based SLP.

Additionally, it was shown that the UTs could estimate the phase variations related to the transponder LOs as part of the CSI. The effect of this impairment is determined by the phase noise of the LOs' frequency reference at the transponder and the delay of the precoding loop. Our simulations used an 8x8 MU-MISO precoding system to compare the impact of three different frequency references for linear and non-linear precoding methods. The simulations assumed a GEO satellite transponder where all the LOs shared a single frequency reference, which is the optimal scenario from a synchronization point of view. If this assumption does not hold, for instance, if the LOs use different frequency references or in distributed satellite systems, the performance degradation shown in our simulations will be more substantial. In addition, the effects of the Doppler shift in the feeder link will affect each FDM carrier differently depending on its center frequency, increasing the performance degradation shown. Therefore, our simulation results provide an upper bound for the precoding performance in GEO satellite systems.

Analyzing the simulation results included in this work, we can conclude that, in general, SLP outperforms ZF and MMSE for high E_s/N_0 scenarios. On the other hand, for lower values of E_s/N_0, the slight difference between SLP and MMSE performance may not justify the high complexity of SLP implementation. According to our simulation results, the E_s/N_0 threshold value where SLP outperforms MMSE increases with the modulation order. However, we can see that SLP is more affected by the hardware impairments inherent to satellite communication systems. For instance, according to our simulation results, the performance of a system with a high-quality crystal oscillator ($\sigma_y^2(0.5) = 2.321$), and SLP differs considerably from the ideal scenario, without the phase uncertainties inherent to hardware implementations. However, it is better than the performance of the equivalent system using linear precoding techniques.

Finally, the authors would like to highlight that the main contribution of this work is the formal demonstration of the accurate performance of the precoding technique, which is not affected by the phase uncertainties in the forward downlink. Another significant result of this study is the conclusion that using a common frequency reference to process all the beams at the transponder does not avoid the phase uncertainties related to the FDM in the forward uplink. This fact has to be considered to set the expected performance of practical implementations of MU-MISO precoding systems where a differential phase compensation loop should be included to compensate for this performance degradation.

The phase compensation loop can be designed similarly to a distributed PLL, where the compensation is calculated using the inter-beam differential phase estimated at the user terminals as input. This solution, described in chapter 5, is based on the working principle of PLLs: To calculate a phase output such that the difference between output and input phases is minimum. In our case, one of the beams is considered the reference, and the PLL phase output or compensation is applied to the other beams to keep the differential phases between them and the reference beam constant.

Chapter 4

Two-state Phase Noise Model

4.1 Introduction of the Chapter

Many of the synchronization approaches analyzed in previous chapters consider ideal oscillators, but in practice, the output of an oscillator is not a single spectral line at the nominal frequency, but it has some sideband power that is translated into phase and frequency instabilities [268]. The phase misalignment between the distributed nodes affects the performance of DBF beyond the synchronization algorithm used. Using a common LO as a clock reference might seem like a solution to this problem, but it is not an alternative in distributed systems, such as DSS. In this context, the main challenge is coordinating the transmission of multiple geographically distant antennas that cannot use a common LO. The lack of a common oscillator also appears in single satellite systems due to technical constraints, such as independence between payloads, autonomy, robustness, cross-interference between RF channels, and redundancy, where the whole system should not rely on the same oscillator [16], [269].

Some authors have dealt with this problem during the precoding design and implementation. For example, in [270], Gharanjik *et al.* propose a robust design by considering the time-varying phase noise introduced by oscillators onboard the satellite. The robustness is imparted by modeling the phase uncertainty as a random process and ensuring that the outage probability is maintained at desired levels. While in [271], Taricco considers the phase instability of the local oscillators driving the antenna feeds at the satellite payload as one of the phase offset causes in the Precoding implementation. Both studies model the phase uncertainty as a Gaussian random process with zero mean and standard deviation σ, $2° < \sigma < 20°$.

Another relevant work explores the effects of non-ideal oscillators in a multi-antenna hybrid digital-analog beamforming transceiver architecture [272]. The authors modeled the phase noise as Wiener and Gaussian processes in three different architectures: common LO, independent LOs, and a block-based architecture. Through simulations, they concluded that the phase noise has more impact on the system performance when modeled as a Wiener process in an independent LOs architecture. In that case, for a phase noise standard deviation of 10°, there is an error of more than 7°at the beam pointing, and the sidelobe level increases in almost 2 dB with respect to the common LO architecture. Another example is [273], where the authors analyze the impact of the oscillator phase noise on the performance of Massive MIMO-OFDM systems considering the phase noise as a Wiener process.

However, in practice, oscillator noise is affected by additional phenomena not included in the aforementioned models. Many authors have studied this topic, searching for advanced models to characterize oscillator near-carrier PSD [274], [275]. Empirical models suggest that the phase noise PSD can be described as a sum of power-law processes $h_\alpha |f|^\alpha$ with $\alpha \in \{-4, -3, -2, -1, 0\}$ [268]. According to this idea, the random walk frequency noise, $h_{-4}|f|^{-4}$, continues increasing infinitely while frequency approaches the oscillator's nominal value. However, more recent researches consider an additional Gaussian session segment [274], which is more similar to the real characteristic. This model, represented in Fig. 4.1, includes the frequency drifts of a practical system, which is similar to a frequency modulation or spreading of the main carrier.

This chapter describes the hardware implementation of the model for the oscillator phase noise and obtains the resulting SNIR at the UTs. The phase noise is modeled according to the two-state model proposed by Galleani in [22]. The model implementation is validated in a hardware testbed emulating a 2 × 2 precoding-enabled system.

4.2 Oscillator phase noise model

The output voltage $u_0(t)$ of a generic oscillator with nominal frequency f_0 is

$$u_0(t) = [A + a(t)] \cos[2\pi f_0 t + \phi(t)], \tag{4.1}$$

where A is the mean amplitude of the oscillator output, $a(t)$ is the zero-mean amplitude noise and $\phi(t)$ is an error term due to the LO phase noise. We consider that the effects of

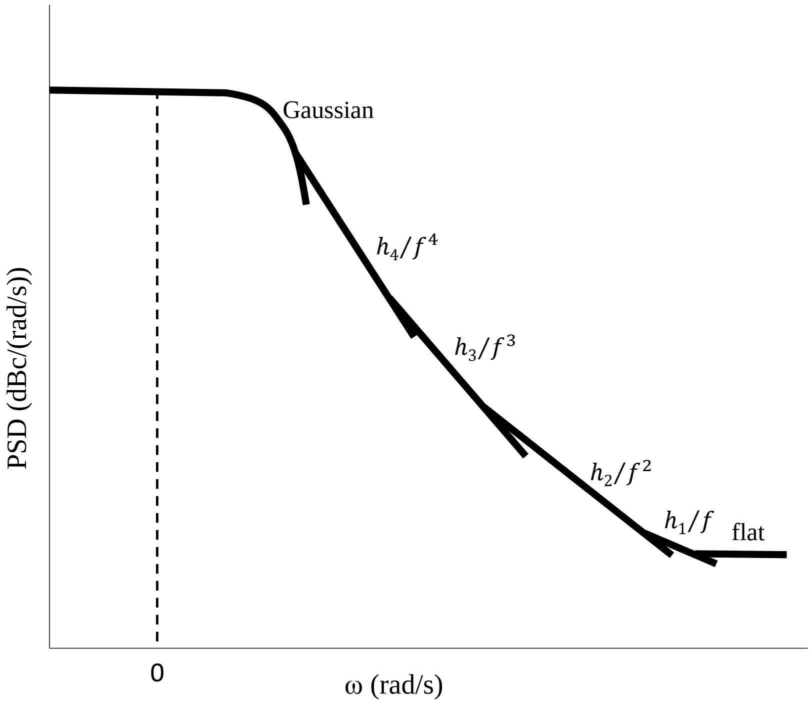

Figure 4.1: Oscillator PSD characteristic near the nominal frequency [274]

amplitude noise are overshadowed by the effects of phase noise, which is a common assumption in published work in this field [22, 275].

From (4.1), we can obtain two fundamental quantities used to characterize clocks: phase and frequency deviation. The frequency deviation $y(t)$, is defined as the time derivative of the phase deviation $x(t) = \frac{\phi(t)}{2\pi f_0}$:

$$y(t) = \frac{\mathrm{d}x(t)}{\mathrm{d}t}. \tag{4.2}$$

Numerous measurements have shown that the continuous phase noise PSD $S_\phi(f)$ tends to be well approximated by a sum of power-law processes

$$S_\phi(f) = \begin{cases} \sum_{\alpha=-4}^{0} h_\alpha f^\alpha & 0 < f < f_h \\ 0 & f \geq f_h, \end{cases} \tag{4.3}$$

where f_h is the high-frequency cut-off of an infinitely sharp low-pass filter [274]. These $h_\alpha f^\alpha$ terms are related to random walk frequency modulated (FM), flicker FM, white FM, flicker and white phase noise respectively [276].

4.2.1 Two-state Phase Noise Model

As described in [277], the output phase noise combines contributions from the reference oscillator and a PLL synthesizer. At offset frequencies above 10 kHz, the noise power is dominated by the PLL synthesizer's voltage-controlled oscillator (VCO) phase noise as well as spurs due to digital-to-analog converter (DAC) quantization noise and non-linearities. For synchronization purposes, we are concerned with oscillator drift at time scales larger or equal to 100 μs, which is determined by noise power at offset frequencies below 10 kHz. At this frequency range, performance is dominated by the reference oscillator and shows two regions: white FM phase noise ($\alpha = 2$) and random walk FM phase noise ($\alpha = 4$) [275]. This is known as the two-state clock noise model. Experimental evidence confirms that the frequency deviation of a cesium clock is made by these two noises, namely, white noise and Wiener process [275]. The last one is responsible for the random walk nature of the frequency deviation, while the white noise accounts for the local oscillations. Therefore, the frequency deviation can be written as

$$y(t) = \xi_1(t) + x_2(t), \tag{4.4}$$

where $\xi_1(t)$ denotes a zero-mean Gaussian random process, $\xi_1(t) \backsim \mathcal{N}(0, q_1)$, and $x_2(t)$ is a Wiener process.

The Wiener process, or Brownian motion, is the prototype of random walks. It is characterized because the increments between two consecutive samples are normally distributed independent processes, $\Delta w \backsim \mathcal{N}(0, t)$. In continuous time:

$$x_2(t) = \int_0^t \xi_2(\dot{t})\mathrm{d}\dot{t}, \tag{4.5}$$

where $\xi_2(t) \backsim \mathcal{N}(0, q_2)$.

To obtain the two-state model of the phase noise, we substitute (4.2) and (4.5) in (4.4):

$$\frac{\mathrm{d}x(t)}{\mathrm{d}t} = \xi_1(t) + \int_0^t \xi_2(\dot{t})\mathrm{d}\dot{t}. \tag{4.6}$$

Taking the derivative for both sides, we obtain:

$$x(t) = x_1(t) = \int_0^t \xi_1(\ddot{t}) + \int_0^{\ddot{t}} \xi_2(\dot{t})\mathrm{d}\dot{t}\mathrm{d}\ddot{t}. \tag{4.7}$$

Equation (4.7), shown in graphical form in Fig. 4.2, describes the two-state clock noise model [275].

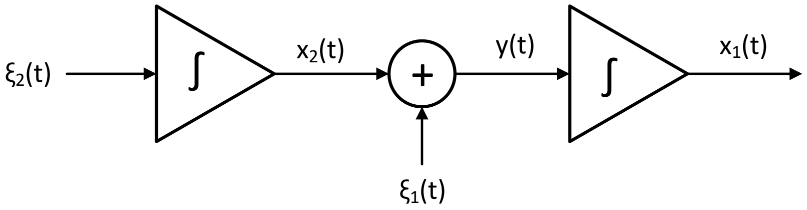

Figure 4.2: Two-state clock model [275]

Discrete-Time Implementation

To implement the system in Fig 4.2, it is useful to express (4.6) in the state-space form:

$$\begin{bmatrix} x_1'(t) \\ x_2'(t) \end{bmatrix} = \begin{bmatrix} 0 & 1 \\ 0 & 0 \end{bmatrix} \begin{bmatrix} x_1(t) \\ x_2(t) \end{bmatrix} + \begin{bmatrix} \xi_1(t) \\ \xi_2(t) \end{bmatrix}, \tag{4.8}$$

where the inputs ξ_1 and ξ_2 are two independent zero-mean Gaussian random processes with a correlation matrix $\mathbf{R}_{\boldsymbol{\xi}_1,\boldsymbol{\xi}_2}(\tau) = \begin{bmatrix} q_1 & 0 \\ 0 & q_2 \end{bmatrix}$; x_1 and x_2 are the states and x_1', x_2' refer to their derivatives [275]. A discrete-time equivalent expression for (4.8) was obtained in [22] and has the form:

$$\mathbf{x}[k] = \begin{bmatrix} 1 & T_s \\ 0 & 1 \end{bmatrix} \mathbf{x}[k-1] + \boldsymbol{\eta}[k-1], \tag{4.9}$$

with $\mathbf{x}[k] = \begin{bmatrix} x_1[k] \\ x_2[k] \end{bmatrix}$, $\boldsymbol{\eta}[k] = \begin{bmatrix} \eta_1[k] \\ \eta_2[k] \end{bmatrix}$ and T_s sampling period.

The covariance matrix of $\boldsymbol{\eta}[k]$ is given by

$$\mathbf{C}_{\mathbf{J1},\mathbf{J2}}[k] = \begin{bmatrix} q_1 T_s + q_2 \frac{T_s^3}{3} & q_2 \frac{T_s^2}{2} \\ q_2 \frac{T_s^2}{2} & q_2 T_s \end{bmatrix}. \tag{4.10}$$

According to [278], q_1 and q_2 are directly related to the Allan variance $\sigma_y^2(\tau)$ through

$$\sigma_y^2(\tau) = \frac{q_1}{\tau} + \frac{q_2 \tau}{3}. \tag{4.11}$$

This is a typical tool used to characterize the noise in oscillators and could be obtained from experimental measurements. Besides, the Allan variance is related to the noise PSD in (4.3) by [276]

$$\sigma_y^2(\tau) = h_{-4}\frac{2\pi^2}{3}\tau + h_{-3}2\ln 2 + h_{-2}\frac{1}{2\tau} + h_{-1}\frac{1.038 + 3\ln(2\pi f_h \tau)}{4\pi^2\tau^2} + h_0\frac{3f_h}{4\pi^2\tau^2}. \tag{4.12}$$

For the two-state model implemented in this chapter, we only consider the first and the third terms in (4.12). Then, equalling (4.11) and (4.12) we obtain

$$\begin{aligned} q_1 &= \frac{h_{-2}}{2} \\ q_2 &= 2\pi^2 h_{-4} \end{aligned} \tag{4.13}$$

Using these equivalences, the two-state model can be generated for any real or theoretical phase noise PSD. For instance, for $h_{-2} = 1.25 \cdot 10^{-4}$ and $h_{-4} = 0.49$ Fig. 4.3 shows the estimated PSD for the output of the Two-state model. As it can be appreciated, the PSD has both slopes: -40 dB/dec and -20 dB/dec, corresponding to f^{-4} and f^{-2} terms in (4.3) and it is -72.04 dBc/Hz at 10 Hz.

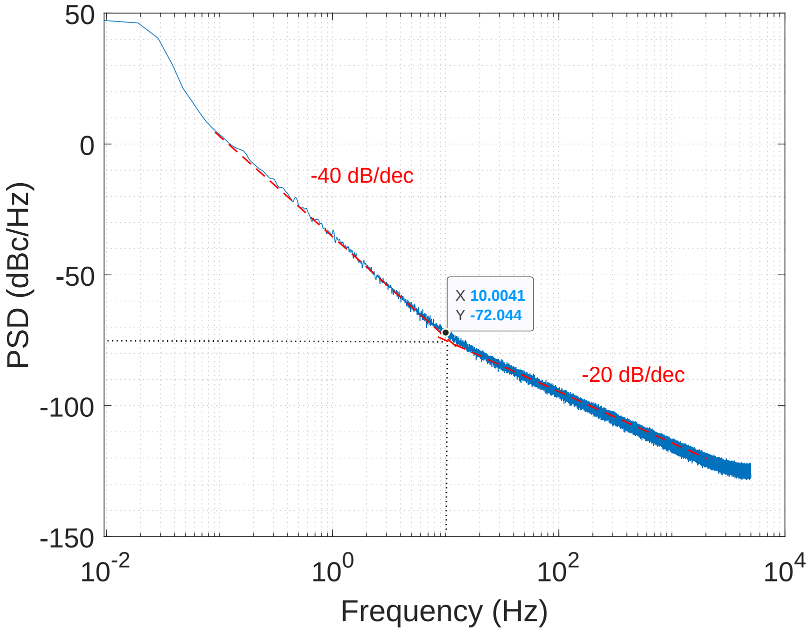

Figure 4.3: Estimated PSD of the phase noise samples generated with the Two-state model

Besides, Fig. 4.4 shows 20 realizations with a duration of one second. As the figure suggests, the two-state phase noise behavior is smoother than that of a simple Wiener process since it contains a Wiener process plus an integrated Wiener process. This is confirmed by Fig. 4.5, which represents the mean and variance of the realizations shown in Fig. 4.4. As it can be appreciated, the variance grows quadratically with time, while the variance of a Wiener process increases linearly. Specific details about the implementation of the Two-state model are analyzed below.

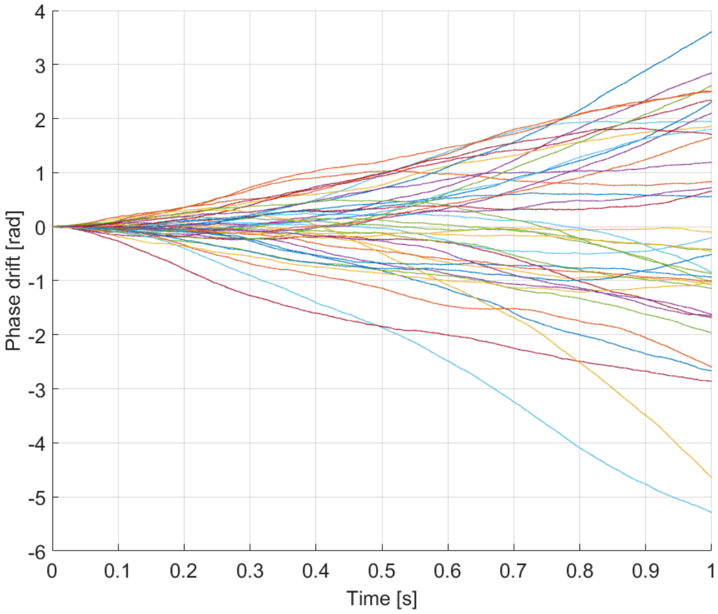

Figure 4.4: Two-state model's output. Some realizations of the phase noise random process

4.3 Hardware Implementation of the Oscillator Phase Noise Model

Figure 4.6 represents the block diagram of the two-state model hardware implementation. The model requires as input two independent zero-mean Gaussian random vectors with unitary variance, $p_1[k]$ and $p_2[k]$. Inputs σ_1 and σ_2 represent the standard deviation of $p_1[k]$ and $p_2[k]$ respectively.

The diagram in Fig. 4.6 was implemented as an intellectual property (IP) block using Vivado HLS. Figure 4.7 shows the hardware implementation of the Phase Noise Generator

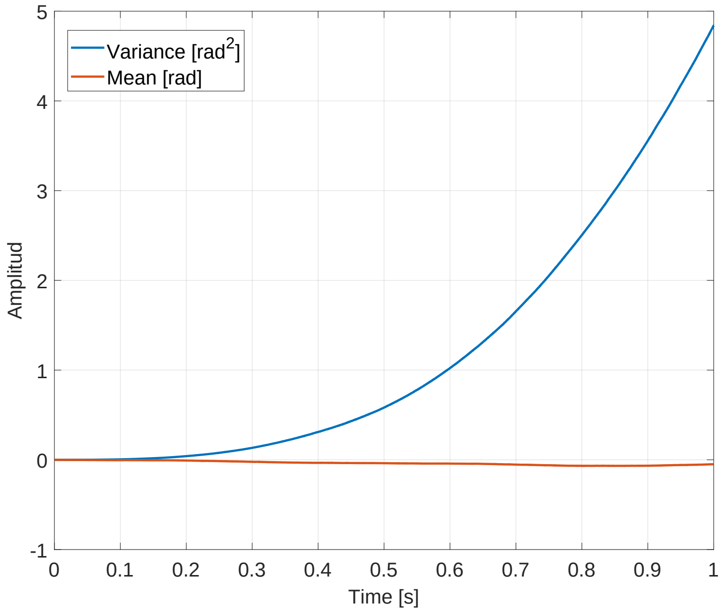

Figure 4.5: Mean and variance of the realizations represented in Fig. 4.4

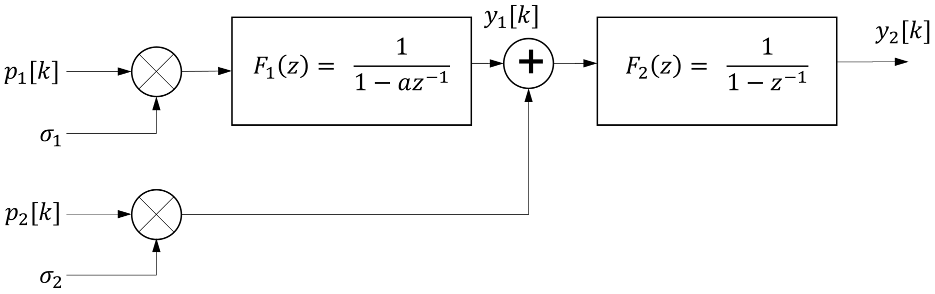

Figure 4.6: Block diagram of the two-state model implementation

block. In the figure, the two pseudo-random generators provide $p_1[k]$ and $p_2[k]$, and the values of sigma_1 (σ_1) and sigma_2 (σ_2) are defined at the user interface. The inputs sigma_1 and sigma_2 are obtained from the desired phase noise mask using algorithm 1.

The target phase noise mask, in logarithmic scale, can be described by the parameters: h_{-2} for the -20 dB/dec slope and h_{-4} for the -40 dB/dec slope:

$$S_\phi(f) = 10\log\left(\frac{h_{-4}}{f^4} + \frac{h_{-2}}{f^2}\right). \tag{4.14}$$

Additionally, the PSD obtained from the two-state model can be described by the coordinate pair $(f_\phi; A_\phi)$ where both regions ($\alpha = 4$ and $\alpha = 2$) intercept. Hereafter this point $(f_\phi; A_\phi)$ will be used to identify the phase noise masks. For instance, (10 Hz; -75 dBc/Hz)

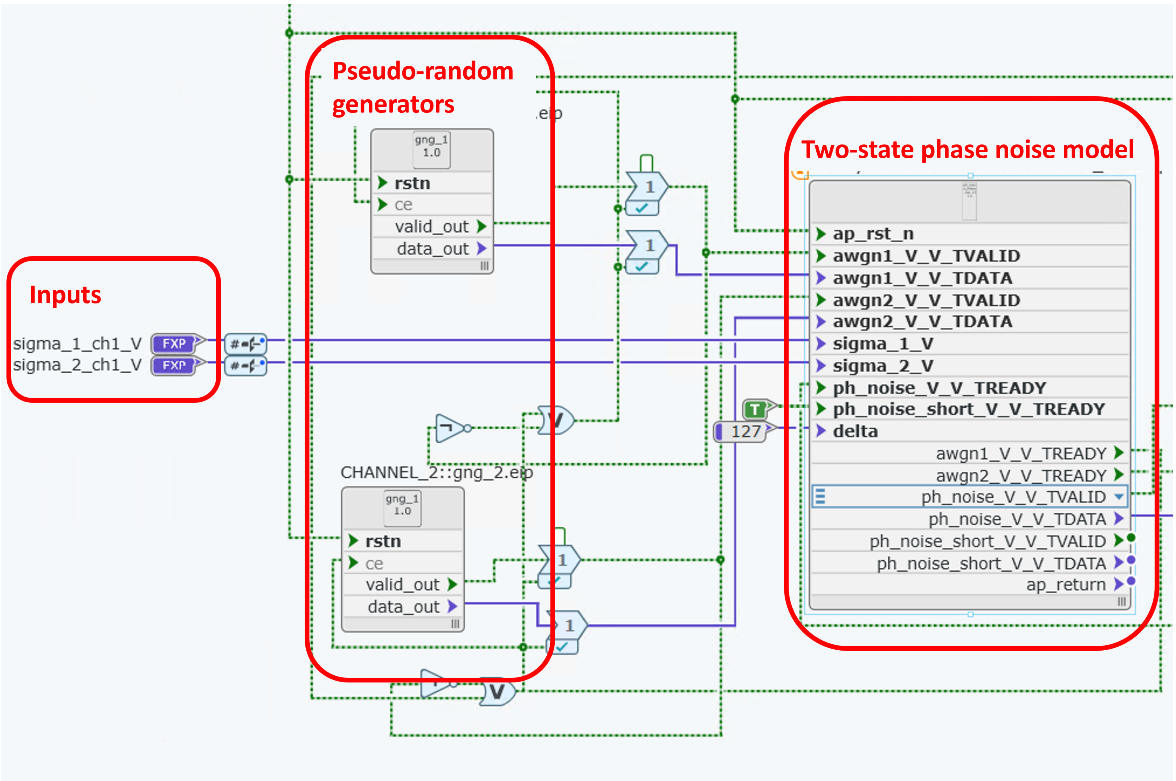

Figure 4.7: Hardware implementation of the two-state model

refers to the two-state PSD with a -40 dB/dec slope region for $f < 10$ Hz and -20 dB/dec slope region for $f > 10$ Hz; $S_\phi(10) = -75$ dBc/Hz as shown in Fig. 4.3.

The Phase Noise Generator block was integrated with the MIMO end-to-end satellite emulator presented in [279] as part of the channel emulator (ChEm). This allows including the phase noise for all the LOs in the system independently.

Algorithm 1 Calculate variance algorithm

```
procedure VAR_CALC($A_\phi, f_\phi, f_s$)
    $h_4 \leftarrow 10^{A_\phi/10} * (2\pi f_\phi)^4$
    $h_2 \leftarrow 10^{A_\phi/10} * (2\pi f_\phi)^2$
    $q_1 \leftarrow h_2/2$
    $q_2 \leftarrow 2\pi^2 h_4$
    $\sigma_1 \leftarrow q_1/f_s + q_2/(3f_s^3)$
    $\sigma_2 \leftarrow q_2/f_s$
    return $(\sigma_1, \sigma_2)$
end procedure
```

4.4 Validation of the Implementation

The implementation of the Phase Noise Generator block was tested using a hardware-in-the-loop (HIL) approach before its integration with the MIMO end-to-end satellite emulator. The HIL consists only of collecting in the host computer the phase (noise) samples produced by the generator block shown in 4.7. The results obtained with the received streams show the same shape as the ones generated with Matlab simulations. This is expected as these phase samples do not even include the effects of the numerically-controlled oscillator (NCO) multipliers and the actual RF hardware.

To further validate the output of the Phase Noise Generator block, we configured the in-lab demonstrator to emulate a 2×1 system. We set the oscillator phase noise in one of the transmitters and left the second one as ideal (no phase noise). At the receiver, the CSI is estimated for each transmitter. The phase difference between both CSI estimations is equivalent to the differential phase noise introduced at the transmitters. Then, we recorded in Labview the CSI and with those samples, we calculated the phase noise PSD in Matlab. The output of the Phase Noise Generator block was considered correct if the phase noise PSD calculated from the UT's CSI matched the phase noise mask described by the parameters set at the ChEm.

The sample rate at the ChEm was 32 Msps. The channel matrix was set with constant values

$$\mathbf{H} = \begin{bmatrix} 0.5 + 0i & 0.1 + 0i \\ 0.1 + 0i & 0.5 + 0i \end{bmatrix}.$$

At the UT, the sample rate was 12.4 Msps, with an oversampling factor of 4. The additive Gaussian noise was set to -∞ dB to avoid estimation errors at the receiver.

The CSI estimated at each receiver was recorded in Labview as a *.dat file using the setup in Fig. 4.8. The data was imported in Matlab and the phase noise PSD was calculated using the algorithm 2.

Table 4.1 and Fig. 4.9 to Fig. 4.13 show some examples of the input parameters and the block output. For the parameters of the phase noise mask, DVB-S2X 1, the first integrator of the Phase Noise Generator, saturates, and it is impossible to obtain the -40 dB/dec slope at the output. Figure 4.12 represents the -40 dB/dec slope for different input parameters from strd_dev_1 $= 4.9508 \cdot 10^{-9}$ to strd_dev_1 $= 4.9508 \cdot 10^{-7}$, keeping strd_dev_2 $= 0$, to show the

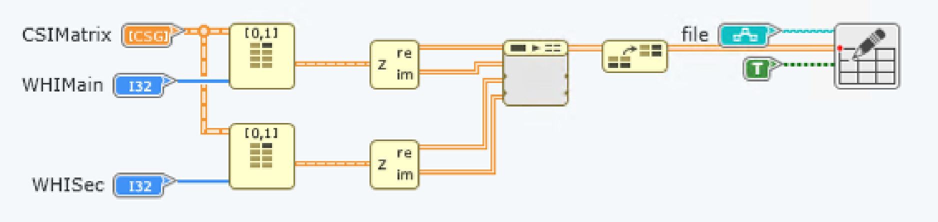

Figure 4.8: Labview setup to record CSI estimations in a *.dat file.

Algorithm 2 Calculate PSD algorithm

```
procedure PSD_CALC($\phi, f_s, W, N$)
    $\phi \leftarrow \phi[1 : W * N]$
    $\mathbf{f} \leftarrow \text{linspace}(0, f_s/2, W/2)$
    $win \leftarrow \text{chebwin}(W, 200)$
    $\mathbf{\Phi} \leftarrow \text{reshape}(\phi, [W, N])$
    $\mathbf{\Phi}_w = (\mathbf{\Phi} - \text{mean}(\mathbf{\Phi})). * win/\sqrt{\text{mean}(win.^2)}$
    $S \leftarrow \text{abs}(\text{fft}(\mathbf{\Phi}_w)/\sqrt{W}).^2$
    $S_{av} \leftarrow \text{mean}(S, 2)$
    $S_{av} \leftarrow S_{av}[1 : W/2]$
    $S_{dB} = 10 * \log(S_{av}/f_s)$
    return $S_{dB}$
end procedure
```

saturation of the first integrator for values of strd_dev_1 $\geq 4.9508 \cdot 10^{-8}$.

Table 4.1: Phase noise mask examples

Name	Description	Input parameters	Comments
Example 1. Figure 4.10	(10 Hz; -75 dBc/Hz)	$\sigma_1 = 4.889 \cdot 10^{-13}$ $\sigma_2 = 1.930 \cdot 10^{-7}$	-20 dB slope not well defined due to the noise floor (-78 dBc/Hz)
DVB-S2X 1. Figure 4.11	(100 Hz; -25 dBc/Hz)	$\sigma_1 = 4.950 \cdot 10^{-8}$ $\sigma_2 = 1.930 \cdot 10^{-3}$	Tables 7 and 8 of [280]
DVB-S2X 2. Figure 4.13	(10 Hz; -5 dBc/Hz)	$\sigma_1 = 4.950 \cdot 10^{-9}$ $\sigma_2 = 1.930 \cdot 10^{-3}$	This plot touches (100 Hz; -25 dBc/Hz)
Noise floor. Figure 4.9	Used as reference.	$\sigma_1 = 0$ $\sigma_2 = 0$	N/A

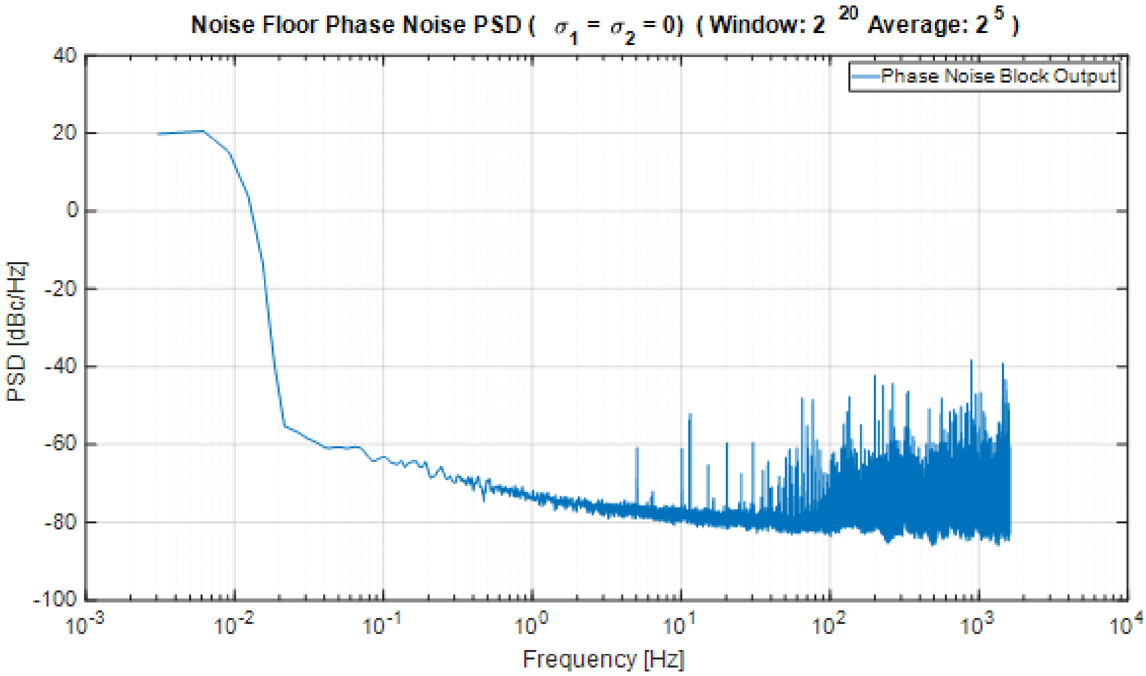

Figure 4.9: Noise Floor PSD

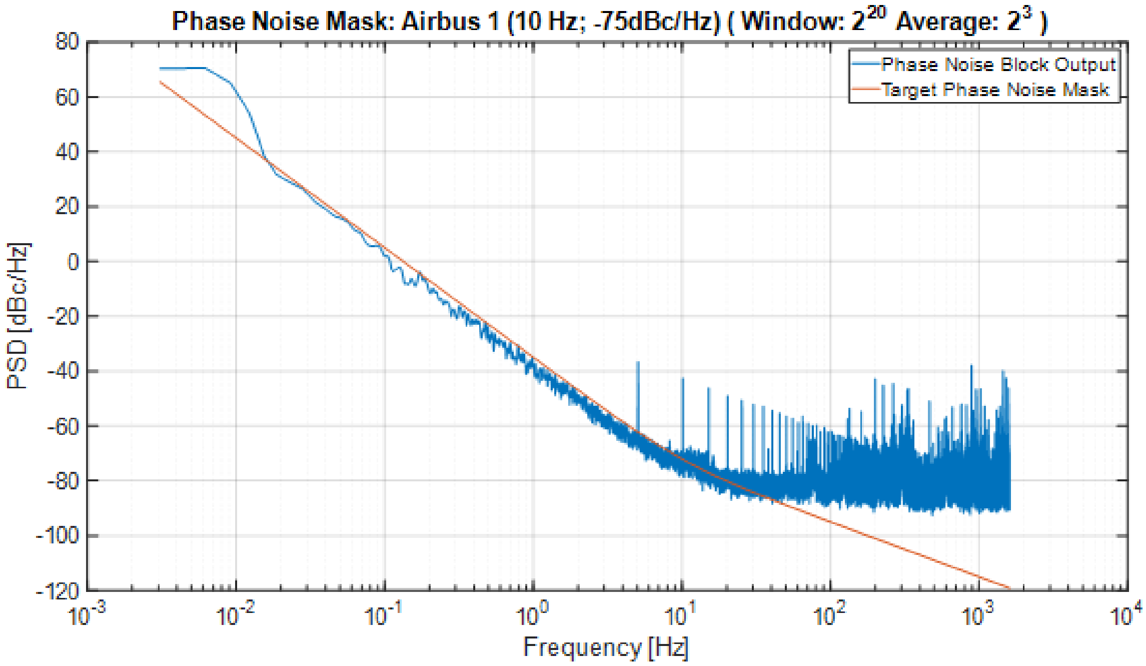

Figure 4.10: Example 1 phase noise mask (10 Hz ; -75 dBc/Hz) PSD

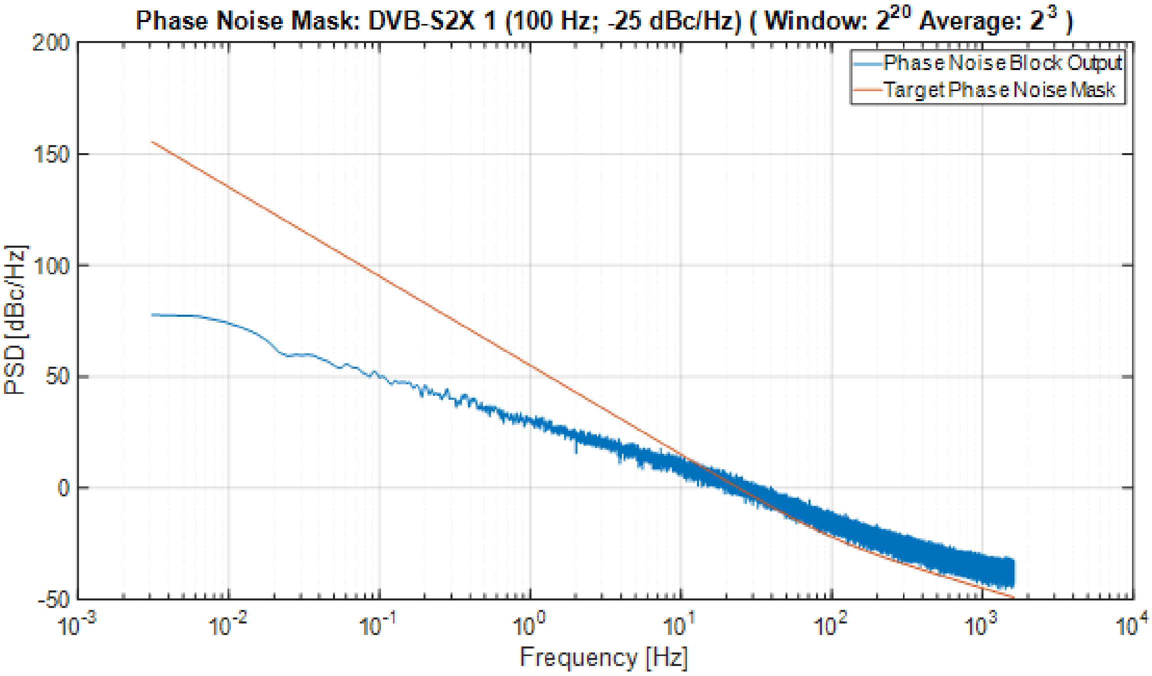

Figure 4.11: DVB-S2X 1 phase noise mask PSD

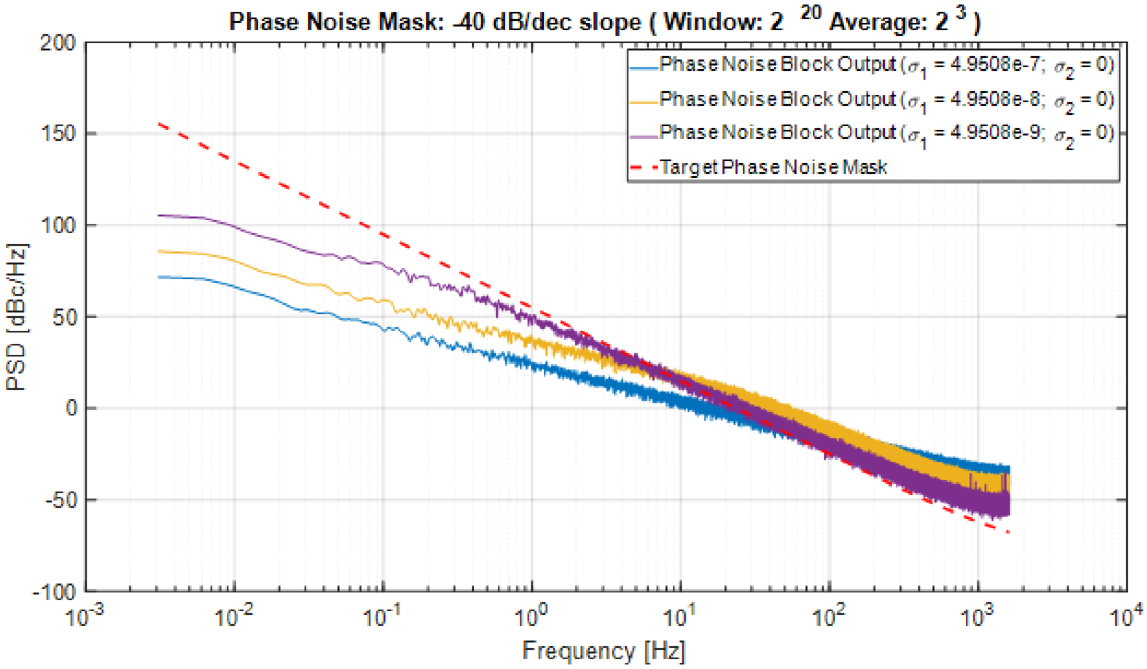

Figure 4.12: Analysis of the first integrator saturation

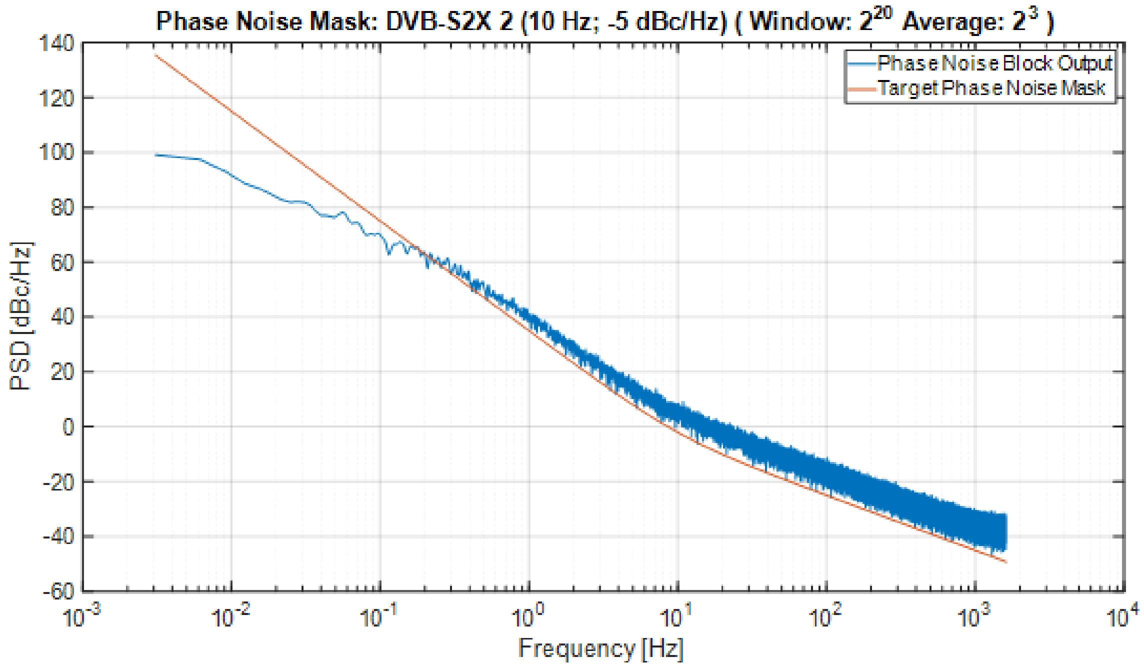

Figure 4.13: DVB-S2X 2 phase noise mask PSD

4.5 Conclusions of the Chapter

The implementation of the two-state model was described in this chapter. It improves the emulation of MIMO channels by including hardware impairments. This will be used to model the phase noise at the LOs to validate the results in chapter 3. Besides, the Phase Generator block is part of the MIMO end-to-end satellite emulator in chapter 5. Additionally, both the Matlab model and the hardware block are used in other projects that are not included in this document.

Chapter 5

Accurate Phase Synchronization for Precoding-enabled GEO Multibeam Satellite Systems

5.1 Introduction of the Chapter

Practical implementations of the precoding technique must deal with the phase noise introduced by different system components, such as the LOs used for up and down conversion at each system element (GW, satellite, and UTs). The UT perceives the differential phase error as part of the CSI, which the precoding matrix will compensate for. However, the variation rate of this differential phase error is faster than CSI estimation loop frequency, which implies that the compensation applied by the precoding matrix is not enough, thus degrading the system performance [281]. To solve this problem, we propose a phase compensation loop with a faster response than the typical precoding loop. Our design estimates and compensates for the phase error between beams in a sample-based mode. Meanwhile, the precoding matrix is calculated and applied by groups of symbols or frames following a conventional precoding implementation. Additionally, we compare several methods for combining the estimations of the differential phase between beams.

In brief, this chapter presents the phase synchronization method required to enable the precoding implementations in the GEO scenario. The proposed solution requires only small modifications to the already deployed satellite system. The only modification with respect to traditional precoding design is including a controller at the GW.

The rest of this chapter is organized as follows: section 5.2 describes the system model. Meanwhile, section 5.3 details the design of the proposed phase synchronization method. The hardware implementation is described in section 5.4. Section 5.5 contains the validation of the proposed solution using the MIMO end-to-end satellite emulator, and section 5.6 concludes the chapter.

5.2 System Model

We consider a GEO satellite generating N beams towards $K \leq N$ single-antenna UTs. We collect in $\boldsymbol{h}_k \in \mathbb{C}^{N\times 1}$ the complex (i.e., magnitude and phase) coefficients of the frequency-flat slow fading channels between the beams generated at the GW and the k-th UT. At a given symbol period, independent data symbols $\{s_k : 1 \leq k \leq K\}$ are to be transmitted to the UTs, where s_k denotes the symbol intended for the k-th user. Under the above assumptions, the received vector containing the symbol-sampled complex baseband signals of all K UTs can be modeled as

$$\boldsymbol{r} = \boldsymbol{H}\boldsymbol{W}\boldsymbol{s} + \boldsymbol{z}, \tag{5.1}$$

where $\boldsymbol{H} = [\boldsymbol{h}_1 \cdots \boldsymbol{h}_K]^T$ denotes the $K\times N$ complex-valued channel matrix, $\boldsymbol{W}$ stands for the $N \times K$ precoding matrix, $\boldsymbol{s} = [s_1 \cdots s_K]^T$ is a $K \times 1$ complex-valued vector containing the UTs' intended modulated symbols, and $\boldsymbol{z}$ collects independent additive noise components at the UTs' receivers, which are circularly symmetric complex Gaussian random variables with zero mean and variance $\sigma^2 = k_\mathrm{B} T_e B$, where k_B is the Boltzmann's constant, T_e is the equivalent noise temperature at the input of the receiver [282], and B is the UT bandwidth.

The actual channel matrix can be written as

$$\boldsymbol{H} = \begin{bmatrix} |h_{11}|\mathrm{e}^{j\psi_{11}} & \cdots & |h_{1N}|\mathrm{e}^{j\psi_{1N}} \\ |h_{21}|\mathrm{e}^{j\psi_{21}} & \cdots & |h_{2N}|\mathrm{e}^{j\psi_{2N}} \\ \vdots & \ddots & \vdots \\ |h_{K1}|\mathrm{e}^{j\psi_{K1}} & \cdots & |h_{KN}|\mathrm{e}^{j\psi_{KN}} \end{bmatrix}, \tag{5.2}$$

where $h_{i,j} = |h_{i,j}|\mathrm{e}^{j\psi_{i,j}}$ denotes the channel coefficient between the k-th UT and the j-th generated beam in the transmit antenna, for any $i \in \{1, 2, ..., K\}$ and $j \in \{1, 2, ..., N\}$, and $|h_{i,j}|$ and $\psi_{i,j}$ respectively represent its magnitude and phase.

However, we have to include a time-varying matrix $\boldsymbol{\Phi}(t)$ to represent the estimated channel matrix available at the GW after collecting the measurements from all the K UTs. $\mathbf{\Phi}(t) \triangleq \text{diag}(e^{j\epsilon_1(t)}, e^{j\epsilon_2(t)}, ..., e^{j\epsilon_K(t)})$ accounts for the phase drift due to the hardware impairments described in [281]. The complete channel matrix can then be written as

$$\hat{\boldsymbol{H}}(t) = \boldsymbol{H}\mathbf{\Phi}(t). \tag{5.3}$$

The detailed description of the model used to emulate $\mathbf{\Phi}(t)$ was provided in chapter 4.

5.3 Differential Phase Compensation Loop

The proposed closed-loop phase synchronization method is depicted in Fig. 5.1, where only phase and frequency variables are represented. In the figure, $\boldsymbol{\phi}(k) = \begin{bmatrix} \phi_1(k) & \phi_2(k) & ... & \phi_N(k) \end{bmatrix}^{\mathrm{T}}$ is an $N \times 1$ vector containing the phase drift of each beam. We define k as the discrete-time variable such that $t(k) = kT_s$ with sampling time T_s. The objective of our design is to pre-compensate the superframe data streams to minimize the value of $\boldsymbol{\phi_e}(k) = \boldsymbol{\phi}(k) - \boldsymbol{\phi_c}(k)$ towards zero. From now on, we will refer to $\boldsymbol{\phi_e}(k)$ as the phase error. The variable $\boldsymbol{\phi_c}(k) = \begin{bmatrix} \phi_1^c(k) & \phi_2^c(k) & ... & \phi_N^c(k) \end{bmatrix}^{\mathrm{T}}$ is an $N \times 1$ vector representing the phase of the transmitted beams after compensation. The input $\mathbf{\Psi}$ represents the phase rotation introduced by the channel matrix $\boldsymbol{H}$.

The vector $\boldsymbol{\theta}(k) = \begin{bmatrix} \theta_1(k) & \theta_2(k) & ... & \theta_K(k) \end{bmatrix}^{\mathrm{T}}$ in Fig. 5.1 is a $K \times 1$ vector representing the phase of the received signals at the UTs. The objective of the CSI Estimation block at the UTs is to estimate the attenuation and phase rotation introduced by the channel for each beam using the non-precoded pilots. In a formal notation, the CSI estimated by the kth UT can be represented as a $1 \times N$ complex-valued vector $\hat{\boldsymbol{h}}_i(k) = \begin{bmatrix} \hat{h}_{i1}(k) & \hat{h}_{i2}(k) & ... & \hat{h}_{iN}(k) \end{bmatrix}$ where each element $\hat{h}_{ij}(k) = |\hat{h}_{ij}(k)| e^{j(\hat{\theta}_{ij}(k))}, \quad j \in \{1, 2, ..., N\}$. Note that $\hat{\theta}_{ij}(k)$ are relative phase measurements of the jth beam with respect to the intended beam i. These relative phase estimations are the only measurements in practical precoding implementations, as stated in [281]. In a mathematical notation, $\hat{\theta}_{ij}(k) = \psi_{ij}(k) + \phi_j^e(k) - \psi_{ii}(k) - \phi_i^e(k)$, where $\psi_{ij}(k) + \phi_j^e(k)$ and $\psi_{ii}(k) + \phi_i^e(k)$ are the respective absolute phases of the jth and the ith beams received at the ith UT. Besides, it is essential to note that $\hat{\theta}_{ij}(k)$ contains the differential phase rotation introduced by the channel $(\psi_{ij} - \psi_{ii})$, but also the differential phase drift experienced for the beam $(\phi_j^e(k) - \phi_i^e(k))$. However, it is not possible to measure each of them independently. Additionally, we calculate the carrier frequency offset between beams

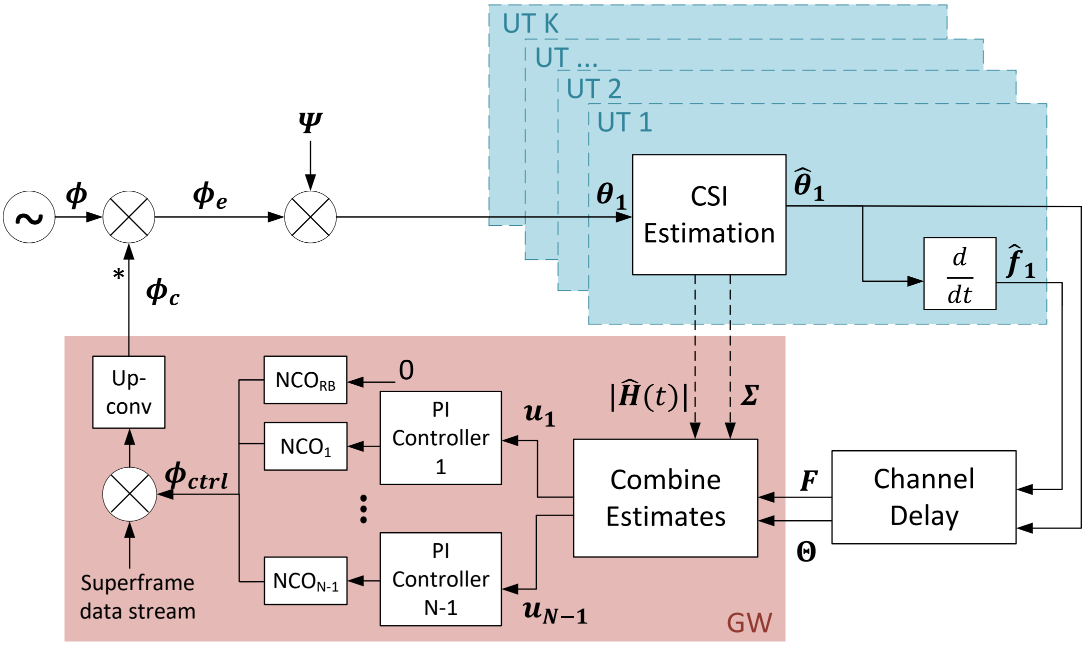

Figure 5.1: Differential phase-error compensation loop.

$\hat{\boldsymbol{f}}(k)$ at each UT to use it in the compensation loop. $\hat{\boldsymbol{f}}(k)$ is a $K \times 1$ vector with elements $\hat{f}_j(k) = \left(\hat{\theta}_j(k) - \hat{\theta}_j(k-1)\right)/2\pi T_s$.

At the GW, the CSI estimation from all the UTs is grouped in a $K \times N$ complex-valued matrix $\hat{\boldsymbol{H}}(k) = \begin{bmatrix} \hat{\boldsymbol{h}}_1(K) & \hat{\boldsymbol{h}}_2(K) & \ldots & \hat{\boldsymbol{h}}_K(K) \end{bmatrix}^{\mathrm{T}}$ which is used to calculate the precoding matrix $\boldsymbol{W}$ in (5.1). For a given set of UTs, the precoding matrix is not calculated continuously, but rather at sufficient intervals to capture the very slow temporal variations of the channel matrix. On the other hand, the compensation loop can operate in a sample-based mode, calculating a compensation phase from each transmitted non-precoded pilot.

The block "Combine Estimates" combines the estimations from all the UTs to generate the inputs for the $N-1$ PI Controllers. In other words, the block uses as inputs two matrices $\boldsymbol{F}(k)$ and $\boldsymbol{\Delta\Theta}(k)$ to provide N vectors $\{\boldsymbol{u_j}(k)\}_{j=1}^{N}$, where $\boldsymbol{u_j}(k) = \begin{bmatrix} f_j(k) & \theta_j(k) \end{bmatrix}^{\mathrm{T}}$. Besides, this block is responsible for choosing the reference beam (RB), whose frequency and phase are not compensated. We will discuss in detail the design of this block in section 5.3.2.

The core of our solution is to calculate a compensation phase using the combined estimates vectors previously described. The PI Controller was designed as a two-steps controller that uses carrier frequency offset at the first step and differential phase later. The design of this block is addressed in section 5.3.1.

The NCO blocks are fed with $f_{ctrl}(k)$ during the first or "coarse" synchronization state. This allows shorter lock times. When the differential frequency between beams $f_n(k)$ decreases below a pre-defined threshold γ, the system starts feeding the NCOs with $\theta_{ctrl}(k)$. We will refer to this state as the "fine" synchronization step.

Variable $\boldsymbol{\phi_{ctrl}}(k) = \begin{bmatrix} \phi_1^{ctrl}(k) & \phi_2^{ctrl}(k) & \dots & \phi_N^{ctrl} \end{bmatrix}^{\mathrm{T}}$ is an $N \times 1$ vector containing the outputs of the N NCOs. For the sake of the design simplicity, $\boldsymbol{\phi_{ctrl}}(k)$ is defined as an $N \times 1$ vector, but the element corresponding to the reference beam is zero. The election of the reference beam is described in section 5.3.2.

5.3.1 PI Controller Design

The input of the j-th controller is $\boldsymbol{u_j}(k) = \begin{bmatrix} \hat{f}_j(k) & \hat{\theta}_j(k) \end{bmatrix}^{\mathrm{T}}$, where $\hat{f}_j(k)$ and $\hat{\theta}_j(k)$ are the estimated differential frequency and phase drift between the reference beam and the j-th beam respectively. We calculate the differential frequency drift using the phase estimates as [283]

$$f_j(k) = \theta_j(k) - \theta_j(k-1)/2\pi T. \tag{5.4}$$

This operation is the derivative block in Fig. 5.1. Matrix $\boldsymbol{F}(k)$ is a $K \times N$ real-valued matrix containing the carrier frequency offset for all the beams from each UT.

The following equation can describe the j-th PI Controller:

$$\begin{bmatrix} f_{ctrl}(k) \\ \theta_{ctrl}(k) \end{bmatrix} = \begin{bmatrix} \frac{K_0^j}{1-z^{-1}} & 0 \\ 0 & K_{P1}^j + \frac{K_{I1}^j}{1-z^{-1}} \end{bmatrix} \begin{bmatrix} \hat{f}_j(k) \\ \hat{\theta}_j(k) \end{bmatrix}, \tag{5.5}$$

where K_0^j is the loop gain for the compensation loop's first or "coarse" state. Meanwhile, K_{P1}^j and K_{I1}^j are the proportional and integral gains of the j-th PI Controller, $j \in \{1, \dots, N-1\}$, for the second state of the loop.

Frequency Synchronization

The frequency synchronization step can be described as a first-order frequency-locked loop (FLL). Fig. 5.2 represents the main components of a digital FLL. As previously described, the Frequency Detector is implemented as a maximum likelihood phase detector plus an integrator. Besides, there is the first-order Loop Filter with gain K_0, an Integrator, and the NCO as a Frequency Controller [283]. The operation of the FLL can be described by its closed-loop frequency response represented in (5.6).

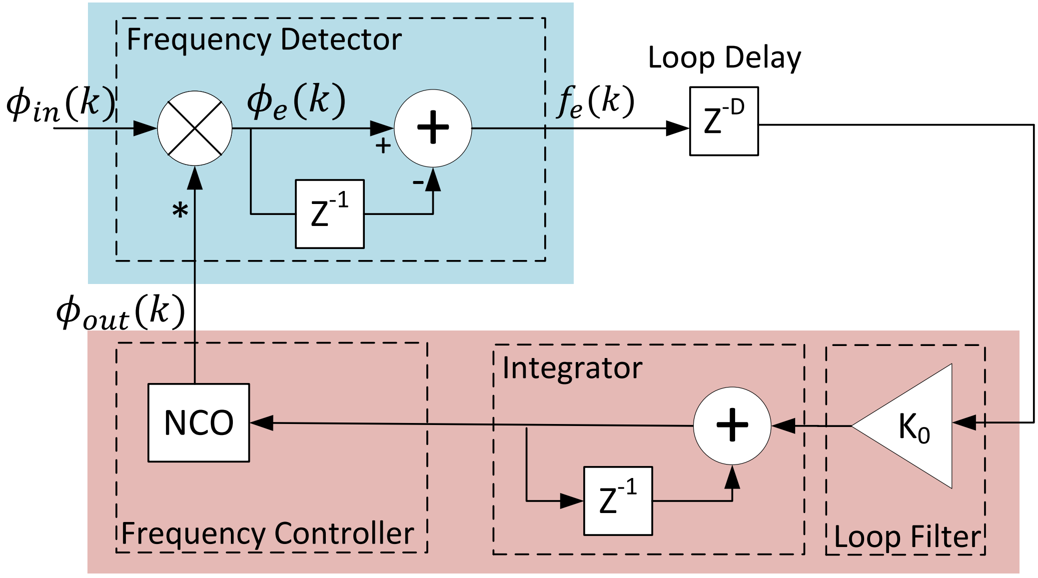

Figure 5.2: Differential phase-error compensation loop. First state: frequency compensation.

$$G_{FLL}(z) = \frac{\phi_{out}(z)}{\phi_{in}(z)} = \frac{K_0 z}{z^D(z-1) - K_0 z}, \tag{5.6}$$

where D is a natural number representing the loop delay in samples. Considering that the compensation loop works with the estimations obtained from the non-precoded pilots, D is calculated as the ratio between the channel delay τ (four times the transmission delay between satellite and Earth) and the pilots' repetition interval T_p.

Considering the stability criterion for digital PLLs with loop delays [283], the loop gain K_0 must satisfy (5.7) to guarantee the FLL stability. Fig. 5.3 shows the maximum delay allowed before the loop becomes unstable for a range of loop gains K, $10^{-6} < K < 1$:

$$0 < K_0 < 2\sin\left(\frac{\pi}{2(2D+1)}\right). \tag{5.7}$$

We can calculate the maximum loop delay by knowing the satellite orbit and the UT position. For the GEO case, where the maximum slant range is around 41 127 km, $D = 3731$, which leads to a loop gain $K \leq 4 \cdot 10^{-4}$. The FLL with loop gain $K_0 = 4 \cdot 10^{-4}$ will remain stable for any delay $D \leq 3731$ pilots. Figure 5.4 shows the error response of the resulting frequency synchronization loop.

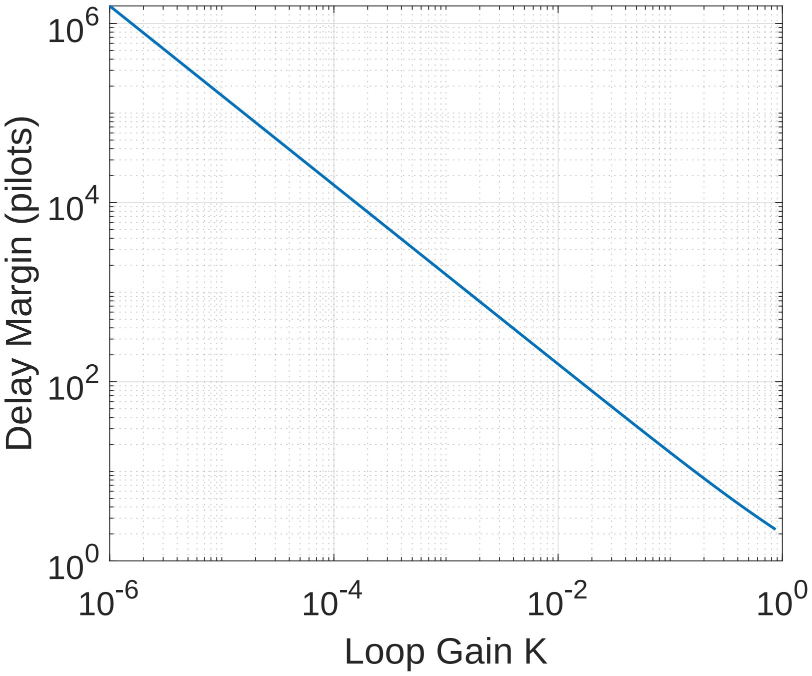

Figure 5.3: Maximum delay allowed to guarantee the stability of the compensation loop during the first state: frequency compensation.

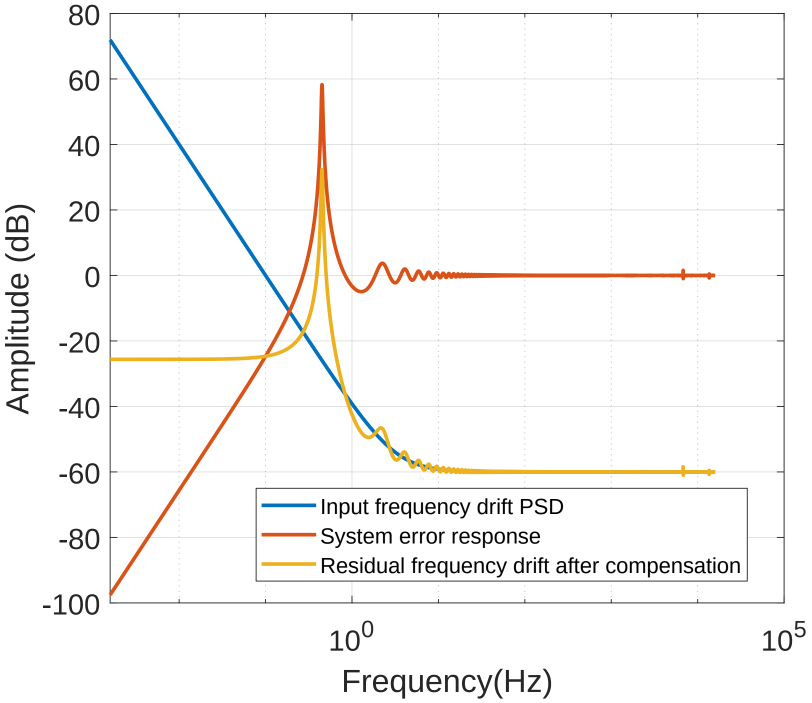

Figure 5.4: System error response of the frequency compensation loop with gain $K = 4 \cdot 10^{-4}$

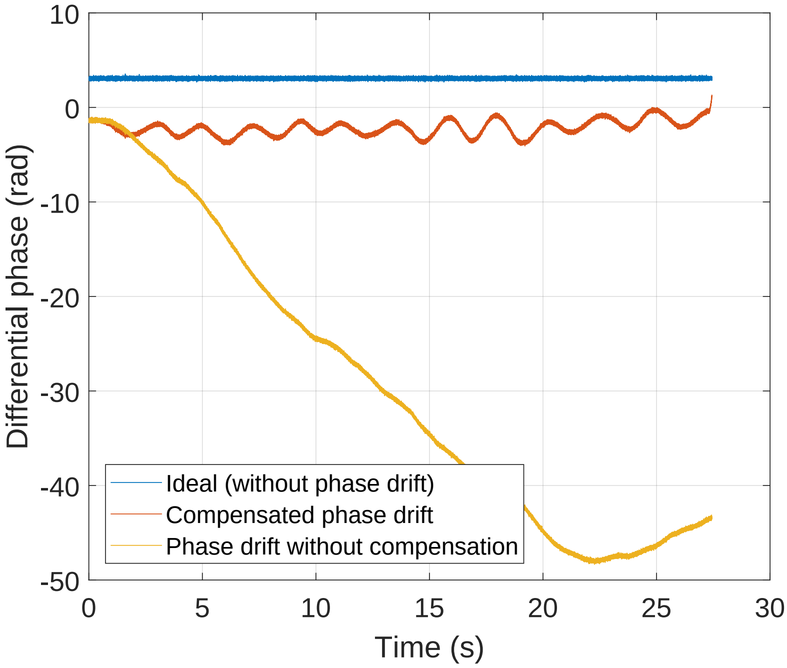

Figure 5.5: Comparison of the phase drift of one beam in a 4x4 GEO multibeam satellite system with and without the frequency compensation loop ($K = 4 \cdot 10^{-4}$).

Phase Synchronization

The design of the fine synchronization step is strongly related to the transfer function of the system $G_p(z)$, also known as the forward-path transfer function. Fig. 5.6 represents a simplification of the diagram in Fig. 5.1, where $G_c(z) = K_{P1} + \frac{K_{I1}}{1-z^{-1}}$ is the transfer function of the PI controller. For the "coarse" synchronization state, the transfer function $G_p(z)$ contains the response of the NCO and the loop delay in pilots D, $G_p(z) = \frac{z^{-D}}{1-z^{-1}}$.

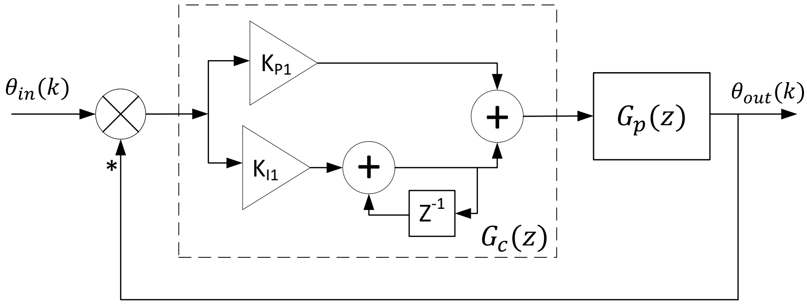

Figure 5.6: Frequency domain PI controller design

The PI controller was designed following the frequency-domain design described in [284].

This procedure calculates the values of K_{P1} and K_{I1} considering the desired PM of the compensated system. The PM is a parameter closely linked to the system's stability. It is defined in [284] as the amount of pure phase delay that can be added before the system becomes unstable.

Theoretically, a system is stable if the PM of the open-loop transfer function of the compensated system is in the interval $0 \leq \text{PM} \leq 90°$. Meanwhile, practical implementations aim for a PM between 45° and 60° [285]. However, the exact value is left to the designer's discretion. Figure 5.7 shows the parameters of the PI controller obtained with the frequency-domain design method mentioned above. To generate the figure, we used as input the interval $0 \leq \text{PM} \leq 90°$.

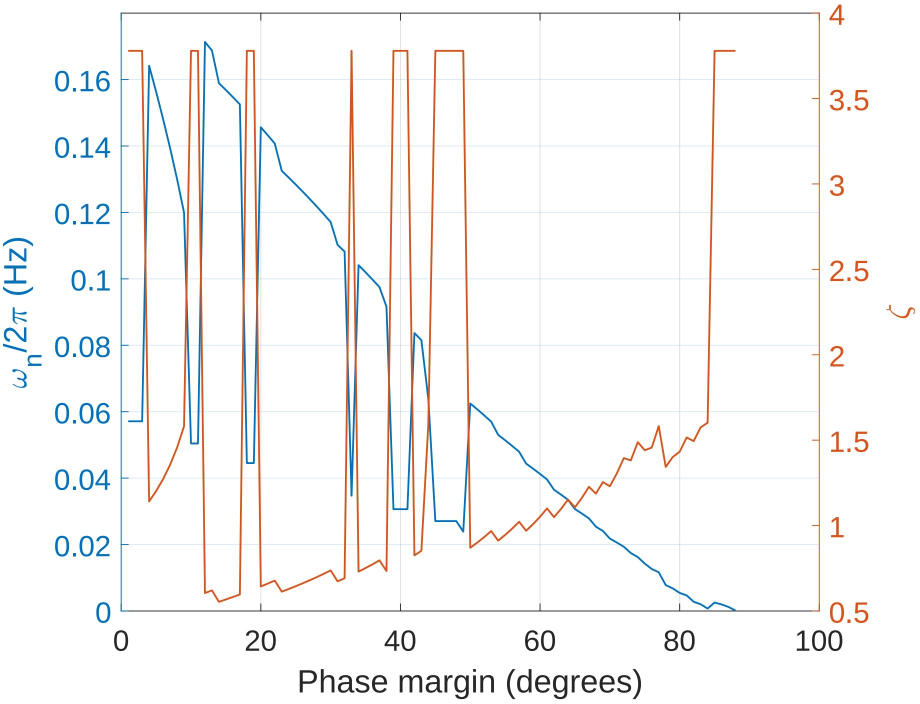

Figure 5.7: Design of the phase compensation loop as a second-order PLL. Values of ω_n (left y-axis) and ζ (right y-axis) for the PM of the open-loop transfer function in the interval $0 \leq$ PM $\leq 90°$

The left axis in Fig. 5.7 represents the natural frequency of the second-order loop $\omega_n = \frac{\sqrt{K_{I1}}}{2\pi T_p}$ while the right axis represents the damping factor $\zeta = \frac{K_{P1}}{2\sqrt{K_{I1}}}$. We select these parameters to exploit the similarities of the second step of our compensation loop with a classical second-order PLL. Additionally, the natural frequency and damping factor parameters offer a more intuitive description of the closed-loop system response. For instance, the natural frequency is directly related to the loop bandwidth, which makes it inversely proportional to the residual phase drift after compensation. This implies that a high value of ω_n is desired to decrease the residual phase drift. Additionally, it is well known that the damping factor of second-order PLLs should be in the interval $0.7 \leq \zeta \leq 1.5$ to guarantee stability. Considering these design criteria, we selected $\omega_n = 0.102$ Hz and $\zeta = 0.751$ for a PM $= 35°$. Fig. 5.8 shows the error response of the system for these parameters.

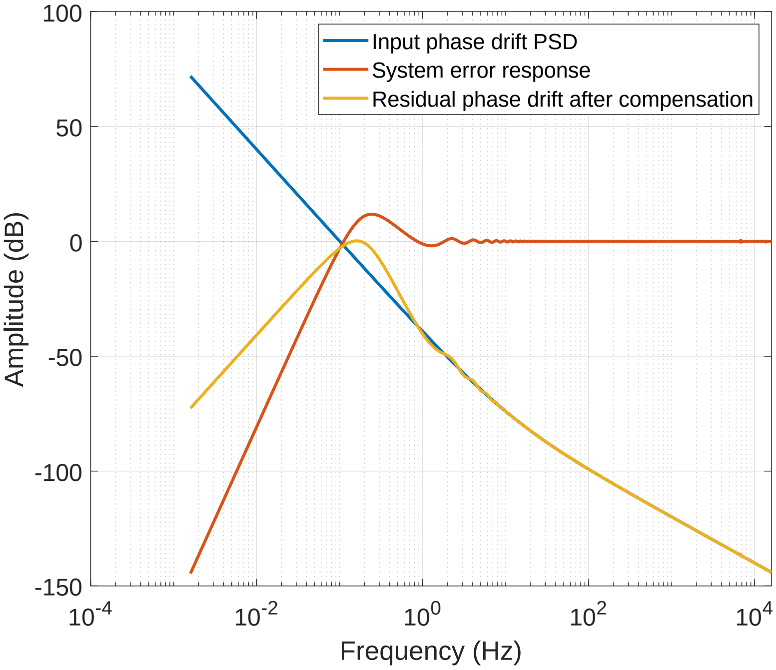

Figure 5.8: System error response of the phase compensation loop designed for an open-loop PM $= 35°$ ($\omega_n = 0.102$ Hz; $\zeta = 0.751$)

Similarly to Fig. 5.3 for the FLL, we obtained the delay margin of the system for the set of parameters 0.01 Hz $\leq \omega_n \leq 100$ Hz and $\zeta \in \{0.5, 0.75, 1, 1.5\}$. This is represented in Fig. 5.9. This figure suggests that for the selected parameters ($\omega_n = 0.102$ Hz; $\zeta = 0.751$), the maximum delay allowed before the loop becomes unstable is higher than the previously considered $D = 3731$ pilots.

Fig. 5.10 shows the PM of the open-loop system response with parameters ($\omega_n = 0.102$ Hz; $\zeta = 0.751$) for a loop delay in the interval $100 < D < 9000$. As mentioned before, for loop delays below the value used for the design D the system remains stable. However, this is not always the case when the loop delay is higher than the value considered for the design ($D = 3731$). The gray zone in Fig. 5.10 represents the loop delay values for which the system

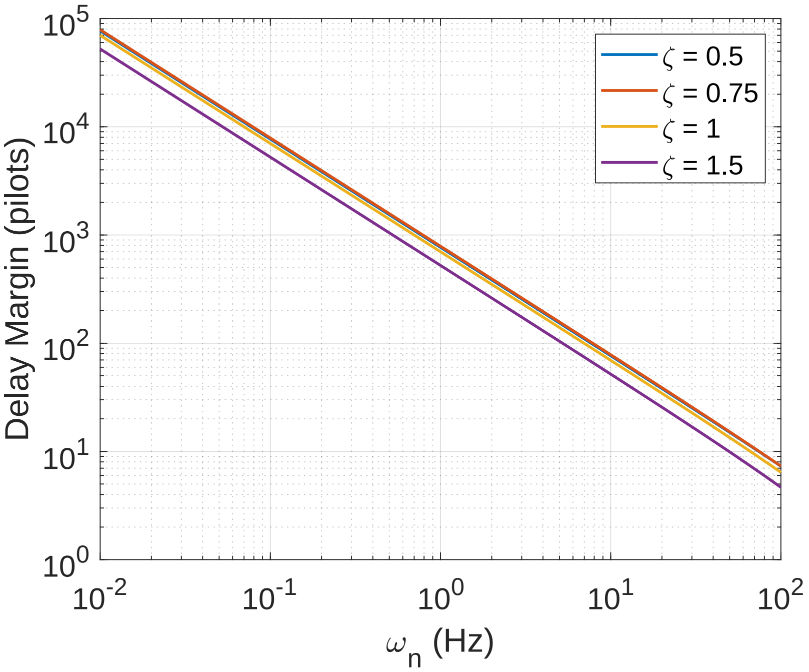

Figure 5.9: Maximum delay allowed to guarantee the stability of the compensation loop during the second state: phase compensation

is unstable $D \geq 7700$ pilots.

Figure 5.11 is an example of the phase drift of one beam in a 4x4 GEO multibeam satellite system with and without the compensation loop ($\omega_n = 0.102$ Hz; $\zeta = 0.751$). In this figure, the yellow line represents the drift in the phase of the estimated CSI when the compensation loop is not enabled, the red curve is the phase of the estimated CSI with the compensation loop, and the blue line represents the ideal scenario where there is no phase drift. This simulation was run in Matlab for a symbol rate $Rs = 6.5$ MSps.

5.3.2 Methods to Combine the Phase Estimations

As part of normal precoding o DVB-S2X operations, the UTs send to the GW their estimated thermal noise σ_i^2, with $i \in \{1, 2, ..., K\}$. Using these measurements, and the estimated CSI's amplitude $|\hat{\boldsymbol{H}}(t)|$ we can define a $K \times N$ matrix $\boldsymbol{\Gamma}$ as:

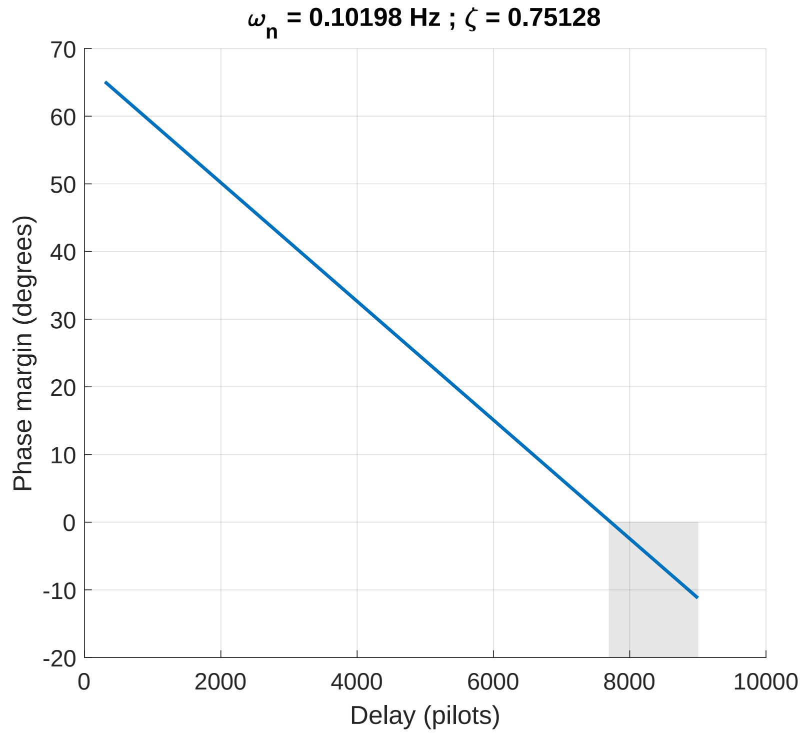

Figure 5.10: Phase Margin of the open-loop system response with parameters ($\omega_n = 0.102$ Hz; $\zeta = 0.751$) when the actual delay of the loop is in the interval $100 \leq D \leq 9000$ pilots. The grey zone represents the values of loop delay that make the loop unstable.

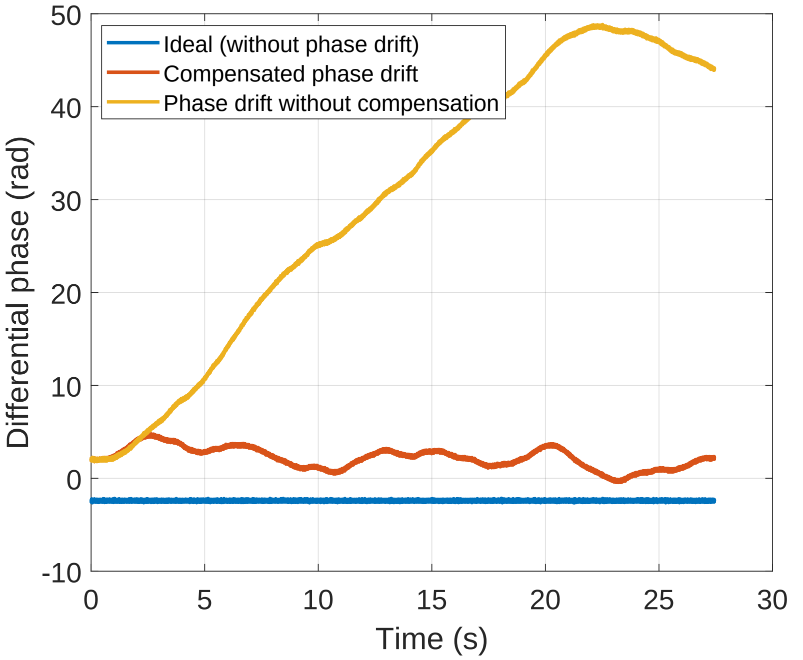

Figure 5.11: Comparison of the phase drift of one beam in a 4x4 GEO multibeam satellite system with and without the phase compensation loop ($\omega_n = 0.102$ Hz; $\zeta = 0.751$).

$$\begin{aligned}\boldsymbol{\Gamma} &= \boldsymbol{\Sigma}|\hat{\boldsymbol{H}}(t)|^2 \\ &= \begin{bmatrix} \frac{|\hat{h}_{11}(t)|^2}{\sigma_1^2} & \frac{|\hat{h}_{12}(t)|^2}{\sigma_1^2} & \dots & \frac{|\hat{h}_{1N}(t)|^2}{\sigma_1^2} \\ \frac{|\hat{h}_{21}(t)|^2}{\sigma_2^2} & \frac{|\hat{h}_{22}(t)|^2}{\sigma_2^2} & \dots & \frac{|\hat{h}_{2N}(t)|^2}{\sigma_2^2} \\ \vdots & \vdots & \ddots & \vdots \\ \frac{|\hat{h}_{K1}(t)|^2}{\sigma_K^2} & \frac{|\hat{h}_{K2}(t)|^2}{\sigma_K^2} & \dots & \frac{|\hat{h}_{KN}(t)|^2}{\sigma_K^2} \end{bmatrix}\end{aligned} \tag{5.8}$$

where $\boldsymbol{\Sigma} = \mathrm{diag}\left(\frac{1}{\sigma_1^2}, \frac{1}{\sigma_2^2}, ..., \frac{1}{\sigma_K^2}\right)$ is a diagonal matrix containing the thermal noise estimation from each UT.

From now on, we will refer to $\boldsymbol{\Gamma}$ as the "Weight" matrix since we use it as a metric for the accuracy of the interference measurement in $\boldsymbol{\Theta}(k)$ and $\boldsymbol{F}(k)$. For the sake of clarity, we rewrite both matrices as (5.9) and (5.10) below.

$$\begin{aligned}\boldsymbol{\Theta}(k) &= \begin{bmatrix} 0 & \theta_{12}(k) & \dots & \theta_{1N}(k) \\ \theta_{21}(k) & 0 & \dots & \theta_{2N}(k) \\ \vdots & \vdots & \ddots & \vdots \\ \theta_{K1}(k) & \theta_{K2}(k) & \dots & \theta_{KN}(k) \end{bmatrix} \\ &= \begin{bmatrix} 0 & \dots & \psi_{1N} + \phi_N^e(k) - \psi_{11} - \phi_1^e(k) \\ \psi_{21} + \phi_1^e(k) - \psi_{22} - \phi_2^e(k) & \dots & \psi_{2N} + \phi_N^e(k) - \psi_{22} - \phi_2^e(k) \\ \vdots & \ddots & \vdots \\ \psi_{K1} + \phi_1^e(k) - \psi_{KK} - \phi_K^e(k) & \dots & \psi_{KN} + \phi_N^e(k) - \psi_{KK} - \phi_K^e(k) \end{bmatrix}\end{aligned} \tag{5.9}$$

$$\begin{aligned}\boldsymbol{F}(k) &= \boldsymbol{\Theta}(k) - \boldsymbol{\Theta}(k-1) \\ &= \begin{bmatrix} 0 & \dots & \phi_N^e(k) - \phi_1^e(k) - \phi_N^e(k-1) + \phi_1^e(k-1) \\ \phi_1^e(k) - \phi_2^e(k) - \phi_1^e(k-1) + \phi_2^e(k-1) & \dots & \phi_N^e(k) - \phi_2^e(k) - \phi_N^e(k-1) + \phi_2^e(k-1) \\ \vdots & \ddots & \vdots \\ \phi_1^e(k) - \phi_K^e(k) - \phi_1^e(k-1) + \phi_K^e(k-1) & \dots & \phi_N^e(k) - \phi_K^e(k) - \phi_N^e(k-1) + \phi_K^e(k-1) \end{bmatrix}\end{aligned} \tag{5.10}$$

It is essential to note that the elements in $\boldsymbol{\Theta}(k)$ are phase measurements with intrinsic estimation errors. Then, the Combine Estimates block's objective is to provide the most accurate differential phase and frequency estimation vectors $\boldsymbol{\theta}(k)$ and $\boldsymbol{f}(k)$ with respect to a reference beam. The resulting combined phase vector $\boldsymbol{\theta}(k)$ can be expressed as $\boldsymbol{\theta}(k) = [C_1 + (\phi_1^e(k) - \phi_{RB}^e(k)) \quad \dots \quad 0 \quad \dots \quad C_N + (\phi_N^e(k) - \phi_{RB}^e(k))]$, where $C_j \in (-\pi, \pi]$ for all $j \in \{1, 2, ..., N\}$ are constants related to the channel phase rotation $\boldsymbol{\Psi}$. Meanwhile, $C_j \approx 0$ for all $j \in \{1, 2, ..., N\}$ in the resulting combined frequency vector $\boldsymbol{f}(k)$.

For the explanation of the estimates combination, we will consider as input the matrix

$\boldsymbol{F}(k)$ and as output the vector $\boldsymbol{f}$, as it is represented in Fig. 5.12. The main reason for this selection is that the derivative operation attenuates the effect of $\boldsymbol{\Psi}$ in $\boldsymbol{F}(k)$ matrix since $C_j \approx 0$. Consequently, combinatorial approaches are feasible, which is not the case when using $\boldsymbol{\Theta}(k)$ as input.

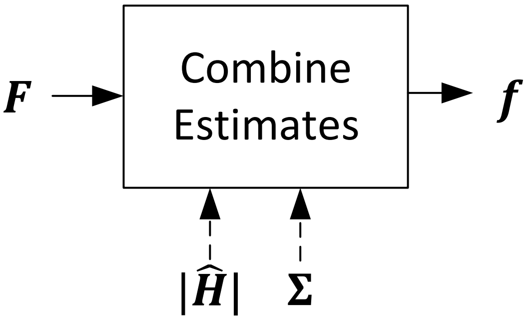

Figure 5.12: Combine estimates block

There are two main groups of possible ways to combine phase measurements: by selection or by combination. The first case refers to the approaches that select the "best" measurement and discard the rest. In contrast, the second case intends to combine the measurements of a unique physical process obtained from different estimators. Among the most popular combinatorial measurement approaches, we can find Equal-gain combining and Weighted averages. However, in this study, we will analyze only the last one since its superior performance has been extensible proven [286, 287]. In addition, we will discuss the basic approach and two other selective approaches.

Basic Approach

This implies using the estimations from the UT with less thermal noise:

$$(i, j) = \text{argmax}\{\boldsymbol{\Sigma}\}. \tag{5.11}$$

Since $\boldsymbol{\Sigma}$ is a diagonal matrix, $i = j$

$$\boldsymbol{f} = \boldsymbol{F}(i, :), \tag{5.12}$$

and the Reference beam is the i-th UT intended beam. Note that this approach does not consider the CSI's amplitude matrix $|\hat{\boldsymbol{H}}(t)|$.

Best Receiver Approach

The second approach considers that depending on their geographical location, the UTs receives the interference beams with different power. This implies that more accurate estimations can be obtained from the UT that receives more power for the higher number of beams. The goal of this approach is to select that particular UT and use its phase measurements for the compensation loop.

First, we calculate the "total weight" for each UT as $q_k = \sum_{n=1}^{N} \left(\frac{|\hat{h}_{kn}(t)|^2}{\sigma_k^2} \right)$, where $\frac{|\hat{h}_{kn}(t)|^2}{\sigma_k^2}$ are the elements of matrix $\mathbf{\Gamma}$. In a vector form $\boldsymbol{q} = \begin{bmatrix} q_1 & ... & q_k & ... & q_K \end{bmatrix}$ is a vector that contains a metric of the quality of the UTs. Note that this approach requires making zero the main diagonal of $\mathbf{\Gamma}$ to remove the influence of the intended beam.

Then, the reference beam is the intended beam for the receiver $i = \text{argmax}\{\boldsymbol{q}\}$ and the output vector is

$$\boldsymbol{f} = \boldsymbol{F}(i, :). \tag{5.13}$$

The "Best receiver" approach is very similar to the Basic approach since all the measurements are obtained from a single UT. However, As it can be seen in 5.13, choosing a different UT can improve the accuracy of the phase estimations. Another interesting fact about this approach is that it is possible to know in advance which may be the "Best receiver" by knowing the UTs' location and the footprint of the beams.

Best Estimation Approach

The "Best estimation" approach explores the idea that there is no need to use the measurements from only one UT. The phase difference between two beams is estimated in the intended receiver of each of them. Then, the "Best estimation" approach compares the weight of both estimations to select the more reliable measurement.

The algorithm takes two input arguments: the estimated CFO $\boldsymbol{F}$ and the "Weight" matrix $\mathbf{\Gamma}$. Basically, it iterates over each beam (j) and UT (i) pair to calculate the weights and select the best estimates. This loop performs the following steps:

- Check Conditions: The algorithm compares the weights of the current pair of estimations ($\mathbf{\Gamma}(i, j)$ and $\mathbf{\Gamma}(j, i)$. If $\mathbf{\Gamma}(i, j)$ is larger, it selects the weight and value of the ith UT measurement, ($\mathbf{\Gamma}(i, j)$ and $\boldsymbol{F}(i, j)$). Otherwise, it selects the weight and the negated phase value of the jth UT measurement ($\mathbf{\Gamma}(j, i)$ and $-1\boldsymbol{F}(i, j)$).

- Update the recorded Weight and Phase arrays: The algorithm updates the *weight* and phBestEst arrays with the selected weight and phase values.

Then, the algorithm identifies the reference beam by summing the weights for each beam in *weight* and selecting the one with the maximum sum. Finally, it selects in phBestEst the measurements relative to the reference beam. The pseudocode for this algorithm is shown in Algorithm 3.

Algorithm 3 "Best estimation" algorithm

```
procedure BESTEST($\boldsymbol{F}, \boldsymbol{\Gamma}$)
    $[Nu, Nt] \leftarrow size(\boldsymbol{F})$
    for $j = 1 : Nt$ do
        for $i = 1 : Nu$ do
            if $j \neq i$ then
                if $\boldsymbol{\Gamma}(j,i) > \boldsymbol{\Gamma}(i,j)$ then
                    $weight(j,i) \leftarrow \boldsymbol{\Gamma}(j,i)$
                    $phBestEst(j,i) \leftarrow \boldsymbol{F}(j,i)$
                else
                    $weight(j,i) \leftarrow \boldsymbol{\Gamma}(i,j)$
                    $phBestEst(j,i) \leftarrow -1 * \boldsymbol{F}(i,j)$
                end if
            end if
        end for
    end for
    $rowSum \leftarrow \mathrm{sum}(weight)$                                   ▷ Sum by row
    $refBeam \leftarrow \mathrm{index}(\max(rowSum))$
    $combinedEst \leftarrow \mathrm{wrapToPi}(phBestEst(refBeam))$
    return $(combinedEst, refBeam)$
end procedure
```

Weighted Average Approach

The "Weighted average" approach combines all the measurements from all the UTs using the values in $\boldsymbol{\Gamma}$ as weights. This method selects as RB the beam received by the highest number of UTs. Formally, the beam $i = \mathrm{argmax}\{\boldsymbol{q}\}$ is the RB, where $\boldsymbol{q}$ is a $1 \times N$ vector of elements

$$q_n = \sum_{k=1}^{K} \left\{ \frac{|\hat{h}_{kn}(t)|^2}{\sigma_k^2} \right\}. \tag{5.14}$$

The elements $f_n,\ \ n \in \{1, ..., N\}$ of the resulting frequency estimation vector $\boldsymbol{f}$ are calculated as follows:

$$f_n = \sum_{k=1}^{K} \left(\frac{\gamma_{kn}}{\sum_{k=1}^{K} \gamma_{kn}} \left(F(k,n) - F(k,RB)\right) \right), \tag{5.15}$$

where $\gamma_{kn} = \sqrt{\frac{|\hat{h}_{kRB}|^2 |\hat{h}_{kn}|^2}{\sigma_k^2 (|\hat{h}_{kRB}|^2 + |\hat{h}_{kn}|^2)}}$ is a metric for the accuracy of the differential estimation between beams n and RB measured at the k-th UT. It is worth noting that γ_{kn} is obtained as a combination of the weights $\frac{|\hat{h}_{kn}(t)|^2}{\sigma_k^2}$ and $\frac{|\hat{h}_{kRB}(t)|^2}{\sigma_k^2}$ from (5.8) for the measurements $F(k,n)$ and $F(k,RB)$ respectively.

Comparison of the Combination Approaches

Figure 5.13 represents the MAE of the different combination approaches. The MAE is calculated as the average of the absolute difference between the actual value α, and the result of the combination $\hat{\alpha}_i$, as it is described in (5.16).

$$MAE = 20 \log \left(\frac{1}{N} \sum_{i=1}^{N} |\alpha - \hat{\alpha}_i| \right). \tag{5.16}$$

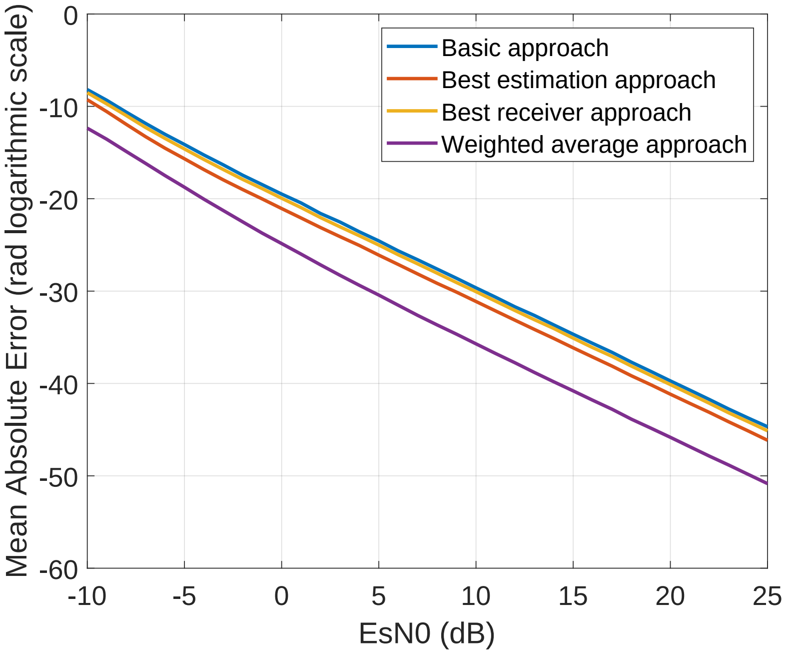

Figure 5.13: Comparison of the frequency combination approaches. MAE of the resulting frequency vector after the frequency estimation and combination over 10^4 independent iterations in a 4×4 system.

The curves in Fig. 5.13 were generated by Monte Carlo simulations of the phase drift estimation and combination in a 4×4 system. The objective of our experiment is to compare the accuracy of the combination approaches described before. To that end, a phase drift vector $\boldsymbol{\alpha}$ was added to the pilots and transmitted through a randomly generated channel. At the UTs, the CSI's phase estimates were combined using the four approaches to calculate the MAE of each of them. The experiments were run for a set of energy per symbol to noise power spectral density ratio $EsN0 \in \{-10, ..., 25\}$. This parameter only refers to the intended beam and does not consider the interference power.

The phase drift vector $\boldsymbol{\alpha} = \begin{bmatrix} \alpha_1 & ... & \alpha_4 \end{bmatrix}^{\mathrm{T}}$ had four independent elements α_n uniformly distributed with values $\alpha_n \in (-\pi; \pi)$. The transmitted pilots were predefined orthogonal Walsh-Hadamard sequences of 32 BPSK-modulated symbols, and the channel matrix was independently generated for each simulation as a 4×4 complex random matrix. The UTs performed the correlation between the received signal and the expected Walsh-Hadamard sequences to obtain the CSI estimation. Then, we calculated the frequency drift between consecutive pilots using (5.4) and applied the combination approaches described before. The MAE between the resulting vectors after combination $\hat{\boldsymbol{\alpha}}$, and the original phase drift $\boldsymbol{\alpha}$ were averaged over 10 thousand independent iterations and represented in Fig. 5.13.

As illustrated in Fig. 5.13, all the combination approaches considering (5.8) outperform the Basic approach with a constant ratio over the $EsN0$ set of values. Numerically, the accuracy improvement of each approach with respect to the basic one is 4.4% for the "Best estimation" approach, 1.2% for the "Best receiver" approach, and 17.5% for the "Weighted average" approach.

5.4 Hardware Implementation

For the experimental validation, we employ the in-house developed MIMO end-to-end satellite emulator based on SDR platforms. The proposed architecture consists of a multichannel GW with precoding capabilities, a MIMO satellite ChEm, a set of independent UTs, and a return-link emulator.

In general terms, the demonstrator can be described as follows. The GW subsystem generates the data packets according to the DVB-S2X standard, using Superframe Format II structure, and applies the selected precoding method: ZF, MMSE, or MMSE per-antenna power-constrained (MMSE PAC). The ChEm replicates the whole forward link chain, from the intermediate frequency (IF) input of the gateway block up-converter, towards the low-noise block down-converter IF output at the UT. It emulates the impairments present in the GW, the payload, the downlink channel, and the UTs. The UT subsystems implement the synchronization and decoding features in the DVB-S2X compliant receivers and perform the CSI estimation. Finally, the return-link emulator allows each UT to send its estimated CSI to the GW.

The GW, ChEm, and UT subsystems are being implemented using a set of SDR platforms, specifically the USRP-2944R from National Instruments. The physical interfaces of the channel emulator with the gateway and the user terminals are provided by the interconnection of the 50-Ω ports of the SDRs, employing IF modulated signals. The SDR platforms in the GW and the ChEm are synchronized with the same clock reference. This eliminates any timing misalignment due to their LOs, allowing precise control of the time mismatch according to the implemented impairment models.

All system components have been successfully tested considering a GEO satellite scenario [288–290]. This includes the use of implementations of the GW and UTs subsystems in the precoding validation over a live GEO link [290]. The testbed is upgraded by including the PI controller and combine estimations blocks at the GW. The following subsections will describe the implementation of these blocks.

5.4.1 PI Controller Implementation

The PI controller was implemented as an intellectual property block using Vivado HLS. Figure 5.14 shows the resulting block in LABVIEW. As it can be appreciated, it has two main inputs: *gamma* and *fed*. The first one is an array with the values of the proportional K_P and integral K_I gains. The second input, *fed*, is the differential frequency or phase used to calculate the output *fnco*, which is the compensation phase calculated by the PI controller.

Four block instances were connected in the GW's USRP, as shown in Fig. 5.15. The compensation calculated by the PI controller is applied to the superframe data streams by the NCO blocks represented in the figure.

5.4.2 Combine Estimations Implementation

The "Combine Estimations block" was implemented as a switch-case structure in the GW's Host PC. A drop-down menu at the user interface allows selecting the desired approach.

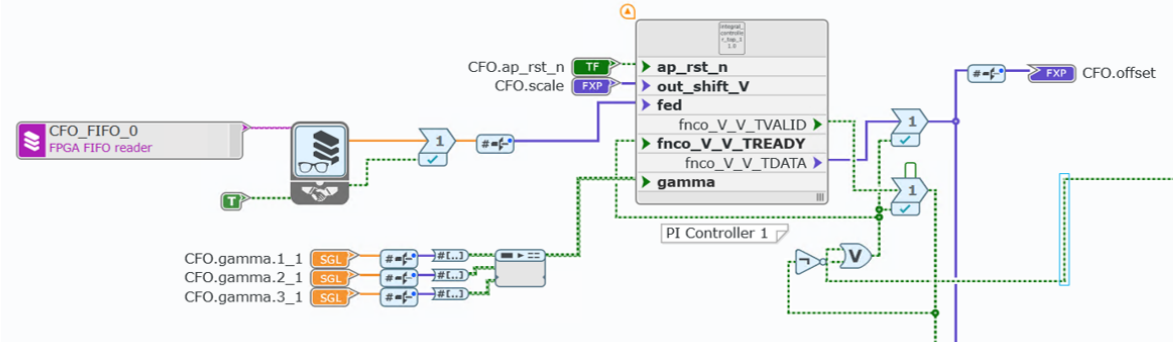

Figure 5.14: PI controller block

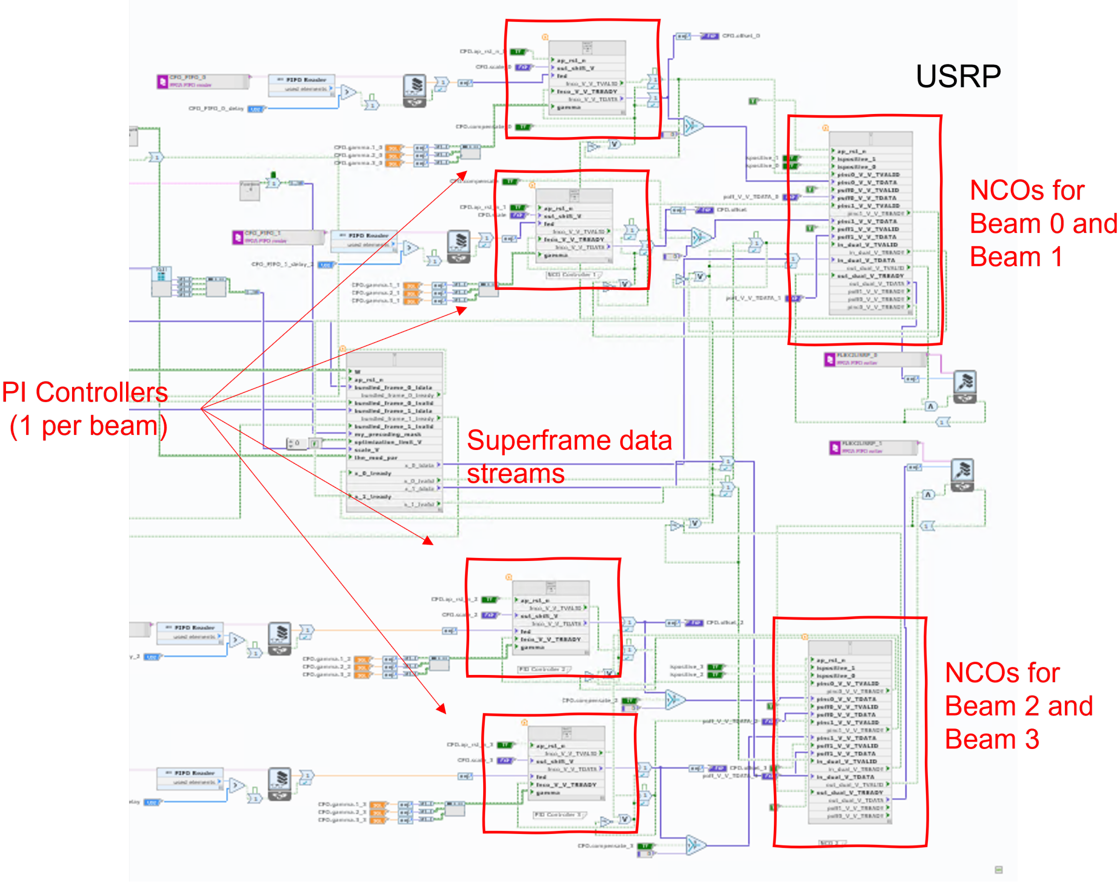

Figure 5.15: PI controller used at the GW

We added the option of manually setting the reference beam in addition to the previously described methods: Basic approach, "Best receiver," "Best estimation," and "Weighted average." This can be appreciated in Fig. 5.16, which also contains an example of the carrier frequency and phase offset matrices that the block uses as inputs to generate the corresponding output vectors. Other parameters, such as the UTs SNR, the Weight Matrix $\mathbf{\Gamma}$, and the Reference Beam are displayed for debugging purposes.

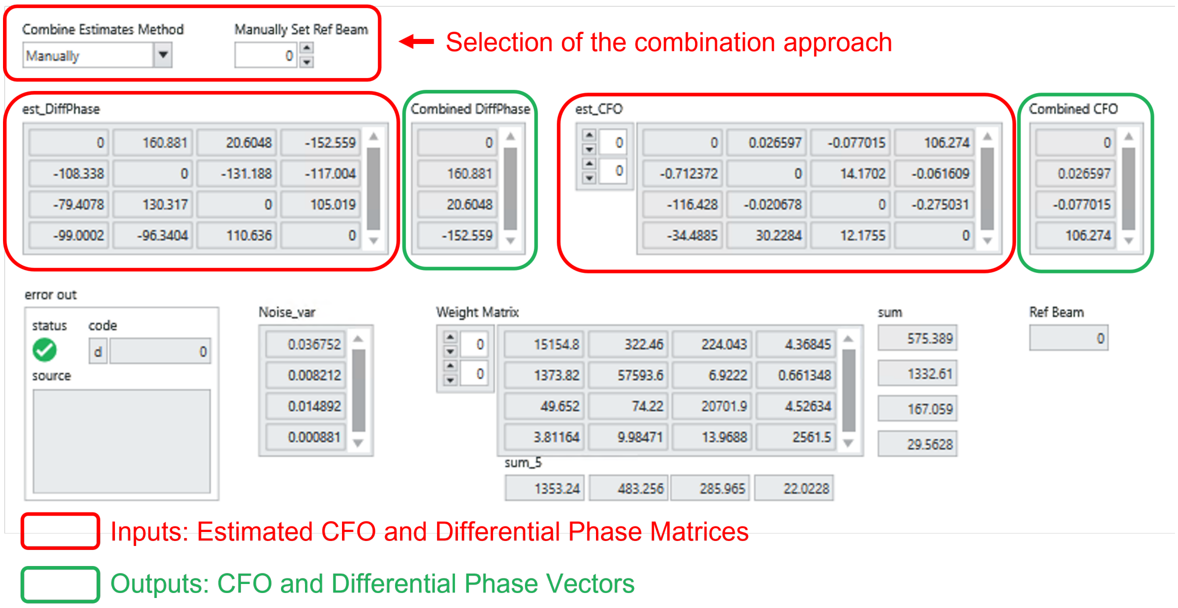

Combine Estimates Method: Manually

Manually Set Ref Beam: 0

Selection of the combination approach

est_DiffPhase

0	160.881	20.6048	-152.559
-108.338	0	-131.188	-117.004
-79.4078	130.317	0	105.019
-99.0002	-96.3404	110.636	0

Combined DiffPhase

0
160.881
20.6048
-152.559

est_CFO

0	0.026597	-0.077015	106.274
-0.712372	0	14.1702	-0.061609
-116.428	-0.020678	0	-0.275031
-34.4885	30.2284	12.1755	0

Combined CFO

0
0.026597
-0.077015
106.274

error out

status ✓

code: d 0

source

Noise_var

0.036752
0.008212
0.014892
0.000881

Weight Matrix

15154.8	322.46	224.043	4.36845
1373.82	57593.6	6.9222	0.661348
49.652	74.22	20701.9	4.52634
3.81164	9.98471	13.9688	2561.5

sum_5

1353.24	483.256	285.965	22.0228

sum

575.389
1332.61
167.059
29.5628

Ref Beam: 0

🟥 Inputs: Estimated CFO and Differential Phase Matrices

🟩 Outputs: CFO and Differential Phase Vectors

Figure 5.16: GUI Combine Estimations

Fig. 5.17 to Fig. 5.20 show the implementation of the different combining estimation approaches. In these figures, the inputs are in orange, while the outputs are in green. Due to their simplicity, the Basic approach and the "Best receiver" methods were implemented using LABVIEW's blocks. However, for the "Best estimation" and the "Weighted average" cases, the Interface for MATLAB functionality allowed us to run the MATLAB functions from LABVIEW.

5.5 Results

In this section, we evaluate the performance of the phase synchronization algorithm described before. To that end, we set the MIMO end-to-end satellite test-bed to emulate a 4 × 4 precoding-enabled GEO satellite system.

As a first experiment, we set the phase noise mask (10 Hz; -75 dBc/Hz) in Fig. 4.3 for the

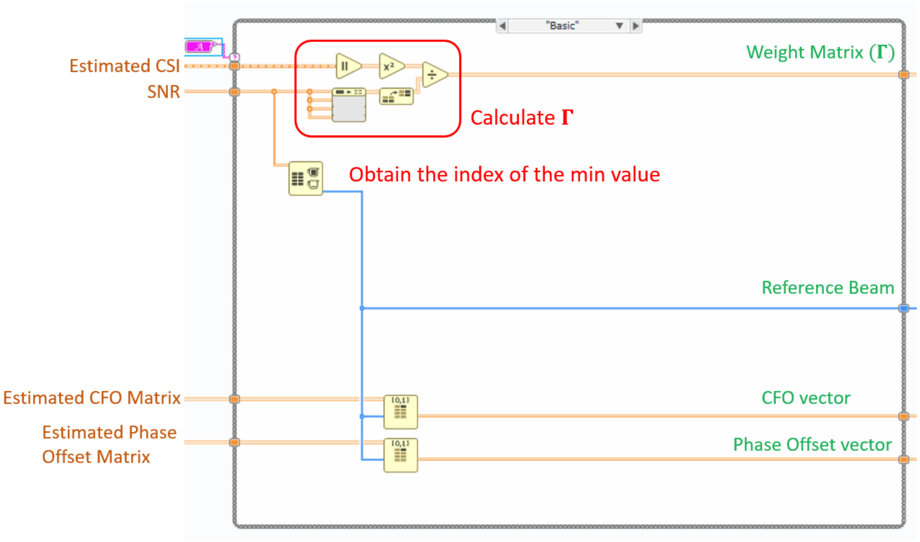

Figure 5.17: Combine estimations: Basic approach implementation

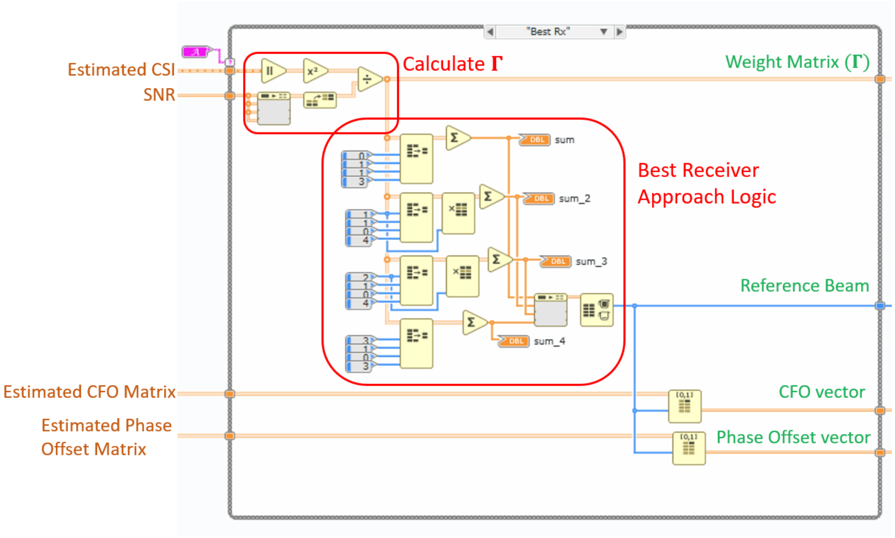

Figure 5.18: Combine estimations: ”Best receiver” approach implementation

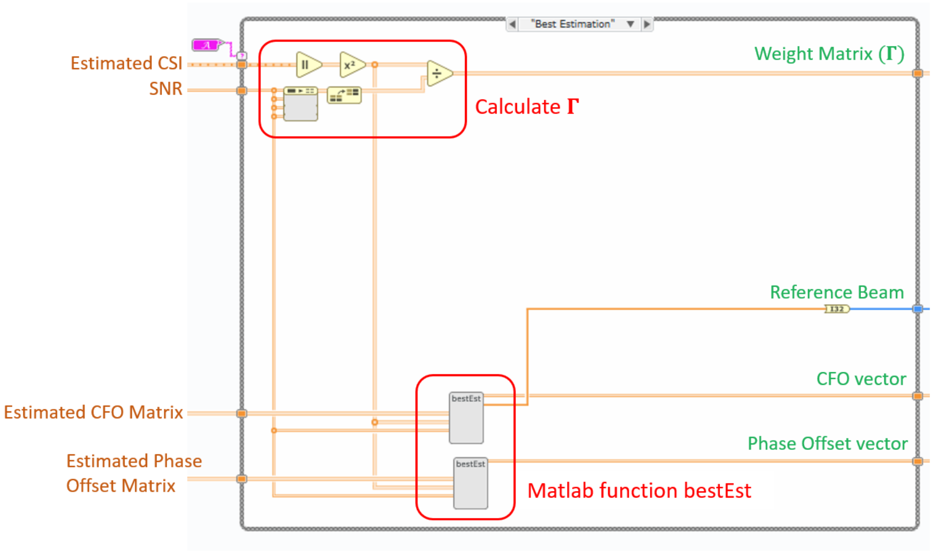

Figure 5.19: Combine estimations: "Best estimation" approach implementation

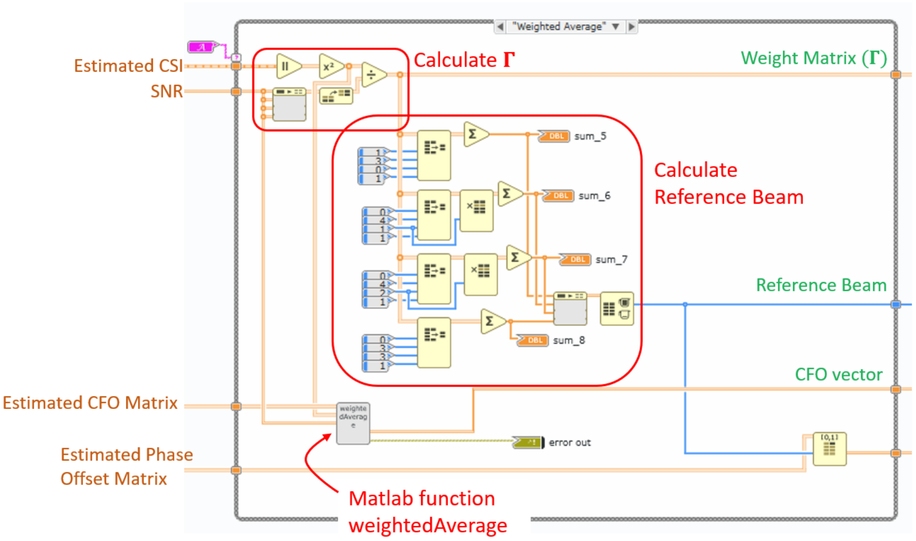

Figure 5.20: Combine estimations: "Weighted average" approach implementation

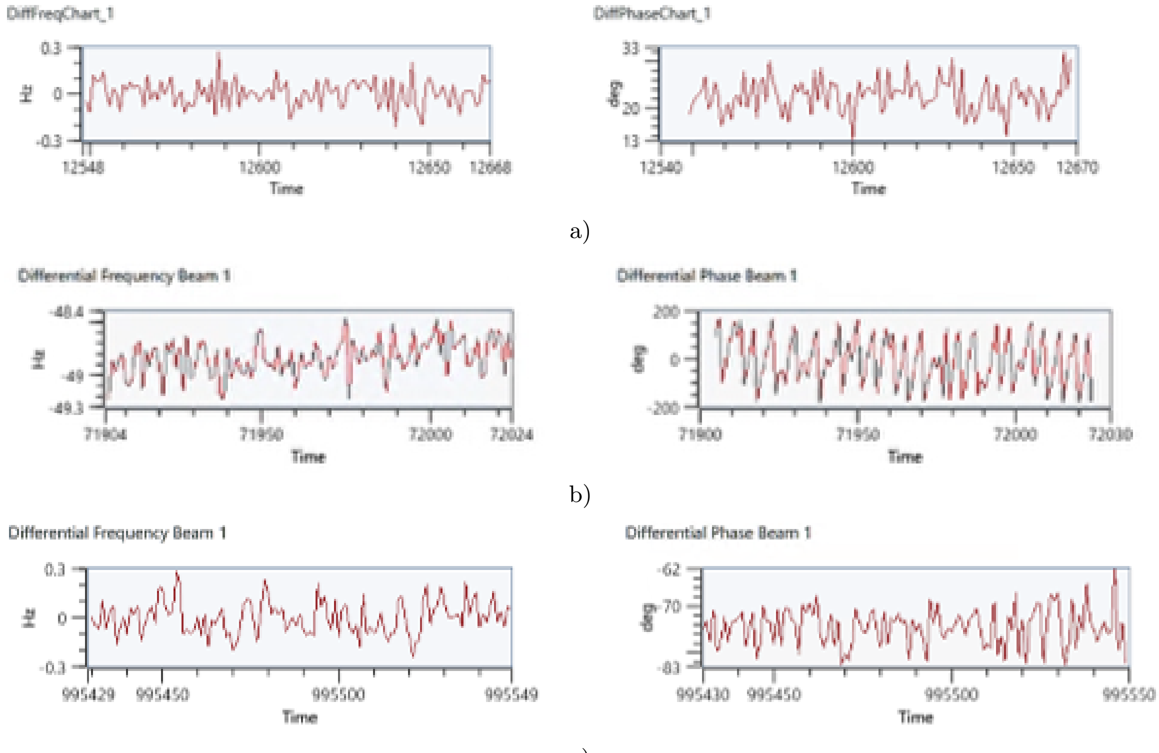

a)

b)

c)

Figure 5.21: Frequency and phase drift with LOs phase noise at the uplink and downlink: a) Ideal case without LOs' phase noise, b) Phase noise only in the uplink, c) Phase noise only in the downlink.

LOs in the uplink and the downlink independently. Fig. 5.21 shows the differential frequency and phase for beam one measured at the UT zero. These are the differential frequency and phase measurements between beams zero and one. We included the ideal case in the figure, where the LOs do not have phase noise, as a comparison baseline. Note that unlike the downlink case (c)), the phase noise in the uplink channel (b)) does affect the system performance.

The second experiment was designed to validate the design of the phase compensation loop. In this case, we set the phase noise mask (10 Hz; -75 dBc/Hz) in the uplink and analyzed the differential frequency and phase between beams zero and one measured at UT zero. The results of this experiment are shown in Fig. 5.22. As it can be appreciated in the figure, the first state of the proposed compensation loop reduces the frequency drift below 1 Hz. However, this is insufficient to stabilize the differential phase (see Fig. 5.22 c). Finally, the differential phase is compensated when the fine synchronization state is enabled.

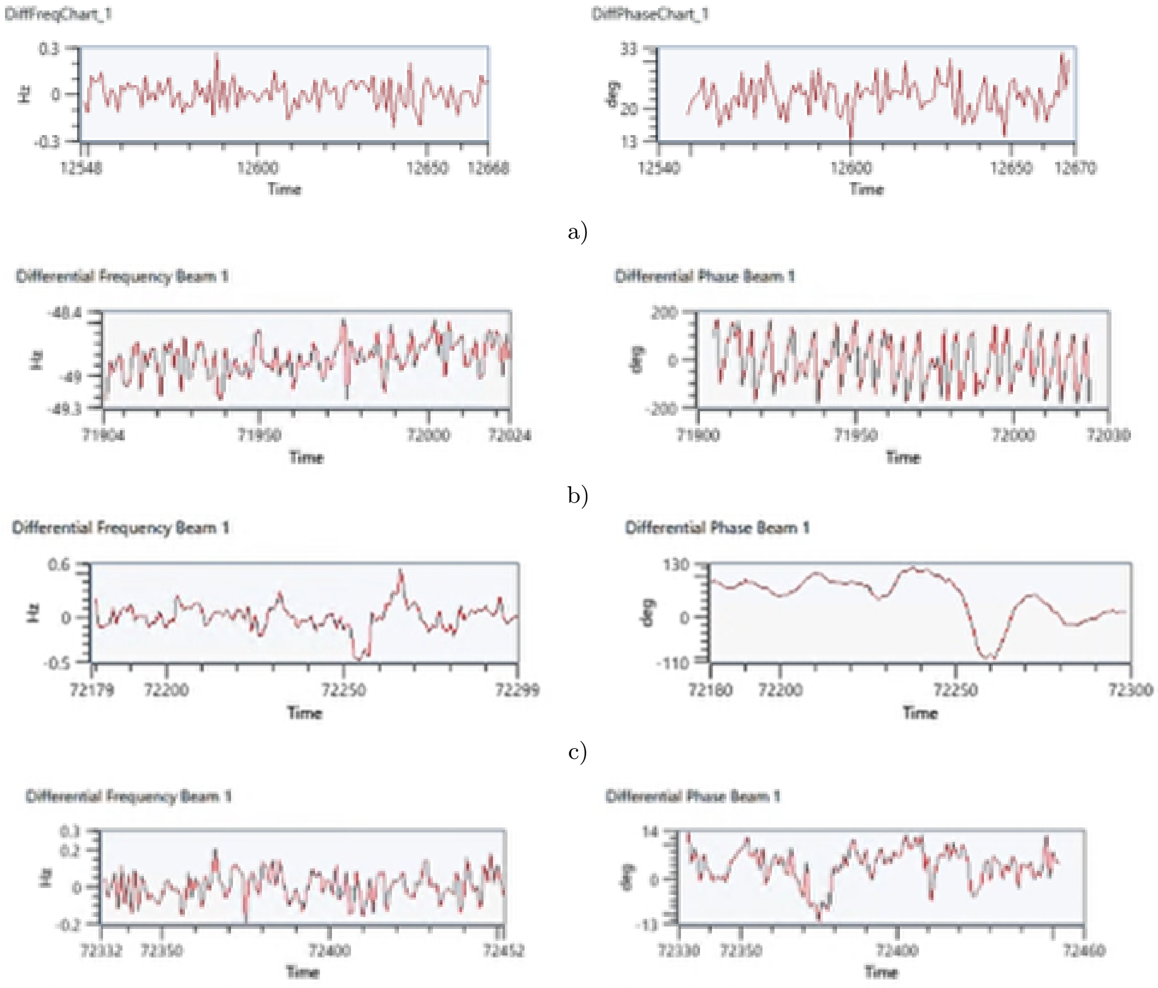

a)

b)

c)

d)

Figure 5.22: Frequency and phase drift during the phase synchronization: a) Ideal case without LOs' phase noise, b) Phase noise in the uplink channel, phase compensation loop disabled, c) Phase compensation loop enabled, working in the first state (frequency synchronization), phase noise only in the uplink channel, d) Phase compensation loop enabled, working in the second state (phase synchronization), phase noise only in the uplink channel.

5.6 Conclusions of the Chapter

This chapter describes the design and implementation of the phase compensation loop required to enable the precoding technique in GEO scenarios. One key strength of the proposed solution is its simplicity since it only requires small modifications to the previously considered precoding implementations. Specifically, including a PI controller at the GW. Due to their proven effectiveness, the PI controllers are very popular in industrial control systems.

Additionally, this study has proposed different approaches for using the UTs' phase measurements and compared its performance through Matlab simulations. The hardware implementation of the compensation loop and the phase measurements combination was described, as well as the implementation of the two-state phase noise model. These blocks were integrated into the in-house developed MIMO end-to-end satellite emulator based on SDR platforms to validate the performance of the proposed closed-loop synchronization method.

Chapter 6

Conclusions and Further Work

This PhD thesis has addressed the synchronization of CDSS. We assumed accurate time synchronization and relative positioning among the satellites and focused our work on the phase synchronization problems related to the implementation of cohesive transmission. The study case used in this document was precoding-enabled multibeam satellite systems.

The most significant of these synchronization impairments is the phase noise of the LOs in the satellite system. In this regard, the two-state phase noise model was implemented and integrated into the channel emulator of the MIMO end-to-end satellite emulator. This makes possible the evaluation of precoding techniques using a more realistic environment. Besides, it allowed us to validate the results included in this thesis.

This document formally demonstrates that the uplink phase variations affect precoding performance even when all the LOs share a single reference frequency. Previous works assumed that using a single reference frequency was enough for multibeam satellite systems. Additionally, we identified the individual contribution of each system element to the overall synchronization uncertainties in practical precoding implementations. We compared the robustness to synchronization impairments of different precoding techniques such as MMSE, ZF, and SLP. Besides, for linear and non-linear precoding, we formally demonstrated that the UTs can track slow time variations in the channel as long as they equally affect all the beams.

The compensation loop to mitigate these impairments was designed, implemented, and integrated into the GW of the MIMO end-to-end satellite emulator. The solution has the form of a closed-loop algorithm. It uses the periodical channel phase measurements sent to the GW by the UTs as part of the traditional precoding implementation. The PI controller included in the GW calculates the compensation phase required to align the grades of all the beams to the phase of the designated reference beam. The method works in two steps; first, a rough synchronization state that can be described as a distributed FLL where the PI controller uses the frequency offset among the beams. Then, there is a fine synchronization state that can be described as a distributed PLL where the controller uses the differential phase between beams.

Different approaches to combine the channel phase estimations obtained from the UTs were explored. We considered: a basic approach, using only the UTs thermal noise; two other selective methods named ”Best receiver” and ”Best estimation,” using the amplitude of the channel estimated by the UTs and the thermal noise; and the weighted average combinatorial approach.

The compensation loop and the combine estimations hardware implementations were used in an experiment to assess the feasibility of the precoding techniques for GEO satellite systems.

6.1 Future Works

This PhD thesis can be seen as a first approach to the challenging topic of synchronization of CDSSs. There are still several open challenges to make cohesive transmission and reception from space something widespread. Hereby, we name some of them:

Relaxing the time synchronization and positioning alignment assumptions: The analysis in this thesis assumed accurate time synchronization and relative positioning among the satellites. Some algorithms to achieve these requirements were included in chapter 2. However, the selection of the specific algorithms and their combination with the phase synchronization method proposed in this thesis is still missing. Additionally, the analysis of the performance of the proposed solution for different levels of time synchronization and position alignment accuracy can be another extension of this research.

Open-loop phase synchronization scheme: The closed-loop synchronization method proposed in chapter 5 was designed for a precoding-enabled DSS, which requires the channel estimation from the UTs. However, this may not be the case for other DSS where open-loop phase synchronization methods may be more suitable. Achieving phase synchronization without the receiver’s feedback is a possible extension of this thesis.

Considering the resources constraint of small satellites: Further research directions may consider the design of the phase synchronization under the resource constraint of small satellites. Some of the intrinsic characteristics of small satellites make challenging accurate phase synchronization. For instance, limited onboard resources and communications capabilities, low stability of the clock, and the difficulty in having precise attitude determination and control due to their size and weight. Conversely, the inter-satellite distance that can be achieved with small spacecraft DSS, from a few meters to several kilometers, makes possible synchronization methods that are not feasible when the satellites are separated by hundred or thousand kilometers. Then, the design of an accurate phase synchronization technique considering these aspects is still an open challenge.

Appendix A

Proof of theorems in chapter 3

A.1 Proof of Theorem 6

We start from the definition of $\mathbf{Q}_\mathrm{r}$ by recalling that

$$\mathbf{Q}_\mathrm{r}^\mathrm{T}\mathbf{Q}_\mathrm{r} = [\mathbf{A}^{-1}]_{\mathrm{r,r}}^\mathrm{T}[\bar{\mathbf{H}}^\dagger]_\mathrm{r}^\mathrm{T}[\bar{\mathbf{H}}^\dagger]_\mathrm{r}[\mathbf{A}^{-1}]_{\mathrm{r,r}} \tag{A.1}$$

Therefore, we can obtain

$$\begin{aligned}\mathbf{p}^\mathrm{T}\mathbf{Q}_\mathrm{r}^\mathrm{T}\mathbf{Q}_\mathrm{r}\,\mathbf{p} \geq \lambda_{\min}&\left([\bar{\mathbf{H}}^\dagger]_\mathrm{r}^\mathrm{T}[\bar{\mathbf{H}}^\dagger]_\mathrm{r}\right)\\ &\times \mathbf{p}^\mathrm{T}[\mathbf{A}^{-1}]_{\mathrm{r,r}}^\mathrm{T}[\mathbf{A}^{-1}]_{\mathrm{r,r}}\,\mathbf{p},\end{aligned} \tag{A.2}$$

where $\lambda_{\min}(\cdot)$ denotes the maximum eigenvalue. In addition,

$$\begin{aligned}\lambda_{\min}\left([\bar{\mathbf{H}}^\dagger]_\mathrm{r}^\mathrm{T}[\bar{\mathbf{H}}^\dagger]_\mathrm{r}\right) &= \lambda_{\min}\left([\bar{\mathbf{H}}^{\dagger\mathrm{T}}\bar{\mathbf{H}}^\dagger]_{\mathrm{r,r}}\right)\\ &= \lambda_{\min}\left([(\bar{\mathbf{H}}\bar{\mathbf{H}}^\mathrm{T})^{-1}]_{\mathrm{r,r}}\right) \triangleq \lambda.\end{aligned} \tag{A.3}$$

Since $\bar{\mathbf{H}}$ is full column rank, it follows that $\bar{\mathbf{H}}^\mathrm{T}\bar{\mathbf{H}} \succ 0$, and hence $(\bar{\mathbf{H}}\bar{\mathbf{H}}^\mathrm{T})^{-1} \succ 0$. Due to the fact that removing rows and columns of a matrix does not affect its positive/negative definiteness, we further conclude that $[(\bar{\mathbf{H}}\bar{\mathbf{H}}^\mathrm{T})^{-1}]_{\mathrm{r,r}} \succ 0$, and thus, all its eigenvalues, including the minimum one, are positive. Therefore, we always have $\lambda > 0$. Consequently, using (A.2), we can obtain a lower bound on τ^2 as

$$\begin{aligned} \tau^2 &= \underset{p \in S^{2L-1}}{min} \ \frac{1}{2L} \ \mathbf{p}^{\mathrm{T}} \mathbf{Q}_{\mathrm{r}}^{\mathrm{T}} \mathbf{Q}_{\mathrm{r}} \, \mathbf{p} \\ &\geq \underset{p \in S^{2L-1}}{min} \ \frac{\lambda}{2L} \ \mathbf{p}^{\mathrm{T}} [\mathbf{A}^{-1}]_{\mathrm{r,r}}^{\mathrm{T}} [\mathbf{A}^{-1}]_{\mathrm{r,r}} \, \mathbf{p} \\ &= \underset{p \in S^{2L-1}}{min} \ \frac{\lambda}{2L} \ \mathbf{p}^{\mathrm{T}} [\mathbf{A}^{-T} \, \mathbf{A}^{-1}]_{\mathrm{r,r}} \, \mathbf{p}, \end{aligned} \tag{A.4}$$

where the last equality can easily be verified by exploiting the block-diagonal structure of $\mathbf{A}$. In order to derive an explicit expression for the lower bound in (A.4), one needs to solve the following constrained minimization problem:

$$\mathcal{P}1: \quad \underset{p \in S^{2L-1}}{min} \quad \mathbf{p}^{\mathrm{T}} [(\mathbf{A}\,\mathbf{A}^{\mathrm{T}})^{-1}]_{\mathrm{r,r}} \, \mathbf{p}. \tag{A.5}$$

Using the definition of $\mathbf{S}^{2L-1}$, the problem $\mathcal{P}1$ can be rewritten as

$$\begin{aligned} \mathcal{P}1: \quad & \underset{p}{min} \quad \mathbf{p}^{\mathrm{T}} [(\mathbf{A}\,\mathbf{A}^{\mathrm{T}})^{-1}]_{\mathrm{r,r}} \, \mathbf{p} \\ & \text{s.t.} \quad \mathbf{p}^{\mathrm{T}} \mathbf{1} = 1 \\ & \qquad\;\; \mathbf{p} \succeq \mathbf{0}. \end{aligned} \tag{A.6}$$

Let us first consider a relaxation of (A.6) by ignoring the non-negativity constraints, i.e.,

$$\begin{aligned} \mathcal{P}2: \quad & \underset{p}{min} \quad \mathbf{p}^{\mathrm{T}} [(\mathbf{A}\,\mathbf{A}^{\mathrm{T}})^{-1}]_{\mathrm{r,r}} \, \mathbf{p} \\ & \text{s.t.} \quad \mathbf{p}^{\mathrm{T}} \mathbf{1} = 1 \end{aligned} \tag{A.7}$$

Since the matrix $\mathbf{A}$ has a block-diagonal structure, we can write $\mathbf{A}\mathbf{A}^{\mathrm{T}} = \operatorname{blkdiag}\left(\mathbf{A}_1\mathbf{A}_1^{\mathrm{T}}, ..., \mathbf{A}_K\mathbf{A}_K^{\mathrm{T}}\right)$. Accordingly, $(\mathbf{A}\mathbf{A}^{\mathrm{T}})^{-1} = \operatorname{blkdiag}\left((\mathbf{A}_1\mathbf{A}_1^{\mathrm{T}})^{-1}, ..., (\mathbf{A}_K\mathbf{A}_K^{\mathrm{T}})^{-1}\right)$, and thus

$$[(\mathbf{A}\,\mathbf{A}^{\mathrm{T}})^{-1}]_{\mathrm{r,r}} = \operatorname{blkdiag}\left((\mathbf{A}_1\mathbf{A}_1^{\mathrm{T}})^{-1}, ..., (\mathbf{A}_L\mathbf{A}_L^{\mathrm{T}})^{-1}\right). \tag{A.8}$$

Similarly, we can partition $\mathbf{p}$ as $\mathbf{p} = [\mathbf{p}_1, ..., \mathbf{p}_L]^{\mathrm{T}}$ such that for any $l \in \{1, ..., L\}$, $\mathbf{p}_l \in \mathbb{R}^2$ corresponds to the block $\mathbf{A}_l \mathbf{A}_l^{\mathrm{T}}$ in $\mathbf{A}\mathbf{A}^{\mathrm{T}}$. As a result, the problem $\mathcal{P}2$ can be recast as

$$\begin{aligned} \mathcal{P}2: \quad & \underset{\{p_l\}_{l=1}^{L}}{min} \quad \sum_{l=1}^{L} \mathbf{p}_l^{\mathrm{T}} (\mathbf{A}_l\, \mathbf{A}_l^{\mathrm{T}})^{-1}\, \mathbf{p}_l \\ & \text{s.t.} \quad \mathbf{1}^{\mathrm{T}} \sum_{l=1}^{L} \mathbf{p}_l = 1 \end{aligned} \tag{A.9}$$

Applying the method of Lagrange multipliers, we can obtain the Lagrangian of (A.9) as

$$\mathcal{L}(\mathbf{p}_1, ..., \mathbf{p}_L, \mu) = \sum_{l=1}^{L} \mathbf{p}_l^{\mathrm{T}} (\mathbf{A}_l\, \mathbf{A}_l^{\mathrm{T}})^{-1} \mathbf{p}_l + \mu \left(\mathbf{1}^{\mathrm{T}} \sum_{l=1}^{L} \mathbf{p}_l - 1 \right), \tag{A.10}$$

where μ denotes the Lagrange multiplier. From (A.10), by taking partial derivative with respect to $\mathbf{p}_l$, it follows that

$$\frac{\partial \mathcal{L}(\mathbf{p}_1, ..., \mathbf{p}_L, \mu)}{\partial \mathbf{p}_l} = 2(\mathbf{A}_l\, \mathbf{A}_l^{\mathrm{T}})^{-1} \mathbf{p}_l + \mu\, \mathbf{1}, \tag{A.11}$$

Equating (A.11) to zero, we obtain

$$\mathbf{p}_l^* = -\frac{1}{2} \mu^*\, \mathbf{A}_l\, \mathbf{A}_l^{\mathrm{T}} \mathbf{1}, \tag{A.12}$$

Substituting (A.12) for $\mathbf{p}_l$ in the constraint of $\mathcal{P}2$ results in

$$\begin{aligned} 1 &= -\frac{1}{2} \mathbf{1}^{\mathrm{T}} \sum_{l=1}^{L} \mu^*\, \mathbf{A}_l\, \mathbf{A}_l^{\mathrm{T}} \mathbf{1} \\ &= -\frac{1}{2} \mu^* \sum_{l=1}^{L} \mathbf{1}^{\mathrm{T}} \mathbf{A}_l\, \mathbf{A}_l^{\mathrm{T}} \mathbf{1} \\ &= -\mu^* \sum_{l=1}^{L} 1 + \cos \phi_l, \end{aligned} \tag{A.13}$$

From (A.13), we obtain

$$\mu^* = \frac{-1}{\sum_{l=1}^{L} 1 + \cos \phi_l} \tag{A.14}$$

By replacing μ^* in (A.12), the optimal solution to $\mathcal{P}2$ is obtained by

$$\mathbf{p}_l^* = \frac{1 + \cos \phi_l}{2 \sum_{l=1}^{L} 1 + \cos \phi_l} \mathbf{1}, \tag{A.15}$$

It is immediate from (A.15) that $\mathbf{p}_l^* \succeq \mathbf{0}$ for all $l = 1, 2, ..., L$. Therefore, $\mathbf{p}^* = [\mathbf{p}_1^*, ..., \mathbf{p}_L^*]^{\mathrm{T}}$ is also a feasible (and clearly the optimal) solution to the problem $\mathcal{P}1$. Thus, problems $\mathcal{P}1$ and $\mathcal{P}2$ are equivalent. The optimum of $\mathcal{P}1$ can then be computed by substituting (A.15) in the objective function of $\mathcal{P}2$, which yields

$$\sum_{l=1}^{L} \mathbf{p}_l^{*T} (\mathbf{A}_l \, \mathbf{A}_l^{\mathrm{T}})^{-1} \, \mathbf{p}_l^* = \frac{1}{2} \left(\frac{1}{L + \sum_{l=1}^{L} \cos \phi_l} \right). \tag{A.16}$$

Finally, plugging(A.16) into (A.4), gives the following positive lower bound on τ^2:

$$\tau^2 \geq \frac{\lambda}{2L} \left(\frac{1}{L + \sum_{l=1}^{L} \cos \phi_l} \right) \triangleq \tau_{\min}^2. \tag{A.17}$$

A.2 Proof of Theorem 7

Using the lower bound $\tau_{\min}^2$ provided in (A.17), the regularizing function can be evaluated as

$$f(\bar{\mathbf{H}}, \mathbb{X}) = \frac{\lambda}{2} \, \mathrm{E} \left\{ \frac{1}{L^2 + L \sum_{l=1}^{L} \cos \phi_l} \right\}. \tag{A.18}$$

The reciprocal form of the expectation's argument in (A.18) is nonlinear in both L and $\cos \phi_l$, which makes the expectation computationally intractable. Denoting $\Phi \triangleq L^2 + L \sum_{l=1}^{L} \cos \phi_l$ and using the Taylor expansion of $\mathrm{E}\{1/\Phi\}$ around $\mathrm{E}\{\Phi\}$, we can obtain an approximation for the regularizing function as

$$f(\bar{\mathbf{H}}, \mathbb{X}) \approx \frac{\lambda}{2} \left(\frac{1}{\mathrm{E}\left\{\Phi\right\}} + \mathcal{O}\left(\frac{1}{\mathrm{E}\left\{\Phi\right\}^3} \right) \right). \tag{A.19}$$

Next, we can write $\mathrm{E}\{\Phi\}$ as

$$\mathrm{E}\{\Phi\} = \mathrm{E}\left\{L^2\right\} + \mathrm{E}\left\{ L \sum_{l=1}^{L} \cos \phi_l \right\} \tag{A.20}$$

Recall that L is a binomial random process with a success rate $M_{\mathrm{b}}/M \triangleq \beta$ over a total number of K trials. Hence $\mathrm{E}\{L\} = K\beta$, $\mathrm{Var}\{L\} = K\beta(1-\beta)$, and $\mathrm{E}\{L^2\} = K\beta(1-\beta) + K^2\beta^2$. On the other hand, the second expectation in the right-hand side of (A.20) is obtained as

$$\begin{aligned}
&\mathrm{E}\left\{L\sum_{l=1}^{L}\cos\phi_l\right\}\\
&=\sum_{j=0}^{K}\mathrm{E}\left\{L\sum_{l=1}^{L}\cos\phi_l\middle|L=j\right\}\Pr\{L=j;K,\beta\}\\
&=\sum_{j=0}^{K}\mathrm{E}\left\{j\sum_{l=1}^{j}\cos\phi_l\right\}\Pr\{L=j;K,\beta\}\\
&=\mathrm{E}\left\{\cos\phi_l\right\}\sum_{j=0}^{K}j^2\,\Pr\{L=j;K,\beta\}\\
&=\mathrm{E}\left\{\cos\phi_l\right\}\left(K\beta(1-\beta)+K^2\beta^2\right).
\end{aligned}\tag{A.21}$$

Consequently,

$$\mathrm{E}\{\Phi\}=\left(K\beta(1-\beta)+K^2\beta^2\right)\left(1+\mathrm{E}\left\{\cos\phi_l\right\}\right)\tag{A.22}$$

Due to the fact that $\mathrm{E}\left\{\Phi\right\}^3\approx\mathcal{O}(K^6)$, for moderately large values of K, it follows from (A.19) and (A.22) that

$$\begin{aligned}
f(\bar{\mathbf{H}},\mathbb{X})&\approx\frac{\lambda}{2}\left(\frac{1}{\mathrm{E}\left\{\Phi\right\}}\right)\\
&=\frac{\lambda}{2}\left(\frac{1}{(K\beta(1-\beta)+K^2\beta^2)}\right)\left(\frac{1}{1+\mathrm{E}\left\{\cos\phi_l\right\}}\right).
\end{aligned}\tag{A.23}$$

It is worth noting that Φ is strictly positive on $[0,\pi)$, thus $1/\Phi$ is strictly convex in the given interval. As a result, based on the Jensen's inequality, we have $\mathrm{E}\{1/\Phi\}\geq 1/\mathrm{E}\{\Phi\}$, which means that the approximation in (A.23) is in fact a lower bound on $f(\bar{\mathbf{H}},\mathbb{X})$.

We further remark that the expectation $\mathrm{E}\left\{\cos\phi_l\right\}$ must be taken over symbol time. However, for a sufficiently large number of symbol periods, by a direct application of the law of large numbers, this expectation can equally be taken over the constellation $\mathbb{X}$, i.e.,

$$\mathrm{E}\{\cos\phi_l\}=\frac{1}{M_\mathrm{b}}\sum_{i\in\mathbf{bd}(\mathbb{X})}\cos\phi_i.\tag{A.24}$$

Replacing the expectation (A.24) in (A.23) yields the expression provided in Theorem 7.

Bibliography

[1] R. Radhakrishnan, W. Edmonson, F. Afghah, R. Rodriguez-Osorio, F. Pinto, and S. Burleigh, "Survey of Inter-satellite Communication for Small Satellite Systems: Physical Layer to Network Layer View," *IEEE Communications Surveys and Tutorials*, vol. 18, no. 4, pp. 2442–2473, sep 2016. [Online]. Available: http://arxiv.org/abs/1609.08583

[2] R. Mudumbai, G. Barriac, and U. Madhow, "On the feasibility of distributed beamforming in wireless networks," *IEEE Transactions on Wireless Communications*, vol. 6, no. 5, pp. 1754–1763, May 2007.

[3] F. Adachi, A. Boonkajay, T. Saito, and Y. Seki, "Distributed mimo cooperative transmission technique and its performance," in *2019 IEEE/CIC International Conference on Communications in China (ICCC)*, 2019, pp. 213–218.

[4] G. Krieger, I. Hajnsek, K. P. Papathanassiou, M. Younis, and A. Moreira, "Interferometric synthetic aperture radar (sar) missions employing formation flying," *Proceedings of the IEEE*, vol. 98, no. 5, pp. 816–843, May 2010.

[5] P. Savazzi and A. Vizziello, "Carrier synchronization in distributed mimo satellite links," in *2015 IEEE International Conference on Wireless for Space and Extreme Environments (WiSEE)*, 2015, pp. 1–6.

[6] R. J. Barton, "Distributed MIMO Communication Using Small Satellite Constellations," in *IEEE International Conference on Wireless for Space and Extreme Environments (WiSEE)*. IEEE, 2014.

[7] Y. Chen, D. Liang, H. Yue, D. Liu, X. Wu, H. Zhang, Y. Jiao, K. Liu, and R. Wang, "Implementation of a Phase Synchronization Scheme Based on Pulsed Signal at Carrier Frequency for," *Sensors*, pp. 1–14, 2020.

[8] J. C. Merlano-Duncan, L. Martinez-Marrero, J. Querol, S. Kumar, A. Camps, S. Chatzinotas, and B. Ottersten, “A Remote Carrier Synchronization Technique for Coherent Distributed Remote Sensing Systems,” *IEEE Journal of Selected Topics in Applied Earth Observations and Remote Sensing*, vol. 14, pp. 1909–1922, 2021.

[9] Z. H. U. Yaowei, X. U. Zhaobin, J. I. N. Xiaojun, G. U. O. Xiaoxu, and J. I. N. Zhonghe, “Integrated method for measuring distance and time difference between small satellites,” in *Journal of Systems Engineering and Electronics*, vol. 32, no. 3, 2021, pp. 596–606.

[10] X. Jiuling, Z. Chaojie, W. Chunhui, and J. Xiaojun, “Approach to inter-satellite time synchronization for micro-satellite cluster,” *Journal of Systems Engineering and Electronics*, vol. 29, no. 4, pp. 805–815, 2018.

[11] H. J. Ma, H. Wu, J. Wu, M. Li, K. Wang, Z. He, and D. Zhao, “Design and implementation of dual one-way precise ranging and time synchronization system,” in *2013 Joint European Frequency and Time Forum and International Frequency Control Symposium, EFTF/IFC 2013*, vol. 3, no. 4. IEEE, 2013, pp. 831–834.

[12] Z. Qu, J. Chen, and N. Wu, “Consensus clock synchronization for distributed satellite system based on distributed pi controller,” in *2021 IEEE 15th International Conference on Electronic Measurement and Instruments (ICEMI)*, 2021, pp. 114–119.

[13] P. Sundaramoorthy, E. Gill, and C. Verhoeven, “Beamforming with spacecraft under reduced localization and clock constraints,” *IEEE Transactions on Aerospace and Electronic Systems*, vol. 52, no. 3, pp. 1197–1208, 2016.

[14] L. Gun and H. Feijiang, “Precise two way time synchronization for distributed satellite system,” in *2009 IEEE International Frequency Control Symposium Joint with the 22nd European Frequency and Time forum*. IEEE, apr 2009, pp. 1122–1126. [Online]. Available: http://ieeexplore.ieee.org/document/5168372/

[15] H. Yan, S. Hanna, K. Balke, R. Gupta, and D. Cabric, “Software Defined Radio Implementation of Carrier and Timing Synchronization for Distributed Arrays,” in *2019 IEEE Aerospace Conference*, nov 2018. [Online]. Available: http://arxiv.org/abs/1811.02098

[16] M. A. Vazquez, A. Perez-Neira, D. Christopoulos, S. Chatzinotas, B. Ottersten, P.-D. Arapoglou, A. Ginesi, and G. Tarocco, "Precoding in Multibeam Satellite Communications: Present and Future Challenges," *IEEE Wireless Communications*, vol. 23, no. December, pp. 88–95, 2016.

[17] O. Kodheli, E. Lagunas, N. Maturo, S. K. Sharma, B. Shankar, J. F. M. Montoya, J. C. M. Duncan, D. Spano, S. Chatzinotas, S. Kisseleff, J. Querol, L. Lei, T. X. Vu, and G. Goussetis, "Satellite Communications in the New Space Era: A Survey and Future Challenges," *IEEE Communications Surveys & Tutorials*, pp. 1–45, 2020. [Online]. Available: http://arxiv.org/abs/2002.08811

[18] L. M. Marrero, J. C. M. Duncan, J. Querol, S. Chatzinotas, A. Camps, and B. Ottersten, "A design strategy for phase synchronization in Precoding-enabled DVB-S2X user terminals," *IEEE International Conference on Communications*, 2021.

[19] J. A. Nanzer, R. L. Schmid, T. M. Comberiate, and J. E. Hodkin, "Open-Loop Coherent Distributed Arrays," *IEEE Transactions on Microwave Theory and Techniques*, vol. 65, no. 5, pp. 1662–1672, may 2017. [Online]. Available: http://ieeexplore.ieee.org/document/7803582/

[20] M. Á. Díaz, N. Courville, C. Mosquera, G. Liva, and G. E. Corazza, "Non-linear interference mitigation for broadband multimedia satellite systems," in *2007 International Workshop on Satellite and Space Communication, IWSSC'07*, 2007, pp. 61–65.

[21] L. Martinez Marrero, J. C. Merlano Duncan, J. Querol, S. Chatzinotas, A. J. Camps Carmona, and B. Ottersten, "Effects of multiple oscillator phase noise in Precoding performance," in *ICSSC2019*, Okinawa, Japan, 2019. [Online]. Available: http://orbilu.uni.lu/handle/10993/40625

[22] L. Galleani, "A tutorial on the two-state model of the atomic clock noise," *Metrologia*, vol. 45, no. 6, 2008.

[23] A. A. Nasir, S. Durrani, H. Mehrpouyan, S. D. Blostein, and R. A. Kennedy, "Timing and carrier synchronization in wireless communication systems: a survey and classification of research in the last 5 years," *Eurasip Journal on Wireless Communications and Networking*, vol. 2016, no. 1, 2016. [Online]. Available: http://dx.doi.org/10.1186/s13638-016-0670-9

[24] B. Sundararaman, U. Buy, and A. D. Kshemkalyani, “Clock synchronization for wireless sensor networks: a survey,” *Ad Hoc Networks*, vol. 3, no. 3, pp. 281–323, may 2005. [Online]. Available: https://linkinghub.elsevier.com/retrieve/pii/S1570870505000144

[25] R. Newman and M. Hammoudeh, “Pennies from Heaven: A retrospective on the use of wireless sensor networks for planetary exploration,” *Proceedings of the 2008 NASA/ESA Conference on Adaptive Hardware and Systems, AHS 2008*, pp. 263–270, 2008.

[26] D. Selva, A. Golkar, O. Korobova, I. L. Cruz, O. L. de Weck, and P. Collopy, “Distributed Earth Satellite Systems : What Is Needed to Move Forward?” *Journal of Aerospace Information Systems*, no. August, 2017.

[27] “Home Globalstar AP,” (Accessed on 05/03/2019). [Online]. Available: https://www.globalstar.com/en-ap/

[28] K. Maine, C. Devieux, and P. Swan, “Overview of IRIDIUM satellite network,” *Wescon Conference Record*, pp. 483–490, 1995.

[29] “SpaceX,” (Accessed on 07/03/2023). [Online]. Available: https://www.spacex.com/

[30] “OneWeb - eoPortal Directory - Satellite Missions,” (Accessed on 05/03/2019). [Online]. Available: https://directory.eoportal.org/web/eoportal/satellite-missions/o/oneweb

[31] B. D. Tapley, S. Bettadpur, M. Watkins, and C. Reigber, “The gravity recovery and climate experiment: Mission overview and early results,” *Geophysical Research Letters*, vol. 31, no. 9, pp. 1–4, may 2004. [Online]. Available: http://doi.wiley.com/10.1029/2004GL019920

[32] G. D. Racca and P. W. McNamara, “The LISA Pathfinder Mission,” *Space Science Reviews*, vol. 151, no. 1-3, pp. 159–181, mar 2010. [Online]. Available: http://link.springer.com/10.1007/s11214-009-9602-x

[33] “PRISMA (Prototype) - eoPortal Directory - Satellite Missions,” (Accessed on 05/03/2019). [Online]. Available: https://directory.eoportal.org/web/eoportal/satellite-missions/p/prisma-prototype

[34] "Technologies / Proba Missions / Space Engineering and Technology / Our Activities / ESA," (Accessed on 05/03/2019). [Online]. Available: http://www.esa.int/Our_Activities/Space_Engineering_Technology/Proba_Missions/Technologies2

[35] E. Maurer, R. Kahle, F. Mrowka, G. Morfill, A. Ohndorf, and S. Zimmermann, "Operational aspects of the TanDEM-X Science Phase," in *SpaceOps 2016 Conference*. Reston, Virginia: American Institute of Aeronautics and Astronautics, may 2016. [Online]. Available: http://arc.aiaa.org/doi/10.2514/6.2016-2459

[36] "The von Karman Institute for Fluid Dynamics," (Accessed on 05/03/2019). [Online]. Available: https://www.qb50.eu/index-2.html

[37] S. Engelen, C. Verhoeven, and M. Bentum, "Olfar, A Radio Telescope Based on Nano-Satellites in Moon Orbit," *AIAA/USU Conference on Small Satellites*, aug 2010. [Online]. Available: https://digitalcommons.usu.edu/smallsat/2010/all2010/20

[38] O. Brown and P. Eremenko, "Fractionated Space Architectures: A Vision for Responsive Space," 2006. [Online]. Available: https://apps.dtic.mil/docs/citations/ADA504007

[39] J. A. Ruiz-De-Azua, A. Calveras, and A. Camps, "A Novel Dissemination Protocol to Deploy Opportunistic Services in Federated Satellite Systems," *IEEE Access*, vol. 8, pp. 142 348 – 142 365, 2020.

[40] A. Camps, J. F. Munoz-Martin, J. A. Ruiz-de Azua, L. Fernandez, A. Perez-Portero, D. Llavería, C. Herbert, M. Pablos, A. Golkar, A. Gutiérrez, C. António, J. Bandeiras, J. Andrade, D. Cordeiro, S. Briatore, N. Garzaniti, F. Nichele, R. Mozzillo, A. Piumatti, M. Cardi, M. Esposito, C. van Dijk, N. Vercruyssen, J. Barbosa, J. Hefele, R. Koeleman, B. C. Dominguez, M. Pastena, G. Filippazzo, and A. Reagan, "Fsscat: The federated satellite systems 3cat mission: Demonstrating the capabilities of cubesats to monitor essential climate variables of the water cycle [instruments and missions]," *IEEE Geoscience and Remote Sensing Magazine*, vol. 10, no. 4, pp. 260–269, 2022.

[41] S. Prager, M. S. Haynes, and M. Moghaddam, "Wireless Subnanosecond RF Synchronization for Distributed Ultrawideband Software-Defined Radar Networks," *IEEE Transactions on Microwave Theory and Techniques*, vol. 68, no. 11, pp. 4787–4804, 2020.

[42] H. Poincaré, “La mesure du temps,” *Revue de Métaphysique et de Morale*, vol. 6, no. 1, pp. 1–13, 1898.

[43] A. Einsten, “Zur elektrodynamik bewegter körper,” *Annalen der Physik*, vol. 322, no. 10, pp. 891–921, 1905.

[44] D. Kirchner, “Two-Way Time Transfer Via Communication Satellites,” *Proceedings of the IEEE*, vol. 79, no. 7, pp. 983–990, 1991.

[45] Z. Shengkang and Z. Li, “Ultra-Short Term Clock Offset Prediction for Two- Way Satellite Time Synchronization,” in *2013 Joint European Frequency and Time Forum and International Frequency Control Symposium (EFTF/IFC)*. IEEE, 2013, pp. 335–338.

[46] L. Xiaochun, “Autonomous Time Synchronization Algorithm and Time Synchronization Link Performance Analysis in the Satellite Constellation,” in *6th International Conference on Wireless Communications Networking and Mobile Computing (WiCOM)*, no. 10673011. IEEE, 2010, pp. 15–18.

[47] L. J. Pan, T. Jiang, L. Y. Zhou, H. Xu, and W. D. Chen, “A research on high-precision time-synchronization and ranging system between satellites,” *2008 International Conference on Microwave and Millimeter Wave Technology Proceedings, ICMMT*, vol. 2, no. 1, pp. 926–929, 2008.

[48] D. L. Mills, *Computer Network Time Synchronization: The Network Time Protocol on Earth and in Space*, 2nd ed. CRC Press, 2006.

[49] *IEEE Standard for a Precision Clock Synchronization Protocol for Networked Measurement and Control Systems.* IEEE Standard 1588-2008, 2008.

[50] B. Shi, D. Zhang, and J. Hu, “Preliminary Investigation in Wide Area Protection Protocol,” in *2015 IEEE International Symposium on Precision Clock Synchronization for Measurement, Control, and Communication (ISPCS)*. IEEE, 2015.

[51] E. F. Dierikx, A. E. Wallin, T. Fordell, J. Myyry, P. Koponen, M. Merimaa, T. J. Pinkert, J. C. Koelemeij, H. Z. Peek, and R. Smets, “White rabbit precision time protocol on long-distance fiber links,” *IEEE Transactions on Ultrasonics, Ferroelectrics, and Frequency Control*, vol. 63, no. 7, pp. 945–952, 2016.

[52] K. L. Noh, Q. M. Chaudhari, E. Serpedin, and B. W. Suter, “Novel clock phase offset and skew estimation using two-way timing message exchanges for wireless sensor networks,” *IEEE Transactions on Communications*, vol. 55, no. 4, pp. 766–777, 2007.

[53] J. Elson, L. Girod, and D. Estrin, “Fine-grained network time synchronization using reference broadcasts,” *SIGOPS Oper. Syst. Rev.*, vol. 36, no. SI, p. 147–163, Dec. 2003. [Online]. Available: https://doi.org/10.1145/844128.844143

[54] K. L. Noh, E. Serpedin, and K. Qaraqe, “A new approach for time synchronization in wireless sensor networks: Pairwise broadcast synchronization,” *IEEE Transactions on Wireless Communications*, vol. 7, no. 9, pp. 3318–3322, 2008.

[55] S. Rucksana, C. Babu, and S. Saranyabharathi, “Efficient timing-sync protocol in wireless sensor network,” in *2015 International Conference on Innovations in Information, Embedded and Communication Systems (ICIIECS).* Coimbatore, India: IEEE, 2015.

[56] M. Maróti, B. Kusy, G. Simon, and Á. Lédeczi, “The flooding time synchronization protocol,” in *SenSys’04 - Proceedings of the Second International Conference on Embedded Networked Sensor Systems*, no. January, 2004, pp. 39–49.

[57] F. Shi, S. Member, X. Tuo, S. X. Yang, S. Member, and J. Lu, “Rapid-Flooding Time Synchronization for Large-Scale Wireless Sensor Networks,” *IEEE Transactions on Industrial Informatics*, vol. 16, no. 3, pp. 1581–1590, 2020.

[58] S. Roehr, P. Guldeny, and M. Vossiek, “Method for high precision clock synchronization in wireless systems with application to radio navigation,” in *Proceedings - 2007 IEEE Radio and Wireless Symposium, RWS*, 2007, pp. 551–554.

[59] H. Fiedler, G. Krieger, M. Zink, M. Younis, M. Bachmann, S. Huber, I. Hajnsek, and A. Moreira, “The TanDEM-X mission: an overview,” in *2008 International Conference on Radar.* IEEE, 9 2008, pp. 60–64. [Online]. Available: http://ieeexplore.ieee.org/document/4653892/

[60] D. Zachariah, S. Dwivedi, P. Handel, and P. Stoica, “Scalable and Passive Wireless Network Clock Synchronization in LOS Environments,” *IEEE Transactions on Wireless Communications*, vol. 16, no. 6, pp. 3536–3546, 2017.

[61] M. Segura, S. Niranjayan, H. Hashemi, and A. F. Molisch, "Experimental demonstration of nanosecond-accuracy wireless network synchronization," in *IEEE International Conference on Communications*, vol. 2015-Septe. IEEE, 2015, pp. 6205–6210.

[62] B. Denis, J. B. Pierrot, and C. Abou-Rjeily, "Joint distributed synchronization and positioning in UWB Ad Hoc networks using TOA," *IEEE Transactions on Microwave Theory and Techniques*, vol. 54, no. 4, pp. 1896–1910, 2006.

[63] A. Dongare, P. Lazik, N. Rajagopal, and A. Rowe, "Pulsar: A wireless propagation-aware clock synchronization platform," in *Proceedings of the IEEE Real-Time and Embedded Technology and Applications Symposium, RTAS*. IEEE, 2017, pp. 283–292.

[64] S. Knappe, V. Shah, P. D. D. Schwindt, L. Hollberg, and J. Kitching, "A microfabricated atomic clock," *Applied Physics Letters*, vol. 85, no. 9, 2004.

[65] R. Exel, "Receiver design for time-based ranging with IEEE 802.11b signals," *International Journal of Navigation and Observation*, vol. 2012, 2012.

[66] F. Gardner, "A bpsk/qpsk timing-error detector for sampled receivers," *IEEE Transactions on Communications*, vol. 34, no. 5, pp. 423–429, 1986.

[67] T. Schmidl and D. Cox, "Robust frequency and timing synchronization for ofdm," *IEEE Transactions on Communications*, vol. 45, no. 12, pp. 1613–1621, 1997.

[68] S. Jayaprakasam, S. K. A. Rahim, and C. Y. Leow, "Distributed and Collaborative Beamforming in Wireless Sensor Networks: Classifications, Trends, and Research Directions," *IEEE Communications Surveys and Tutorials*, vol. 19, no. 4, pp. 2092–2116, 2017. [Online]. Available: http://ieeexplore.ieee.org/document/7959572/

[69] U. M. Raghuraman Mudumbai, Ben Wild and K. Ramchandran, "Distributed Beamforming using 1 Bit Feedback: from Concept to Realization," in *Proc. 44th Allerton Conf. Commun., Control, Comp.,*. Monticello, IL: Springer, 2006, pp. 1020–1027. [Online]. Available: https://www.semanticscholar.org/paper/Distributed-Beamforming-using-1-Bit-Feedback-{%}3A-from-Mudumbai-Wild/5d90988c0a82b8ac6d81e5f133a27c6f4fd34fe6

[70] I. Thibault, G. E. Corazza, and L. Deambrogio, "Random, deterministic, and hybrid algorithms for distributed beamforming," in *2010 5th Advanced*

Satellite Multimedia Systems Conference and the 11th Signal Processing for Space Communications Workshop. IEEE, sep 2010, pp. 221–225. [Online]. Available: http://ieeexplore.ieee.org/document/5586901/

[71] J. Lee, S. Lee, and J. Park, "Fast Phase Synchronization with Clustering and One-Bit Feedback for Distributed Beamforming in a Wireless Sensor Network," in *2018 IEEE 87th Vehicular Technology Conference (VTC Spring)*. IEEE, jun 2018, pp. 1–4. [Online]. Available: https://ieeexplore.ieee.org/document/8417563/

[72] M.-O. Pun, D. Brown, and H. Poor, "Opportunistic collaborative beamforming with one-bit feedback," *IEEE Transactions on Wireless Communications*, vol. 8, no. 5, pp. 2629–2641, may 2009. [Online]. Available: http://ieeexplore.ieee.org/document/4927478/

[73] C.-S. Tseng, J. Denis, and C. Lin, "On the Robust Design of Adaptive Distributed Beamforming for Wireless Sensor/Relay Networks," *IEEE Transactions on Signal Processing*, vol. 62, no. 13, pp. 3429–3441, jul 2014. [Online]. Available: http://ieeexplore.ieee.org/document/6823738/

[74] S. Song, J. S. Thompson, P.-J. Chung, and P. M. Grant, "Exploiting Negative Feedback Information for One-Bit Feedback Beamforming Algorithm," *IEEE Transactions on Wireless Communications*, vol. 11, no. 2, pp. 516–525, feb 2012. [Online]. Available: http://ieeexplore.ieee.org/document/6112152/

[75] N. Xie, K. Xu, and J. Chen, "Exploiting Cumulative Positive Feedback Information for One-Bit Feedback Synchronization Algorithm," *IEEE Transactions on Vehicular Technology*, vol. 67, no. 7, pp. 5821–5830, jul 2018. [Online]. Available: https://ieeexplore.ieee.org/document/8270599/

[76] I. Thibault, A. Faridi, G. E. Corazza, A. V. Coralli, and A. Lozano, "Design and Analysis of Deterministic Distributed Beamforming Algorithms in the Presence of Noise," *IEEE Transactions on Communications*, vol. 61, no. 4, pp. 1595–1607, apr 2013. [Online]. Available: http://ieeexplore.ieee.org/document/6461034/

[77] W. Tushar, D. B. Smith, A. Zhang, T. A. Lamahewa, and T. Abhayapala, "Distributed transmit beamforming: Phase convergence improvement using enhanced

one-bit feedback," in *2012 IEEE Wireless Communications and Networking Conference (WCNC)*. IEEE, apr 2012, pp. 528–532. [Online]. Available: http://ieeexplore.ieee.org/document/6214424/

[78] P. Jeevan, S. Pollin, A. Bahai, and P. P. Varaiya, "Pairwise Algorithm for Distributed Transmit Beamforming," in *2008 IEEE International Conference on Communications*. IEEE, 2008, pp. 4245–4249. [Online]. Available: http://ieeexplore.ieee.org/document/4533833/

[79] A. Kumar, R. Mudumbai, and S. Dasgupta, "Scalable algorithms for joint beam and null-forming using distributed antenna arrays," in *2014 IEEE Global Communications Conference*. IEEE, dec 2014, pp. 4042–4047. [Online]. Available: http://ieeexplore.ieee.org/document/7037440/

[80] S. Goguri, B. Peiffer, R. Mudumbai, and S. Dasgupta, "A class of scalable feedback algorithms for beam and null-forming from distributed arrays," in *2016 50th Asilomar Conference on Signals, Systems and Computers*. IEEE, nov 2016, pp. 1447–1451. [Online]. Available: http://ieeexplore.ieee.org/document/7869616/

[81] D. R. Brown, P. Bidigare, S. Dasgupta, and U. Madhow, "Receiver-coordinated zero-forcing distributed transmit nullforming," in *2012 IEEE Statistical Signal Processing Workshop (SSP)*. IEEE, aug 2012, pp. 269–272. [Online]. Available: http://ieeexplore.ieee.org/document/6319679/

[82] D. R. Brown, R. David, and P. Bidigare, "Improving coherence in distributed MISO communication systems with local accelerometer measurements," in *2015 49th Annual Conference on Information Sciences and Systems (CISS)*. IEEE, mar 2015, pp. 1–6. [Online]. Available: http://ieeexplore.ieee.org/document/7086846/

[83] D. Brown, G. Prince, and J. McNeill, "A method for carrier frequency and phase synchronization of two autonomous cooperative transmitters," in *IEEE 6th Workshop on Signal Processing Advances in Wireless Communications, 2005*. IEEE, 2005, pp. 260–264. [Online]. Available: http://ieeexplore.ieee.org/document/1505912/

[84] L. Belostotski, T. Landecker, and D. Routledge, "A technique for microwave ranging and remote phase synchronization," *IEEE Transactions on Instrumentation*

and Measurement, vol. 51, no. 3, pp. 551–559, jun 2002. [Online]. Available: http://ieeexplore.ieee.org/document/1017727/

[85] D. Brown and H. Poor, "Time-Slotted Round-Trip Carrier Synchronization for Distributed Beamforming," *IEEE Transactions on Signal Processing*, vol. 56, no. 11, pp. 5630–5643, nov 2008. [Online]. Available: http://ieeexplore.ieee.org/document/4542555/

[86] M. Mañosas-Caballú and G. Seco-Granados, "Robust time-slotted round-trip carrier and timing synchronization for distributed beamforming," in *Proceedings of the ... European Signal Processing Conference (EUSIPCO).*, Barcelona, Spain, 2011. [Online]. Available: https://ieeexplore-ieee-org.proxy.bnl.lu/document/7073883

[87] S. B. Amor, S. Affes, F. Bellili, U. Vilaipornsawai, L. Zhang, and P. Zhu, "Multi-Node ML Time and Frequency Synchronization for Distributed MIMO-Relay Beamforming Over Time-Varying Flat-Fading Channels," *IEEE Transactions on Communications*, vol. 67, no. 4, pp. 2702–2715, apr 2019. [Online]. Available: https://ieeexplore.ieee.org/document/8585093/

[88] M. A. Alvarez and U. Spagnolini, "Distributed Time and Carrier Frequency Synchronization for Dense Wireless Networks," *IEEE Transactions on Signal and Information Processing over Networks*, vol. 4, no. 4, pp. 683–696, dec 2018. [Online]. Available: https://ieeexplore.ieee.org/document/8309380/

[89] Y.-S. Tu and G. Pottie, "Coherent cooperative transmission from multiple adjacent antennas to a distant stationary antenna through AWGN channels," in *Vehicular Technology Conference. IEEE 55th Vehicular Technology Conference. VTC Spring 2002 (Cat. No.02CH37367)*, vol. 1, no. February 2002. IEEE, 2002, pp. 130–134. [Online]. Available: http://ieeexplore.ieee.org/document/1002678/

[90] H. Ochiai, P. Mitran, H. Poor, and V. Tarokh, "Collaborative beamforming for distributed wireless ad hoc sensor networks," *IEEE Transactions on Signal Processing*, vol. 53, no. 11, pp. 4110–4124, nov 2005. [Online]. Available: http://ieeexplore.ieee.org/document/1519680/

[91] G. Barriac, R. Mudumbai, and U. Madhow, "Distributed Beamforming for Information Transfer in Sensor Networks," in *IPSN 2004 : Third International*

Symposium on Information Processing in Sensor Networks. Berkeley, California, USA: Association for Computing Machinery, 2004, p. 452. [Online]. Available: https://ieeexplore-ieee-org.proxy.bnl.lu/document/1307326

[92] M. M. Rahman, S. Dasgupta, and R. Mudumbai, "A distributed consensus approach to synchronization of RF signals," in *2012 IEEE Statistical Signal Processing Workshop, SSP 2012.* IEEE, 2012, pp. 281–284.

[93] R. D. Preuss and D. R. Brown, "Two-Way Synchronization for Coordinated Multicell Retrodirective Downlink Beamforming," *IEEE Transactions on Signal Processing*, vol. 59, no. 11, pp. 5415–5427, nov 2011. [Online]. Available: http://ieeexplore.ieee.org/document/5957340/

[94] T. P. Bidigare, U. Madhow, D. R. Brown, R. Mudumbai, A. Kumar, B. Peiffer, and S. Dasgupta, "Wideband distributed transmit beamforming using channel reciprocity and relative calibration," in *2015 49th Asilomar Conference on Signals, Systems and Computers.* IEEE, nov 2015, pp. 271–275. [Online]. Available: http://ieeexplore.ieee.org/document/7421129/

[95] Ning Xie, Xu Bao, Hui Wang, and Xiaohui Lin, "Fast open-loop synchronization for distributed downlink beamforming," in *2013 47th Annual Conference on Information Sciences and Systems (CISS).* IEEE, mar 2013, pp. 1–6. [Online]. Available: http://ieeexplore.ieee.org/document/6552293/

[96] A. Bletsas, A. Lippman, and J. Sahalos, "Simple, zero-feedback, distributed beamforming with unsynchronized carriers," *IEEE Journal on Selected Areas in Communications*, vol. 28, no. 7, pp. 1046–1054, sep 2010. [Online]. Available: http://ieeexplore.ieee.org/document/5555903/

[97] A. Bletsas, A. Lippman, and J. N. Sahalos, "Zero-Feedback, Collaborative Beamforming for Emergency Radio: Asymptotic Analysis," *Mobile Networks and Applications*, vol. 16, no. 5, pp. 589–599, oct 2011. [Online]. Available: http://link.springer.com/10.1007/s11036-010-0276-0

[98] D. Richard Brown, P. Bidigare, and U. Madhow, "Receiver-coordinated distributed transmit beamforming with kinematic tracking," in *2012 IEEE International*

Conference on Acoustics, Speech and Signal Processing (ICASSP). IEEE, mar 2012, pp. 5209–5212. [Online]. Available: http://ieeexplore.ieee.org/document/6289094/

[99] T. M. Comberiate, K. S. Zilevu, J. E. Hodkin, and J. A. Nanzer, "Distributed transmit beamforming on mobile platforms using high-accuracy microwave wireless positioning," in *Proc. of SPIE Conference*, K. I. Ranney and A. Doerry, Eds., vol. 9829. International Society for Optics and Photonics, may 2016, p. 98291S. [Online]. Available: http://proceedings.spiedigitallibrary.org/proceeding.aspx?doi=10.1117/12.2231793

[100] J. E. Hodkin, K. S. Zilevu, M. D. Sharp, T. M. Comberiate, S. M. Hendrickson, M. J. Fitch, and J. A. Nanzer, "Microwave and millimeter-wave ranging for coherent distributed RF systems," *IEEE Aerospace Conference Proceedings*, vol. 2015-June, pp. 1–7, 2015.

[101] M. Ming, Y. Luo, Y. R. Liang, J. Y. Zhang, H. Z. Duan, H. Yan, Y. Z. Jiang, L. F. Lu, Q. Xiao, Z. Zhou, and H. C. Yeh, "Ultraprecision intersatellite laser interferometry," *International Journal of Extreme Manufacturing*, vol. 2, no. 2, 2020.

[102] F. Ales, P. F. Gath, U. Johann, and C. Braxmaier, "Modeling and simulation of a laser ranging interferometer acquisition and guidance algorithm," *Journal of Spacecraft and Rockets*, vol. 51, no. 1, pp. 226–238, 2014.

[103] D. Bykhovsky, D. Kedar, and S. Arnon, "Fiber-ring delay line for high-resolution intersatellite ranging," *IEEE Photonics Technology Letters*, vol. 27, no. 6, pp. 673–676, 2015.

[104] Y. Luo, H. Li, Y. Liang, H. Z. Duan, J. Zhang, and H. C. Yeh, "A preliminary prototype of laser frequency stabilization for spaceborne interferometry missions," in *2016 European Frequency and Time Forum, EFTF 2016.* IEEE, 2016.

[105] Y. Tian, J. Zhong, X. Lin, H. Yang, and D. Kang, "Inter-Satellite Integrated Laser Communication/Ranging Link with Feedback-Homodyne Detection and Fractional Symbol Ranging," in *2019 IEEE International Conference on Space Optical Systems and Applications, ICSOS 2019*, 2019.

[106] R. M. Calvo, J. Poliak, J. Surof, and R. Wolf, “Evaluation of optical ranging and frequency transfer for the Kepler system : PPreliminary laboratory tests,” in *2020 European Navigation Conference, ENC 2020*, 2020, pp. 1–9.

[107] J. L. Macarthur and A. S. Posner, “Satellite-to-satellite range-rate measurement,” *Geoscience and Remote Sensing, IEEE Transactions on*, vol. GE-23, no. 4, pp. 517–523, 1985.

[108] J. Kim and B. D. Tapley, “Simulation of Dual One-Way Ranging Measurements,” *Journal of Spacecraft and Rockets*, vol. 40, no. 3, pp. 419–425, may 2003. [Online]. Available: https://arc.aiaa.org/doi/10.2514/2.3962

[109] J. Yang, Y. Yang, L. F. Liang, and L. Liu, “Research on digital phase-locked loop about K/Ka-band high precision receiver,” in *Proceedings - 2010 International Conference on Intelligent System Design and Engineering Application, ISDEA 2010*, vol. 2. IEEE, 2010, pp. 185–188.

[110] M. Alawieh, N. Hadaschik, N. Franke, and C. Mutschler, “Inter-satellite ranging in the Low Earth Orbit,” in *2016 10th International Symposium on Communication Systems, Networks and Digital Signal Processing, CSNDSP 2016*. IEEE, 2016.

[111] X. Xiaoyi, W. Chunhui, and J. Zhonghe, “Design, analysis and optimization of random access inter-satellite ranging system,” *Journal of Systems Engineering and Electronics*, vol. 31, no. 5, pp. 871–883, 2020.

[112] L. Wang, X. Li, Y. Yang, and L. Liu, “Research on inter-satellite ranging and velocity measurement method based on Doppler frequency measurement,” in *2012 2nd International Conference on Consumer Electronics, Communications and Networks, CECNet 2012 - Proceedings*, no. 60901017. IEEE, 2012, pp. 3446–3450.

[113] S. Rui, X. Guodong, and L. Shengchang, “Inter-satellite ranging system design in formation,” in *2008 2nd International Symposium on Systems and Control in Aerospace and Astronautics, ISSCAA 2008*. IEEE, 2008, pp. 1–5.

[114] Y. Yang, Y. Li, C. Rizos, A. G. Dempster, and X. Yue, “Inter-satellite ranging augmented GPS relative navigation for satellite formation flying,” *Journal of Navigation*, vol. 67, no. 3, pp. 437–449, 2014.

[115] Z. Wang, H. Huan, and M. Wang, “Determining the Initial Value of Carrier Phase Smoothing Pseudorange by Least Squares Straight Line Fitting Technique,” *Proceedings of 2019 IEEE International Conference on Artificial Intelligence and Computer Applications, ICAICA 2019*, pp. 303–307, 2019.

[116] R. Hatch, “The synergism of GPS code and carrier measurements,” in *3rd International Geodetic Symposium on Satellite Doppler Positioning*, Las Cruces, NM, 1982, pp. 1213–1231.

[117] Y. Tang, Y. Wang, and J. Chen, “Impact of finite bandwidth for inter-satellite ranging using direct sequence spread spectrum signal,” in *2016 IEEE International Conference on Signal and Image Processing, ICSIP 2016.* IEEE, 2017, pp. 488–492.

[118] R. Xue, T. Wang, and H. Tang, “A Novel Chip Pulse Employed by Ranging Code Based on Simultaneous Transmitting CPM Modulation and PN Ranging in Inter-Satellite Links of GNSS,” *IEEE Access*, vol. 8, pp. 132 860–132 870, 2020.

[119] A. M. Crisan, A. Martian, and D. Coltuc, “Inter-satellite radio frequency ranging in a hybrid OFDM communication-metrology system,” *2018 15th Workshop on Positioning, Navigation and Communications, WPNC 2018*, pp. 3–7, 2018.

[120] B. Xiang, F. Yan, Y. Zhang, F. Shen, W. Xia, and L. Shen, “A New Inter-Satellite Ranging Method Based on Pseudo-Range and Dual-Frequency Carrier Phase,” in *2019 11th International Conference on Wireless Communications and Signal Processing (WCSP).* IEEE, 2019.

[121] B. Xiang, F. Yan, F. Shen, W. Xia, S. Xing, Y. Wu, and L. Shen, “Selection of frequency pairs and accuracy analysis in inter-satellite carrier ranging,” in *2019 IEEE Globecom Workshops, GC Wkshps 2019 - Proceedings*, 2019, pp. 0–4.

[122] R. Sun, J. Guo, and E. Gill, “Antenna array based line-of-sight estimation using a GNSS-like inter-satellite ranging system,” in *6th ESA Workshop on Satellite Navigation Technologies: Multi-GNSS Navigation Technologies Galileo’s Here, NAVITEC 2012 and European Workshop on GNSS Signals and Signal Processing.* IEEE, 2012.

[123] Z. Yue, B. Lian, and C. Tang, “GPS/INS integrated navigation algorithm based on the double-difference of time/inter-satellite with carrier phase,” in *2017 IEEE International*

Conference on Signal Processing, Communications and Computing, ICSPCC 2017, vol. 2017-Janua, 2017, pp. 1–6.

[124] P. J. Teunissen, "The least-squares ambiguity decorrelation adjustment: a method for fast GPS integer ambiguity estimation," *Journal of Geodesy*, vol. 70, pp. 65–82, 1995.

[125] J. Wendel, O. Meister, R. Mönikes, and G. F. Trommer, "Time-differenced carrier phase measurements for tightly coupled GPS/INS integration," in *Record - IEEE PLANS, Position Location and Navigation Symposium*, vol. 2006, 2006, pp. 54–60.

[126] R. Kroes, *Precise Relative Positioning of Formation Flying Spacecraft using GPS.* Doctoral thesis, 2006. [Online]. Available: http://resolver.tudelft.nl/uuid:1a68ee94-3d55-44b9-9d8b-25fa44e96922

[127] O. D'Amico Simone and Montenbruck, "Differential GPS: An Enabling Technology for Formation Flying Satellites," in *Small Satellite Missions for Earth Observation*, H.-P. Sandau Rainer and Roeser and V. Arnoldo, Eds. Berlin, Heidelberg: Springer Berlin Heidelberg, 2010, pp. 457–465.

[128] R. Kroes, O. Montenbruck, W. Bertiger, and P. Visser, "Precise GRACE baseline determination using GPS," *GPS Solutions*, vol. 9, no. 1, pp. 21–31, apr 2005. [Online]. Available: http://link.springer.com/10.1007/s10291-004-0123-5

[129] A. Renga, M. Grassi, and U. Tancredi, "Relative Navigation in LEO by Carrier-Phase Differential GPS with Intersatellite Ranging Augmentation," *International Journal of Aerospace Engineering*, vol. 2013, pp. 1–11, 2013. [Online]. Available: http://www.hindawi.com/journals/ijae/2013/627509/

[130] P. J. G. Nadarajah Nandakumaran and Teunissen and V. Sandra, "Attitude Determination and Relative Positioning for LEO Satellites Using Arrays of GNSS Sensors," in *IAG 150 Years*, P. Rizos Chris and Willis, Ed. Cham: Springer International Publishing, 2016, pp. 743–749.

[131] P. Teunissen, "A General Multivariate Formulation of the Multi-Antenna GNSS Attitude Determination Problem," *Artificial Satellites*, vol. 42, no. 2, jan 2007. [Online]. Available: https://content.sciendo.com/doi/10.2478/v10018-008-0002-3

[132] K. M. Cheung and C. Lee, "A trilateration scheme for relative positioning," *IEEE Aerospace Conference Proceedings*, pp. 1–10, 2017.

[133] M. Casti, S. Fineschi, A. Bemporad, G. Capobianco, F. Landini, D. Loreggia, V. Noce, M. Romoli, C. Thizy, and D. Galano, "Fine positioning algorithms for the ESA/PROBA-3 formation flying mission," *2019 IEEE International Workshop on Metrology for AeroSpace, MetroAeroSpace 2019 - Proceedings*, pp. 121–125, 2019.

[134] G. Capobianco, S. Fineschi, D. Loreggia, A. Bemporad, F. Landini, M. Casti, V. Noce, M. Romoli, D. Galano, and C. Thizy, "The in-flight calibration procedures of the shadow position sensors (SPS), a very accurate optical metrology system of the ESA/PROBA-3 formation flying mission," in *2019 IEEE International Workshop on Metrology for AeroSpace, MetroAeroSpace 2019 - Proceedings*, 2019, pp. 479–483.

[135] L. Buinhas, E. Ferrer-Gil, and R. Forstner, "IRASSI: InfraRed astronomy satellite swarm interferometry - Mission concept and description," in *IEEE Aerospace Conference Proceedings*, vol. 2016-June, 2016.

[136] L. Buinhas, M. Philips-Blum, K. Frankl, T. Pany, B. Eissfeller, and R. Forstner, "Formation operations and navigation concept overview for the IRASSI space interferometer," *IEEE Aerospace Conference Proceedings*, vol. 2018-March, pp. 1–16, 2018.

[137] H. Linz, D. Bhatia, L. Buinhas, M. Lezius, E. Ferrer, R. Förstner, K. Frankl, M. Philips-Blum, M. Steen, U. Bestmann, W. Hänsel, R. Holzwarth, O. Krause, and T. Pany, "InfraRed Astronomy Satellite Swarm Interferometry (IRASSI): Overview and study results," *Advances in Space Research*, vol. 65, no. 2, pp. 831–849, 2020.

[138] M. Weiqing, R. Liu, Y. Xinxin, and E. Kamel, "Analysis of precision estimation of RF metrology in satellite formation flying," in *2015 International Conference on Wireless Communications and Signal Processing, WCSP 2015.* IEEE, 2015, pp. 0–4.

[139] L. R. G. Carrillo, F. M. Palacios, E. S. E. Quesada, and K. Alexis, "Adaptive high order sliding mode control for relative positioning and trajectory tracking of spacecraft formation flying," *24th Mediterranean Conference on Control and Automation, MED 2016*, pp. 1095–1101, 2016.

[140] X. Dan, C. Xibin, and W. Yunhua, “Decentralized determination of relative orbit for formation flying satellite,” in *1st International Symposium on Systems and Control in Aerospace and Astronautics*, vol. 2006, 2006, pp. 338–343.

[141] S. Wang and P. Cui, “Autonomous orbit determination using pulsars and inter-satellite ranging for Mars orbiters,” in *2018 IEEE Aerospace Conference*, Big Sky, MT, USA, 2018.

[142] Z. Liu, L. Du, Y. Zhu, Z. Qian, J. Wang, and S. Liang, “Investigation on GEO satellite orbit determination based on CEI measurements of short baselines,” *The Journal of Navigation*, vol. 72, no. 6, pp. 1585 – 1601, 2019.

[143] M. Sadeghi, F. Behnia, and H. Haghshenas, “Positioning of Geostationary Satellite by Radio Interferometry,” *IEEE Transactions on Aerospace and Electronic Systems*, vol. 55, no. 2, pp. 903–917, 2019.

[144] G. Michalak, K. H. Neumayer, and R. Konig, “Precise orbit determination of the kepler navigation system - A simulation study,” in *2020 European Navigation Conference, ENC 2020*, 2020, pp. 1–10.

[145] L. Chen, H. Lin, Z. Lu, J. Li, and G. Ou, “High Orbital Spacecraft Fast Positioning Algorithm Assisted by Inter-Satellite Links,” in *2019 2nd International Conference on Information Systems and Computer Aided Education, ICISCAE 2019*, 2019, pp. 598–602.

[146] P. P. Sundaramoorthy, E. Gill, and C. J. Verhoeven, “Enhancing ground communication of distributed space systems,” *Acta Astronautica*, vol. 84, pp. 15–23, 2013. [Online]. Available: http://dx.doi.org/10.1016/j.actaastro.2012.10.032

[147] G. Krieger, M. Zonno, J. Mittermayer, A. Moreira, S. Huber, and M. Rodriguez-Cassola, “MirrorSAR: A fractionated space transponder concept for the implementation of low-cost multistatic SAR missions,” in *Proceedings of the European Conference on Synthetic Aperture Radar, EUSAR*, vol. 2018-June, 2018, pp. 1359–1364.

[148] P. Xiao, B. Liu, and W. Guo, “ConGaLSAR: A Constellation of Geostationary and Low Earth Orbit Synthetic Aperture Radar,” *IEEE Geoscience and Remote Sensing Letters*, vol. 17, no. 12, pp. 2085–2089, 2020.

[149] J. C. Merlano-Duncan, J. Querol, L. Martinez-Marrero, J. Krivochiza, A. Camps, S. Chatzinotas, and B. Ottersten, "SDR Implementation of a Testbed for Synchronization of Coherent Distributed Remote Sensing Systems," in *IGARSS 2020 - 2020 IEEE International Geoscience and Remote Sensing Symposium*. Waikoloa, HI, USA: IEEE, 2020, pp. 6588–6591.

[150] P. Ubolkosold, S. Knedlik, and O. Loffeld, "Clock synchronization protocol for distributed satellite networks," in *Proceedings. 2005 IEEE International Geoscience and Remote Sensing Symposium, 2005. IGARSS '05.*, vol. 1. Seoul, South Korea: IEEE, 2005, pp. 681–684. [Online]. Available: http://ieeexplore.ieee.org/document/1526267/

[151] Y. Zhang, D. Liang, and Z. Dong, "Analysis of time and frequency synchronization errors in spaceborne parasitic InSAR system," in *International Geoscience and Remote Sensing Symposium (IGARSS)*. IEEE, 2006, pp. 3047–3050.

[152] M. Younis, R. Metzig, and G. Krieger, "Performance Prediction of a Phase Synchronization Link for Bistatic SAR," *IEEE Geoscience and Remote Sensing Letters*, vol. 3, no. 3, pp. 429–433, jul 2006. [Online]. Available: http://ieeexplore.ieee.org/document/1658020/

[153] Z. He, F. He, H. Huang, and D. Liang, "A hardware-in-loop simulation and evaluation approach for spaceborne distributed SAR," in *International Geoscience and Remote Sensing Symposium (IGARSS)*. IEEE, 2011, pp. 886–889.

[154] J. C. Merlano-Duncan, J. J. Mallorquí, and P. López-Dekker, "Carrier phase synchronisation scheme for very long baseline coherent arrays," *Electronics letters*, vol. 48, no. 15, pp. 950–951, 2012.

[155] A. Monti Guarnieri, A. Broquetas, A. Recchia, F. Rocca, and J. Ruiz-Rodon, "Advanced Radar Geosynchronous Observation System: ARGOS," *IEEE Geoscience and Remote Sensing Letters*, vol. 12, no. 7, pp. 1406–1410, jul 2015. [Online]. Available: http://ieeexplore.ieee.org/document/7055288/

[156] A. M. Guarnieri, A. Broquetas, F. López-dekker, and F. Rocca, "A Geostationary MIMO SAR Swarm for Quasi-continuous Observation," in *IEEE International Geoscience and Remote Sensing Symposium (IGARSS) 2015*, 2015, pp. 2785–2788.

[157] D. Liang, K. Liu, H. Zhang, Y. Deng, D. Liu, Y. Chen, C. Li, H. Yue, and R. Wang, "A High-Accuracy Synchronization Phase-Compensation Method Based on Kalman Filter for Bistatic Synthetic Aperture Radar," *IEEE Geoscience and Remote Sensing Letters*, vol. 17, no. 10, pp. 1722–1726, 2019.

[158] G. Jin, R. Wang, K. Liu, D. Liu, D. Liang, H. Zhang, N. Ou, Y. Zhang, Y. Deng, and C. Li, "An Advanced Phase Synchronization Scheme for LT-1," *IEEE Transactions on Geoscience and Remote Sensing*, vol. 58, no. 3, pp. 1735–1746, 2020.

[159] Y. Zhang, H. Zhang, N. Ou, K. Liu, D. Liang, Y. Deng, and R. Wang, "First Demonstration of Multipath Effects on Phase Synchronization Scheme for LT-1," *IEEE Transactions on Geoscience and Remote Sensing*, vol. 58, no. 4, pp. 2590–2604, 2020.

[160] D. Liang, K. Liu, H. Zhang, Y. Chen, H. Yue, D. Liu, Y. Deng, H. Lin, T. Fang, C. Li, and R. Wang, "The Processing Framework and Experimental Verification for the Non-interrupted Synchronization Scheme of LuTan-1," *IEEE Transactions on Geoscience and Remote Sensing*, pp. 1–11, 2020.

[161] A. Lovascio, A. D'Orazio, and V. Centonze, "Design of COTS-based radio-frequency receiver for cubesat applications," in *2019 IEEE International Workshop on Metrology for AeroSpace, MetroAeroSpace 2019 - Proceedings*. IEEE, 2019, pp. 399–404.

[162] L. Yu, S. Zhang, N. Wu, and C. Yu, "FPGA-based Hardware-in-the-Loop Simulation of User Selection Algorithms for Cooperative Transmission Technology over LOS Channel on Geosynchronous Satellites," *IEEE Access*, pp. 1–1, 2022.

[163] M. R. Maheshwarappa, M. Bowyer, and C. P. Bridges, "Software Defined Radio (SDR) architecture to support multi-satellite communications," in *IEEE Aerospace Conference Proceedings*, vol. 2015-June. IEEE, 2015, pp. 1–10.

[164] G. Interdonato, E. Björnson, H. Quoc Ngo, P. Frenger, and E. G. Larsson, "Ubiquitous cell-free Massive MIMO communications," *EURASIP Journal on Wireless Communications and Networking*, vol. 2019, no. 1, p. 197, 2019. [Online]. Available: https://doi.org/10.1186/s13638-019-1507-0

[165] Ö. T. Demir and E. Björnson, "Max-Min Fair Wireless-Powered Cell-Free Massive MIMO for Uncorrelated Rician Fading Channels," in *2020 IEEE Wireless Communications and Networking Conference (WCNC)*, 2020, pp. 1–6.

[166] H. Ngo, A. Ashikhmin, H. Yang, E. Larsson, and T. Marzetta, "Cell-free massive mimo versus small cells," *IEEE Wireless Communications*, vol. 16, no. 3, pp. 1834–1850, 1 2017.

[167] S. Jeong, A. Farhang, and M. Flanagan, "Collaborative Vs. Non-Collaborative CFO Estimation for Distributed Large-Scale MIMO Systems," in *IEEE Vehicular Technology Conference*, vol. 2020-Novem, 2020.

[168] G. Borg, Z. U. D. Javaid, and A. Khandaker, "The physical and engineering requirements of scalable, decentralised, distributed, large-scale MIMO," in *Proceedings of the 3rd International Conference on Informatics and Computing, ICIC 2018.* IEEE, 2018, pp. 3–8.

[169] F. Qamar, K. B. Dimyati, M. N. Hindia, K. A. B. Noordin, and A. M. Al-Samman, "A comprehensive review on coordinated multi-point operation for LTE-A," *Computer Networks*, vol. 123, no. May, pp. 19–37, 2017. [Online]. Available: http://dx.doi.org/10.1016/j.comnet.2017.05.003

[170] Z. Gu and Z. Zhang, "Mode selection for CoMP transmission with nonideal synchronization," *China Communications*, vol. 15, no. 12, pp. 132–146, 2018.

[171] Z. Chaloupka, L. Ries, A. Samperi, P. Waller, and M. Crisci, "Phase synchronization for 5G using mass market GNSS receivers," in *2018 European Frequency and Time Forum, EFTF 2018.* IEEE, 2018, pp. 192–196.

[172] V. Jungnickel, K. Manolakis, S. Jaeckel, M. Lossow, P. Farkas, M. Schlosser, and V. Braun, "Backhaul requirements for inter-site cooperation in heterogeneous LTE-Advanced networks," in *2013 IEEE International Conference on Communications Workshops, ICC 2013*, 2013, pp. 905–910.

[173] Y. Tian, K. L. Lee, C. Lim, and A. Nirmalathas, "Performance evaluation of CoMP for downlink 60-GHz radio-over-fiber fronthaul," in *MWP 2017 - 2017 International Topical Meeting on Microwave Photonics*, vol. 2017-Decem, 2017, pp. 1–4.

[174] G. Song, W. Wang, D. Chen, and T. Jiang, "KPI / KQI-Driven Coordinated Multipoint in 5G : Measurements, Field Trials, and Technical Solutions," *IEEE Wireless Communications*, no. October, pp. 23–29, 2018.

[175] A. M. Hamza and J. W. Mark, "A timing synchronization scheme in coordinated basestations cooperative communications," in *2012 International Conference on Wireless Communications and Signal Processing, WCSP 2012*. IEEE, 2012, pp. 3–8.

[176] S. Y. Huang, Y. H. Lin, and J. H. Deng, "Novel time offset pre-processing and interference cancellation for downlink OFDMA CoMP system," in *Proceedings, APWiMob 2014: IEEE Asia Pacific Conference on Wireless and Mobile 2014*. IEEE, 2014, pp. 102–108.

[177] L. Zhao, K. Liang, G. Cao, R. Qian, and D. López-Pérez, "An enhanced signal-timing-offset compensation algorithm for coordinated multipoint-to-multiuser systems," *IEEE Communications Letters*, vol. 18, no. 6, pp. 983–986, 2014.

[178] A. Dammann and R. Raulefs, "Exploiting position information for synchronization in coordinated multipoint transmission," in *IEEE Vehicular Technology Conference*. IEEE, 2013.

[179] H. Pilaram, M. Kiamari, and B. H. Khalaj, "Distributed synchronization and beamforming in uplink relay asynchronous OFDMA CoMP networks," *IEEE Transactions on Wireless Communications*, vol. 14, no. 6, pp. 3471–3480, 2015.

[180] A. M. Hamza, J. W. Mark, and E. A. Sourour, "Interference analysis and mitigation for time-asynchronous OFDM CoMP systems," *IEEE Transactions on Wireless Communications*, vol. 17, no. 7, pp. 4780–4791, 2018.

[181] S. Iwelski, B. Badic, Z. Bai, R. Balraj, C. Kuo, E. Majeed, T. Scholand, G. Bruck, and P. Jung, "Feedback generation for CoMP transmission in unsynchronized networks with timing offset," *IEEE Communications Letters*, vol. 18, no. 5, pp. 725–728, 2014.

[182] M. R. Khanzadi, R. Krishnan, and T. Eriksson, "Effect of synchronizing coordinated base stations on phase noise estimation," in *ICASSP, IEEE International Conference on Acoustics, Speech and Signal Processing - Proceedings*. IEEE, 2013, pp. 4938–4942.

[183] L. Chang, J. Zhang, X. Li, B. Liu, and K. Sun, “Joint synchronization and channel estimation for the uplink coordinated multi-point systems,” in *2012 7th International ICST Conference on Communications and Networking in China, CHINACOM 2012 - Proceedings*. IEEE, 2012, pp. 384–389.

[184] T. Koivisto, T. Kuosmanen, and T. Roman, “Estimation of time and frequency offsets in LTE coordinated multi-point transmission,” in *IEEE Vehicular Technology Conference*. IEEE, 2013, pp. 3–7.

[185] “Octoclock clock distribution module with GPSDO - ETTUS research — ETTUS research, a national instruments brand — the leader in software defined radio (sdr),” https://www.ettus.com/all-products/octoclock-g/, (Accessed on 05/25/2020).

[186] “USRP2 - ETTUS knowledge base,” https://kb.ettus.com/USRP2, (Accessed on 05/25/2020).

[187] F. Quitin, U. Madhow, M. M. U. Rahman, and R. Mudumbai, “Demonstrating distributed transmit beamforming with software-defined radios,” in *2012 IEEE International Symposium on a World of Wireless, Mobile and Multimedia Networks (WoWMoM)*. IEEE, jun 2012, pp. 1–3. [Online]. Available: http://ieeexplore.ieee.org/document/6263729/

[188] Munkyo Seo, M. Rodwell, and U. Madhow, “A feedback-based distributed phased array technique and its application to 60-GHz wireless sensor network,” in *2008 IEEE MTT-S International Microwave Symposium Digest*. IEEE, jun 2008, pp. 683–686. [Online]. Available: http://ieeexplore.ieee.org/document/4632924/

[189] D. Scherber, P. Bidigare, R. ODonnell, M. Rebholz, M. Oyarzun, C. Obranovich, W. Kulp, D. Chang, and D. R. B. III, “Coherent Distributed Techniques for Tactical Radio Networks: Enabling Long Range Communications with Reduced Size, Weight, Power and Cost,” in *MILCOM 2013 - 2013 IEEE Military Communications Conference*. IEEE, nov 2013, pp. 655–660. [Online]. Available: http://ieeexplore.ieee.org/document/6735697/

[190] P. Bidigare, M. Oyarzyn, D. Raeman, D. Chang, D. Cousins, R. O’Donnell, C. Obranovich, and D. R. Brown, “Implementation and demonstration of receiver-coordinated distributed transmit beamforming across an ad-hoc radio network,” in

2012 Conference Record of the Forty Sixth Asilomar Conference on Signals, Systems and Computers (ASILOMAR). IEEE, nov 2012, pp. 222–226. [Online]. Available: http://ieeexplore.ieee.org/document/6488994/

[191] S. Mghabghab, H. Ouassal, and J. A. Nanzer, "Wireless frequency synchronization for coherent distributed antenna arrays," *2019 IEEE International Symposium on Antennas and Propagation and USNC-URSI Radio Science Meeting, APSURSI 2019 - Proceedings*, pp. 1575–1576, 2019.

[192] "USRP X310 high performance software defined radio - ETTUS research — ETTUS research, a national instruments brand — the leader in software defined radio (SDR)," https://www.ettus.com/all-products/x310-kit/, (Accessed on 05/26/2020).

[193] "USRP N210 software defined radio (SDR) - ETTUS research — ETTUS research, a national instruments brand — the leader in software defined radio (SDR)," https://www.ettus.com/all-products/un210-kit/, (Accessed on 05/26/2020).

[194] C. Bocanegra, K. Alemdar, S. Garcia, C. Singhal, and K. R. Chowdhury, "NetBeam: Networked and Distributed 3-D Beamforming for Multi-user Heterogeneous Traffic," in *2019 IEEE International Symposium on Dynamic Spectrum Access Networks (DySPAN).* Newark, NJ, USA, USA: IEEE, 2019, pp. 1–10.

[195] M. M. Rahman, H. E. Baidoo-Williams, R. Mudumbai, and S. Dasgupta, "Fully wireless implementation of distributed beamforming on a software-defined radio platform," in *2012 ACM/IEEE 11th International Conference on Information Processing in Sensor Networks (IPSN).* IEEE, apr 2012, pp. 305–315. [Online]. Available: http://ieeexplore.ieee.org/document/6920945/

[196] R. K. Pooler, J. S. Sunderlin, R. H. Tillman, and R. L. Schmid, "A Precise RF Time Transfer Method for Coherent Distributed System Applications," in *2018 USNC-URSI Radio Science Meeting (Joint with AP-S Symposium).* IEEE, jul 2018, pp. 5–6. [Online]. Available: https://ieeexplore.ieee.org/document/8602642/

[197] R. L. Schmid, T. M. Comberiate, J. E. Hodkin, and J. A. Nanzer, "A Distributed RF Transmitter Using One-Way Wireless Clock Transfer," *IEEE Microwave and Wireless Components Letters*, vol. 27, no. 2, pp. 195–197, feb 2017. [Online]. Available: http://ieeexplore.ieee.org/document/7839937/

[198] B. Peiffer, R. Mudumbai, A. Kruger, A. Kumar, and S. Dasgupta, "Experimental demonstration of a distributed antenna array pre-synchronized for retrodirective transmission," in *2016 Annual Conference on Information Science and Systems (CISS)*. IEEE, mar 2016, pp. 460–465. [Online]. Available: http://ieeexplore.ieee.org/document/7460546/

[199] R. Frank, S. Zadoff, and R. Heimiller, "Phase shift pulse codes with good periodic correlation properties," *IRE Transactions on Information Theory*, vol. 8, no. 6, pp. 381–382, 1962.

[200] M. W. S. Overdick, J. E. Canfield, A. G. Klein, and D. R. B. III, "A software-defined radio implementation of timestamp-free network synchronization," in *IEEE International Conference on Acoustics, Speech, and Signal Processing (ICASSP) 2017*. New Orleans, LA, USA: IEEE, 2017, pp. 1193–1197.

[201] M. A. Alvarez, W. Thompson, and U. Spagnolini, "Distributed time and frequency synchronization: USRP hardware implementation," in *2015 IEEE International Conference on Communication Workshop (ICCW)*. IEEE, jun 2015, pp. 2157–2162. [Online]. Available: http://ieeexplore.ieee.org/document/7247501/

[202] J. Kim and S. W. Lee, "Flight performance analysis of GRACE K-band ranging instrument with simulation data," *Acta Astronautica*, vol. 65, no. 11-12, pp. 1571–1581, 12 2009. [Online]. Available: https://www.sciencedirect.com/science/article/pii/S0094576509002446

[203] J. B. Thomas, "An Analysis of Gravity-Field Estimation Based on Intersatellite Dual-1-Way Biased Ranging," National Aeronautics and Space Administration (NASA), Pasadena, California, Tech. Rep. May, may 1999. [Online]. Available: https://ntrs.nasa.gov/search.jsp?R=20040008637

[204] "LISA - Laser Interferometer Space Antenna - NASA Home Page." [Online]. Available: https://lisa.nasa.gov/

[205] A. Budianu, R. T. Rajan, S. Engelen, A. Meijerink, C. J. Verhoeven, and M. J. Bentum, "OLFAR: Adaptive topology for satellite swarms," in *62nd International Astronautical Congress 2011, IAC 2011*, vol. 9. International

Astronautical Federation (IAF), 10 2011, pp. 7086–7094. [Online]. Available: https://research.utwente.nl/en/publications/olfar-adaptive-topology-for-satellite-swarms

[206] R. T. Rajan, G. Leus, and A.-J. van der Veen, "Joint relative position and velocity estimation for an anchorless network of mobile nodes," *Signal Processing*, vol. 115, pp. 66–78, 10 2015. [Online]. Available: https://www.sciencedirect.com/science/article/pii/S0165168415000894

[207] D. G. Enzer, R. T. Wang, and W. M. Klipstein, "GRAIL- A microwave ranging instrument to map out the lunar gravity field," in *2010 IEEE International Frequency Control Symposium, FCS 2010*. IEEE, 2010, pp. 572–577.

[208] K. Oudrhiri, S. Asmar, S. Esterhuizen, C. Goodhart, N. Harvey, D. Kahan, G. Kruizinga, M. Paik, D. Shin, and L. White, "An innovative direct measurement of the GRAIL absolute timing of Science Data," in *IEEE Aerospace Conference Proceedings*. IEEE, 2014, pp. 1–9.

[209] H. Wu, Z. Sun, and X. Zhou, "Deep learning-based frame and timing synchronization for end-to-end communications," *Journal of Physics: Conference Series*, vol. 1169, pp. 012–060, Feb 2019.

[210] Y. Wang, C. Zhang, Q. Peng, and Z. Wang, "Learning to detect frame synchronization," in *Neural Information Processing*, M. Lee, A. Hirose, Z.-G. Hou, and R. M. Kil, Eds. Berlin, Heidelberg: Springer Berlin Heidelberg, 2013, pp. 570–578.

[211] D. Zibar, L. H. H. de Carvalho, M. Piels, A. Doberstein, J. Diniz, B. Nebendahl, C. Franciscangelis, J. Estaran, H. Haisch, N. G. Gonzalez, J. C. R. F. de Oliveira, and I. T. Monroy, "Application of machine learning techniques for amplitude and phase noise characterization," *Journal of Lightwave Technology*, vol. 33, no. 7, pp. 1333–1343, 2015.

[212] V. D. Nguyen, S. K. Sharma, T. X. Vu, S. Chatzinotas, and B. Ottersten, "Efficient federated learning algorithm for resource allocation in wireless iot networks," *IEEE Internet of Things Journal*, vol. 8, no. 5, pp. 3394–3409, 2021.

[213] J. Zhang, H. Tu, Y. Ren, J. Wan, L. Zhou, M. Li, and J. Wang, "An adaptive synchronous parallel strategy for distributed machine learning," *IEEE Access*, vol. 6, pp. 19 222–19 230, 2018.

[214] A. Gerbessiotis and L. Valiant, "Direct bulk-synchronous parallel algorithms," *Journal of Parallel and Distributed Computing*, vol. 22, no. 2, pp. 251–267, 1994.

[215] V. Mnih, A. P. Badia, M. Mirza, A. Graves, T. Lillicrap, T. Harley, D. Silver, and K. Kavukcuoglu, "Asynchronous methods for deep reinforcement learning," in *Proceedings of The 33rd International Conference on Machine Learning*, ser. Proceedings of Machine Learning Research, M. F. Balcan and K. Q. Weinberger, Eds., vol. 48, New York, New York, USA, 20–22 Jun 2016, pp. 1928–1937.

[216] Q. Ho, J. Cipar, H. Cui, J. K. Kim, S. Lee, P. B. Gibbons, G. A. Gibson, G. R. Ganger, and E. P. Xing, "More effective distributed ml via a stale synchronous parallel parameter server," in *Proceedings of the 26th International Conference on Neural Information Processing Systems - Volume 1*, ser. NIPS'13. Red Hook, NY, USA: Curran Associates Inc., 2013, p. 1223–1231.

[217] J. Wang, W. Tu, L. C. K. Hui, S. M. Yiu, and E. K. Wang, "Detecting time synchronization attacks in cyber-physical systems with machine learning techniques," in *2017 IEEE 37th International Conference on Distributed Computing Systems (ICDCS)*, 2017, pp. 2246–2251.

[218] S. Bae, S. Kim, and J. Kim, "Efficient frequency-hopping synchronization for satellite communications using dehop-rehop transponders," *IEEE Transactions on Aerospace and Electronic Systems*, vol. 52, no. 1, pp. 261–274, 2016.

[219] S. Lee, S. Kim, M. Seo, and D. Har, "Synchronization of frequency hopping by lstm network for satellite communication system," *IEEE Communications Letters*, vol. 23, no. 11, pp. 2054–2058, 2019.

[220] J. Tong, R. Song, Y. Liu, C. Wang, Q. Zhou, and W. Wang, "Enhanced synchronization of 5g integrated satellite systems in multipath channels," in *2020 International Conference on Computer Vision, Image and Deep Learning (CVIDL)*, 2020, pp. 617–621.

[221] H. Guo, Q. Yang, H. Wang, Y. Hua, T. Song, R. Ma, and H. Guan, "Spacedml: Enabling distributed machine learning in space information networks," *IEEE Network*, vol. 35, no. 4, pp. 82–87, 2021.

[222] L. Sun, Y. Gao, W. Huang, P. Li, Y. Zhou, and J. Yang, "Autonomous Time Synchronization Using BeiDou Inter-satellite Link Ranging," *ICSIDP 2019 - IEEE International Conference on Signal, Information and Data Processing 2019*, 2019.

[223] G. Giorgi, B. Kroese, and G. Michalak, "Future GNSS constellations with optical inter-satellite links. Preliminary space segment analyses," in *IEEE Aerospace Conference Proceedings*, vol. 2019-March. IEEE, 2019, pp. 1–13.

[224] P. Henkel, "Precise point positioning for next-generation GNSS," *2020 European Navigation Conference, ENC 2020*, pp. 1–11, 2020.

[225] J. A. Ruiz-De-Azua, A. Camps, and A. Calveras Auge, "Benefits of Using Mobile Ad-Hoc Network Protocols in Federated Satellite Systems for Polar Satellite Missions," *IEEE Access*, vol. 6, pp. 56 356–56 367, 2018.

[226] J. A. R. de Azua, A. Calveras, and A. Camps, "From monolithic satellites to the internet of satellites paradigm: When space, air, and ground networks become interconnected," in *Computer-Mediated Communication*, I. Dey, Ed. Rijeka: IntechOpen, 2022, ch. 2. [Online]. Available: https://doi.org/10.5772/intechopen.97200

[227] L. Fernandez, J. A. Ruiz-de Azua, A. Calveras, and A. Camps, "On-demand satellite payload execution strategy for natural disasters monitoring using LoRa: Observation requirements and optimum medium access layer mechanisms," *Remote Sensing*, vol. 13, no. 19, 2021. [Online]. Available: https://www.mdpi.com/2072-4292/13/19/4014

[228] J. A. De Azua, A. Calveras, and A. Camps, "Internet of Satellites (IoSat): Analysis of Network Models and Routing Protocol Requirements," *IEEE Access*, vol. 6, pp. 20 390–20 411, 2018.

[229] A. Ghasempour and S. K. Jayaweera, "Data synchronization for throughput maximization in distributed transmit beamforming," in *2017 Cognitive Communications for Aerospace Applications Workshop (CCAA)*. IEEE, jun 2017, pp. 1–4. [Online]. Available: http://ieeexplore.ieee.org/document/8001606/

[230] P. Sriploy and T. Chanpuek, "The enhancement of wireless sensor network in smart farming using distributed beamforming," in *1st International ECTI Northern Section Conference on Electrical, Electronics, Computer and Telecommunications Engineering, ECTI-NCON 2018.* IEEE, 2018, pp. 5–9.

[231] J. Diao, M. Hedayati, and Y. E. Wang, "Experimental Demonstration of Distributed Beamforming on Two Flying Mini-Drones," in *2019 United States National Committee of URSI National Radio Science Meeting (USNC-URSI NRSM)*, Boulder, CO, USA, 2019, pp. 97–98.

[232] S. Mohanti, C. Bocanegra, J. Meyer, G. Secinti, M. Diddi, H. Singh, and K. Chowdhury, "AirBeam: Experimental demonstration of distributed beamforming by a swarm of UAVs," in *IEEE 16th International Conference on Mobile Ad Hoc and Smart Systems, MASS 2019*, Monterey, CA, USA, 2019, pp. 162–170.

[233] A. Lan, J. Yan, L. Wu, F. Zhao, and J. Wu, "A study on in-orbit calibration for a spaceborne distributed interferometer," in *International Geoscience and Remote Sensing Symposium (IGARSS)*, vol. 2018-July, 2018, pp. 1043–1046.

[234] R. M. Dreifuerst, R. W. Heath, M. N. Kulkarni, and J. Charlie, "Deep Learning-based Carrier Frequency Offset Estimation with One-Bit ADCs," in *IEEE Workshop on Signal Processing Advances in Wireless Communications, SPAWC*, vol. 2020-May, 2020.

[235] E. Perahia and R. Stacey, *Next generation wireless LANs: 802.11 n and 802.11 ac.* Cambridge university press, 2013.

[236] L. T. Berger, A. Schwager, P. Pagani, and D. M. Schneider, "Mimo line communications," *IEEE Communications Surveys and Tutorials*, vol. 17, no. 1, pp. 106–124, 2014.

[237] 3GPP TS 38.211, "NR; Physical channels and modulation," *3rd Generation Partnership Project (3GPP), Technical Specification Group Radio Access Network*, vol. 17, 2021.

[238] K.-U. Storek, R. T. Schwarz, and A. Knopp, "Multi-satellite multi-user mimo precoding: Testbed and field trial," in *ICC 2020 - 2020 IEEE International Conference on Communications (ICC)*, 2020, pp. 1–7.

[239] J. Krivochiza, J. C. M. Duncan, J. Querol, N. Maturo, L. M. Marrero, S. Andrenacci, J. Krause, and S. Chatzinotas, "End-to-end precoding validation over a live GEO satellite forward link," *IEEE Access*, vol. 4, pp. 1–10, 2021.

[240] B. Shankar, M. E. Lagunas, S. Chatzinotas, and B. Ottersten, "Precoding for satellite communications: Why, how and what next?" *IEEE Communications Letters*, 2021.

[241] S. M. Ivari, M. Caus, M. A. Vazquez, M. R. Soleymani, Y. R. Shayan, and A. I. Perez-Neira, "Precoding and scheduling in multibeam multicast noma based satellite communication systems," in *2021 IEEE International Conference on Communications Workshops (ICC Workshops)*, 2021, pp. 1–6.

[242] A. Guidotti and A. Vanelli-Coralli, "Design trade-off analysis of precoding multi-beam satellite communication systems," in *2021 IEEE Aerospace Conference (50100)*, 2021, pp. 1–12.

[243] G. Taricco and A. Ginesi, "Precoding for flexible high throughput satellites: Hot-spot scenario," *IEEE Transactions on Broadcasting*, vol. 65, no. 1, pp. 65–72, 2019.

[244] A. m. Al-Nimrat, M. Smadi, O. A. Saraereh, and I. Khan, "An efficient channel estimation scheme for mmwave massive mimo systems," in *2019 IEEE International Conference on Communication, Networks and Satellite (Comnetsat)*, 2019, pp. 1–8.

[245] E. T. . 376-1, "ETSI TR 102 376-1: "Digital Video Broadcasting (DVB); Implementation Guidelines for the Second Generation System for Broadcasting, Interactive Services, News Gathering and Other Broadband Satellite Applications; Part 1: DVB-S2"," European Telecommunications Standards Institute (ETSI), Tech. Rep., 2015.

[246] A. Li, D. Spano, J. Krivochiza, S. Domouchtsidis, C. G. Tsinos, C. Masouros, S. Chatzinotas, Y. Li, B. Vucetic, and B. Ottersten, "A tutorial on interference exploitation via symbol-level precoding: Overview, state-of-the-art and future directions," *IEEE Communications Surveys and Tutorials*, vol. 22, no. 2, pp. 796–839, 2020.

[247] Y. Liu and W.-K. Ma, "Symbol-Level Precoding is Symbol-Perturbed zf When Energy Efficiency is Sought," in *2018 IEEE International Conference on Acoustics, Speech and Signal Processing (ICASSP)*, no. 2. IEEE, 2018, pp. 3869–3873.

[248] A. Li and C. Masouros, "Interference exploitation precoding made practical: Optimal closed-form solutions for PSK modulations," *IEEE Transactions on Wireless Communications*, vol. 17, no. 11, pp. 7661–7676, 2018.

[249] A. Li, C. Masouros, B. Vucetic, Y. Li, and A. L. Swindlehurst, "Interference exploitation precoding for multi-level modulations: Closed-form solutions," *IEEE Transactions on Communications*, vol. 69, no. 1, pp. 291–308, 2021.

[250] A. Haqiqatnejad, F. Kayhan, and B. Ottersten, "Power minimizer symbol-level precoding: A closed-form suboptimal solution," *IEEE Signal Process. Lett.*, vol. 25, no. 11, pp. 1730–1734, Nov. 2018.

[251] ——, "An approximate solution for symbol-level multiuser precoding using support recovery," in *IEEE Workshop on Signal Processing Advances in Wireless Communications, SPAWC*, vol. 2019-July. IEEE, 2019, pp. 19–23.

[252] J. Krivochiza, J. Merlano-Duncan, S. Andrenacci, S. Chatzinotas, and B. Ottersten, "Closed-form solution for computationally efficient symbol-level precoding," in *2018 IEEE Global Communications Conference (GLOBECOM)*, 2018, pp. 1–6.

[253] J. Guerreiro, R. Dinis, and P. Montezuma, "Analytical Performance Evaluation of Precoding Techniques for Nonlinear Massive MIMO Systems with Channel Estimation Errors," *IEEE Transactions on Communications*, vol. 66, no. 4, pp. 1440–1451, 2018.

[254] R. Krishnan, M. R. Khanzadi, N. Krishnan, Y. Wu, A. GraellAmat, T. Eriksson, and R. Schober, "Linear Massive MIMO Precoders in the Presence of Phase Noise - A Large-Scale Analysis," *IEEE Transactions on Vehicular Technology*, vol. 65, no. 5, pp. 3057–3071, 2016.

[255] O. Raeesi, A. Gokceoglu, Y. Zou, E. Björnson, and M. Valkama, "Performance Analysis of Multi-User Massive MIMO Downlink under Channel Non-Reciprocity and Imperfect CSI," *IEEE Transactions on Communications*, vol. 66, no. 6, pp. 2456–2471, 2018.

[256] T. Kebede, Y. Wondie, and J. Steinbrunn, "Massive MIMO Linear Precoding Techniques Performance Assessment," in *2021 International Symposium on Networks, Computers and Communications, ISNCC 2021*. IEEE, 2021.

[257] A. B. V, T.-h. Precoding, and A. S. Model, “Performance Analysis of Precoding Techniques for Massive MU-MIMO Systems,” in *2016 18th International Conference on Transparent Optical Networks (ICTON).* IEEE, 2015.

[258] A. Guidotti, C. Amatetti, F. Arnal, B. Chamaillard, and A. Vanelli-Coralli, “Location-assisted precoding in 5G LEO systems: architectures and performances,” in *2022 Joint European Conference on Networks and Communications and 6G Summit, EuCNC/6G Summit 2022.* IEEE, 2022, pp. 154–159.

[259] B. R. Elbert, *Introduction to satellite communication*, ser. Artech House space applications series. Norwood, Mass: Artech House, 2008.

[260] E. Bjornson, M. Bengtsson, and B. Ottersten, “Optimal multiuser transmit beamforming: A difficult problem with a simple solution structure [Lecture Notes],” *IEEE Signal Processing Magazine*, vol. 31, no. 4, pp. 142–148, 2014.

[261] N. Fatema, G. Hua, Y. Xiang, D. Peng, and I. Natgunanathan, “Massive MIMO Linear Precoding: A Survey,” *IEEE Systems Journal*, vol. 12, no. 4, pp. 3920–3931, 2018.

[262] C. Masouros and G. Zheng, “Exploiting known interference as green signal power for downlink beamforming optimization,” *IEEE Trans. Signal Process.*, vol. 63, no. 14, pp. 3628–3640, Jul. 2015.

[263] M. Alodeh, S. Chatzinotas, and B. Ottersten, “Constructive multiuser interference in symbol level precoding for the MISO downlink channel,” *IEEE Trans. Signal Process.*, vol. 63, no. 9, pp. 2239–2252, May 2015.

[264] A. Haqiqatnejad, F. Kayhan, and B. Ottersten, “Constructive interference for generic constellations,” *IEEE Signal Process. Lett.*, vol. 25, no. 4, pp. 586–590, Apr. 2018.

[265] A. Haqiqatnejad, F. Kayhan, and Ottersten, “Symbol-level precoding design based on distance preserving constructive interference regions,” *IEEE Trans. Signal Process.*, vol. 66, no. 22, pp. 5817–5832, Nov. 2018.

[266] M. Slawski and M. Hein, “Non-negative least squares for high-dimensional linear models: Consistency and sparse recovery without regularization,” *Electronic J. Statistics*, vol. 7, pp. 7661–7676, 2013.

[267] A. Haqiqatnejad, F. Kayhan, and B. Ottersten, "Energy-Efficient Hybrid Symbol-Level Precoding for Large-Scale mmWave Multiuser MIMO Systems," *IEEE Transactions on Communications*, vol. 69, no. 5, pp. 3119–3134, 2021.

[268] J. Rutman, "Characterization of Phase and Frequency Instabilities in Precision Frequency Sources: Fifteen Years of Progress." *Proceedings of the IEEE*, vol. 66, no. 9, pp. 1048–1075, 1978.

[269] Y. Yang, W. Wang, and X. Gao, "Distributed RZF Precoding for Multiple-Beam MSC Downlink," *IEEE Transactions on Aerospace and Electronic Systems*, vol. 54, no. 2, pp. 968–977, 2018.

[270] A. Gharanjik, M. R. Bhavani Shankar, P. D. Arapoglou, M. Bengtsson, and B. Ottersten, "Robust precoding design for multibeam downlink satellite channel with phase uncertainty," in *ICASSP, IEEE International Conference on Acoustics, Speech and Signal Processing - Proceedings*, vol. 2015-Augus, 2015, pp. 3083–3087.

[271] G. Taricco, "Linear Precoding Methods for Multi-Beam Broadband Satellite Systems," in *European Wireless 2014; 20th European Wireless Conference; Proceedings of*, 2014, pp. 1–6.

[272] Mubarak Umar Aminu, J. Lehtomäki, and Markku Juntti, "Beamforming and Transceiver Optimization with Phase Noise for mmWave and THz Bands," in *16th International Symposium on Wireless Communication Systems ISWCS 2019*, Oulu, Finland, 2019.

[273] R. Krishnan, M. R. Khanzadi, N. Krishnan, A. G. Amat, T. Eriksson, N. Mazzali, and G. Colavolpe, "On the Impact of Oscillator Phase Noise on the Uplink Performance in a Massive MIMO-OFDM System," *IEEE Signal Processing Letters*, pp. 1–5, 2014.

[274] A. Chorti and M. Brookes, "A spectral model for RF oscillators with power-law phase noise," *IEEE Transactions on Circuits and Systems I: Regular Papers*, vol. 53, no. 9, pp. 1989–1999, 2006.

[275] J. Mcneill, S. Razavi, K. Vedula, and D. Richard, "Experimental Characterization and Modeling of Low-Cost Oscillators for Improved Carrier Phase Synchronization," in *2017 IEEE International Instrumentation and Measurement Technology Conference*

(I2MTC), Turin, Italy, 2017. [Online]. Available: http://spinlab.wpi.edu/pubs/McNeill{_}I2MCT{_}2017.pdf

[276] I. Standards, *IEEE Std 1139-2008 (Revision of IEEE Std 1139-1999) IEEE Standard Definitions of Physical Quantities for Fundamental Frequency and Time Metrology–Random Instabilities*, 2009, vol. 2008, no. February.

[277] J. A. McNeill and D. S. Ricketts, *The Designer's Guide to Jitter in Ring Oscillators.* Springer, 2009, no. 1.

[278] C. Zucca and P. Tavella, "The clock model and its relationship with the Allan and related variances," *IEEE Transactions on Ultrasonics, Ferroelectrics and Frequency Control*, vol. 52, no. 2, pp. 289–296, feb 2005. [Online]. Available: http://ieeexplore.ieee.org/document/1406554/

[279] J. Duncan, J. Querol, N. Maturo, J. Krivochiza, D. Spano, N. Saba, L. Marrero, S. Chatzinotas, and B. Ottersten, "Hardware precoding demonstration in multibeam UHTS communications under realistic payload characteristics," in *ICSSC2019*, vol. 2019, no. CP774, 2019.

[280] ETSI, "Digital Video Broadcasting (DVB); Implementation guidelines for the second generation system for Broadcasting, Interactive Services, News Gathering and other broadband satellite applications; Part 2: S2 Extensions (DVB-S2X)," Technical Report ETSI TR 102 376-2 V1.2.1 (2021-01), 2021.

[281] L. M. Marrero, A. Haqiqatnejad, J. C. M. Duncan, S. Chatzinotas, and B. Ottersten, "Multiuser-MISO Precoding under Channel Phase Uncertainty in Satellite Communication Systems," *IEEE Open Journal of Vehicular Technology*, vol. PP, pp. 1–21, 2022.

[282] D. M. Pozar, *Microwave engineering*, 4th ed. Danvers, MA: John Wiley & Sons, 2012.

[283] Fuyun Ling, "Digital Frequency-Locked Loop," in *Synchronization in Digital Communication Systems.* Cambridge University Press, 2017, ch. Carrier Sy, pp. 193–270.

[284] F. Golnaraghi, *Design of Control Systems.* New York: Wiley, 2010.

[285] J. Bergmans, "Effect of loop delay on phase margin of first-order and second-order control loops," *IEEE Transactions on Circuits and Systems II: Express Briefs*, vol. 52, no. 10, pp. 621–625, 2005.

[286] F. Adachi, “Phase-combining diversity using adaptive decision-aided branch-weight estimation for reception of faded m-ary dpsk signals,” *IEEE Transactions on Vehicular Technology*, vol. 46, no. 3, pp. 786–790, 1997.

[287] F. Lavancier and P. Rochet, “A general procedure to combine estimators,” *Computational statistics & data analysis*, vol. 94, pp. 175–192, 2016.

[288] J. Duncan, J. Krivochiza, S. Andrenacci, S. Chatzinotas, and B. Ottersten, “Hardware demonstration of precoded communications in multi-beam UHTS systems,” in *36th International Communications Satellite Systems Conference (ICSSC 2018)*, 2018, pp. 1–5.

[289] N. Maturo, J. C. M. Duncan, J. Krivochiza, J. Querol, D. Spano, S. Chatzinotas, and B. Ottersten, “Demonstrator of precoding technique for a multi-beams satellite system,” in *2019 8th International Workshop on Tracking, Telemetry and Command Systems for Space Applications (TTC)*, 2019, pp. 1–8.

[290] J. Krivochiza, J. C. M. Duncan, J. Querol, N. Maturo, L. M. Marrero, S. Andrenacci, J. Krause, and S. Chatzinotas, “End-to-end precoding validation over a live GEO satellite forward link,” *IEEE Access*, pp. 1–10, 2021.